PARITY NONCONSERVATION FOR NEUTRON RESONANCES IN ^{81}Br AND ^{232}Th

CHRISTEN MARK FRANKLE

NORTH CAROLINA STATE UNIVERSITY
DEPARTMENT OF PHYSICS
and
TRIANGLE UNIVERSITIES NUCLEAR
LABORATORY
1991

ABSTRACT

FRANKLE, CHRISTEN MARK. Parity Nonconservation for Neutron Resonances in ^{81}Br and ^{232}Th. (Under the direction of Gary E. Mitchell.)

The helicity dependence of the neutron total cross section was measured for epithermal neutrons scattered from ^{81}Br and ^{232}Th. The experiment was performed at the Los Alamos Neutron Scattering Center located at Los Alamos National Laboratory. The neutron beam was polarized by transmission through a dynamically polarized proton sample, and the neutron spin was flipped every ten seconds with a magnetic spin rotator. Transmitted neutrons were detected with an array of seven ^{6}Li doped glass scintillation detectors located 56m from the neutron source. Results were obtained for one ^{81}Br resonance and 23 ^{232}Th resonances. The 0.88eV state in ^{82}Br has a longitudinal asymmetry of 1.77±0.33%. Seven states in ^{233}Th displayed parity violation effects of statistical significance greater than 2.4 standard deviations; two states had parity violations on the order of 10%. The parity violating matrix element was assumed to be a Gaussian random variable with mean zero and variance M^2. With a maximum likelihood analysis, the root-mean-square parity violating matrix element for the mixing of s-wave and p-wave states in ^{233}Th was determined to be $M=(1.39\ +0.63\ -0.42)$meV.

PARITY NONCONSERVATION FOR NEUTRON RESONANCES IN ^{81}Br AND ^{232}Th

by

CHRISTEN MARK FRANKLE

A thesis submitted to the Graduate Faculty of
North Carolina State University
in partial fulfillment of the
requirements for the Degree of
Doctor of Philosophy

DEPARTMENT OF PHYSICS

Raleigh

1991

APPROVED BY:

Chair of Advisory Committee

To the glory of God.

ACKNOWLEDGEMENTS

I offer my greatest thanks to my wife, Stephanie, not only for her love and support but also for many very helpful physics discussions and for finding my minus sign errors and missing factors of two.

I would like to thank Dr. G.E. Mitchell for all of his help during my graduate career, and especially for his assistance with the dissertation.

I gratefully acknowledge the work of all of the members of the TRIPLE collaboration, Dr. J.D. Bowman, Miss J.E. Bush, Dr. P.P.J. Delheij, Dr. C.R. Gould, Dr. D.G. Haase, Dr. J.N. Knudson, Dr. G.E. Mitchell, Dr. S.I. Penttila, Dr. H. Postma, Dr. N.R. Roberson, Dr. S.J. Seestrom, Dr. J.J. Szymanski, Dr. B. Tippens, Dr. S.H. Yoo, Dr. V.W. Yuan, and Mr. X. Zhu.

A great deal of thanks belongs to the unsung hero of these experiments, Mr. R.N. Mortensen, whose dedication (and superior pizza making ability!) is much appreciated.

I owe a debt of gratitude to Dr. N.M. Larson, whose assistance with the code SAMMY was invaluable.

The superior work of Mr. A.W. Lovette and Mr. E.P. Harris in the construction of the target chiller is sincerely appreciated.

I would also like to thank my parents for their love, support, and encouragement throughout my life.

The efforts of the support and operations personnel at Los Alamos National Laboratory are appreciated.

Some of the drawings in this dissertation are used courtesy of Los Alamos National Laboratory.

This work was funded by the United States Department of Energy.

TABLE OF CONTENTS

LIST OF FIGURES

LIST OF TABLES

CHAPTER I

Introduction

The possible observation of parity nonconservation via neutron-nucleus scattering was first proposed by Michel [Mi64]. When passed through a crystalline material, transversely polarized thermal neutrons behave analogously to a polarized electromagnetic wave passing through a refractive medium. Michel proposed that if parity were not conserved, then the polarization axis of transversely polarized thermal neutrons would rotate as the neutrons passed through the material. This rotation was later observed by Forte *et al.* [Fo80] Stodolsky [St74] discussed the possibility of observing a difference in the total cross section for longitudinally polarized neutrons of opposite helicity. Sushkov and Flambaum [Su82] noted that these effects could be quite large in heavy nuclei. Bunakov and Gudkov [Bu81][Bu83] give explicit expressions for the cross section difference when two compound nuclear states of the same spin but opposite parity mixed. This effect was first observed by Alfimenkov *et al.* [Al83] A more detailed description of the historical development is given in chapter II.

The observation of these very large parity violating effects in the helicity dependence of the total neutron cross section initiated a reconsideration of the physics of parity violation in heavy nuclei. There were two obstacles to the successful application of this new approach. The experimental difficulty was the energy limitation imposed by the use of reactors as the neutron source. This limitation was overcome by using the new, very high intensity spallation neutron source (LANSCE) at Los Alamos National Laboratory. A detailed description of the LANSCE facility

will be given in chapter IV. The analysis difficulty was perceived to be that the wavefunctions were very complicated and could not be determined in detail. This problem was overcome by adopting a statistical approach. The extreme complexity of the wavefunctions describing the resonances is assumed to ensure that the parity violating matrix element is itself a stochastic variable. Thus the stage was set for an entirely new approach to parity violation studies in heavy nuclei.

The Time Reversal Invariance and Parity at Low Energies (TRIPLE) collaboration formed in 1987 with the goal of studying parity violation and later time reversal invariance violation in the compound nuclear system. Personnel from North Carolina State University, Duke University, Los Alamos National Laboratory, TRIUMF, and Delft are currently involved in the collaboration. The collaboration utilizes the new, super intense epithermal neutron source at Los Alamos National Laboratory. The high intensity and large energy range permits the study of a much larger number of compound nuclear states than possible with reactors. During the 1989 run season data were taken on ^{238}U [Bo90]. A total of 17 resonances were studied and encouraging results obtained. Four of the states exhibited parity violations of statistical significance greater than two standard deviations. A parity violating matrix element of $M=(0.58 +0.50 -0.25)$meV was obtained. The results reported here are from data obtained during the 1989 and 1990 run seasons. Significant parity violating asymmetries were observed in states of ^{82}Br and ^{233}Th via the scattering of longitudinally polarized neutrons from targets of natural bromine and ^{232}Th.

Chapter II provides a short history of parity nonconservation measurements. Chapter III describes the theoretical background for the analysis of parity nonconservation experiments, while chapter IV describes the experimental ap-

paratus. Chapter V reports on auxiliary measurements designed to determine the limitations of the various pieces of experimental apparatus. Determination of the neutron polarization is also discussed in this chapter. The data analysis and the results are presented in chapter VI.

CHAPTER II

Historical Background

2.0 Introduction

The relative magnitude of the parity nonconserving force to the parity conserving force in the nucleon-nucleon interaction is expected to be on the order of 10^{-7}. (For example, see the review article by Desplanques, Donahue, and Holstein [De80].) Results consistent with this value have been measured in several experiments [Ca77][Ba80][Au84] [Au86] in the two and three body system. An experiment with polarized protons on alpha particles gave a null result to the same order of magnitude as the two and three body experiments [He82].

Although parity nonconservation was studied experimentally in heavy nuclei since the late 1950's, until recently these measurements have not received much theoretical attention. The discovery by Alfimenkov *et al.* [Al83] of extremely large parity violating effects in heavy nuclei stimulated a reexamination of parity nonconservation in such nuclei. To help underline the significance of the results of Alfimenkov *et al.*, the history of parity nonconservation experiments will be reviewed. A qualitative argument for the large size of the effects will given at the end of this chapter, and a more formal derivation will be presented in chapter III.

2.1 Parity Nonconservation in β-decay

Prior to 1934, three types of forces were known: gravi-

tational, electromagnetic, and strong. All three of these forces conserve parity. In 1934 Fermi [Fe34] proposed the existence of a fourth force, the weak force, in order to explain the β-decay of nuclei. At that time the weak force was also thought to conserve parity. It was some 20 years later that Lee and Yang [Le56] first suggested that parity might not be conserved in weak interactions. At that time there was no experimental evidence to show conclusively whether parity was or was not conserved in the weak interaction. The nonconservation of parity was first observed experimentally by Wu *et al.* [Wu57] in the β-decay of oriented ^{60}Co. Wu and her colleagues measured the number of decay electrons emitted at $\theta=0$ and $\theta=\pi$ with respect to the polarization axis of the ^{60}Co nuclei. A large asymmetry was observed; the experimental asymmetry in the decay of electrons from oriented ^{60}Co was accepted as evidence for the violation of spatial parity.

2.2 Parity Nonconservation in Light Nuclei

The weak interaction Hamiltonian, H_W, can be divided into three parts, pure leptonic (e.g., $\mu^- \rightarrow e^- + \bar{\nu}_e + \nu_\mu$), semi-leptonic (e.g., $\pi^- \rightarrow \mu^- + \bar{\nu}_\mu$, $\Lambda^0 \rightarrow p + e^- + \bar{\nu}_e$), and non-leptonic (e.g., $K^+ \rightarrow \pi^+ + \pi^0$) [Bl73]. The semi- and non-leptonic interactions can in turn be divided into strangeness conserving ($\Delta S=0$) and strangeness nonconserving ($\Delta S=1$) parts. Effects generated by the $\Delta S=0$ part are virtually impossible to see in elementary particle processes since they form only a small ($<10^{-6}$) background to the overwhelming strong interaction processes. As a result this term can be studied only in nuclear processes, where it gives rise to a

weak parity violating potential between nucleons. This potential has been parametrized by Desplanques, Donahue, and Holstein [De80] in terms of the parity violating coupling constants for pseudoscalar (π) and vector (ρ,ω) meson exchange. The π exchange vertex, f_π, has been of particular interest because it is expected to be dominated by neutral current (J_z) contributions [Ad85].

A number of experiments have also been performed in light nuclei. Adelburger *et al.* [Ad75] measured a non-zero left-right asymmetry in the gamma decay of polarized $^{19}F^*$. Several experiments [Ba78][Bi80][Ah82] attempted to observe circular polarization in the 1.1MeV decay γ-rays from $^{18}F^*$. A similar experiment [Sn78] used the 2.8MeV decay γ-rays from $^{21}Ne^*$. Parity forbidden β decays were observed [Ad83] in the β decay of ^{18}Ne and ^{19}Ne. Another group [Fi83] was successful in observing a parity forbidden resonance in the $^{16}O(\alpha,\gamma)$ reaction. In addition, the possibility of measuring parity violation in the $^{13}C(p,p)$ reaction has been explored [Ad84].

The data from p-p scattering, and from γ-decay studies in ^{18}F, ^{19}F, and ^{21}Ne indicate that h_ρ^0, the weak coupling constant for isoscalar ρ exchange, is non-zero, $\sim(2\text{-}3)\times10^{-6}$, and that f_π is smaller than expected, and possibly zero. These experiments have been very challenging and the measurements will not be easily improved upon. One interest in parity violation in heavy nuclei is therefore in finding alternate ways of determining the strengths of these meson exchange couplings.

2.3 Parity Nonconservation in the Compound Nuclear System

After the discovery of parity violation in β-decay, Tanner and Wilkinson [Ta57][Wi58a][Wi58b][Wi58c] proposed a number of other types of decay experiments, primarily emphasizing parity forbidden decays. In the next few years, a number of such experiments were performed [Br57][Ga57][Ku57][He58][Se58][Bo59][Al61][Gr61][Ka61][Se61][Se61a]. In all experiments either extremely small or zero asymmetries were observed. Blin-Stoyle suggested that for $(\vec{n},\gamma)$ reactions in general [Bl60] and for the $^{113}Cd(\vec{n},\gamma)$ reaction in particular [Bl61], there might be enhancement of the parity violating effect due to the structure of the compound nucleus. Haas, Leipuner, and Adair [Ha59] previously had attempted this experiment, but did not observe a significant effect.

In 1964 Abov, Krupchitsky, and Oratovsky [Ab64] performed the first $X(\vec{n},\gamma)$ experiment which observed parity violation. Unlike the β-decay experiment, this measurement used an unpolarized target nucleus and a polarized incident neutron beam. In this measurement the neutron polarization with respect to the neutron beam direction was changed from -90° to +90°, and a pair of NaI γ-ray detectors were used to search for a left-right asymmetry in the emitted capture γ-rays. Abov *et al.* were successful in observing a parity violating asymmetry of $(-3.7\pm0.9)\times10^{-4}$ in the $^{113}Cd(\vec{n},\gamma)$ reaction. This experiment was later repeated and the results confirmed [Wa67][Ab68][Wa69][Ab72]. The observation of this asymmetry stimulated interest in similar $(\vec{n},\gamma)$ and (n,γ) measurements with cold and thermal neutron beams

[Lo69][Al72][Fe73][Ga73][Da76][He78][Be79][Ko81][Av85]. Numerous small effects were observed. A comprehensive review was provided recently by Krupchitsky [Kr87].

In 1980 Forte *et al.* [Fo80] successfully observed neutron spin rotation due to parity violation. Using a beam of cold (E_n=1.6meV) neutrons from a high flux reactor at Grenoble, they performed a neutron polarizer-analyzer experiment, similar to an optical polarizer-analyzer experiment. The beam was transversely polarized with a magnetically saturated Fe-Co film evaporated onto a polyethylene sheet. The analyzer and polarizer were identical. The target was a highly enriched sample of ^{117}Sn (84% ^{117}Sn). A rotation of $(36.7\pm2.7)\times10^{-6}$ rad/cm was observed. Additional measurements of this type were performed by Heckel *et al.* [He82a]; parity violation was observed in a number of nuclei.

Vladimirsky and Andreev proposed in 1961 that if parity were not conserved then an asymmetry might be observable in the angular distribution of fragments from a fission reaction. Danilyan *et al.* first observed this effect using thermal neutrons on ^{235}U [Da77]. The following year they also reported an effect using ^{239}Pu as a target [Da78].

Interest in these experiments increased dramatically after the observation in the early 1980's of extremely large parity violating asymmetries by the Dubna group. These experiments were stimulated by the work of Sushkov and Flambaum [Su82]. Alfimenkov *et al.* performed an $X(\vec{n},n)$ total cross section experiment with the neutron beam polarized parallel and antiparallel to the beam direction. Neutron energies up to a few eV were used. The parity violating asymmetry is defined as

$$\mathcal{P} = \frac{\sigma^+ - \sigma^-}{\sigma^+ + \sigma^-}, \qquad (2.3.1)$$

where σ is the resonant cross section of the state exhibiting the parity violation and +(-) indicates neutron polarization parallel(antiparallel) to the beam direction. Alfimenkov *et al.* [Al83,84] observed an asymmetry of $\mathcal{P}$=7.3±0.5% in the 0.734eV state of ^{140}La, as well as smaller asymmetries for resonances in ^{81}Br, ^{111}Cd, and ^{117}Sn. The ^{140}La result has been confirmed at IAE ($\mathcal{P}$=7.6±0.6%) [Bi87], KEK ($\mathcal{P}$=9.7±0.5%) [Ma89], and Los Alamos ($\mathcal{P}$=9.2±1.7%) [Bo89]. Recently the TRIPLE collaboration measured $\mathcal{P}$=9.9±0.5% and $\mathcal{P}$=9.5±0.4% for neutron transmission and double lanthanum experiments, respectively [Yu91]. The double lanthanum technique will be discussed in more detail in section 5.5.3. The ^{140}La 0.734eV resonance is shown in figure 2.3.1 and the observed asymmetry for the neutron transmission experiment in figure 2.3.2.

2.4 Enhancement Estimates for Epithermal Neutron Scattering on Heavy Nuclei

The scattering of nucleons from nuclei is one method of probing the nucleon-nucleon (NN) interaction. It is now known that the strength of the weak force is approximately 10^{-7} that of the strong force. This was observed to be the case in NN scattering. The extremely large difference between the observed 10% asymmetry in ^{140}La and the expected 10^{-7} asymmetry led to a great increase of interest in the topic of parity violation in neutron-nucleus scattering.

To understand qualitatively the origin of the 10% asymmetry in ^{140}La, one must consider the fundamental differences between NN scattering and neutron-nucleus scattering. NN scattering involves only two nucleons, and the related few body measurements involve only a limited number of nucleons. However, neutron-nucleus scattering on heavy

Figure 2.3.1 Neutron transmission spectrum of the 0.734eV resonance in ^{140}La.

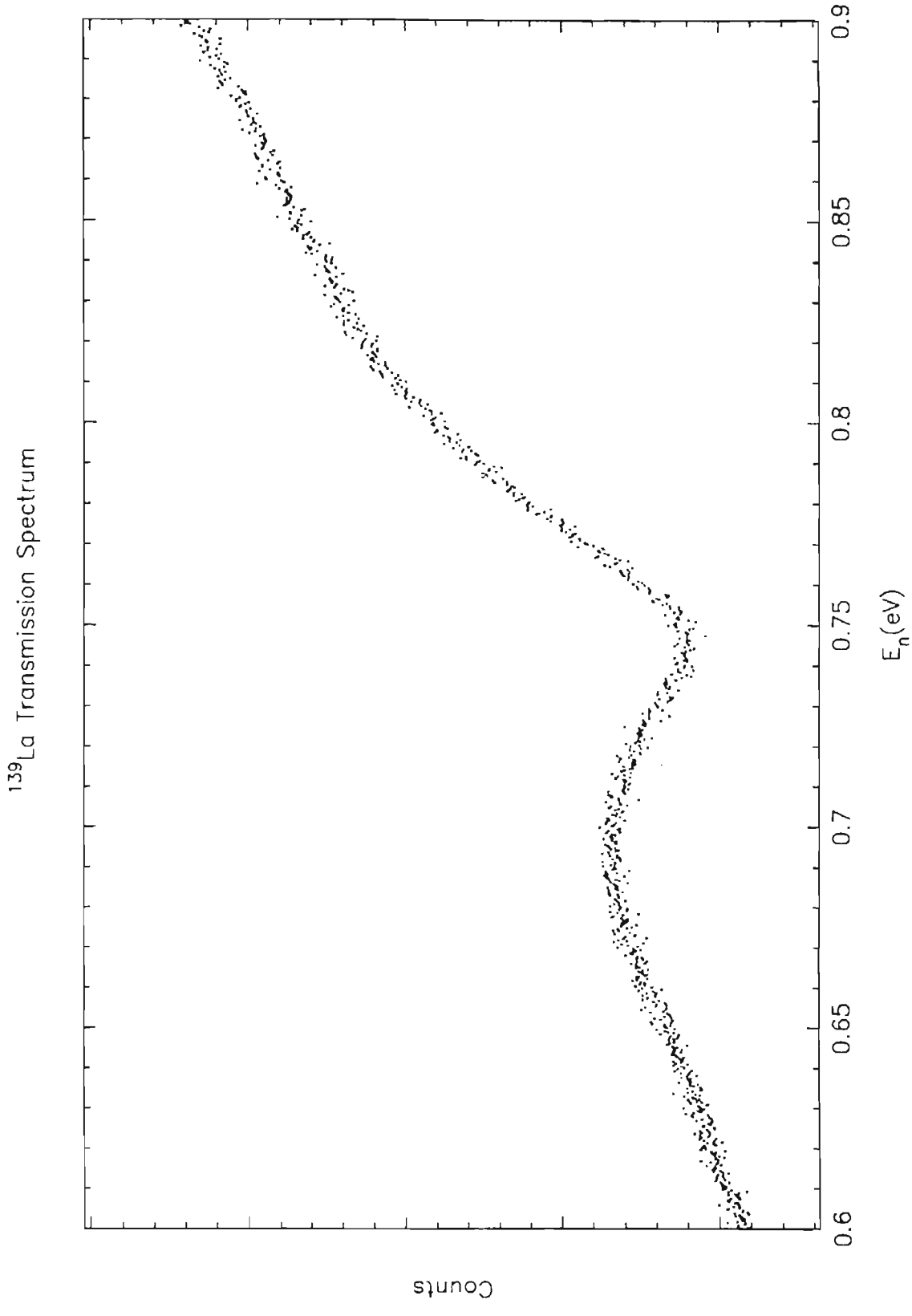
^{139}La Transmission Spectrum
Counts
0.6
0.65
0.7
0.75
0.8
0.85
0.9
E_n(eV)

Figure 2.3.2 Observed asymmetry for the 0.734eV ^{140}La p-wave resonance. The data displayed are averaged over three channels.

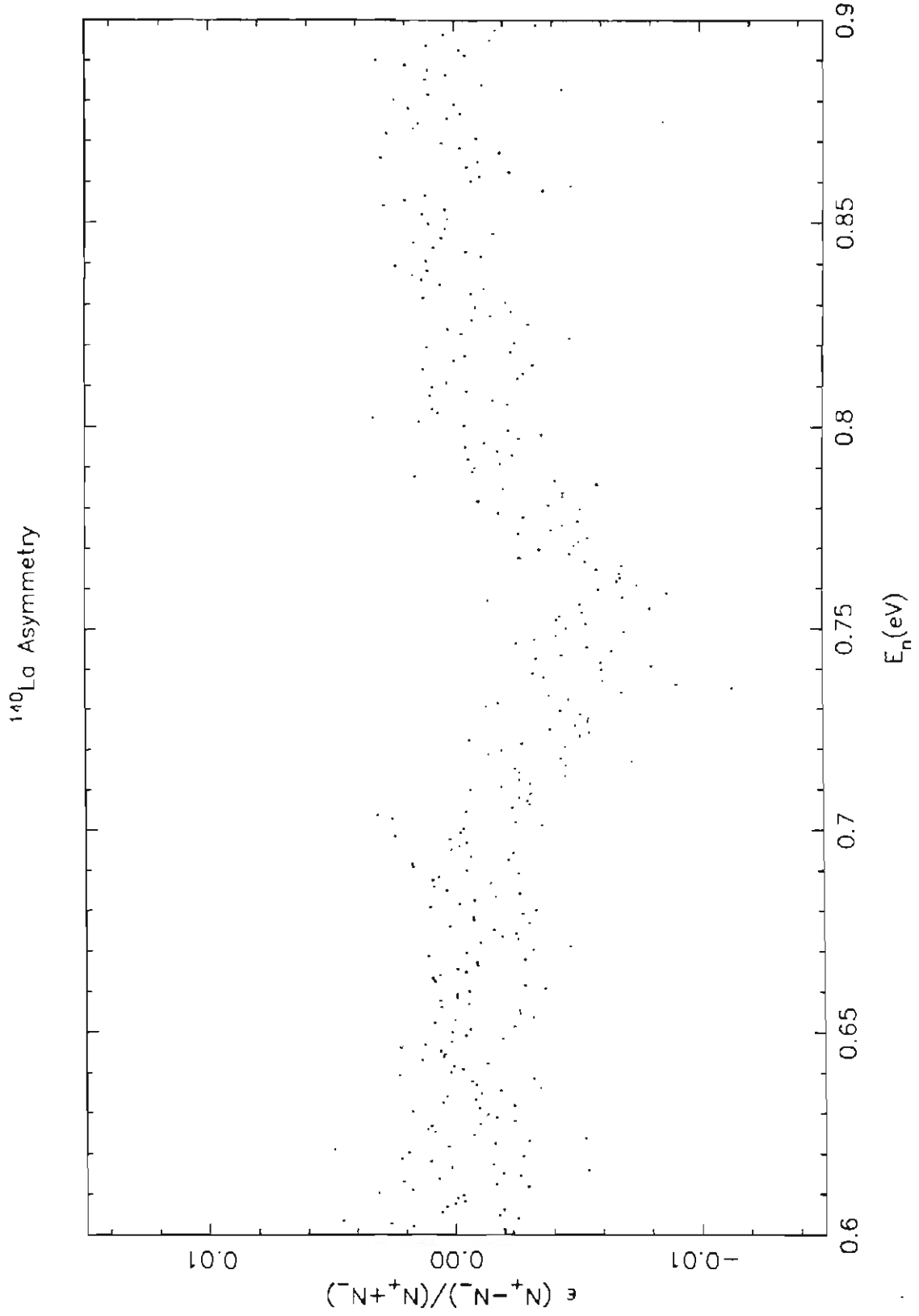
^{140}La Asymmetry
$\varepsilon\ (N_+ - N_-)/(N_+ + N_-)$
-0.01
0.00
0.01
0.6
0.65
0.7
0.75
0.8
0.85
0.9
E_n(eV)

nuclei (A≥100) involves many particles, which leads to an extremely complex wavefunction for the system. In this regime it is impossible to describe the details of the wavefunctions. Instead one views the system statistically. With statistical techniques it is possible to make predictions about the system without requiring detailed knowledge of the wavefunctions.

For experiments of the type previously described the parity violating asymmetry is known to have the form [Bu81][Mi89][Go90]

$$\mathcal{P} \approx P_z \frac{V}{E_s - E_p} x_j \sqrt{\frac{\Gamma_n^s}{\Gamma_n^p}}, \qquad (2.4.1)$$

where P_z is the neutron polarization, V is the matrix element which represents the mixing of two states with the same angular momentum but opposite parity, E_s and E_p are the energies of the two states, x_j is the entrance channel mixing parameter, and Γ_n^s and Γ_n^p are the neutron widths of the two states. A derivation of the cross section asymmetry will be given in section 3.4. In NN scattering the quantity $\mathcal{P}$ is a more direct measure of the weak interaction and is known to be on the order of 10^{-7}. Some of the quantities in eq. (2.4.1) have quite different values for the scattering of neutrons from heavy nuclei, as opposed to scattering from very light nuclei. Considering the changes in the values of these parameters between A~1 and A~200 provides a qualitative understanding of the origin of the large observed asymmetries.

The difference E_s-E_p is the level spacing between s-wave and p-wave states. For very light nuclei the average spacing is on the order of MeV, while in heavy nuclei it can be as small as a few eV. Therefore the factor $1/(E_s-E_p)$ can in-

crease (as A changes from A~1 to A~200) by as much as 10^6. The quantity V will decrease to approximately $V/\sqrt{N}$, [De84] where N represents the number of single particle components in the nuclear wavefunction. For very heavy nuclei $N\sim10^6$. This gives a combined net average increase in $V/(E_s-E_p)$ of about 10^3. This increase is referred to as "dynamical enhancement". In addition, the s-wave and p-wave penetrabilities scale differently. The s-wave penetrability is proportional to kR while the p-wave penetrability is proportional to $(kR)^3$. For epithermal neutrons on heavy nuclei, $kR<<1$. Therefore, an additional enhancement may arise from the ratio of the neutron widths. Typical values for Γ_n^s and Γ_n^p in heavy nuclei are 100meV and 0.01meV, respectively. With these typical widths the average ratio $\sqrt{\Gamma_n^s/\Gamma_n^p}$ is of order 100. (Note that in unfavorable cases this ratio could be less than one, or de-enhancement.) The increase in the quantity $\sqrt{\Gamma_n^s/\Gamma_n^p}$ is referred to as "structural enhancement". In reasonably favorable cases, combining the two enhancements leads to an overall enhancement of the order of 10^5, which raises the expected value of $\mathcal{P}$ to 10^{-2}. Therefore 1% parity violation effects are qualitatively reasonable in heavy nuclei.

With this qualitative understanding of the mechanisms responsible for the large enhancements to $\mathcal{P}$, one can estimate which nuclei are the most favorable candidates for experimental study. The remaining problem is to perform the experiments and analyze the data. In order to perform the analysis, detailed, quantitative expressions are required. The following chapter will be devoted to the theory necessary to understand and analyze these PNC experiments.

CHAPTER III

Theory

3.0 Introduction

In a neutron scattering reaction $^{A}X(n,n)$ with epithermal neutrons, states in the nucleus ^{A+1}X are formed. These states are long lived ($\sim 10^{-14}$s) compared to the transit time of a neutron across the nucleus ($\sim 10^{-19}$s). The nucleus ^{A+1}X is called the compound nucleus (CN). The compound nucleus concept was first proposed by Bohr [Bo37] and was further developed by Bethe [Be37]. Because the states formed in the CN live so long, they can be said to "forget" the details of how they were formed. The implication is that the decay of the CN is independent of the formation process. Therefore a peak (resonance) in the neutron cross section at a neutron energy E_n provides information about a state in the ^{A+1}X nucleus at an energy of E_n+S_n, where S_n is the neutron separation energy. This compound nucleus concept forms the basis for the theory developed in the next two sections.

3.1 Nuclear Scattering Cross Sections

First consider a reaction of the following type: $a+X \rightarrow b+Y$. Consider 'a' to be the projectile, 'X' the target, and 'b' and 'Y' the remaining fragments. Often there is more than one possibility for the remaining nuclei (b_1+Y_1, b_2+Y_2, etc.). Each different possibility is referred to as a channel [Br40]. The cross section is de-

fined as the number of detected particles per nucleus per unit time divided by the number of incident particles per unit area per unit time; the cross section is a key quantity of interest experimentally. Therefore we wish to obtain an expression for the cross section that can be applied to our particular experiment.

The quantity of interest is the total cross section, labeled σ_{TOT}. The total cross section can be separated into a pure scattering cross section plus the cross section for reactions, or $\sigma_{TOT}=\sigma_{SC}+\sigma_{R}$. (Detailed derivations may be found in Schiff [Sc68], Blatt and Weisskopf [Bl52], and Preston [Pr62].) Here the derivation is sketched.

Consider an incident plane wave of the form

$$\psi = Ae^{ikz} = Ae^{ikr\cos\theta}. \qquad (3.1.1)$$

The exponential can be expanded in terms of Legendre polynomials:

$$e^{ikr\cos\theta} = \sum_{\ell} A_{\ell} Y_{\ell 0} = \sum_{\ell} A_{\ell} P_{\ell}(\cos\theta). \qquad (3.1.2)$$

If both sides are multiplied by $P_{\ell'}(\cos\theta)$ and integrated over θ, the following expression is obtained for A_{ℓ}

$$A_{\ell} = (2\ell+1)i^{\ell} j_{\ell}(kr), \qquad (3.1.3)$$

where the $j_{\ell}(kr)$ are the spherical Bessel functions. Substituting eq. (3.1.3) into eq. (3.1.2), one obtains

$$e^{ikz} = \sqrt{4\pi}\sum_{\ell}\sqrt{2\ell+1}\,i^{\ell} j_{\ell}(kr) Y_{\ell 0}. \qquad (3.1.4)$$

For large z, the spherical Bessel function has the following asymptotic form:

$$j_{\ell}(z) \approx \frac{1}{z}\sin\left(z - \frac{\ell\pi}{2}\right). \qquad (3.1.5)$$

Then, applying the large z expansion to eq. (3.1.4),

$$e^{ikz} = \frac{\sqrt{4\pi}}{kr}\sum_{\ell}\sqrt{2\ell+1}\,i^{\ell}\sin\left(kr-\frac{\ell\pi}{2}\right)Y_{\ell 0} \qquad (3.1.6a)$$

$$= \frac{\sqrt{\pi}}{kr}\sum_{\ell}\sqrt{2\ell+1}\,i^{\ell+1}\left[e^{-i\left(kr-\frac{\ell\pi}{2}\right)}-e^{i\left(kr-\frac{\ell\pi}{2}\right)}\right]Y_{\ell 0}. \qquad (3.1.6b)$$

This is proportional to the incident wavefunction, ψ_{in}. It should be noted that

$$\psi_{in} = \psi_{tot} - \psi_{sc}\,. \qquad (3.1.7)$$

If eq. (3.1.6b) is rewritten and a convenient zero added, one has

$$e^{ikz} = \frac{\sqrt{\pi}}{kr}\sum_{\ell}\sqrt{2\ell+1}\,i^{\ell+1}\left[e^{-i\left(kr-\frac{\ell\pi}{2}\right)}-(1-U_{\ell}+U_{\ell})e^{i\left(kr-\frac{\ell\pi}{2}\right)}\right]Y_{\ell 0}. \qquad (3.1.8)$$

The quantity U_{ℓ} has magnitude less than one and characterizes the effect of a reaction on the cross section. Writing ψ_{in} in this form permits the identification of the components which form ψ_{tot} and ψ_{sc}:

$$\psi_{tot} \propto \frac{\sqrt{\pi}}{kr}\sum_{\ell}\sqrt{2\ell+1}\,i^{\ell+1}\left[e^{-i\left(kr-\frac{\ell\pi}{2}\right)}-(U_{\ell})e^{i\left(kr-\frac{\ell\pi}{2}\right)}\right]Y_{\ell 0}\ and \qquad (3.1.9a)$$

$$\psi_{sc} \propto \frac{\sqrt{\pi}}{kr}\sum_{\ell}\sqrt{2\ell+1}\,i^{\ell+1}\left[(1-U_{\ell})e^{i\left(kr-\frac{\ell\pi}{2}\right)}\right]Y_{\ell 0}. \qquad (3.1.9b)$$

Now calculate the basic expressions for the cross section. If $\sigma_{sc}=N_{sc}/N_{in}$ and noting that the probability density current is defined as

$$\vec{J} = \frac{\hbar}{2im}\left(\psi^{*}\nabla\psi - \psi\nabla\psi^{*}\right), \tag{3.1.10}$$

then the expressions for N_{sc} and N_{in} are:

$$N_{sc} \propto \int \frac{\hbar}{2im}\left(\frac{\partial\psi_{sc}}{\partial r}\psi_{sc}^{*} - \psi_{sc}\frac{\partial\psi_{sc}^{*}}{\partial r}\right) r^{2}\sin(\theta)\,d\theta\,d\varphi \quad \textit{and} \tag{3.1.11}$$

$$N_{in} \propto \frac{\hbar}{2im}\left(\frac{\partial\psi_{in}}{\partial z}\psi_{in}^{*} - \psi_{in}\frac{\partial\psi_{in}^{*}}{\partial z}\right). \tag{3.1.12}$$

Note that N_{sc} is the number of particles scattered per nucleus per unit time and N_{in} is the number of particles incident per unit area per unit time. Inserting eq. (3.1.9b) into eq. (3.1.11) and evaluating the integral, one obtains

$$N_{sc} \propto \frac{\pi}{mk}\frac{\hbar}{}\sum_{\ell}(2\ell+1)\left|1-U_{\ell}\right|^{2}. \tag{3.1.13}$$

Similarly, one obtains the following for N_{in}:

$$N_{in} \propto \frac{\hbar k}{m}. \tag{3.1.14}$$

Then the scattering cross section is written as

$$\sigma_{sc} = \frac{\pi}{k^{2}}\sum_{\ell}(2\ell+1)\left|1-U_{\ell}\right|^{2}. \tag{3.1.15}$$

One can also obtain an expression for the reaction cross section, $\sigma_R = N_{tot}/N_{in}$, where N_{tot} has the form

$$N_{tot} \propto \int \frac{\hbar}{2im}\left(\frac{\partial\psi_{tot}}{\partial r}\psi_{tot}^{*} - \psi_{tot}\frac{\partial\psi_{tot}^{*}}{\partial r}\right) r^{2}\sin(\theta)\,d\theta\,d\varphi. \tag{3.1.16}$$

Upon evaluating N_{tot} one obtains

$$N_{tot} \propto \frac{\pi}{mk^{2}}\frac{\hbar}{}\sum_{\ell}(2\ell+1)\left(1-\left|U_{\ell}\right|^{2}\right). \tag{3.1.17}$$

Observe that N_{tot} is the number of particles absorbed per nucleus per unit time. Dividing eq. (3.1.17) by N_{in} then gives the reaction cross section:

$$\sigma_R = \frac{\pi}{k^2}\sum_{\ell}(2\ell+1)\left(1-|U_\ell|^2\right). \qquad (3.1.18)$$

While this has been a general derivation of the cross section for a nuclear reaction, it is of limited usefulness. All of the information connected with the nuclear behavior is contained in U_ℓ. The important result from this derivation is the form of the cross section. Any more complicated theory will have the same form.

Now return to the reaction X(a,b)Y. Label the system of a+X and all of its quantum numbers by the letter c, denoting the entrance channel. Similarly denote the system b+Y and all of its quantum numbers by c', the exit channel. The cross section for a system which forms via entrance channel c and decays via exit channel c' will be denoted $\sigma_{cc'}$. An expression for $\sigma_{cc'}$ will be obtained in two steps. First, the cross section is related to the R-matrix, which contains information about the nuclear states. The R-matrix was first introduced by Wigner and Eisenbud [Wi47]; since then several review articles have been published [La58][Vo62]. The derivation of the R-matrix will be performed in two parts, first deriving an R function appropriate for a single channel and then generalizing to the multichannel R-matrix. Secondly, the angular correlation function will be derived, which will contain information about the variation of the intensity of exit particles with respect to the polar and azimuthal angles.

3.2 Derivation of the Cross Section via an R-Matrix Approach

3.2.0 Introduction

One of the fundamental ideas of R-matrix theory is that there is a well defined nuclear radius, a_c, that can be associated with each channel. Within this radius, all nuclear interactions take place. Outside, only Coulomb and other long range interactions affect the system.

3.2.1 Single Channel Case

With the concept of a channel radius in mind, one can define the total wavefunction, Ψ, for the system as

$$\Psi = \varphi\chi\psi_{a1}\psi_{a2}. \qquad (3.2.1.1)$$

Here φ is the wavefunction of the motion of the center of mass, χ is the wavefunction representing the relative motion of the two particles, and ψ_{a1} and ψ_{a2} are the internal wavefunctions of the two particles.

Consider the relative motion of the particles. It is convenient to introduce the regular and irregular Coulomb wavefunctions F_ℓ and G_ℓ. The F_ℓ and G_ℓ functions are defined in terms of spherical Bessel functions as follows:

$$F_\ell = \rho\, j_\ell(\rho) \qquad (3.2.1.2a)$$

$$G_\ell = \rho\eta_\ell(\rho). \qquad (3.2.1.2b)$$

Certain combinations of F_ℓ and G_ℓ are useful, namely

$$I_\ell = (G_\ell - iF_\ell)e^{i\omega_\ell} \qquad (3.2.1.3a)$$

$$O_\ell = (G_\ell + iF_\ell)e^{-i\omega_\ell}. \qquad (3.2.1.3b)$$

It is first necessary to find a solution for the radial part of the relative motion wavefunction. The radial equation is

$$\frac{d^2u_\ell}{dr^2}+\frac{2\mu}{\hbar^2}\left[E-V-\frac{\ell(\ell+1)\hbar^2}{2\mu r^2}\right]u_\ell=0 \qquad (3.2.1.4)$$

with the boundary condition $u_\ell(0)=0$. Note that

$$\chi=(I_\ell-U_\ell O_\ell)Y_\ell^m \qquad (3.2.1.5)$$

is a solution of eq. (3.2.1.4). U_ℓ will be considered further later.

Next consider the internal wavefunctions. For the compound nuclear system, there is some complete set of radial eigenstates $\{u_\lambda\}$. Any general state, u_E, can then be expanded in terms of the set $\{u_\lambda\}$. The expansion coefficients, A_λ, are found by

$$A_\lambda=\int_0^c u_\lambda^* u_E\,dr. \qquad (3.2.1.6)$$

From the Schroedinger equation for u_E and u_λ one has

$$\frac{d^2u_E}{dr^2}+\frac{2\mu}{\hbar^2}(E-V')u_E=0 \quad and \qquad (3.2.1.7a)$$

$$\frac{d^2u_\lambda}{dr^2}+\frac{2\mu}{\hbar^2}(E_\lambda-V')u_\lambda=0. \qquad (3.2.1.7b)$$

Multiplying eq. (3.2.1.7a) by u_λ^* and the complex conjugate of eq. (3.2.1.7b) by u_E and then subtracting and integrating, one obtains

$$\int_0^{a_c}\left(u_\lambda^{\bullet}\frac{d^2u_E}{dr^2}-u_E\frac{d^2u_\lambda^{\bullet}}{dr^2}\right)dr+\frac{2\mu}{\hbar^2}(E-E_\lambda)\int_0^{a_c}u_E u_\lambda^{\bullet}dr=0, \qquad (3.2.1.8)$$

which reduces to

$$\int_0^{a_c}\frac{d}{dr}\left(u_\lambda^{\bullet}\frac{du_E}{dr}-u_E\frac{du_\lambda^{\bullet}}{dr}\right)dr+\frac{2\mu}{\hbar^2}(E-E_\lambda)A_\lambda=0. \qquad (3.2.1.9)$$

Evaluating the integral and applying the boundary condition

$$\left.\frac{du_\lambda}{dr}\right|_{r=a_c}=0, \qquad (3.2.1.10)$$

one can solve for the A_λ in eq. (3.2.1.9) and obtain

$$A_\lambda=\frac{\hbar^2}{2\mu}\frac{1}{E_\lambda-E}u_\lambda^{\bullet}(a_c)\left.\frac{du_E}{dr}\right|_{r=a_c}. \qquad (3.2.1.11)$$

Making use of the definition of the u_E and eq. (3.2.1.11) gives the result

$$u_E=\frac{\hbar^2}{2\mu}\left(\frac{a_c}{a_c}\right)\sum_\lambda\frac{u_\lambda^{\bullet}(a_c)u_\lambda(r)}{E_\lambda-E}\left.\frac{du_E}{dr}\right|_{r=a_c}. \qquad (3.2.1.12)$$

It is convenient to define the R function as

$$R=\left.\frac{u}{r\dfrac{du}{dr}}\right|_{r=a}. \qquad (3.2.1.13)$$

Inserting the wavefunction u_E in place of the general wavefunction u in eq. (3.2.1.13) gives

$$R=\frac{u_E(a_c)}{a_c\left.\dfrac{du_E}{dr}\right|_{r=a_c}}=\frac{\hbar^2}{2\mu\,a_c}\sum_\lambda\frac{u_\lambda^2(a_c)}{E_\lambda-E}. \qquad (3.2.1.14)$$

The very useful quantity

$$\gamma_\lambda \equiv \sqrt{\frac{\hbar^2}{2\mu\, a_c}} u_\lambda(a_c) \qquad (3.2.1.15)$$

is normally referred to as the reduced width amplitude.

To find a similar R function for the exterior region, one takes the radial part of eq. (3.2.1.5) and substitutes it into eq. (3.2.1.13) to yield

$$R = \left.\frac{(I_\ell - U_\ell O_\ell)}{a_c\left(I_\ell' - U_\ell O_\ell'\right)}\right|_{r=a_c}, \qquad (3.2.1.16)$$

where the prime represent a derivative with respect to r. Several convenient quantities are usually defined:

$$L \equiv kr\left.\frac{O'}{O}\right|_{r=a_c} \equiv S + iP \quad and \qquad (3.2.1.17)$$

$$\Omega \equiv \sqrt{\frac{I}{O}}. \qquad (3.2.1.18)$$

Solving eq. (3.2.1.16) for U_ℓ gives

$$U_\ell = \frac{\left.\left(\frac{I_\ell}{O_\ell} - R\rho\frac{I_\ell'}{O_\ell}\right)\right|_{r=a_c}}{\left.\left(1 - R\rho\frac{O_\ell'}{O_\ell}\right)\right|_{r=a_c}}, \qquad (3.2.1.19)$$

where $\rho=kr$.

Substituting the definitions for L and Ω gives the final result

$$U_\ell = \Omega^2\frac{\left(1 - RL^*\right)}{(1 - RL)}. \qquad (3.2.1.20)$$

3.2.2 Multichannel Case

Now one wishes to generalize, making similar arguments but taking into account the possibility of many levels and many channels -- in other words to generalize the R function into an R-matrix. Consider an internal wavefunction ψ. There is a complete set of eigenstates $\{X_\lambda\}$ such that

$$\psi = \sum_\lambda A_\lambda X_\lambda . \qquad (3.2.2.1)$$

Solving for the A_λ gives

$$A_\lambda = \int_\tau X_\lambda^* \psi \, d\tau . \qquad (3.2.2.2)$$

Given that there exists some nuclear Hamiltonian, whose form in general is not known, one can write down the Schroedinger equation

$$HX_\lambda = E_\lambda X_\lambda . \qquad (3.2.2.3)$$

Assuming that time reversal invariance holds,

$$-\frac{\hbar^2}{2\mu}\nabla^2 X_\lambda^* + VX_\lambda^* = E_\lambda X_\lambda^* . \qquad (3.2.2.4)$$

A Schroedinger equation can be constructed for some other level λ',

$$-\frac{\hbar^2}{2\mu}\nabla^2 X_{\lambda'} + VX_{\lambda'} = E_{\lambda'} X_{\lambda'} . \qquad (3.2.2.5)$$

Multiplying eq. (3.2.2.2) by X_λ, and eq. (3.2.2.3) by $X_\lambda{}^*$, and subtracting, one obtains

$$-X_{\lambda'}\frac{\hbar^2}{2\mu}\nabla^2 X_\lambda^* + X_\lambda^*\frac{\hbar^2}{2\mu}\nabla^2 X_{\lambda'} = (E_\lambda - E_{\lambda'})X_{\lambda'} X_\lambda^* . \qquad (3.2.2.6)$$

After integrating and applying Green's theorem to the left

hand side, one obtains

$$\frac{\hbar^2}{2\mu}\int\left(X_\lambda^*\nabla X_{\lambda'}-X_{\lambda'}\nabla X_\lambda^*\right)\cdot d\vec{S}=\left(E_\lambda-E_{\lambda'}\right)\int X_\lambda^* X_{\lambda'}\cdot d\tau=0. \tag{3.2.2.7}$$

The eigenfunctions X_λ can be expressed in term of a radial part, $u_{\lambda c}$, and a surface part, φ_c. This is written as

$$X_\lambda=\sum_c \varphi_c u_{\lambda c}. \tag{3.2.2.8}$$

Putting the new definition of X_λ into the left hand side of eq. (3.2.2.7) gives

$$\sum_c \frac{\hbar^2}{2\mu_c}\int\left(\varphi_c^* u_{\lambda c}^*\nabla\varphi_c u_{\lambda' c}-\varphi_c u_{\lambda' c}\nabla\varphi_c^* u_{\lambda c}^*\right)\cdot d\vec{S}=0. \tag{3.2.2.9}$$

Evaluating the gradient operator and dropping terms which do not survive the dot product leaves

$$\sum_c \frac{\hbar^2}{2\mu_c}\int\left(\varphi_c^*\varphi_c\, u_{\lambda c}^*\frac{\partial u_{\lambda' c}}{\partial r}-\varphi_c\varphi_c^* u_{\lambda' c}\frac{\partial u_{\lambda c}^*}{\partial r}\right)dS=0. \tag{3.2.2.10}$$

After evaluation of the integral one is left with

$$\sum_c \frac{\hbar^2}{2\mu_c}\left(u_{\lambda c}^*\frac{\partial u_{\lambda' c}}{\partial r}-u_{\lambda' c}\frac{\partial u_{\lambda c}^*}{\partial r}\right)\Bigg|_{r=a_c}=0. \tag{3.2.2.11}$$

Next, if instead of using X_λ and $X_{\lambda'}$, one uses X_λ and an arbitrary wavefunction ψ, as in eq. (3.2.2.1), then the result is similar to eq. (3.2.2.11)

$$\sum_c \frac{\hbar^2}{2\mu_c}\left(u_{\lambda c}^*\frac{\partial u_c}{\partial r}-u_c\frac{\partial u_{\lambda c}^*}{\partial r}\right)\Bigg|_{r=a_c}=0. \tag{3.2.2.12}$$

Applying the condition that the derivative of the radial eigenstates is zero on the boundary simplifies eq. (3.2.2.12) to

$$\sum_c \frac{\hbar^2}{2\mu}\left(u_{\lambda c}^{*}\frac{\partial u_c}{\partial r}\right)\Bigg|_{r=a_c} = (E_\lambda - E)\int X_\lambda^{*}\psi\, d\tau. \qquad (3.2.2.13)$$

Putting the definition of A_λ from eq. (3.2.2.2) into eq. (3.2.2.13) and solving for A_λ gives

$$A_\lambda = \frac{\sum_c \frac{\hbar^2}{2\mu}\left(u_{\lambda c}^{*}\frac{\partial u_c}{\partial r}\right)\Big|_{r=a_c}}{E_\lambda - E}. \qquad (3.2.2.14)$$

Eq. (3.2.2.1) can now be updated: (Note the change of index from c to c'.)

$$\psi = \sum_\lambda A_\lambda X_\lambda = \frac{\hbar^2}{2\mu}\sum_{c'}\frac{\partial u_{c'}}{\partial r}\Big|_{r=a_{c'}} \sum_\lambda \frac{u_{\lambda c'}^{*}(a_{c'})}{E_\lambda - E} X_\lambda. \qquad (3.2.2.15)$$

If the following construction is made using eq.(3.2.2.15),

$$\int \varphi_c^{*}\psi\, dS = \frac{\hbar^2}{2\mu}\sum_{c'}\frac{\partial u_{c'}}{\partial r}\Big|_{r=a_{c'}} \sum_\lambda \frac{u_{\lambda c'}^{*}(a_{c'})}{E_\lambda - E}\int \varphi_c^{*} X_\lambda\, dS, \qquad (3.2.2.16)$$

then using the inverse of eq. (3.2.2.8) yields an expression for u_C:

$$u_c(a_c) = \frac{\hbar^2}{2\mu}\sum_{c'}\frac{\partial u_{c'}}{\partial r}\Big|_{r=a_{c'}} \sum_\lambda \frac{u_{\lambda c'}^{*}(a_{c'})}{E_\lambda - E} u_{\lambda c}(a_c). \qquad (3.2.2.17)$$

In order to be consistent with the standard notation, it is necessary to define the following two quantities:

$$V_{\lambda c} = \sqrt{\frac{\hbar^2}{2\mu a_c}}\, u_{\lambda c}(a_c) \quad and \qquad (3.2.2.18a)$$

$$D_{\lambda c} = \sqrt{\frac{\hbar^2 a_c}{2\mu}}\frac{\partial u_{\lambda c}(a_c)}{\partial r}\Bigg|_{r=a_c}. \qquad (3.2.2.18b)$$

Using the definitions of eqs. (3.2.2.18a) and (3.2.2.18b) in eq. (3.2.2.17) gives

$$V_c = \sum_{c'} D_{c'} \frac{\hbar^2}{2\mu\sqrt{a_{c'}}\sqrt{a_c}} \sum_{\lambda} \frac{u^*_{\lambda c'}(a_{c'}) u_{\lambda c}(a_c)}{E_\lambda - E}. \qquad (3.2.2.19)$$

The R-matrix is defined such that eq. (3.2.2.19) becomes

$$V_c = \sum_{c'} R_{cc'} D_{c'}. \qquad (3.2.2.20)$$

Note that the R-matrix of eq. (3.2.2.20) has the same form as the R function of eq. (3.2.1.13). This derivation leads to an R-matrix whose dimension is the number of channels in the problem. One may also derive an alternate scheme where the R-matrix has the dimension of the number of levels. The two schemes are interchangeable and one is chosen over the other only for convenience.

In order to calculate a cross section it is necessary to relate the R-matrix to the scattering matrix, U. Recall that in the exterior region the wavefunction has the form

$$\psi = \mathcal{I} - U\mathcal{O}. \qquad (3.2.2.21)$$

Now rewrite eq. (3.2.2.21) into a new form

$$\psi = \sum_c B_c \mathcal{O}_c + C_c \mathcal{I}_c, \qquad (3.2.2.22)$$

where

$$B_c = -\sum_{c'} U_{cc'} C_{c'}. \qquad (3.2.2.23)$$

Recall that $\mathcal{I}$ and $\mathcal{O}$ have the form

$$\mathcal{W} = Ai^{\ell} Y_\ell^m \frac{W_\ell}{r} \qquad (3.2.2.24)$$

where $\mathbf{W}(\mathcal{W})$ represents either $\mathrm{I}(\mathcal{I})$ or $\mathrm{O}(\mathcal{O})$. For a beam of particles of unit current, $A=1/\sqrt{v}$, where v is the velocity of the particles. Constructing the radial part of the wavefunction for one channel using eqs. (3.2.2.22),

(3.2.2.23), and (3.2.2.24) gives

$$u_c = \left(C_c I_c - \sum_{c'} C_c U_{cc'} O_c \right) v^{-1/2}. \qquad (3.2.2.25)$$

Then evaluating the value and derivative quantities of eq. (3.2.2.18), gives

$$V_c = \sqrt{\frac{\hbar^2}{2\mu a_c}} \left(C_c I_c - \sum_{c'} C_{c'} U_{cc'} O_c \right) v_c^{-1/2} \Big|_{r=a_c} \quad and \qquad (3.2.2.26a)$$

$$D_c = \sqrt{\frac{\hbar^2 a_c}{2\mu}} \left(C_c \frac{\partial I_c}{\partial r}\Big|_{r=a_c} - \sum_{c'} C_{c'} U_{cc'} \frac{\partial O_c}{\partial r}\Big|_{r=a_c} \right) v_c^{-1/2}. \qquad (3.2.2.26b)$$

Putting eqs. (3.2.2.26a) and (3.2.2.26b) into eq. (3.2.2.18) gives

$$\mathrm{v_c^{-1/2}} \sqrt{\frac{\hbar^2}{2\mu\, a_c}} \left(\mathrm{C_c I_c - \sum_{c'} C_{c'} U_{cc'} O_c} \right)\Big|_{r=a_c} = \sum_{c''} \mathrm{R_{cc''}} \sqrt{\frac{\hbar^2 a_{c''}}{2\mu}} \mathrm{v_{c''}^{-1/2}}$$
$$\times \left(\mathrm{C_{c''} \frac{\partial I_{c'}}{\partial r}\Big|_{r=a_c} - \sum_{c'''} C_{c''} U_{c''c'''} \frac{\partial O_{c'}}{\partial r}\Big|_{r=a_{c'}}} \right). \qquad (3.2.2.27)$$

Simplifying eq. (3.2.2.27) and rearranging terms, yields

$$\frac{1}{\sqrt{k_c a_c}} \left(I_c C_c - \sum_{c'} O_c U_{cc'} C_{c'} \right)\Big|_{r=a_c} = \sum_{c''} R_{cc''} \sqrt{\frac{a_{c'}}{k_{c''}}} \left(\frac{\partial I_{c'}}{\partial r}\Big|_{r=a_c} C_{c''} - \sum_{c'''} \frac{\partial O_{c''}}{\partial r}\Big|_{r=a_{c'}} U_{c''c'''} C_{c'''} \right). \qquad (3.2.2.28)$$

The ordering of eq. (3.2.2.28) lends itself to a conversion to matrix notation. Let $\mathbf{k}, \mathbf{a}, \mathbf{I}, \mathbf{O}, \partial\mathbf{I}/\partial\mathbf{r}$, and $\partial\mathbf{O}/\partial\mathbf{r}$ be square, diagonal matrices. $\mathbf{U}$ and $\mathbf{R}$ will be square, non-diagonal matrices and $\mathbf{C}$ will be a vector. These matrices all have the number of channels as their dimension. Rewriting eq. (3.2.2.28) into matrix notation yields

$$k^{-1/2}a^{-1/2}IC - k^{-1/2}a^{-1/2}OUC = Rk^{-1/2}a^{1/2}I'C - Rk^{-1/2}a^{1/2}O'UC \qquad (3.2.2.29)$$

where the prime indicates a partial derivative with respect to r. Rearranging eq. (3.2.2.29) in order to solve for **U** gives

$$\left(RaO'O^{-1} - 1\right)Ok^{-1/2}a^{-1/2}U = \left(RaI'I^{-1} - 1\right)Ik^{-1/2}a^{-1/2}. \qquad (3.2.2.30)$$

Here the symbol 1 indicates the identity matrix. With the definition ρ=ka and recalling the definition of **L** from eq. (3.2.1.17), eq. (3.2.2.30) reduces to

$$U = \rho^{1/2}O^{-1}(1 - RL)^{-1}\left(1 - RL^{*}\right)I\rho^{1/2}. \qquad (3.2.2.31)$$

Utilizing the definition of Ω from eq. (3.2.1.18) gives **U** its final form:

$$U = \Omega P^{1/2}(1 - RL)^{-1}\left(1 - RL^{*}\right)P^{-1/2}\Omega = \Omega W\Omega. \qquad (3.2.2.32)$$

One way to utilize **U** is to insert it into one of the expressions for the cross section (e.g., eq. (3.1.15) or eq. (3.1.17)). Those equations have limited usefulness, however, since they were derived implicitly assuming spinless particles. In order to analyze even the simplest experiments (e.g., low energy ℓ=0 neutron total cross section) one needs more detailed expressions for the cross section that take into account the spins of the particles.

3.3 Angular Correlations

3.3.0 Introduction

Consider once again the reaction $a + X \rightarrow b + Y$. Label the intrinsic spins of the particles as **i**, **I**, **i'**, and **I'**. The orbital angular momentum between 'a' and 'X' will be ℓ and similarly for 'b' and 'Y' the label will be ℓ'. One may couple these angular momenta together in different ways. We choose what is called the channel spin notation. In

this notation **i** and **I** are first coupled to form the 'channel spin', **s**. Then **s** and the orbital angular momentum, $\boldsymbol{\ell}$, are coupled to form the total angular momentum, **J**. (See figure 3.3.0.1.) The same scheme holds for the primed vectors. With the notation established, we wish to find new expressions for the cross section that take spin into account.

3.3.1 Derivation of the Angular Correlation Function

Given a basis set of pure states $\{|\alpha\rangle\}$, and a system which has probabilities p_α of being in state $|\alpha\rangle$ (i.e., the system state is a linear combination of the $\{|\alpha\rangle\}$.), then one can define a density matrix, ρ,

$$\langle n|\rho|n'\rangle = \sum_\alpha \langle n|\alpha\rangle p_\alpha \langle\alpha|n'\rangle. \qquad (3.3.1.1)$$

The $\{|n\rangle\}$ are a complete set of eigenvectors in the representation in which one chooses to work. This density matrix has the property that for a given operator, $\mathcal{Q}$, $\langle\mathcal{Q}\rangle = Tr(\mathcal{Q}\rho)$. Introducing an operator, ε, which represents the detection process of the final state of the system, then

$$\boldsymbol{w} = \langle\varepsilon\rangle = Tr(\varepsilon\rho), \qquad (3.3.1.2)$$

where ε is called the "efficiency" matrix (operator). This approach was first introduced by Fano [Fa53] and Coester and Jauch [Co53]. This topic is described in a comprehensive review article by Devons and Goldfarb [De57]. In general ρ and ε are matrices, but in dealing with angular

Figure 3.3.0.1 Angular momentum coupling scheme in the channel spin representation.

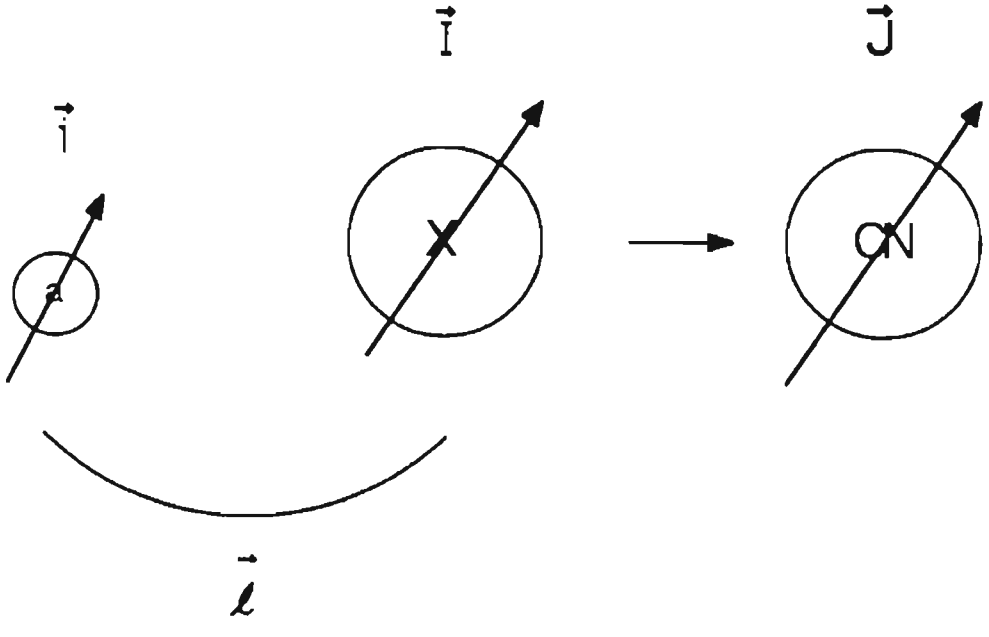

$$\vec{i} + \vec{I} + \vec{\ell} = \vec{J}$$

$$\vec{s} + \vec{\ell} = \vec{J}$$

momenta, spherical tensors are more convenient.

If there exist two angular momenta, $\mathbf{B_1}$ and $\mathbf{B_2}$, with z-projections β_1 and β_2, one can construct the following tensor representations of ρ and ε:

$$\rho_{kn}(B_1,B_2)=\sum_{\beta_1\beta_2}(-1)^{B_2-\beta_2}(B_1\beta_1\,B_2-\beta_2|kn)\langle B_1\beta_1|\rho|B_2\beta_2\rangle \quad and \tag{3.3.1.3}$$

$$\varepsilon_{kn}(B_1,B_2)=\sum_{\beta_1\beta_2}(-1)^{B_2-\beta_2}(B_1\beta_1\,B_2-\beta_2|kn)\langle B_1\beta_1|\varepsilon|B_2\beta_2\rangle. \tag{3.3.1.4}$$

Here $\mathbf{k}=\mathbf{B_1}-\mathbf{B_2}$ and $n=\beta_1-\beta_2$. The choice of phase follows the convention of Edmonds [Ed55]. Eqs. (3.3.1.3) and (3.3.1.4) may be inverted in order to express the matrix elements in terms of the tensors.

$$\langle B_1\beta_1|\rho|B_2\beta_2\rangle=\sum_{kn}(-1)^{B_2-\beta_2}(B_1\beta_1\,B_2-\beta_2|kn)\rho_{kn}(B_1,B_2). \tag{3.3.1.5}$$

$$\langle B_1\beta_1|\varepsilon|B_2\beta_2\rangle=\sum_{kn}(-1)^{B_2-\beta_2}(B_1\beta_1\,B_2-\beta_2|kn)\varepsilon_{kn}(B_1,B_2). \tag{3.3.1.6}$$

The quantity $(B_1\beta_1B_2-\beta_2|kn)$ is a Clebsch-Gordan coefficient. Then evaluating $\boldsymbol{w}$ gives

$$\begin{aligned}\boldsymbol{w}=\mathrm{Tr}(\rho\varepsilon)&=\sum_{B_1\beta_1B_2\beta_2}(\rho\varepsilon)\\&=\sum_{B_1\beta_1B_2\beta_2\,kn}(-1)^{2(B_2-\beta_2)}(B_1\beta_1\,B_2-\beta_2|kn)^2\rho_{kn}(B_1,B_2)\varepsilon^*_{kn}(B_1,B_2)\\&=\sum_{B_1B_2\,kn}\rho_{kn}(B_1,B_2)\varepsilon^*_{kn}(B_1,B_2).\end{aligned} \tag{3.3.1.7}$$

For certain special cases ρ and ε reduce to simple, useful forms (Table 3.3.1.1).

Suppose that **B** is the resultant of **A** and **j**. Then ρ and

Table 3.3.1.1

Special cases of density and efficiency tensors applicable to PNC experiments.

Unpolarized Target

$$\rho_{k_I n_I}(I,I) = \frac{\delta_{k_I,0}\delta_{n_I,0}}{\hat{I}}$$

Angular Momentum for Incident Neutron Beam

$$\rho_{k_\ell n_\ell}(\ell_1,\ell_2) = \frac{\hat{\ell}_1\hat{\ell}_2}{4\pi}(-1)^{\ell_2}\left(\ell_1 0 \ell_2 0 | k_\ell 0\right)\delta_{n_\ell,0}$$

Polarization Insensitive Detector

$$\varepsilon_{k_{I'}n_{I'}}\left(i_1',i_2'\right) = \frac{\delta_{k_{I'},0}\delta_{n_{I'},0}}{\hat{i}'}$$

Detector Placed at θ,ϕ

$$\varepsilon_{k_{\ell'}n_{\ell'}}\left(\ell_1',\ell_2'\right) = \frac{\hat{\ell}_1'\hat{\ell}_2'}{4\pi\hat{k}_{\ell'}}(-1)^{\ell_2'}\left(\ell_1' 0 \ell_2' 0 | k_{\ell'} 0\right) Y_{k_{\ell'}}^{n_{\ell'}*}(\theta,\phi)$$

Final State of Residual Nucleus Unobserved

$$\varepsilon_{k_{I'}n_{I'}}\left(I_1',I_2'\right) = \hat{I}'\delta_{k_{I'},0}\delta_{n_{I'},0}$$

ε decompose in the following manner

$$T_{k_B n_B}(B_1,B_2)=\sum_{k_A n_A k_j n_j}(k_A n_A k_j n_j|k_B n_B)\hat{k}_A\hat{k}_j\hat{B}_1\hat{B}_2\begin{bmatrix}A_1 & j_1 & B_1\\ A_2 & j_2 & B_2\\ k_A & k_j & k_B\end{bmatrix}T_{k_A n_A}(A_1,A_2)T_{k_j n_j}(j_1,j_2).$$

(3.3.1.8)

In eq. (3.3.1.8), T may represent either ρ or ε, the quantity in square brackets is a Wigner 9-j coefficient, and a circumflex indicates the square root of two times the quantity plus one (e.g., $\hat{k}=\sqrt{2k+1}$). This decomposition may be carried out multiple times if either **A** or **j** are resultants of other vectors.

In the previous discussion, it is important to note that ρ characterizes the initial state of the system. In order find the density matrix of the final state, apply a similarity transform to the initial ρ: $\rho(t)=O\rho(t_o)O^{\dagger}$. The quantity O is the interaction operator. Note that for a reaction, the **B′**s are the quantum numbers of the intermediate state (i.e., $A+j\rightarrow B\rightarrow A'+j'$). Then the density tensor for the final state can be written as

$$\rho_{kn}(B_1,B_2)=\rho_{kn}(B_1A_1'j_1',B_2A_2'j_2')=\langle B_1A_1'j_1'|O|B_1A_1j_1\rangle\rho_{kn}(B_1A_1j_1,B_2A_2j_2)$$
$$\times\langle B_2A_2'j_2'|O|B_2A_2j_2\rangle^{*}.$$

(3.3.1.9)

Now consider a particular case, X($\vec{n}$,n)X. Here we will use the angular momentum notation introduced earlier. Using the decomposition technique from eq. (3.3.1.8) one obtains an expression for the density tensor of the total angular momentum:

$$\rho_{k_J n_J}(J_1,J_2)=\sum_{k_s n_s k_\ell n_\ell k_I n_I k_i n_i}(k_s n_s k_\ell n_\ell|k_J n_J)(k_I n_I k_i n_i|k_s n_s)\hat{k}_s\hat{k}_\ell\hat{k}_I\hat{k}_i\hat{J}_1\hat{J}_2\hat{s}_1\hat{s}_2\begin{bmatrix}s_1 & \ell_1 & J_1\\ s_2 & \ell_2 & J_2\\ k_s & k_\ell & k_J\end{bmatrix}\begin{bmatrix}I_1 & i_1 & s_1\\ I_2 & i_2 & s_2\\ k_I & k_i & k_s\end{bmatrix}$$

$$\times\rho_{k_\ell n_\ell}(\ell_1,\ell_2)\rho_{k_I n_I}(I_1,I_2)\rho_{k_i n_i}(i_1,i_2).$$

(3.3.1.10)

From the table of common density and efficiency tensors, for an unpolarized target and polarized neutrons $i_1=i_2=1/2$, $k_I=n_I=0$, and $n_\ell=0$. Putting these values into eq. (3.3.1.10) reduces it to

$$\rho_{k_J n_J}(J_1,J_2)=\sum_{k_s n_s k_\ell n_\ell k_i n_i}(k_s n_s k_\ell 0|k_J n_J)(00k_i n_i|k_s n_s)(\ell_1 0\ell_2 0|k_\ell 0)\frac{\hat{k}_s\hat{k}_\ell\hat{k}_i\hat{J}_1\hat{J}_2\hat{s}_1\hat{s}_2\hat{\ell}_1\hat{\ell}_2}{\hat{I}}\frac{(-1)^{\ell_2}}{4\pi}$$

$$\times\begin{bmatrix}s_1 & \ell_1 & J_1\\ s_2 & \ell_2 & J_2\\ k_s & k_\ell & k_J\end{bmatrix}\begin{bmatrix}I_1 & 1/2 & s_1\\ I_2 & 1/2 & s_2\\ 0 & k_i & k_s\end{bmatrix}\rho_{k_i n_i}(1/2,1/2).$$

(3.3.1.11)

If, in the efficiency tensor, the detectors are polarization insensitive and the final state of the target is not observed, then $k_{i'}=n_{i'}=k_{I'}=n_{I'}=0$ and therefore $k_{s'}=n_{s'}=0$. The efficiency tensor is

$$\varepsilon^{*}_{k_J n_J}(J_1,J_2)=\sum_{k_\ell n_\ell}(00k_\ell n_\ell|k_J n_J)\hat{i}'\hat{I}'\hat{k}_\ell\hat{J}_1\hat{J}_2\hat{s}_1'\hat{s}_2'\begin{bmatrix}s_1' & \ell_1' & J_1\\ s_2' & \ell_2' & J_2\\ 0 & k_\ell & k_J\end{bmatrix}\begin{bmatrix}I_1' & 1/2 & s_1'\\ I_2' & 1/2 & s_2'\\ 0 & 0 & 0\end{bmatrix}\varepsilon^{*}_{k_\ell n_\ell}(\ell_1',\ell_2').$$

(3.3.1.12)

Making use of identities for 9-j symbols with zeros reduces this to

$$\varepsilon^{*}_{k_J n_J}(J_1,J_2)=\sum_{k_\ell n_\ell}\hat{i}'\hat{J}_1\hat{J}_2(-1)^{s'+k_\ell-J_2-\ell_1'}\mathcal{W}(\ell_2' J_2\ell_1' J_1;s' k_\ell)\varepsilon^{*}_{k_\ell n_\ell}(\ell_1',\ell_2') \qquad (3.3.1.13)$$

where the $\mathcal{W}()$ is a Racah [Ra42] coefficient. Putting in

the efficiency tensor for the exit orbital angular momentum gives the final form of the efficiency tensor for the total angular momentum:

$$\varepsilon^{\bullet}_{k_J n_J}(J_1,J_2)=\frac{(-1)^{s'+k_J-J_2-\ell'_1+\ell'_2}}{\sqrt{4\pi}\hat{k}_J}Y^{n_J}_{k_J}\bar{Z}(\ell'_2 J_2 \ell'_1 J_1; s' k_J). \qquad (3.3.1.14)$$

The Z-bar coefficients are those of Biedenharn, Blatt, and Rose [Bi52]. Now one can write down the angular correlation function, $\mathcal{W}$. Summation indices will be replaced by 'q', indicating that the sum is over all angular momenta and tensor indices. Then one has for $\mathcal{W}$,

$$\mathcal{W}=\sum_q \rho_{k_i n_i}\varepsilon^{\bullet}_{k_J n_J}\langle I_1 i_1 \ell_1|O|I'_1 i'_1 \ell'_1\rangle\langle I_2 i_2 \ell_2|O|I'_2 i'_2 \ell'_2\rangle^{\bullet}$$

$$=\sum_q (k_i n_i k_\ell 0|k_J n_J)(\ell_1 0 \ell_2 0|k_\ell 0)\frac{\hat{k}_i\hat{k}_\ell\hat{J}_1\hat{J}_2\hat{\ell}_1\hat{\ell}_2\hat{s}_1\hat{s}_2}{\hat{I}^2\hat{k}_J}\frac{(-1)^{\ell_1+I+k_i-s_1-1/2+s'+\ell'_2+k_J-J_2-\ell'_1}}{\left(\sqrt{4\pi}\right)^3}$$

$$\times\mathfrak{W}(s_1 1/2 s_2 1/2; I k_i)\bar{Z}(\ell'_2 J_2 \ell'_1 J_1; s' k_J)\begin{bmatrix} s_1 & \ell_1 & J_1 \\ s_2 & \ell_2 & J_2 \\ k_s & k_\ell & k_J \end{bmatrix}\rho_{k_i n_i}(1/2,1/2)Y^{n_J}_{k_J}(\theta,\phi)$$

$$\times\langle I_1 i_1 \ell_1|O|I'_1 i'_1 \ell'_1\rangle\langle I_2 i_2 \ell_2|O|I'_2 i'_2 \ell'_2\rangle^{\bullet}. \qquad (3.3.1.15)$$

The angular correlation function may then be related to the differential cross section [De57] by

$$\frac{d\sigma}{d\Omega}=\frac{4\pi^2}{k^2}\mathcal{W}(\theta,\phi). \qquad (3.3.1.16)$$

Integrating over all angles gives

$$\sigma = \sum_{q} \frac{\hat{J}^2 \hat{\ell}_1 \hat{\ell}_2 \hat{s}_1 \hat{s}_2}{\hat{I}^2} \frac{\pi(-1)^{I+k_\ell - s_1 - 1/2 - s_1 + J}}{k^2} (\ell_1 0 \ell_2 0 | k_\ell 0) W(s_1 1/2 s_2 1/2; I k_\ell) W(s_2 \ell_2 s_1 \ell_1; J k_\ell)$$

$$\times \rho_{k,0} \langle I_1 i_1 \ell_1 | O | I'_1 i'_1 \ell'_1 \rangle \langle I_2 i_2 \ell_2 | O | I'_2 i'_2 \ell'_2 \rangle^* . \qquad (3.3.1.17)$$

This is the final expression for the cross section. The only unspecified quantities in eq. (3.3.1.17) are the matrix elements. The matrix elements may be determined using the R-matrix formalism developed above via the relation

$$T_{cc'} = \langle I i \ell J | O | I' i' \ell' J' \rangle = \delta_{cc'} - e^{i(\phi_c + \phi_{c'})} W_{cc'} \qquad (3.3.1.18)$$

where ϕ_c is the hard-sphere phase shift and $W_{cc'}$ is from eq. (3.2.2.32).

3.3.2 Application to Zero Spin Targets

As an example of this technique, we obtain an expression for a zero spin, positive parity target (e.g., ^{232}Th) being bombarded with longitudinally polarized neutrons. In this case (using the same notation as above) I=0 and i=1/2. Therefore the only choice for the channel spin is s=1/2. Experimentally, for epithermal neutrons, the only values of orbital angular momentum that appear are ℓ=0 and ℓ=1. The coupling of ℓ and s allows for J to be either 1/2 or 3/2.

In the evaluation of the cross section, we will explicitly sum the incident quantum numbers but leave the sum over final states until later. The terms in the sum have the following combinations of quantum numbers:

(1) k_ℓ=0, ℓ_1=ℓ_2=0

(2) k_ℓ=0, ℓ_1=ℓ_2=1

(3) k_ℓ=1, ℓ_1=0, ℓ_2=1

(4) $k_{\ell}=1,\ \ell_1=1,\ \ell_2=0.$

Putting these combinations into eq. (3.3.1.17) gives

$$(1)=\frac{2\pi}{\sqrt{2}k^2}\rho_{00}\sum_f\langle 0,1/2,0|f\rangle\langle 0,1/2,0|f\rangle^* \qquad (3.3.2.1a)$$

$$(2)=\frac{2\pi}{\sqrt{2}k^2}\rho_{00}\sum_f\langle 0,1/2,1|f\rangle\langle 0,1/2,1|f\rangle^* \qquad (3.3.2.1b)$$

$$(3)=\frac{2\pi}{\sqrt{2}k^2}\rho_{10}\sum_f\langle 0,1/2,0|f\rangle\langle 0,1/2,1|f\rangle^* \qquad (3.3.2.1c)$$

$$(4)=\frac{2\pi}{\sqrt{2}k^2}\rho_{10}\sum_f\langle 0,1/2,1|f\rangle\langle 0,1/2,0|f\rangle^* \qquad (3.3.2.1d)$$

Summing eqs. (3.3.2.1a)-(3.3.2.1d) gives a final expression for the cross section,

$$\sigma=\frac{\pi}{k^2}\sum_f\left(\begin{array}{l}\frac{2}{\sqrt{2}}\rho_{00}\left|\langle 0,1/2,0|f\rangle\right|^2+\frac{2}{\sqrt{2}}\rho_{00}\left|\langle 0,1/2,1|f\rangle\right|^2+\\ \frac{4}{\sqrt{2}}\rho_{10}Re\left(\langle 0,1/2,0|f\rangle\langle 0,1/2,1|f\rangle^*\right)\end{array}\right). \qquad (3.3.2.2)$$

In the next section this expression will be used to introduce parity nonconservation.

3.4 Parity Nonconservation in Neutron-Nucleus Scattering

If interactions involving the strong, electromagnetic, and gravitational forces are studied parity is conserved. It is only the weak force that does not conserve parity. In the nucleus, the magnitude of the parity violating weak force is about seven orders of magnitude smaller than the normal nucleon-nucleon (NN) strong force. This means that it is acceptable to consider the parity violating part of the nuclear Hamiltonian as a perturbation on the parity

conserving part. Suppose for the moment that there is no weak force. Then a nuclear Hamiltonian, H_o, has a set of eigenstates $\{\psi_n\}$. Since there are no parity violating terms in H_o, the eigenstates all have parity as a good quantum number. If a perturbed Hamiltonian, H', is now introduced it will have a characteristic Schroedinger equation

$$H'\psi_n' = E_n'\psi_n'. \qquad (3.4.1)$$

The primes indicate the perturbed wavefunctions. Consider a set of unperturbed eigenstates which has only two states, ψ_s and ψ_p. If $H'=H_o+\mathcal{V}$, where $\mathcal{V}$ is the parity violating part, and $\mathcal{V}=\mathcal{V}^*$ ($\mathcal{V}$ is real), then one can write down simple expressions for the perturbed wavefunctions in terms of the unperturbed:

$$\psi_s' = \psi_s - \frac{\langle \psi_s | \mathcal{V} | \psi_p \rangle}{E_s - E_p}\psi_p \quad \text{and} \qquad (3.4.2a)$$

$$\psi_p' = \psi_p + \frac{\langle \psi_s | \mathcal{V} | \psi_p \rangle}{E_s - E_p}\psi_s. \qquad (3.4.2b)$$

From now on the matrix element in eqs. (3.4.2a) and (3.4.2b) will be denoted **V**. Recall that the reduced width amplitudes, $\gamma_{\lambda c}$, are directly proportional to the wavefunctions. Therefore, if only two channels are allowed, ℓ=0 and ℓ=1 longitudinally polarized neutrons, there are only two non-zero reduced width amplitudes for the unperturbed system, γ_s and γ_p. The perturbed reduced width amplitudes may then be written as

$$\gamma = \begin{bmatrix} \gamma_s & \dfrac{\mathbf{V}}{E_s - E_p}\gamma_p \\ -\dfrac{\mathbf{V}}{E_s - E_p}\gamma_s & \gamma_p \end{bmatrix}. \qquad (3.4.3)$$

The next step is to calculate the cross section including the parity violating term. Eq. (3.3.2.2) gives an expression for the cross section but with the matrix elements not evaluated. We will use the R-matrix formalism developed earlier to find the matrix elements. Rewriting the R-matrix of eq. (3.2.2.19) into a more convenient form yields

$$R_{cc'} = \sum_{\lambda} \frac{\gamma_{\lambda c}\gamma_{\lambda c'}}{E_\lambda - E}. \qquad (3.4.4)$$

Recall that λ labels the levels and c labels the channels. For the two level, two channel problem $\mathbf{R}$ is easily evaluated. Evaluating eq. (3.4.4) gives

$$\mathbf{R} = \begin{bmatrix} \dfrac{\gamma_{11}^2}{E_1 - E} + \dfrac{\gamma_{21}^2}{E_2 - E} & \dfrac{\gamma_{11}\gamma_{12}}{E_1 - E} + \dfrac{\gamma_{21}\gamma_{22}}{E_2 - E} \\ \dfrac{\gamma_{12}\gamma_{11}}{E_1 - E} + \dfrac{\gamma_{22}\gamma_{21}}{E_2 - E} & \dfrac{\gamma_{12}^2}{E_1 - E} + \dfrac{\gamma_{22}^2}{E_2 - E} \end{bmatrix}. \qquad (3.4.5)$$

Putting the elements of eq. (3.4.3) into eq. (3.4.5) and dropping terms of $\mathbf{V}^2$ and higher yields

$$\mathbf{R} = \begin{bmatrix} \dfrac{\gamma_s^2}{E_s - E} & \dfrac{-\mathbf{V}\gamma_s\gamma_p}{(E_s - E)(E_p - E)} \\ \dfrac{-\mathbf{V}\gamma_s\gamma_p}{(E_s - E)(E_p - E)} & \dfrac{\gamma_p^2}{E_p - E} \end{bmatrix}. \qquad (3.4.6)$$

The goal is to determine the matrix elements $\mathbf{T}$ from eq. (3.3.1.18). A convenient form for $\mathbf{W}$ is

$$\mathbf{W} = 1 + 2i\mathbf{P}^{1/2}(1 - \mathbf{RL})^{-1}\mathbf{RP}^{1/2}. \qquad (3.4.7)$$

One needs to evaluate 1-$\mathbf{RL}$, where $\mathbf{R}$ is from eq. (3.4.6) and

L is from eq. (3.2.1.17). Simplifying 1-**RL** gives

$$1-\mathbf{RL}=\begin{bmatrix} \dfrac{E_s-E-i\Gamma_s/2}{E_s-E} & \dfrac{\mathbf{V}\gamma_p\gamma_s}{(E_s-E)(E_p-E)} \\ \dfrac{\mathbf{V}\gamma_p\gamma_s}{(E_s-E)(E_p-E)} & \dfrac{E_p-E-i\Gamma_p/2}{E_p-E} \end{bmatrix}. \qquad (3.4.8)$$

For convenience, let $[S]=E_S-E-i\Gamma_S/2$, with a similar definition for [P]. Taking the inverse of eq. (3.4.8) yields

$$(1-\mathbf{RL})^{-1}=\begin{bmatrix} \dfrac{E_s-E}{[S]} & \dfrac{-\mathbf{V}\gamma_s\gamma_p}{[S][P]} \\ \dfrac{-\mathbf{V}\gamma_s\gamma_p}{[S][P]} & \dfrac{E_p-E}{[P]} \end{bmatrix}. \qquad (3.4.9)$$

Moving one step further,

$$(1-\mathbf{RL})^{-1}\mathbf{R}=\begin{bmatrix} \dfrac{\gamma_s^2}{[S]} & \dfrac{-\mathbf{V}\gamma_s\gamma_p}{[S][P]} \\ \dfrac{-\mathbf{V}\gamma_s\gamma_p}{[S][P]} & \dfrac{\gamma_p^2}{[P]} \end{bmatrix}. \qquad (3.4.10)$$

W can be evaluated,

$$\mathbf{W}=\begin{bmatrix} 1+\dfrac{i\Gamma_s}{[S]} & \dfrac{-i\mathbf{V}g_sg_p}{[S][P]} \\ \dfrac{-i\mathbf{V}g_sg_p}{[S][P]} & 1+\dfrac{i\Gamma_p}{[P]} \end{bmatrix}. \qquad (3.4.11)$$

Here $g_s=\sqrt{2P_0}\gamma_s$ and $g_p=\sqrt{2P_1}\gamma_p$ where P_0 is the ℓ=0 penetrability and P_1 is the ℓ=1 penetrability. Using the g's preserves the sign information of the reduced width amplitudes. With this result for **W**, the **T** matrix is

$$\mathbf{T}=\begin{bmatrix} \dfrac{-i\Gamma_s e^{2i\phi_s}}{[S]} & \dfrac{i\mathbf{V}g_s g_p e^{i(\phi_s+\phi_p)}}{[S][P]} \\ \dfrac{i\mathbf{V}g_s g_p e^{i(\phi_s+\phi_p)}}{[S][P]} & \dfrac{-i\Gamma_p e^{2i\phi_p}}{[P]} \end{bmatrix}. \qquad (3.4.12)$$

Assume a beam of neutrons polarized longitudinally and define the beam axis as the z axis. The four components of the density matrix for the incident neutrons are

$$\rho_{00}=\frac{1}{\sqrt{2}},\ \rho_{10}=\frac{P_z}{\sqrt{2}},\ \rho_{11}=\rho_{1-1}=0. \qquad (3.4.13)$$

Putting eq. (3.4.13) into eq. (3.3.2.2) and relabeling the matrix element as their equivalent $\mathbf{T}$ matrix components gives

$$\sigma=\frac{\pi}{k^2}\sum_{c'}\left(\left|T_{1c'}\right|^2+\left|T_{2c'}\right|^2+2P_z Re\left(T_{1c'}T_{2c'}^*\right)\right), \qquad (3.4.14)$$

where P_z is the the neutron polarization.

Consider the following sequence of experiments. Measure the cross section for a period of time with neutron polarization P_z. Flip the polarization to $-P_z$ and take data for an equal amount of time. In this case there are two independent cross section measurements, labeled σ^+ and σ^-. The difference in the two measurements is

$$\sigma^+-\sigma^-=\frac{4\pi}{k^2}P_z\sum_{c'}\mathrm{Re}\left(T_{1c'}T_{2c'}^*\right). \qquad (3.4.15)$$

Explicitly evaluating the sum leaves

$$\sigma^+-\sigma^-=\frac{4\pi}{k^2}P_z\mathrm{Re}\left(T_{11}T_{21}^*+T_{12}T_{22}^*\right). \qquad (3.4.16)$$

Inserting the elements of the T matrix from eq. (3.4.12) gives

$$\sigma^+-\sigma^-=\frac{4\pi}{k^2}P_z\mathrm{Re}\left(\frac{g_s g_s}{[S]}\frac{\mathbf{V}g_s g_p}{[S][P]}+\frac{\mathbf{V}g_s g_p}{[S][P]}\frac{g_p g_p}{[P]}\right) \qquad (3.4.17)$$

Here the hard sphere phase shifts have been dropped as they are small for epithermal neutrons. Simplifying eq. (3.4.17) yields the final expression,

$$\sigma^+ - \sigma^- = \frac{4\pi P_z \mathbf{V}}{k^2[S]^2[P]^2} g_s g_p \left(\Gamma_s\left(E_p - E\right) + \Gamma_p\left(E_s - E\right)\right). \tag{3.4.18}$$

The experimental data for the two helicity states can be subtracted and compared with eq. (3.4.18) in order to extract the parity violating matrix element $\mathbf{V}$.

One may also wish to sum the two cross sections in order to obtain the parity violating asymmetry defined in eq. (2.4.1). Use of eq. (3.4.14) yields

$$\sigma^+ + \sigma^- = \frac{2\pi}{k^2}\left(\sum_{c'} |T_{1c'}|^2 + |T_{2c'}|^2\right). \tag{3.4.19}$$

After insertion of the T matrix elements eq. (3.4.19) becomes

$$\sigma^+ + \sigma^- = \frac{2\pi}{k^2}\left(\frac{\Gamma_s^2}{[S]^2} + \frac{\Gamma_p^2}{[P]^2} + \frac{2\mathbf{V}^2 g_s^2 g_p^2}{[S]^2[P]^2}\right). \tag{3.4.20}$$

Dropping the term in $\mathbf{V}^2$ in eq. (3.4.20) and dividing eq. (3.4.18) by eq. (3.4.20) yields

$$\frac{\sigma^+ - \sigma^-}{\sigma^+ + \sigma^-} = \frac{2P_z \mathbf{V} g_s g_p \left(\Gamma_s\left(E_p - E\right) + \Gamma_p\left(E_s - E\right)\right)}{[S]^2[P]^2\left(\frac{\Gamma_s^2}{[S]^2} + \frac{\Gamma_p^2}{[P]^2}\right)}. \tag{3.4.21}$$

If eq. (3.4.21) is evaluated at the energy of the p-wave resonance and then simplified the result is the same as given in eq. (2.4.1):

$$\mathcal{P} = \frac{2\mathbf{V}P_z}{\left(E_s - E_p\right)}\frac{g_s g_p}{\Gamma_p}. \tag{3.4.22}$$

It should be noted that the above discussion is for two levels and two channels. In a real experiment there usu-

ally many channels open. An argument similar to that above can be developed using the level representation of the R-matrix mentioned in section 3.2.2. The use of the level representation allows the dimension of the R-matrix to continue to be two, but accounts for the many open channels. The expression for the difference in the total cross section in this scenario differs only slightly from eq. (3.4.18).

CHAPTER IV

Experimental Apparatus

4.0 Introduction

The experiments on which this dissertation is based were performed at the Clinton P. Anderson Meson Physics Facility (LAMPF) located at Los Alamos National Laboratory (LANL). This chapter will describe the apparatus used in performing these experiments. The accelerator and neutron beam production facilities will be described in the first sections, and the apparatus particular to these experiments will be described in the remainder of the chapter. The data acquisition system will be discussed at the end of this chapter.

4.1 LANSCE

One of the subfacilities available at LAMPF is the Manuel Lujan Jr. Neutron Scattering Center (LANSCE). Figure 4.1.1 is a schematic diagram showing the major subfacilities at LAMPF. LANSCE is a very high intensity source of epithermal neutrons, which makes it an ideal facility at which to perform the present experiments. The production of neutrons at LANSCE is a complex process which involves several species of beam before the final neutrons are produced. Each of the components of the neutron production process will be described below.

4.1.1 Source and Accelerator

To start the process, a duoplasmatron ion source [Al71] produces approximately 300μA of H^- beam at ~20keV. The

Figure 4.1.1 Experimental facilities available at LAMPF.

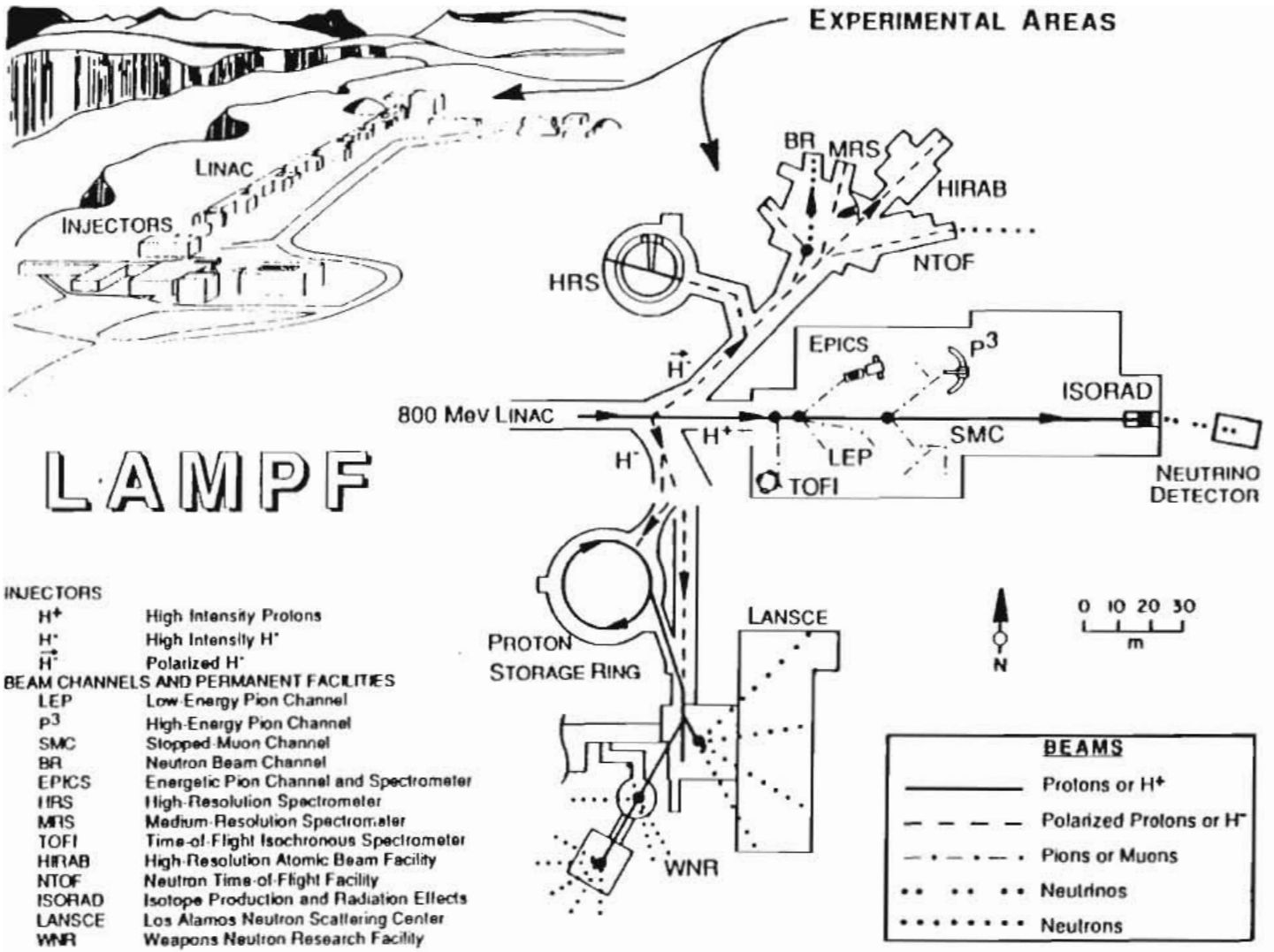
EXPERIMENTAL AREAS
LINAC
INJECTORS
BR
MRS
HIRAB
NTOF
HRS
EPICS
P3
ISORAD
800 Mev LINAC
SMC
LEP
TOFI
NEUTRINO DETECTOR
LAMPF
PROTON STORAGE RING
LANSCE
WNR
N
0 10 20 30
m
BEAMS
Protons or H+
Polarized Protons or H-
Pions or Muons
Neutrinos
Neutrons
INJECTORS
H+ High Intensity Protons
H- High Intensity H-
Polarized H-
BEAM CHANNELS AND PERMANENT FACILITIES
LEP Low-Energy Pion Channel
P3 High-Energy Pion Channel
SMC Stopped-Muon Channel
BR Neutron Beam Channel
EPICS Energetic Pion Channel and Spectrometer
HRS High-Resolution Spectrometer
MRS Medium-Resolution Spectrometer
TOFI Time-of-Flight Isochronous Spectrometer
HIRAB High-Resolution Atomic Beam Facility
NTOF Neutron Time-of-Flight Facility
ISORAD Isotope Production and Radiation Effects
LANSCE Los Alamos Neutron Scattering Center
WNR Weapons Neutron Research Facility

beam is then accelerated to 750keV in a Cockcroft-Walton (CW) electrostatic accelerator. Two other ion source-CW accelerator pairs also inject into the primary linac. One pair provides a high intensity H^+ beam, primarily for pion production, and the other pair provides polarized H^- for studies of high energy nuclear reactions. After being accelerated to 750keV, the H^- beam is "chopped" into pulses of width 725μs which are spaced 8.33ms apart. Each 725μs wide "macropulse" is comprised of many 250ns wide "micropulses".

The primary accelerator consists of two linacs. After being "chopped", the beam is injected into a 201MHz drift tube linac. This first linac accelerates the beam to 100MeV. The beam is then injected into an 805MHz side coupled cavity linac. The 805MHz linac accelerates the beam to its final energy of 800MeV. A schematic of the entire accelerator is shown in figure 4.1.2. Detailed information concerning the two linacs can be found in articles by Nagle *et al.* [Na67] and Knapp *et al.* [Kn68].

4.1.2 Proton Storage Ring

The present type of experiment utilizes a technique called neutron time-of-flight (NTOF). The NTOF method involves producing short (narrow time width) bursts of neutrons and then counting for many short time intervals using a detector located a distance L away from the source. The distance L can be measured and the velocity of the neutrons during each time interval can be calculated. For slow neutrons, $v \ll c$, the velocity and energy are simply related,

$$E = \frac{1}{2}mv^2. \qquad (4.1.2.1)$$

In order to have the best possible time (energy) resolution, a large number of timing intervals is necessary.

Figure 4.1.2 Schematic of the LAMPF site. The accelerator is contained in the structures labeled 'Sector A' and 'Sectors B-H'.

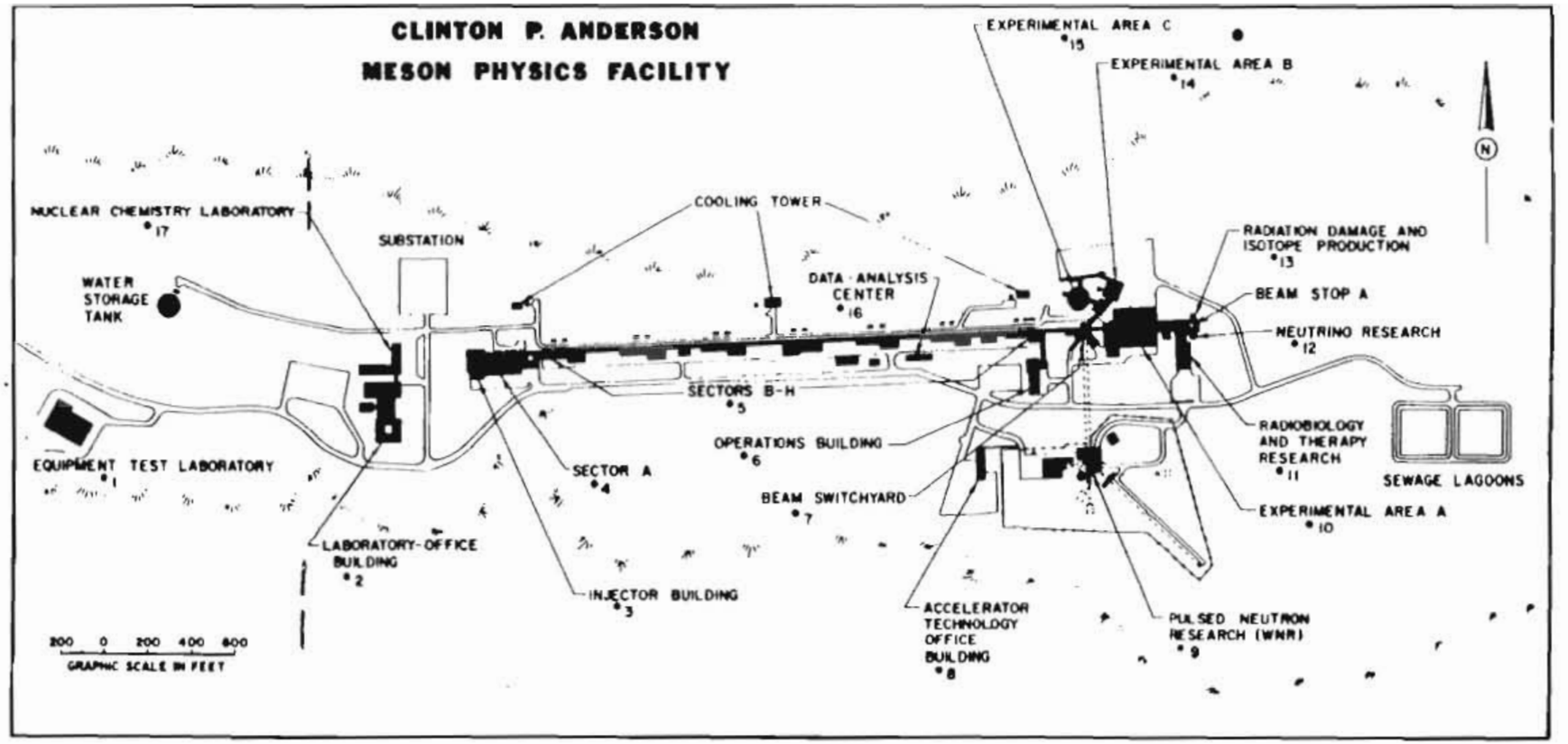
CLINTON P. ANDERSON
MESON PHYSICS FACILITY
EXPERIMENTAL AREA C
15
EXPERIMENTAL AREA B
14
N
NUCLEAR CHEMISTRY LABORATORY
17
SUBSTATION
COOLING TOWER
RADIATION DAMAGE AND ISOTOPE PRODUCTION
13
WATER STORAGE TANK
DATA - ANALYSIS CENTER
16
BEAM STOP A
NEUTRINO RESEARCH
12
SECTORS B-H
5
RADIOBIOLOGY AND THERAPY RESEARCH
11
SEWAGE LAGOONS
EQUIPMENT TEST LABORATORY
1
OPERATIONS BUILDING
6
SECTOR A
4
BEAM SWITCHYARD
7
EXPERIMENTAL AREA A
10
LABORATORY-OFFICE BUILDING
2
INJECTOR BUILDING
3
ACCELERATOR TECHNOLOGY OFFICE BUILDING
8
PULSED NEUTRON RESEARCH (WNR)
9
200 0 200 400 800
GRAPHIC SCALE IN FEET

This can be controlled by an individual experiment. The other significant factor contributing to good time resolution is the time width of the neutron burst. Ideally the neutron burst should be a delta function; in practice a width of a few hundred nanoseconds can be achieved. The function of the proton storage ring (PSR) is to compress each beam pulse from a width of 725μs to a width of 250ns.

The 725μs wide beam pulses from the primary accelerator are "kicked" into line D and the PSR injection channel (Figure 4.1.2.1). The injected H^- beam is first stripped of one electron in a high field stripper magnet. This process takes place with 100% efficiency [Ma89a]. The resultant H^o beam then passes through a dipole magnet into the ring proper, where it is stripped of its electron by a $200\mu g/cm^2$ carbon foil. The second stripping process is approximately 92% efficient with the remaining 8% of the beam going to a beam dump.

Of the 120 beam pulses that leave the primary accelerator each second, 20 are sent down line D to the PSR. The remaining 100 go to line A. As a macropulse is injected into the PSR, each micropulse is circulated once and then bunched with the next micropulse. By repeating this procedure the entire macropulse is accumulated into a single 250ns wide pulse. Up to 2800 micropulses may be accumulated. The pulse is then extracted in a single turn and the extracted beam steered into the neutron production target.

4.1.3 Neutron Production and Moderation

Every 50ms the PSR delivers a pulse of approximately $2x10^{13}$ 800MeV protons to the neutron production target. The neutron production target consists of two large tungsten cylinders, oriented vertically, with the beam incident from above (Figure 4.1.3.1). The process by which neutrons are produced is called spallation. Choices for spallation

Figure 4.1.2.1 Diagram of the PSR showing major ring components and the injection and extraction lines.

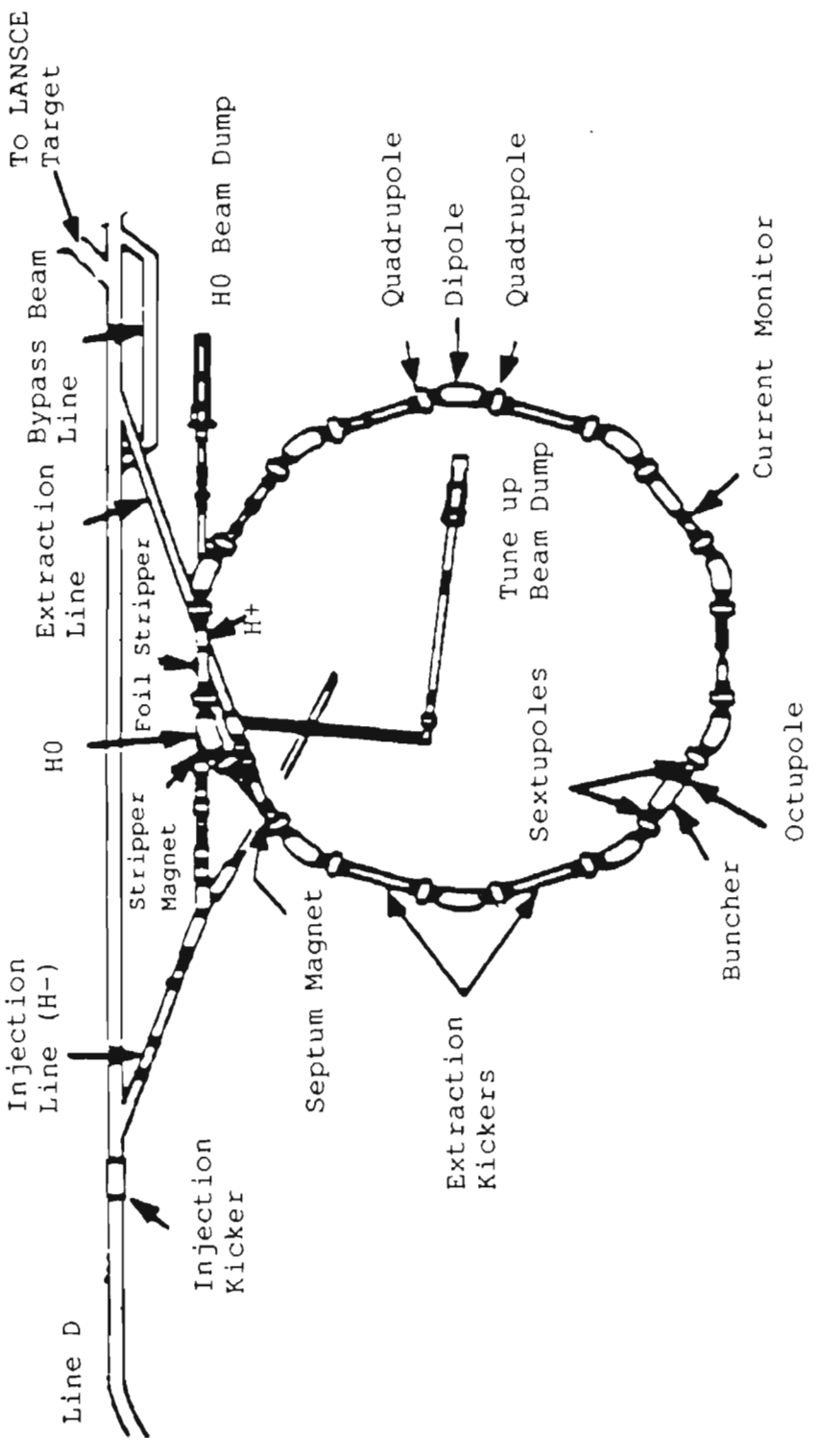
To LANSCE Target
Bypass Beam Line
H0 Beam Dump
Quadrupole
Dipole
Quadrupole
Current Monitor
Extraction Line
Foil Stripper
H+
Tune up Beam Dump
H0
Stripper Magnet
Sextupoles
Octupole
Injection Line (H-)
Septum Magnet
Buncher
Extraction Kickers
Injection Kicker
Line D

Figure 4.1.3.1 Vertical cutaway of the neutron production target and moderator assembly. The targets are located above and below the vertex of the vertical and horizontal centerlines. The beam is incident from above along the vertical centerline. The box labeled 'Al' is the aluminum jacket that surrounds each moderator. The spaces filled with beryllium and nickel are for shielding. The device at the top and to the right of the centerline of the assembly is part of the target cooling apparatus. All dimensions are in inches.

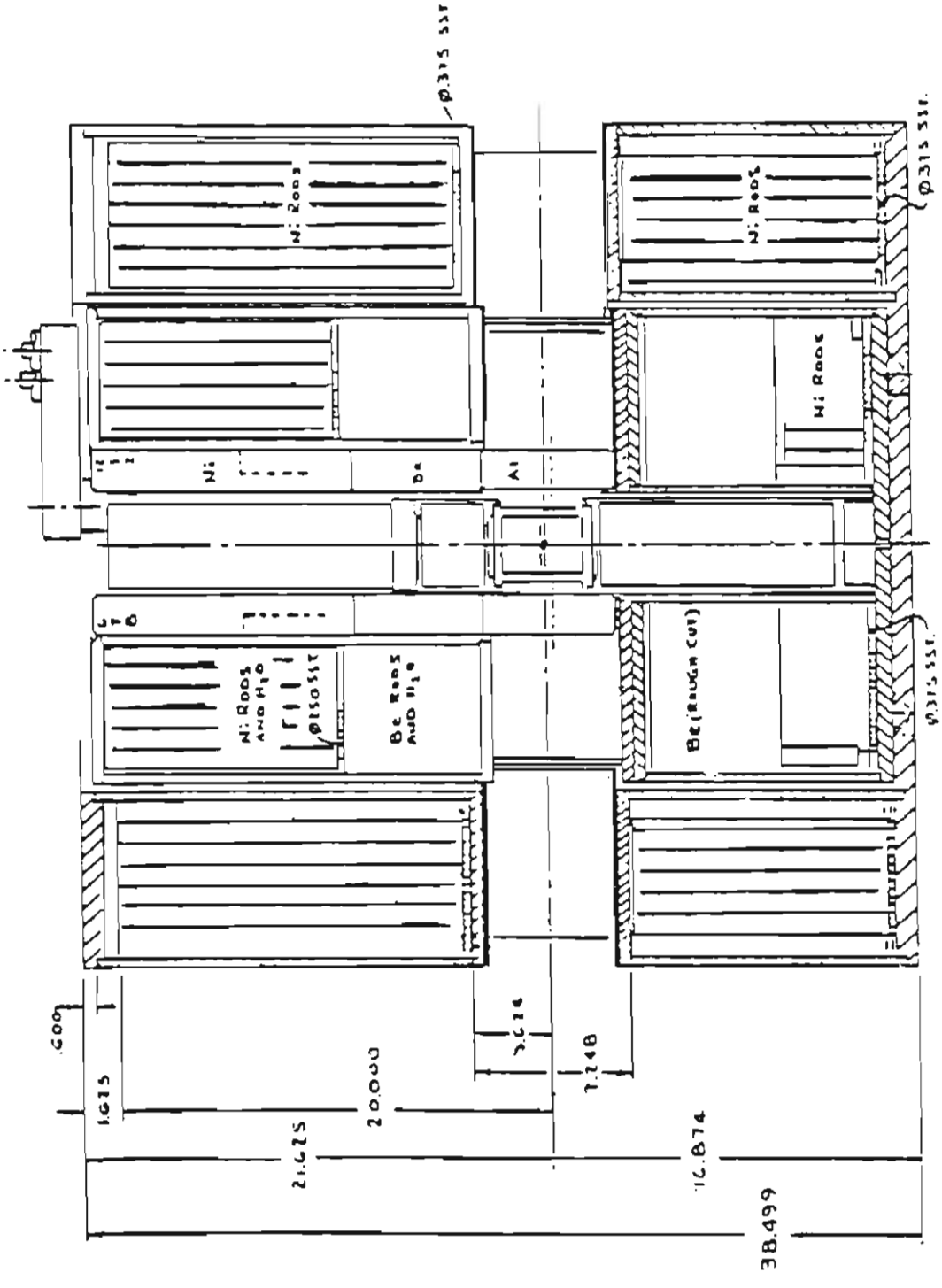
Ni Rods
Ni
Be
Al
Ni Rods
Ni Rods
Ni Rods And H2O
Be Rods And H2O
Be (Rough Cut)
.600
1.615
20.000
21.625
38.499

targets are heavy, neutron rich nuclei in metallic form such as tantalum, tungsten, and uranium. A typical spallation reaction in tungsten produces ~25 neutrons for each incident proton [As85].

Spallation is not a single process, but instead a series of processes which occur in a very short period of time (~ns). When a nucleus is struck by an 800MeV proton, a short-lived cascade of high energy mesons and nucleons is produced. The energy spectrum of these particles extends up to 800MeV and the angular distribution is highly forward peaked [Ki82]. In the deexcitation process, some particles are simply "evaporated" from the nucleus while the remainder are emitted when the nucleus fissions into quasi-stable isotopes. The angular distribution of these particles is nearly isotropic. The average particle energy is a few MeV. High energy gamma rays may be emitted at any time during this process. The number of particles released during evaporation and fission, as well as the total number of particles produced during the entire process, is dependent on the target element.

The spallation process produces many high energy neutrons. In order to be of value in studying resonances in heavy nuclei their energies must be moderated to ~1-1000eV. For nine of the twelve flight paths at LANSCE, the moderating material is water (Figure 4.1.3.2). Thin sheets of gadolinium are placed in and around the moderator in order to reduce the fast neutron leakage from the moderator. Thin boron slabs are also used to prevent time broadening from the thermal neutrons produced in the gadolinium. The specific configuration of these materials can be chosen in such a way so as to obtain either maximum timing resolution or maximum intensity. The moderator serving flight paths 2, 1, and 12 is of the 'high-resolution' type (Figure 4.1.3.3). This experiment was performed on flight path 2.

In addition to the gamma rays produced when the incident

Figure 4.1.3.2 Horizontal cutaway showing the moderators and shielding. The tungsten production target is not shown; this perspective is taken slightly above the horizontal centerline. The box labelled 'Liq. H_2' is the liquid hydrogen moderator serving flight paths 9, 10, and 11. The other three boxes in similar positions about the center are water moderators serving the other nine flight paths. The numeric labels indicate the flight paths served by each moderator. The beryllium and nickel are the same as in figure 4.1.3.1. The other materials indicated are liners for the flight path penetrations.

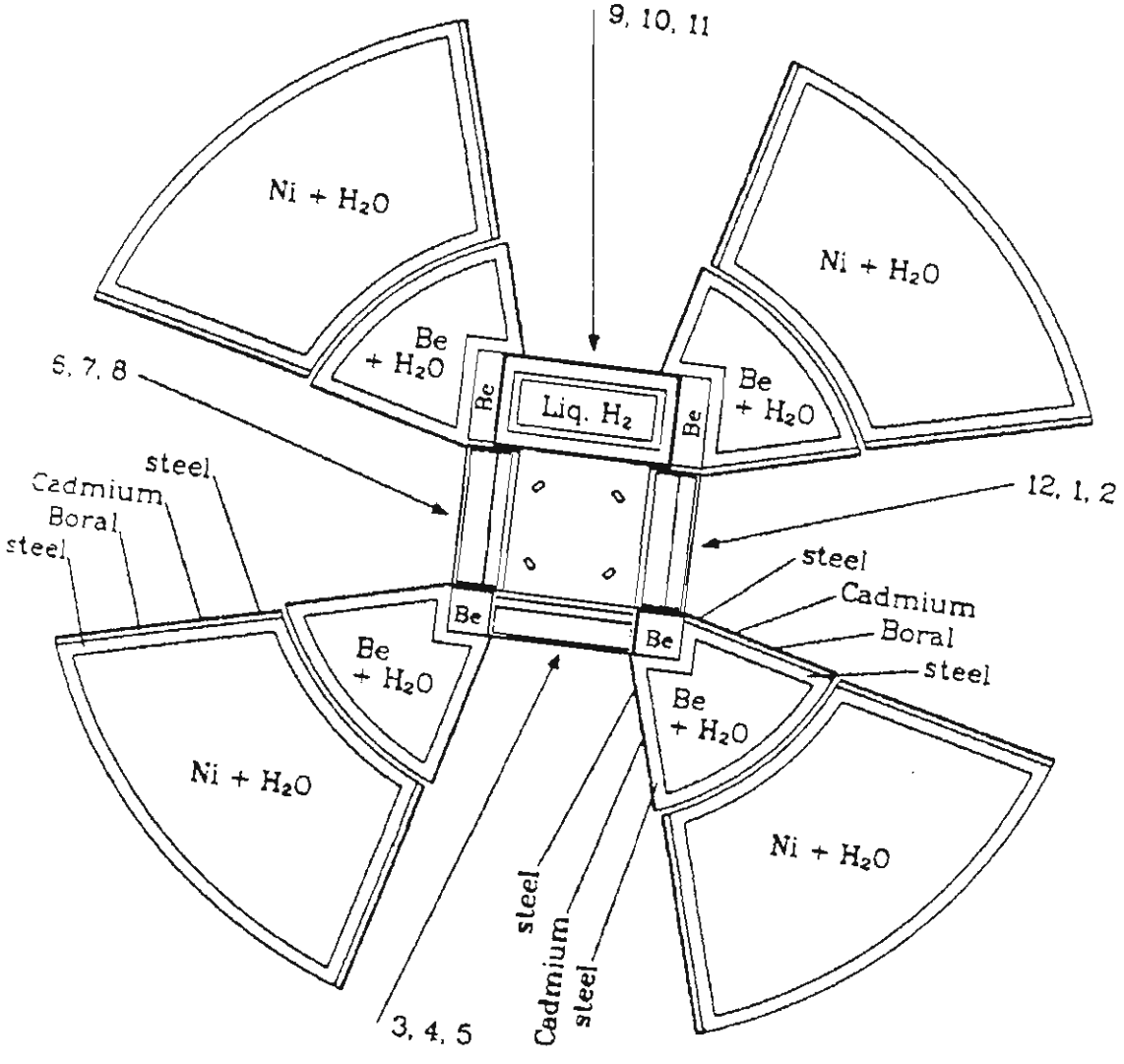
9, 10, 11
Ni + H2O
Ni + H2O
Be + H2O
Be + H2O
Be
Liq. H2
Be
6, 7, 8
12, 1, 2
steel
Cadmium
Boral
steel
steel
Cadmium
Boral
steel
Be
Be
Be + H2O
Be + H2O
Ni + H2O
Ni + H2O
steel
Cadmium
steel
3, 4, 5

Figure 4.1.3.3 Details of the 'high-resolution' moderator serving flight paths 12, 1, and 2 [Ro90].

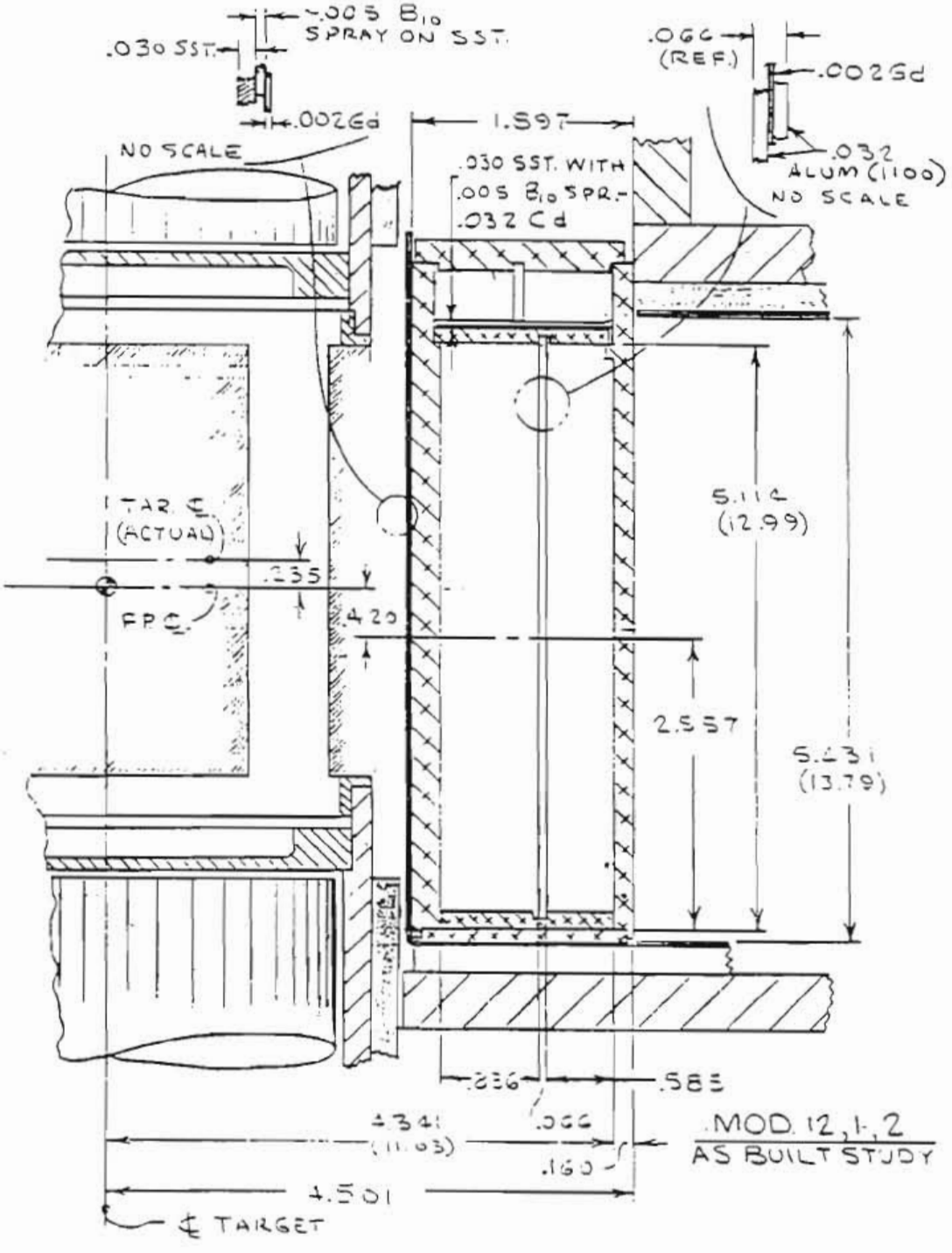
.005 B10 SPRAY ON SST.
.030 SST.
.002Gd
NO SCALE
1.597
.030 SST. WITH .005 B10 SPR.- .032 Cd
.066 (REF.)
.002Gd
.032 ALUM (1100)
NO SCALE
TAR. ℄ (ACTUAL)
.235
FP ℄
.420
5.114 (12.99)
2.557
5.431 (13.79)
.236
.585
4.341 (11.03)
.066
.160
4.501
℄ TARGET
MOD. 12, 1, 2
AS BUILT STUDY

proton beam strikes the neutron production target, many 2.2MeV gamma rays are produced from neutron capture on the hydrogen in the water moderator [Ol81]. These gamma rays together produce what is know as a "gamma flash". The gamma flash is an intense burst of gamma rays which strikes the detectors a few hundred nanoseconds after the incident proton beam has struck the target. The gamma flash has a duration of a few microseconds. During normal running the electronics are saturated during the gamma flash. A time of flight spectrum measured in order to study the gamma flash is shown in figure 4.1.3.4.

The available neutron flux from LANSCE has been simulated [Hu89] and has been found to agree within a factor of two of the measured flux at 1eV [Gi89]. There are several different models for the calculation of the flux from a spallation source. The Los Alamos model had the form

$$C \approx \frac{0.01}{E^{0.9}}, \qquad (4.1.3.1)$$

where C is the number of neutrons per eV per steradian per proton. A simulation of this spectrum is shown in figure 4.1.3.5. During the 1989 run season the TRIPLE collaboration measured this flux at multiple energies. The results are overlaid as data points in figure 4.1.3.5. Note that the measured flux has a somewhat lesser slope than the calculation. This is advantageous for a PNC experiment where states up to several hundred eV are studied.

There is a second, slightly different, model from Los Alamos. It has the form [Ru90]

$$C \approx 0.006 \frac{dE}{E}\left(\frac{E}{20eV}\right)^{0.1}. \qquad (4.1.3.2)$$

Eq. (4.1.3.2) has units of neutrons per steradian per proton.

Figure 4.1.3.4 NTOF spectrum of the gamma flash. Each channel has a time width of 200ns. The beam burst struck the target during channel 1009.

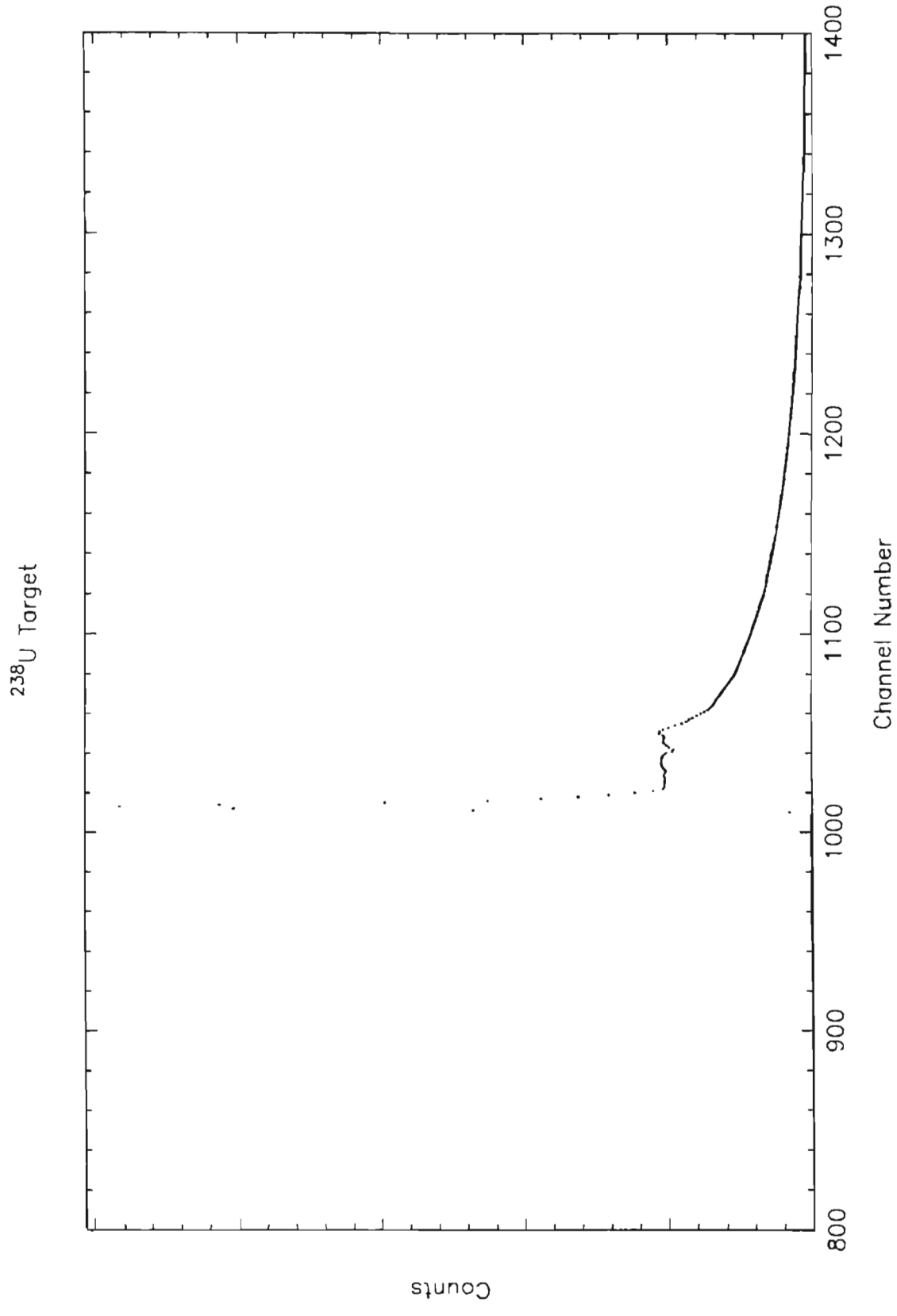
^{238}U Target
Counts
800
900
1000
1100
1200
1300
1400
Channel Number

Figure 4.1.3.5 LANSCE neutron flux versus neutron energy for flight path 2. The solid curve is a simulation and the points represent the measured flux.

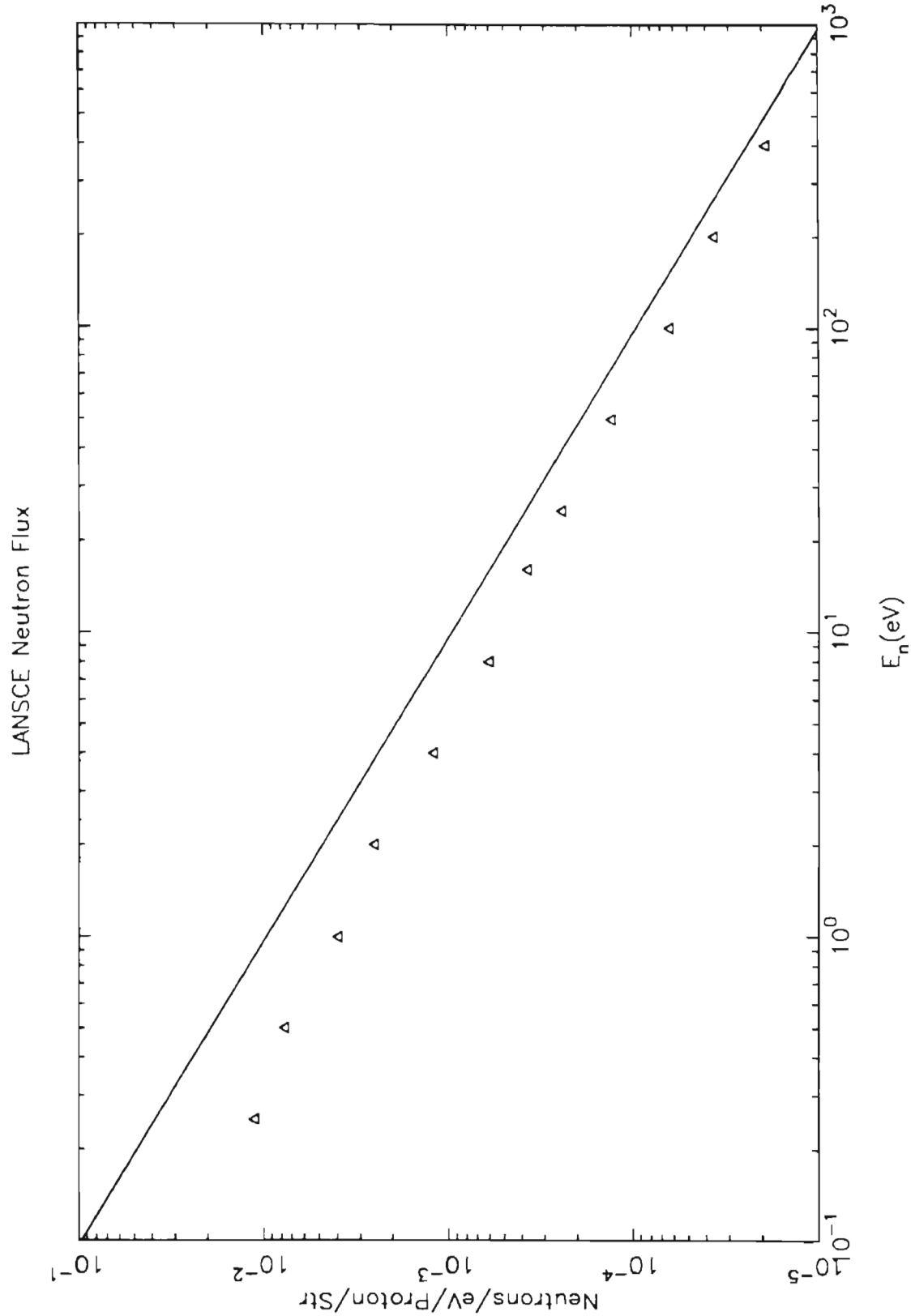
LANSCE Neutron Flux
Neutrons/eV/Proton/Str
10^{-1}
10^{-2}
10^{-3}
10^{-4}
10^{-5}
10^{-1}
10^{0}
10^{1}
10^{2}
10^{3}
E_n(eV)

4.2 Polarized Beam Facility for PNC Experiments at LANSCE

4.2.0 Introduction

LANSCE currently has 12 flight paths available for experiments. Four additional flight paths are currently being added (Figure 4.2.0.1). Flight paths 1, 3, and 6-10 are currently being used to study properties of materials. Flight path 4 is used for nuclear physics experiments. Flight paths 5, 11, and 16 have experimental apparatus under construction. The four new flight paths will be numbered 12-15.

The TRIPLE collaboration has equipped flight path 2 to optimize it for performing polarized neutron transmission PNC experiments. The experimental apparatus includes a neutron spin filter, a "spin flipper", neutron beam monitors, a target chiller, and an array of ^{6}Li glass neutron detectors. The experimental layout is shown schematically in figure 4.2.0.2. Collimation was added to the flight path to ensure that only neutrons which passed through the spin filter would strike the detectors. The location and type of collimation is shown in figure 4.2.0.3. The major pieces of equipment will be described in the following subsections.

4.2.1 Neutron Spin Filter

The (np) scattering cross section has three features which combine to make polarized protons an ideal spin filter for neutrons: the cross section is approximately constant from 1eV to 50keV, the cross section is large (~20b), and the cross section is highly spin dependent. The energy dependence of the (np) scattering cross section is shown in figure 4.2.1.1. The singlet portion of the cross section is much larger than the triplet portion (~67b as

Figure 4.2.0.1 Floor plan of LANSCE experimental rooms 1 and 2.

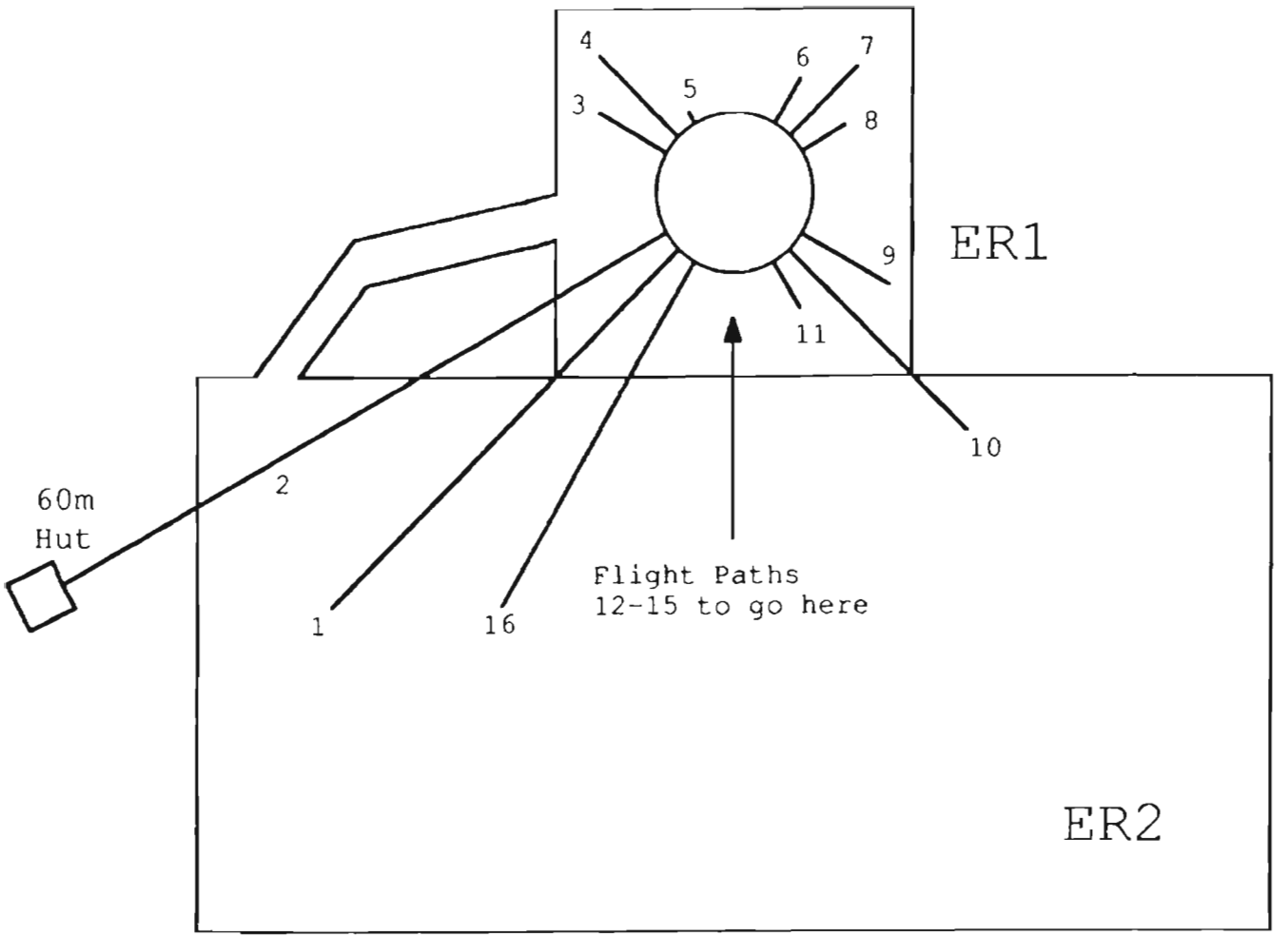
4
5
6
7
3
8
9
11
10
ER1
60m
Hut
2
1
16
Flight Paths
12-15 to go here
ER2

Figure 4.2.0.2 Schematic diagram of the major equipment on flight path 2.

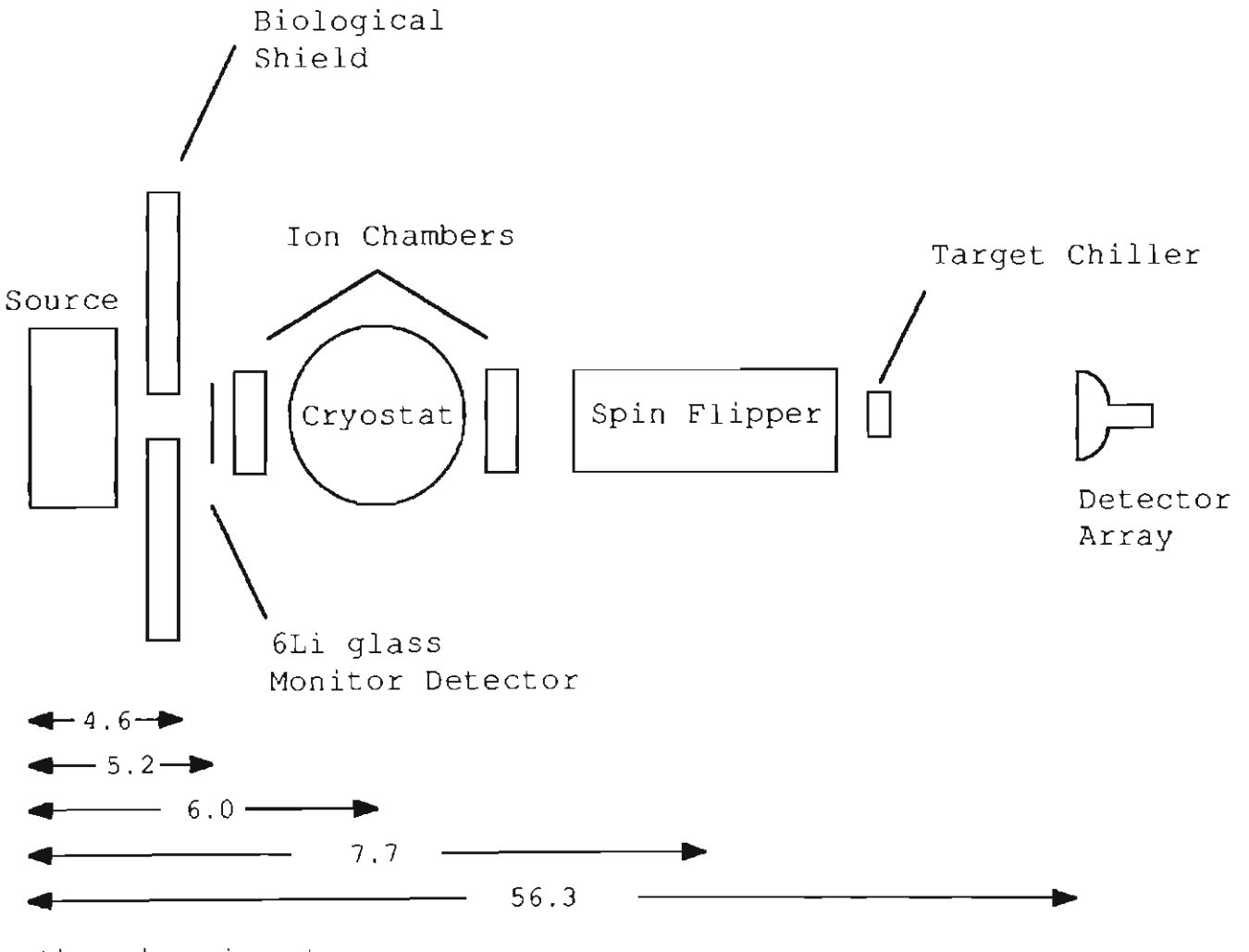

Dimensions in meters.

Figure 4.2.0.3 Schematic diagram of flight path 2 collimators.

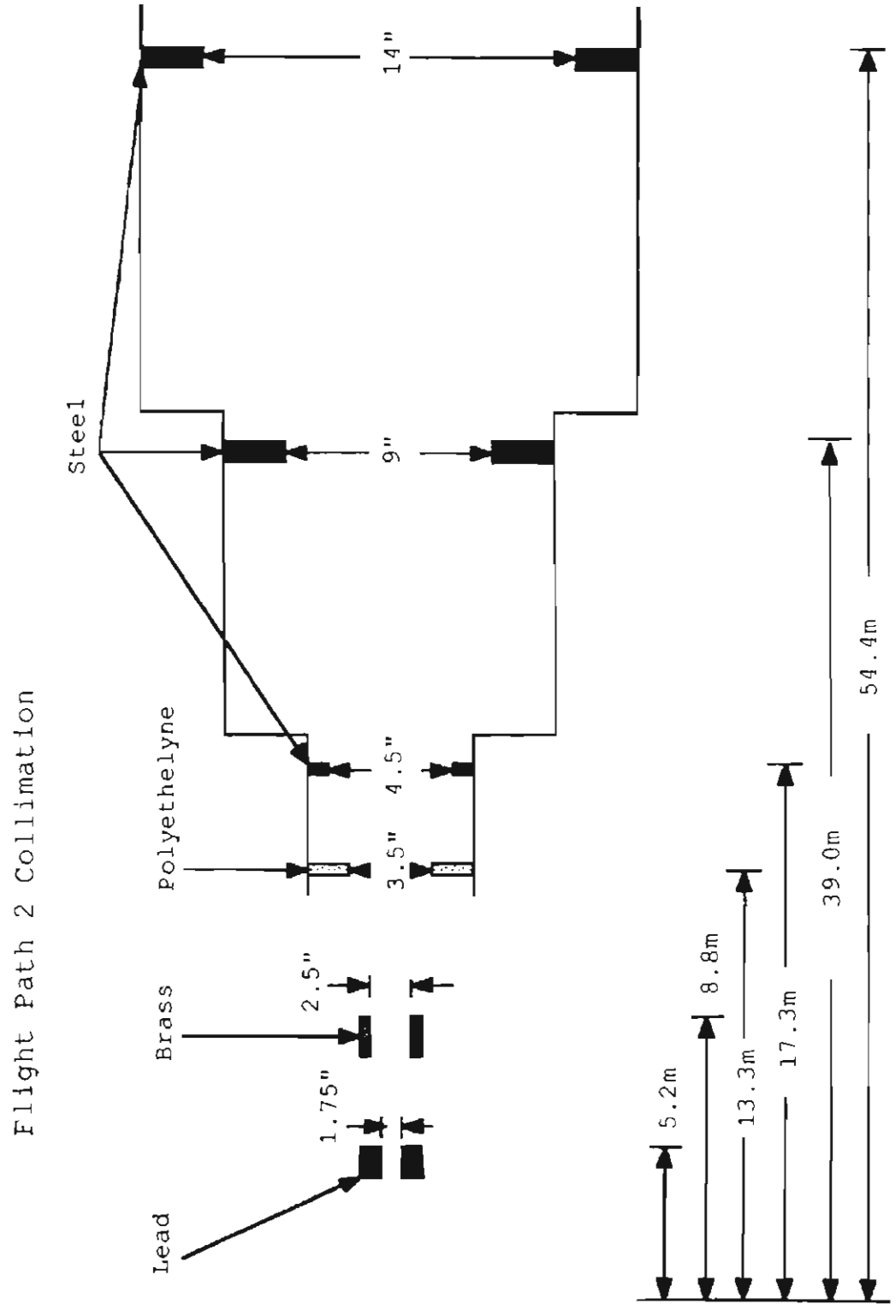
Flight Path 2 Collimation
Steel
Polyethelyne
Brass
Lead
14"
9"
4.5"
3.5"
2.5"
1.75"
5.2m
8.8m
13.3m
17.3m
39.0m
54.4m

Figure 4.2.1.1 The (np) scattering cross section as a function of energy. The points represent the latest evaluation of the (np) scattering cross section [Ha89a].

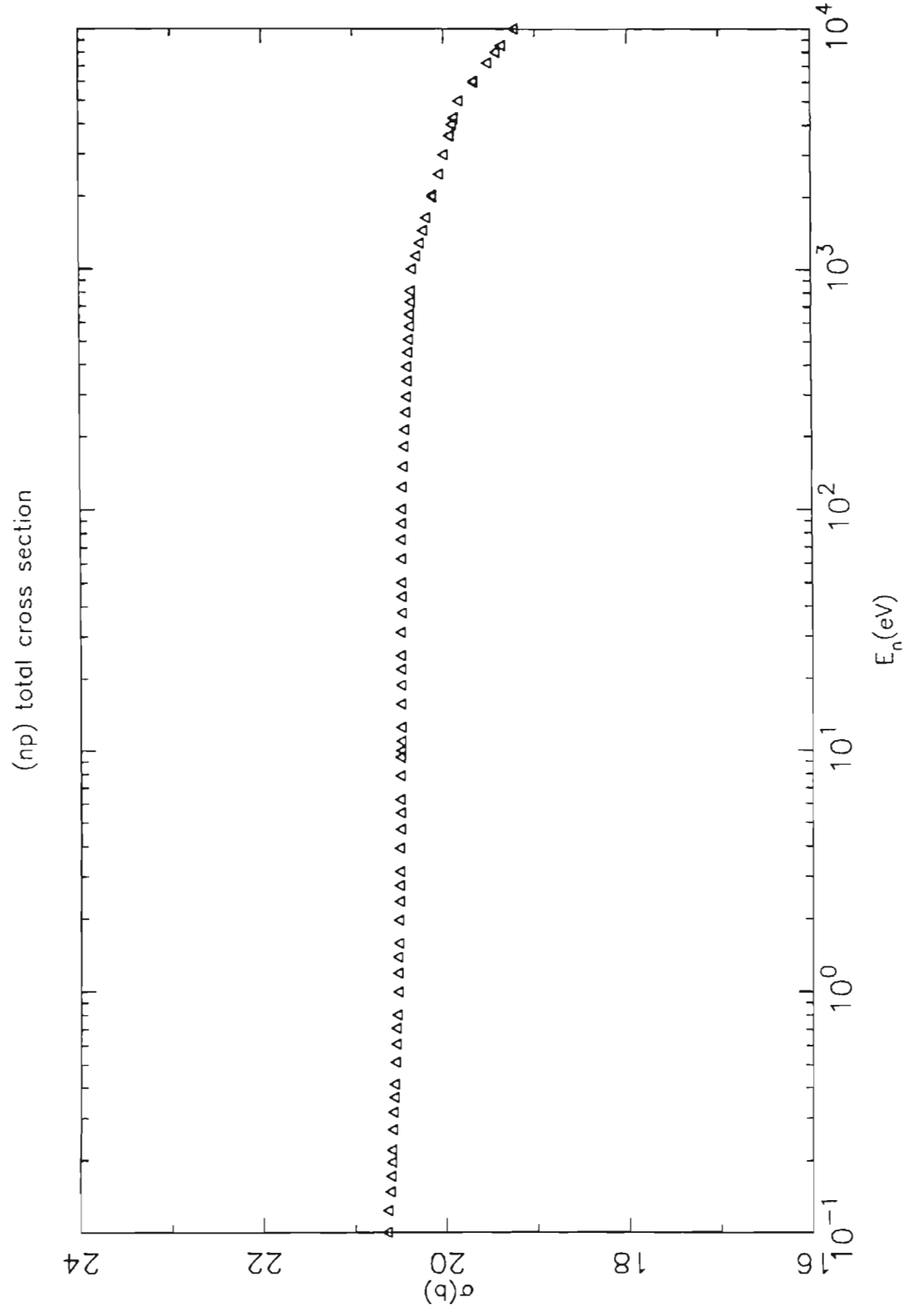
(np) total cross section
σ(b)
16
18
20
22
24
10^{-1}
10^{0}
10^{1}
10^{2}
10^{3}
10^{4}
E_n(eV)

compared to ~4b [Kr88]). Because of this spin dependence neutrons with their spins parallel to those of the protons will preferentially pass through a polarized proton sample.

The polarized proton sample used in this experiment consisted of the protons in the waters of hydration in single crystals of $La_2Mg_3(NO_3)_{12}\cdot 24H_20$ (0.5% ^{142}Nd doped), referred to as LMN. The techniques for polarizing protons in LMN are discussed in Jefferies [Je63] and in Abragam and Borghini [Ab64a]. The polarization process starts with the application of a large uniform magnetic field to the cooled LMN sample. The presence of the field and the low temperature causes the polarization of the electrons. In this configuration the proton-electron pairs in the LMN have energy levels as shown in figure 4.2.1.2. The t_i are the relaxation times for the various transitions. In LMN t_1 is short compared to t_2 and t_3. By applying radiation of frequency $\nu_e+\nu_p$ or $\nu_e-\nu_p$ one of the two flip-flip transitions is induced. Once both spins have been flipped, the electron returns to its initial orientation due to its short relaxation time while the proton remains flipped. The electron is then in a position to induce another flip-flip transition. Therefore, by applying microwaves at frequency $\nu_e+\nu_p$ or $\nu_e-\nu_p$ the protons can be polarized antiparallel or parallel to the field direction.

The proton polarization was monitored by nuclear magnetic resonance (NMR) techniques. A single turn NMR coil was wound around the LMN crystals. If one applies radio-frequency (RF) radiation to the sample at the proton NMR frequency, (ν_p~86MHz at 2T.) then some of the proton spins are flipped. Depending on which state the protons were in initially, radiation is either absorbed, sending

Figure 4.2.1.2 Energy level diagram of an electron-proton pair in an applied magnetic field.

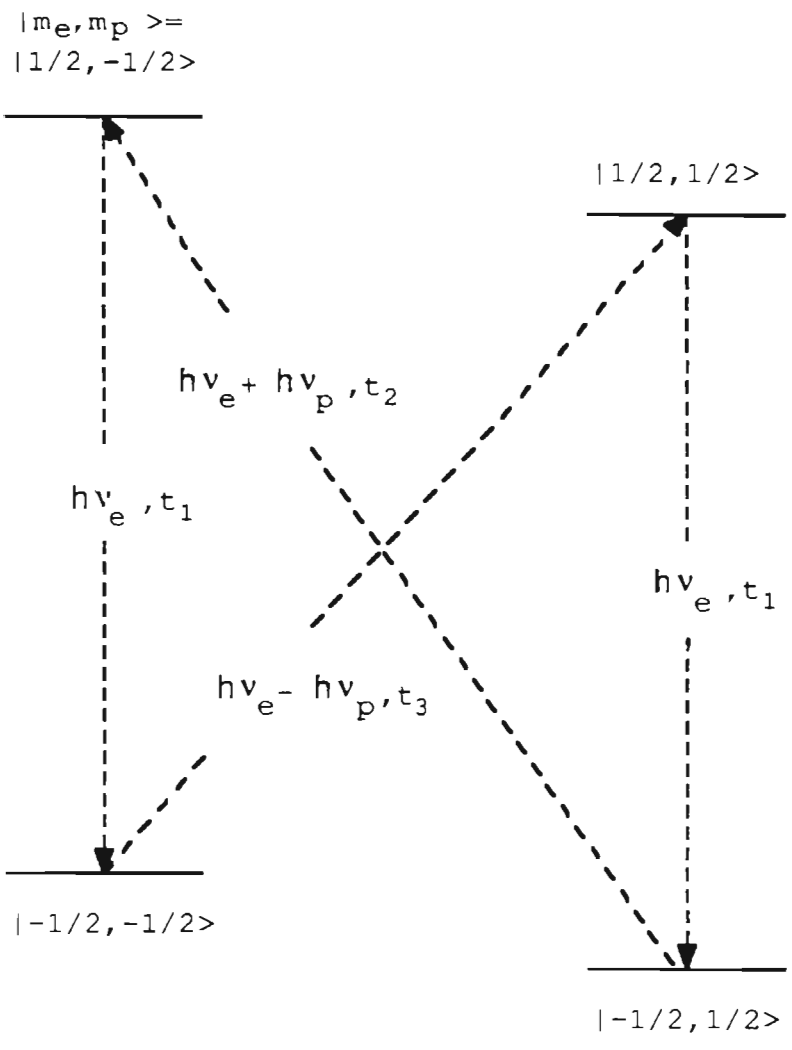
|m_e,m_p >=
|1/2,-1/2>
|1/2,1/2>
hν_e + hν_p ,t_2
hν_e ,t_1
hν_e ,t_1
hν_e - hν_p,t_3
|-1/2,-1/2>
|-1/2,1/2>

the protons into the higher energy state, or the protons are stimulated to emit radiation and make the transition to the lower energy state. The resulting decrease(increase) in the amount of radiation appears as a dip(peak) in a NMR voltage-frequency scan. The polarization was monitored in this way during each data run. Details on how this technique can be used to measure the polarization of the sample will be given in section 5.5.1.

The cryostat used in this experiment to polarize the neutron beam was constructed nearly 20 years ago by Keyworth *et al.* [Ke73] and is shown in figure 4.2.1.3. By present standards the cryostat is quite large, approximately 1m in height and 1m in diameter. It was placed on a pedestal approximately 1m high in order for the neutron beam to pass through the LMN crystals. The cryostat contains three separate cryogenic baths. The two innermost baths contain liquid helium (LHe) and the outer bath liquid nitrogen (LN). The inner LHe bath operates at ~1.1°K and contains the LMN crystals and a split coil superconducting magnet. The outer LHe vessel is at ~4°K and is connected to the inner LHe bath by a needle valve. This passageway allows LHe to flow into the inner bath to replace the LHe which boils away. The outermost vessel, containing LN, is used to shield the LHe vessels from ambient thermal radiation. During normal operation the cryostat consumes about 100 liters (ℓ) of LN and 200ℓ of LHe per day.

The superconducting magnet is of the split coil type, using trim coils to correct field nonuniformities due to winding, etc. The wire used is NbTi monofilament. Keyworth *et al.* [Ke73] reported a measured field homogeneity as one part in 10^5 over the crystal volume at 20.3kOe. After energizing the coils, the magnet was operated in persistent mode and no decay of the field was reported for periods of 36 hours.

Microwaves were supplied by a klystron tube manufactured

Figure 4.2.1.3 Diagram of the neutron spin filter cryostat with major components labelled.

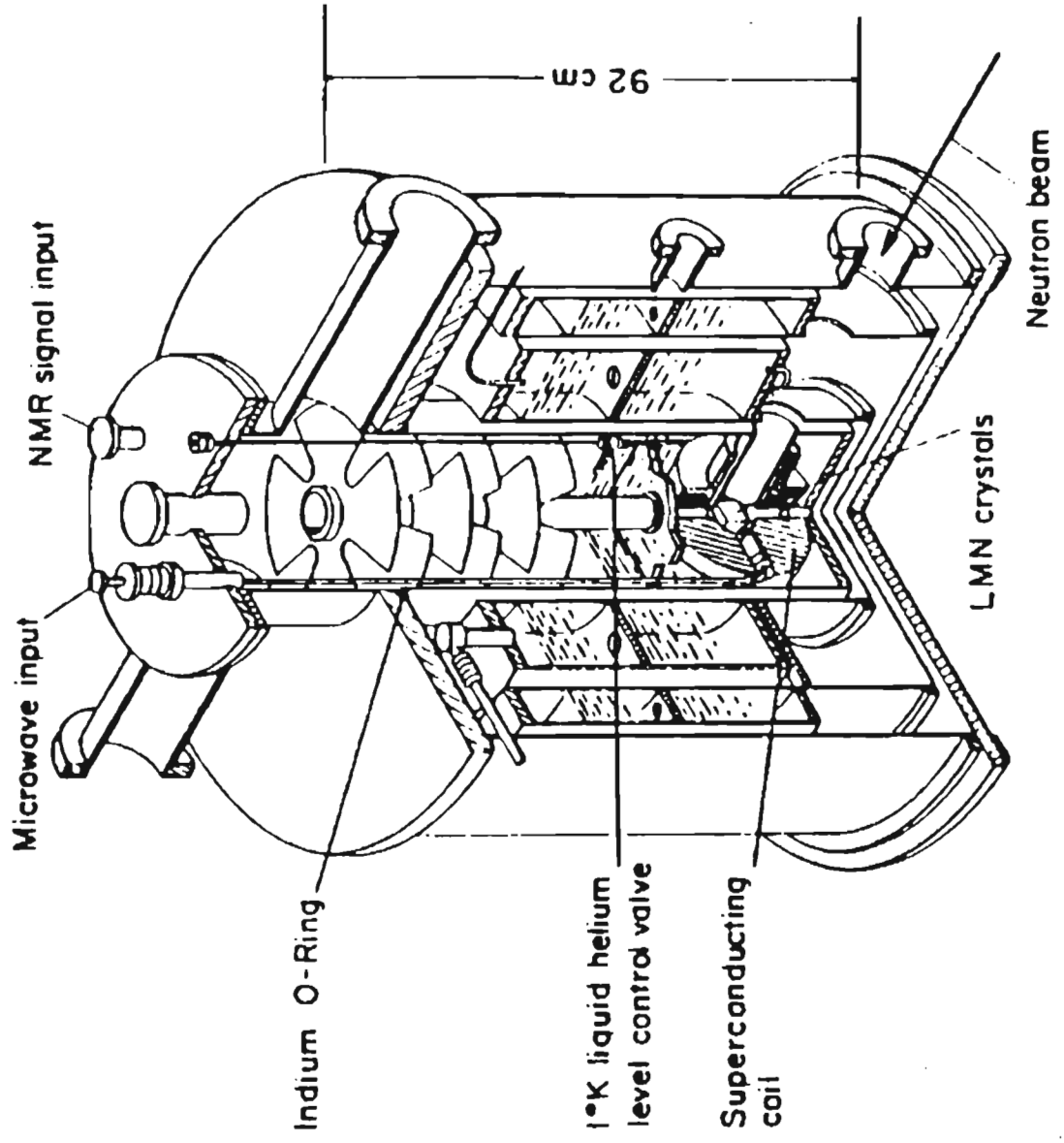
92 cm
NMR signal input
Microwave input
Indium O-Ring
1°K liquid helium
level control valve
Superconducting
coil
LMN crystals
Neutron beam

by Varian Associates. The tube is rated to supply 10 watts at 77GHz and was cooled by a constant temperature water bath. Before the 1990 run season the microwave frequency was manually tuned. At that time the fine tuning was placed under computer control utilizing feedback from a digital frequency meter. The computer attempted to maintain the frequency to ±10MHz during running, though frequency oscillations of a few tens of MHz were normal.

4.2.2 Neutron Spin Flipper

In order to measure the helicity dependence of the reaction it is necessary to change the direction of the neutron spin. Since it is a cumbersome, hour-long procedure to change the neutron spin direction using the cryostat, there is a need for a device which reverses the neutron spin quickly. The neutron spin flipper is located approximately 0.5m downstream from the cryostat (Figure 4.2.0.2). The spin flipper consists of two longitudinal solenoids and two sets of transverse coils (Figure 4.2.2.1). The longitudinal solenoids create a magnetic field (on axis) of the form

$$B_z = -B_0 \sin(\pi z / L), \qquad (4.2.2.1)$$

where B_0 is usually 10^{-2}T and L=1m. This field is parallel to the neutron beam direction for the first meter of the spin flipper and antiparallel for the second meter. During normal operation, current is always applied to the longitudinal solenoids, while current may or may not be applied to the transverse coils. When current is applied to the transverse coils a magnetic field of the form

$$B_y = B_0 \cos(\pi z / L) \qquad (4.2.2.2)$$

is present. B_0 and L have the same magnitude as above, although B_0 for the transverse field may be positive or

Figure 4.2.2.1 Diagram of spin flipper coil configuration.

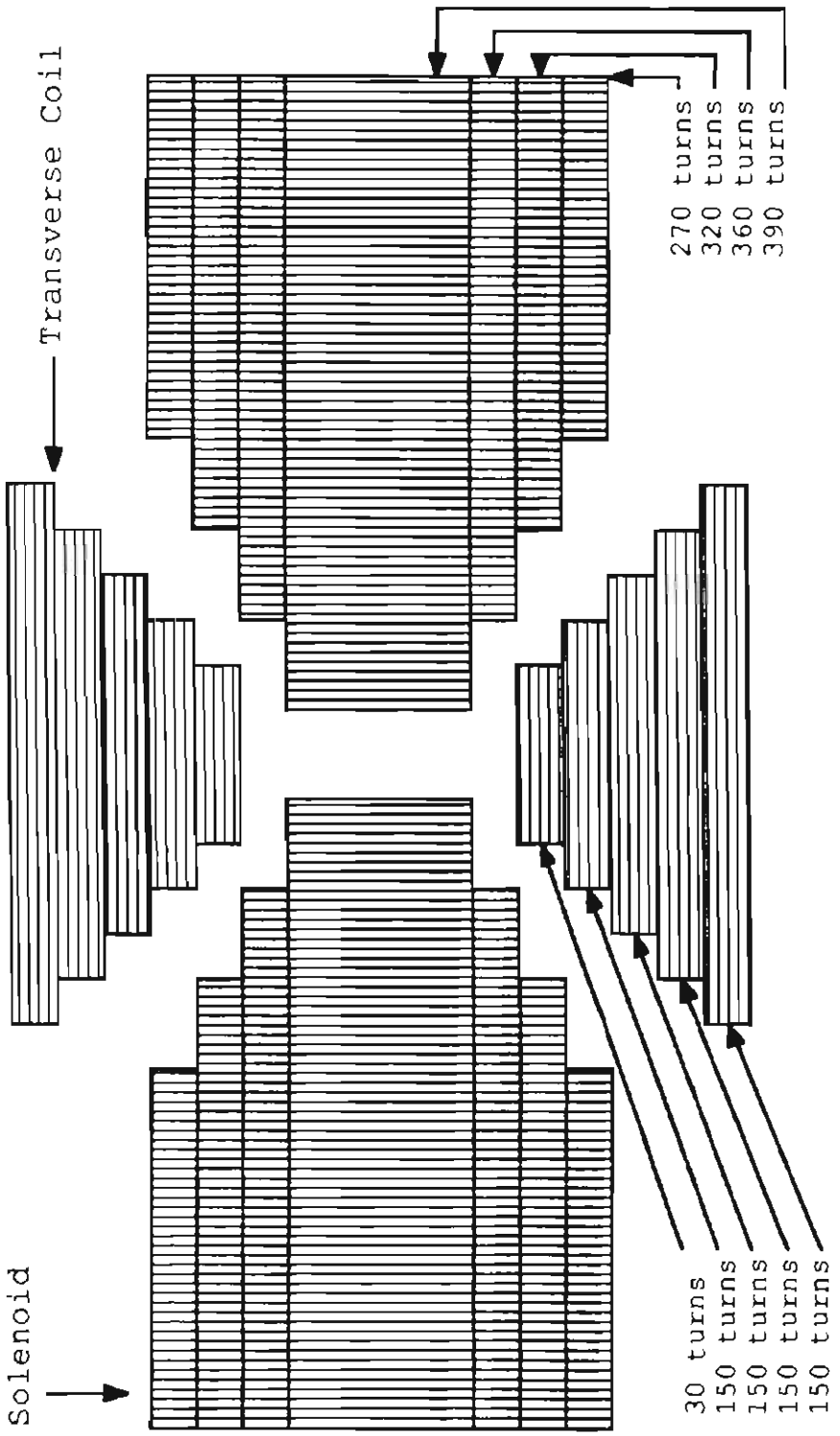
Transverse Coil
270 turns
320 turns
360 turns
390 turns
Solenoid
30 turns
150 turns
150 turns
150 turns
150 turns

negative. When B_y is present, a neutron sees a field of constant magnitude B_0 as it moves along the z axis.

Consider a neutron having spin along the z axis, with the transverse coils off. In this case, with the exception of a small transition region at z=0, the field is always parallel to the z axis (and also parallel to the neutron spin). In the region of parallel B field, there will be no torque on the neutron and consequently its spin direction will not be affected. If the neutron is moving fast enough (E~0.1eV for $B_0=10^{-2}$T) the spin of the neutron will not be able to follow the sharp field transition and will pass through the entire spin flipper system unaffected. Next consider the situation when the transverse coils are energized. The term of the Hamiltonian which describes the interaction of the neutron with the magnetic field is $-\mu\cdot\mathbf{B}$. If the rate at which the neutron precesses about the magnetic field is large compared to the rate at which the magnetic field changes, then the term $\mu\cdot\mathbf{B}$ is approximately constant. Then the neutron spin adiabatically follows the field direction (from +z at z=-L to $\pm$y at z=0 to -z at z=L) and the spin direction is reversed.

In the previous discussion all magnetic fields were assumed to be uniform in both magnitude and direction. This is only approximately true for the actual spin flipper. For coils with finite physical size, the actual magnetic fields must be numerically modeled. Since there are non-uniformities in the spin flipper, the spin flip efficiency is not exactly one. The average efficiency,

$$\bar{\varepsilon}=\frac{\varepsilon_{flip}+\varepsilon_{noflip}}{2}, \qquad (4.2.2.3)$$

as a function energy for $B_0=10^{-2}$T is shown in figure 4.2.2.2. These results are based on numerical simulations

Figure 4.2.2.2 Average efficiency of the spin flipper as a function of energy for $B_0=10^{-2}T$.

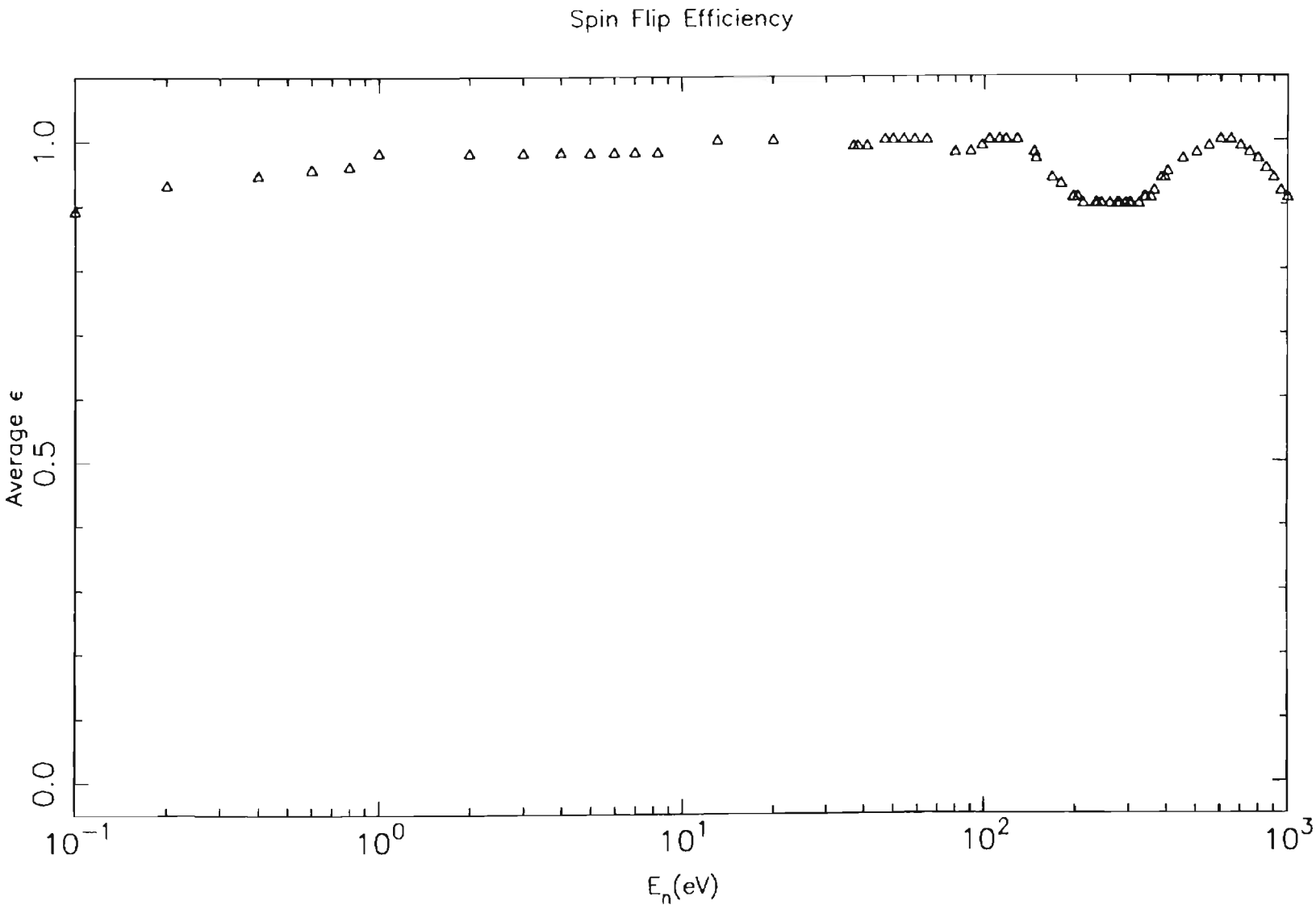
Spin Flip Efficiency
Average ε
1.0
0.5
0.0
10^{-1}
10^{0}
10^{1}
10^{2}
10^{3}
E_n(eV)

[Bo89a].

4.2.3 Neutron Beam Monitoring

During these experiments the intensity of the neutron beam was monitored on a burst by burst basis. Monitoring in this way has two advantages. First, if the beam is excessively unstable during some time period, then data obtained during that time may be rejected. Second, precise values for beam intensity allow the determination of an absolute neutron transmission.

A beam monitor was first installed for the 1989 run season. A single monitor was installed directly in front of the biological shield penetration. This monitor consisted of a 1mm by 76mm by 76mm slab of ^{6}Li loaded glass (NE905) attached to a light pipe, which was itself connected to a photomultiplier tube (PMT). This monitor is shown in figure 4.2.3.1. This type of monitor utilizes the reaction

$$n + {}^{6}Li \rightarrow {}^{7}Li^{*} \rightarrow {}^{4}He + {}^{3}H + 4.8MeV.$$

The scintillation light from the alpha particle and the triton is detected by the PMT. The neutron detection efficiency of this reaction is

$$\varepsilon = 1 - e^{-0.2/\sqrt{E}}, \qquad (4.2.3.1)$$

where E is in eV. This type of detector has the disadvantage that the glass can be damaged by high intensity radiation. Radiation damage was observed during the 1989 run season: the number of counts per microampere of beam slowly decreased (Figure 4.2.3.2).

An improved monitoring system was designed for the 1990 run season. The system adopted was a pair of ion chambers filled with 1atm of ^{3}He gas (Figure 4.2.3.3). One ion chamber was placed in the position of the old ^{6}Li glass monitor and the other on the upstream end of the spin flipper. This tandem monitoring system also allows for

Figure 4.2.3.1 Schematic diagram of the ^{6}Li glass neutron beam monitor.

Lithium Glass Neutron Beam Monitor

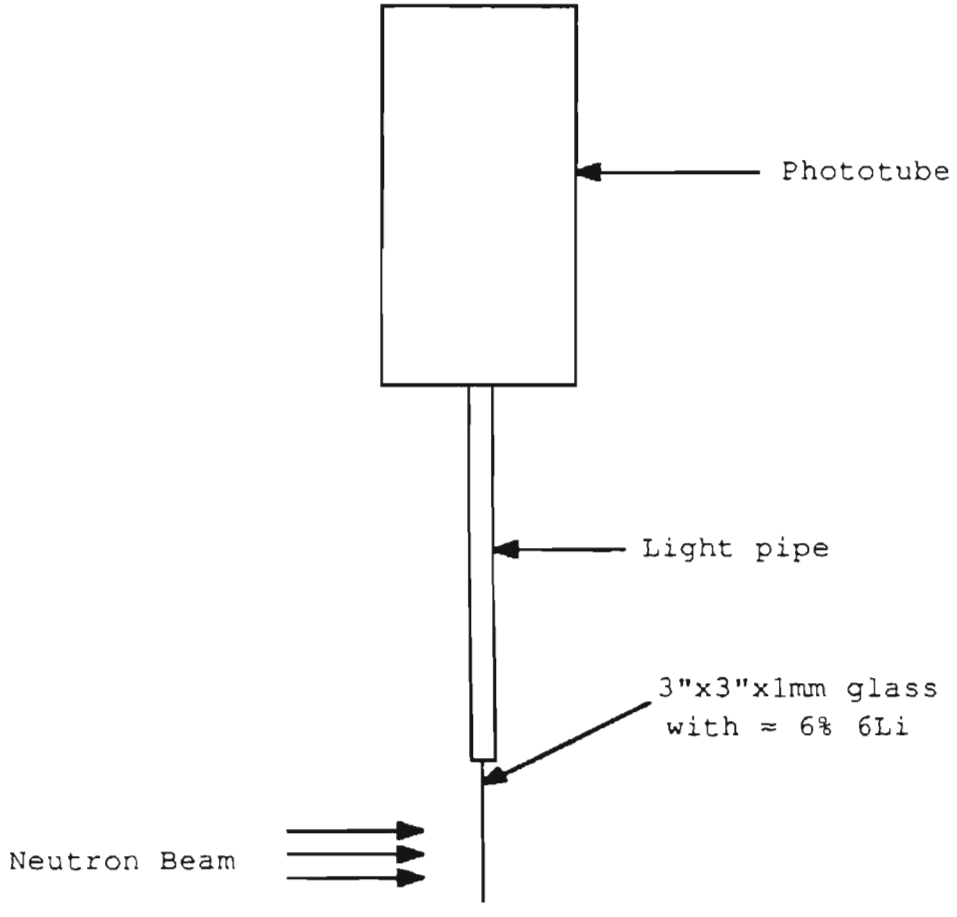

Figure 4.2.3.2 Plot of neutron beam monitor counts per microampere of beam as a function of time. Note the downward trend of the data points. The gap in the center is a cycle break. 9 June 1989 00:00 = 0.0 days.

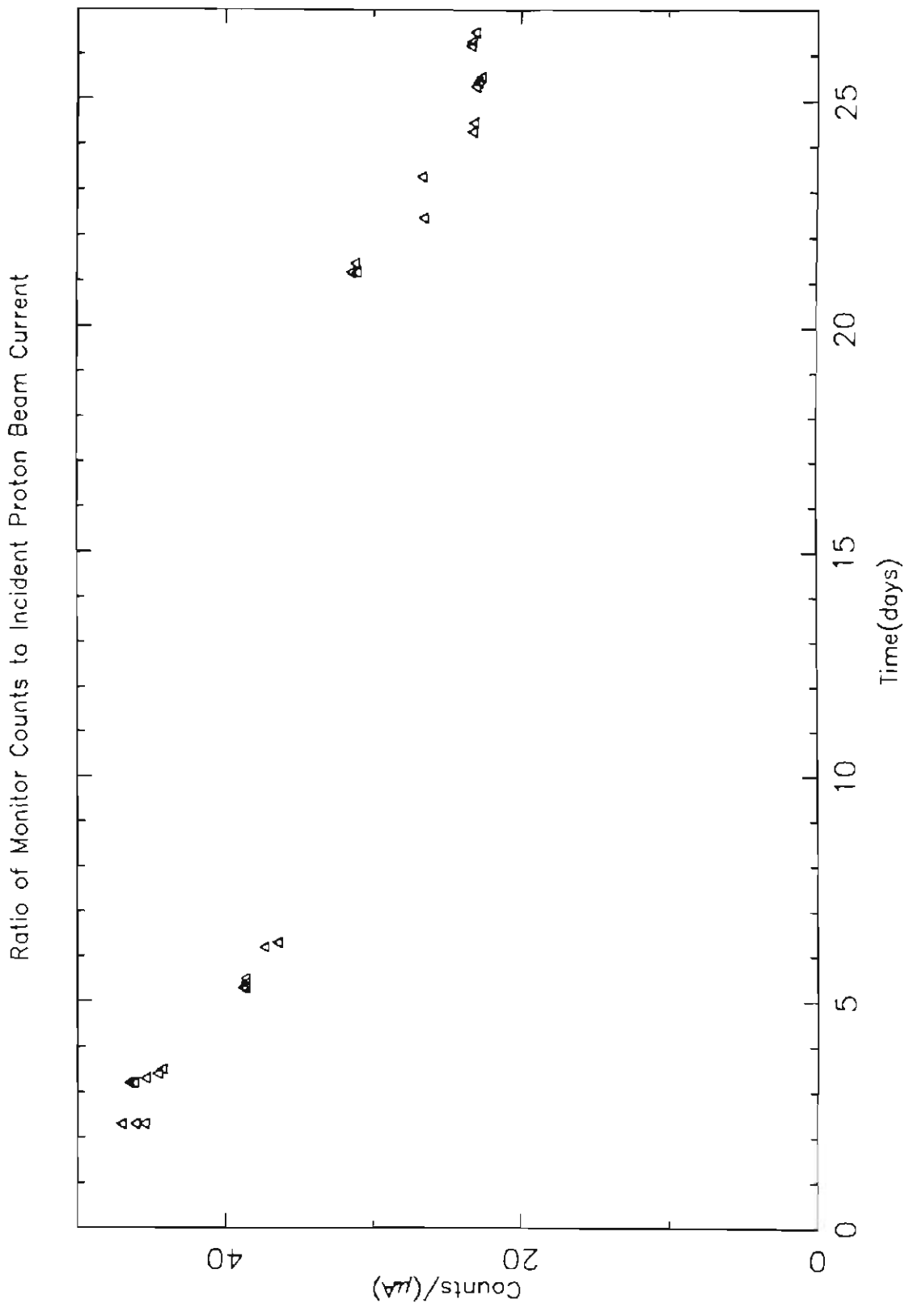
Ratio of Monitor Counts to Incident Proton Beam Current
Counts/(μA)
0
20
40
0
5
10
15
20
25
Time(days)

Figure 4.2.3.3 Diagram of a ^{3}He ion chamber showing construction details.

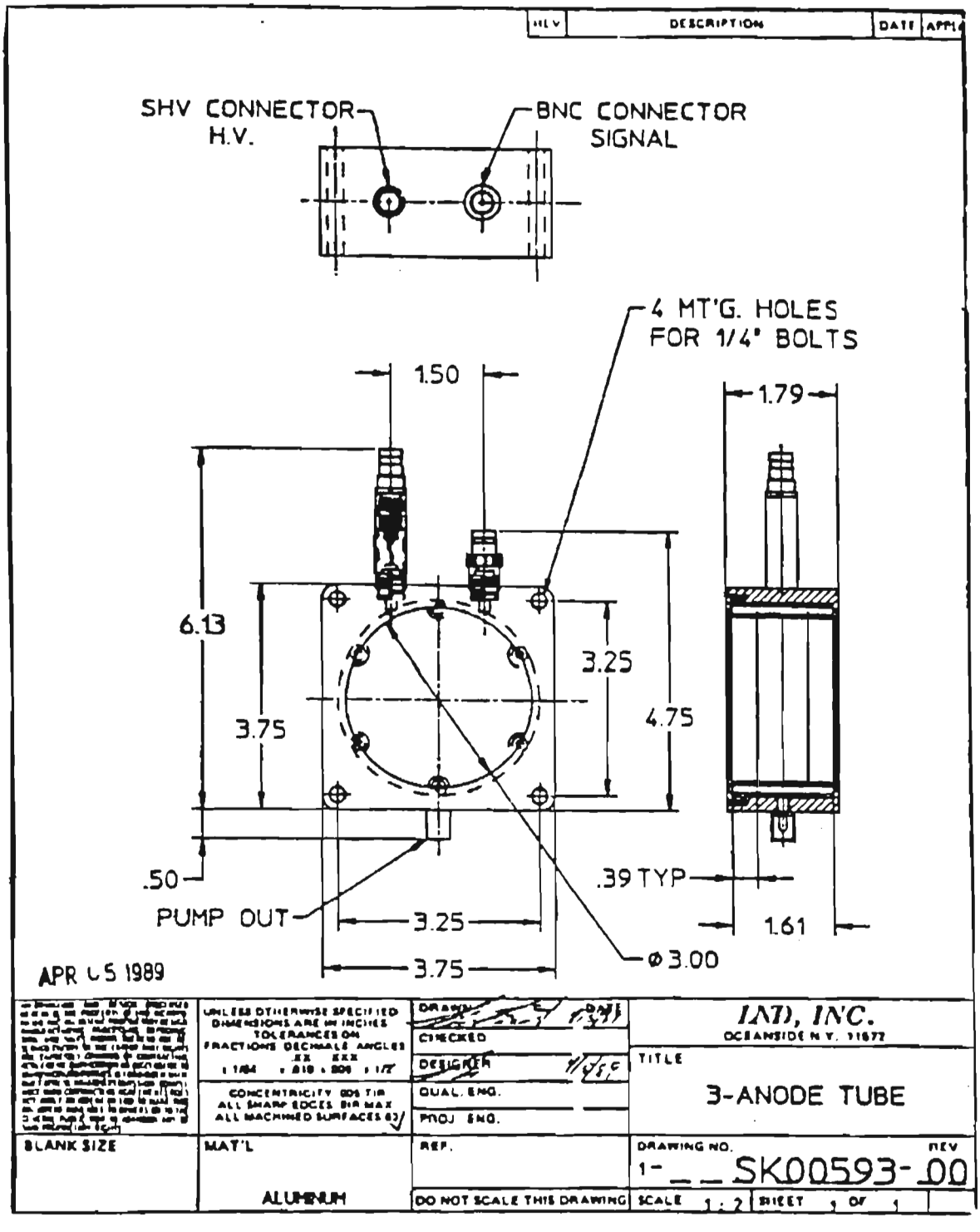
REV
DESCRIPTION
DATE
APPR
SHV CONNECTOR
H.V.
BNC CONNECTOR
SIGNAL
4 MT'G. HOLES
FOR 1/4" BOLTS
1.50
1.79
6.13
3.25
3.75
4.75
.50
PUMP OUT
3.25
3.75
.39 TYP
1.61
Ø 3.00
APR 05 1989
UNLESS OTHERWISE SPECIFIED DIMENSIONS ARE IN INCHES TOLERANCES ON FRACTIONS DECIMALS ANGLES .XX .XXX ± 1/64 ± .010 ± .005 ± 1/2°
CONCENTRICITY .005 TIR ALL SHARP EDGES .010 MAX ALL MACHINED SURFACES 63
DRAWN
CHECKED
DESIGNER
QUAL. ENG.
PROJ. ENG.
IAD, INC.
OCEANSIDE N.Y. 11572
TITLE
3-ANODE TUBE
BLANK SIZE
MAT'L
ALUMINUM
REF.
DO NOT SCALE THIS DRAWING
DRAWING NO.
1- SK00593-00
REV
SCALE 1:2
SHEET 1 OF 1

monitoring of the cryostat for possible ice buildup or other problems. These ion chambers utilize the reaction

$$n + {}^3He \rightarrow {}^4He^* \rightarrow p + {}^3H + 0.8MeV.$$

The proton and the triton ionize the gas and the charge from the electron cascade is collected on a signal electrode. These chambers have an efficiency of

$$\varepsilon = 1 - e^{-0.07/\sqrt{E}}. \qquad (4.2.3.2)$$

Ion chambers have the advantage that they are not susceptible to radiation damage.

4.2.4 Targetry

The bromine target used in this experiment consisted of 750mℓ of "Baker Analyzed" natural bromine liquid. The isotopic abundance of ^{81}Br is 49.31%. The only other naturally occurring bromine isotope is ^{79}Br. The liquid bromine was supplied in a 10.1cm OD reagent bottle, wrapped in plastic, and enclosed in an aluminum safety can. Because of the extreme toxicity and corrosiveness of bromine, it was decided to place the can-bottle assembly in the neutron beam at the end of the spin flipper. The edge of the aluminum can was located 3.1cm from the end of the spin flipper. The average neutron depolarization due to the bromine not being in a uniform guide field was calculated to be 5%. A 3.8cm ID collimator was inserted into the spin flipper to direct the neutron beam through the center of the bottle only. No contaminating resonances were observed due to the bromine sample, though several were attributed to the packaging.

The thorium target prepared for the 1990 run season was a single piece of metallic thorium. It was machined into the form of a right circular cylinder 6.0cm in diameter and 3.1cm long. Natural thorium is 100% ^{232}Th. Trace quanti-

ties of gadolinium and tungsten contaminated the target. In order to improve the resolution of the system, a "target chiller" was fabricated during the 1989-1990 down time. The target chiller bolted onto the downstream end of the spin flipper (Figure 4.2.4.1). The target was cooled to 77°K, with the additional magnetic field providing a continuation of the spin flipper guide field. Further details and tests on the target chiller are given in Appendix A.

4.2.5 Neutron Detectors

The neutron detectors used in this experiment were located 56.3m downstream from the neutron source. At that position the neutron beam has a diameter of nearly 40cm. An array of seven detectors was used to cover the beam area(Figure 4.2.5.1). Each detector consisted of a cylindrical slab of ^{6}Li loaded glass, 13.3cm in diameter and 1cm thick. Glass of this type has a neutron detection efficiency of

$$\varepsilon = 1 - e^{-2.0/\sqrt{E}}. \qquad (4.2.5.1)$$

Each glass slab was attached to a Hamamatsu R1513 PMT. The photocathodes were supplied with voltages ranging from -1500 to -1900 volts. The last four dynodes on each tube were held at -960V, -720V, -480V, and -240V, respectively. This prevented degradation of the tube gain under high current conditions.

4.3 Signal Processing and Data Acquisition

4.3.0 Introduction

The data acquisition electronics for this experiment have slowly evolved over the past several years. At present it is one of the most complex subsystems of the

Figure 4.2.4.1 Schematic diagram showing locations of the target and target chiller with respect to the spin flipper. The diagram is not to scale.

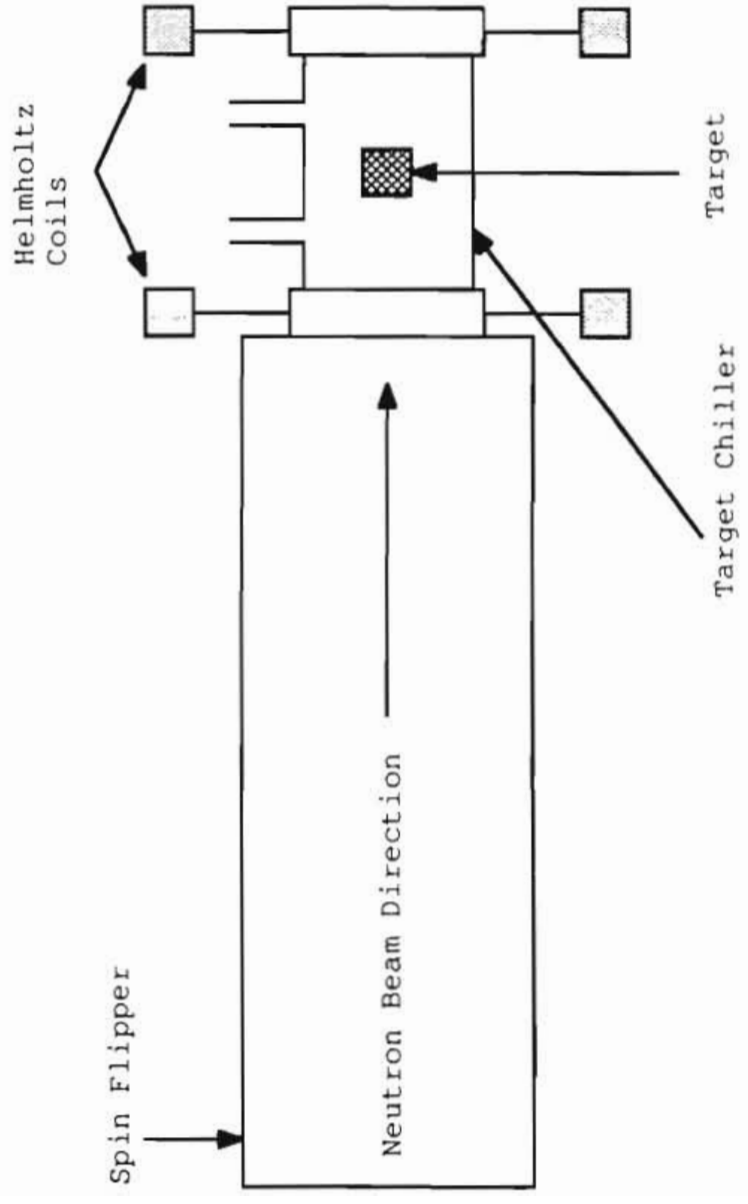
Helmholtz
Coils
Target
Target Chiller
Neutron Beam Direction
Spin Flipper

Figure 4.2.5.1 View of the array of seven neutron detectors as seen from the source.

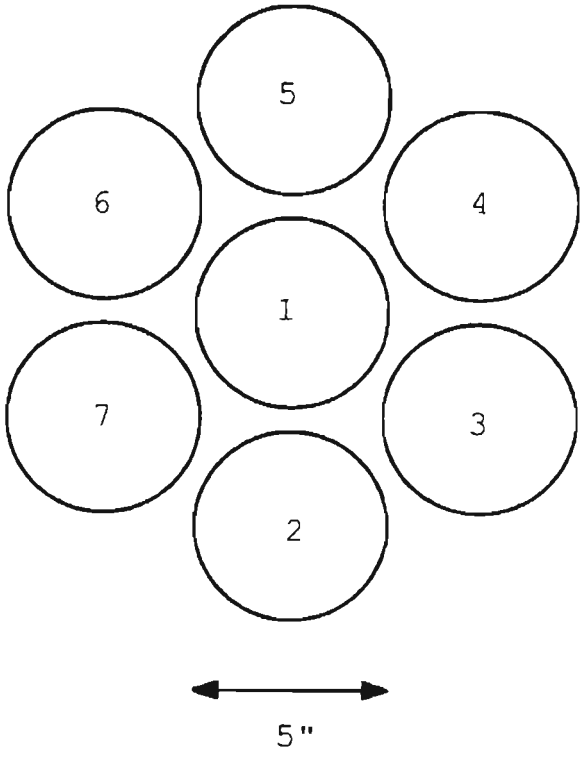
5
6
4
1
7
3
2
5"

experiment. The hardware will be presented first, followed by discussions of the logic and sequencing of the actual production data taking mode.

4.3.1 Detector Signal Processing

The number of neutrons striking a detector can be measured in two ways. If the electronic pulses representing individual neutrons are cleanly separated when they emerge from a PMT, then the pulses are simply counted. At a high intensity source such as LANSCE there are conditions when two or more individual neutron pulses overlap. When overlaps occur the electronics cannot distinguish between a pulse generated by one neutron or several. An alternative method to record the actual number of neutrons is to integrate the PMT output current. In order to obtain the final neutron count some amount of total charge can be attributed to each neutron. In practice it is sufficient to work with the digitized current. Both of these techniques have been used in the present experiments. Specifically, the counting mode was used in taking the bromine data and the current mode for taking the thorium data. The implementation of each method will be discussed below.

The individual neutron pulses from the PMT have a peak height of a few mV and a decay time of about 80ns. In counting mode pulses from each detector are individually shaped using a passive filter. Each signal is then amplified by a factor of 20. The signals are then discriminated with a threshold of about 80mV. This portion of the processing takes place in the 60m detector hut. Discriminated pulses are then sent over ~150m of cable to the data room. The pulses are then discriminated a second time in order to reduce any pickup noise. The seven sets of signals are then combined using a linear fan-in. The combined signal is input to a multiscaler (MS). The MS can be set to count

for time periods ranging from 100ns to 10μs. The counts for each time period are stored in one channel of an 8192 channel spectrum. This process is schematically diagramed in figure 4.3.1.1.

The first step in the current mode process is to fan-in the outputs of the seven PMTs using a hardwired "spider". The combined signal then is passed through a times 10 amplifier. As with the counting mode method this signal then is sent over ~150m of cable to the data room. The signal is then passed through a multipole filter with a time constant equal to the dwell time at which data will be taken. The output from the filter is routed into a 12 bit transient digitizer (TD). The TD then dumps to a 24 bit, 8192 channel signal averaging memory. A schematic of this process is shown in figure 4.3.1.2. A recent article giving further details on the TD and its operation is available [Bo90a].

The memory modules are Computer Automated Measurement And Control (CAMAC) modules. A CAMAC crate can hold up to 25 modules, one of which must be the crate controller. The crate controller is connected to a BiRa Microprogrammable Branch Driver (MBD). The MBD in turn communicates with a VAX model computer over a UNIBUS interface. This experiment utilized a VAXstation II/GPX. The MBD and CAMAC crate controller provide two way communication between the computer and the CAMAC modules. The software used to drive the MBD is the XSYS package, originally developed at TUNL [Ki81]. This experiment uses a revision of XSYS developed at IUCF [Yo87].

4.3.2 Spin Flip Sequencing

The primary goal of flipping the neutron spin in a particular sequence is to minimize systematic errors. The spin flipper is constructed such that when the neutron spin

Figure 4.3.1.1 Block diagram of the electronics used in counting mode.

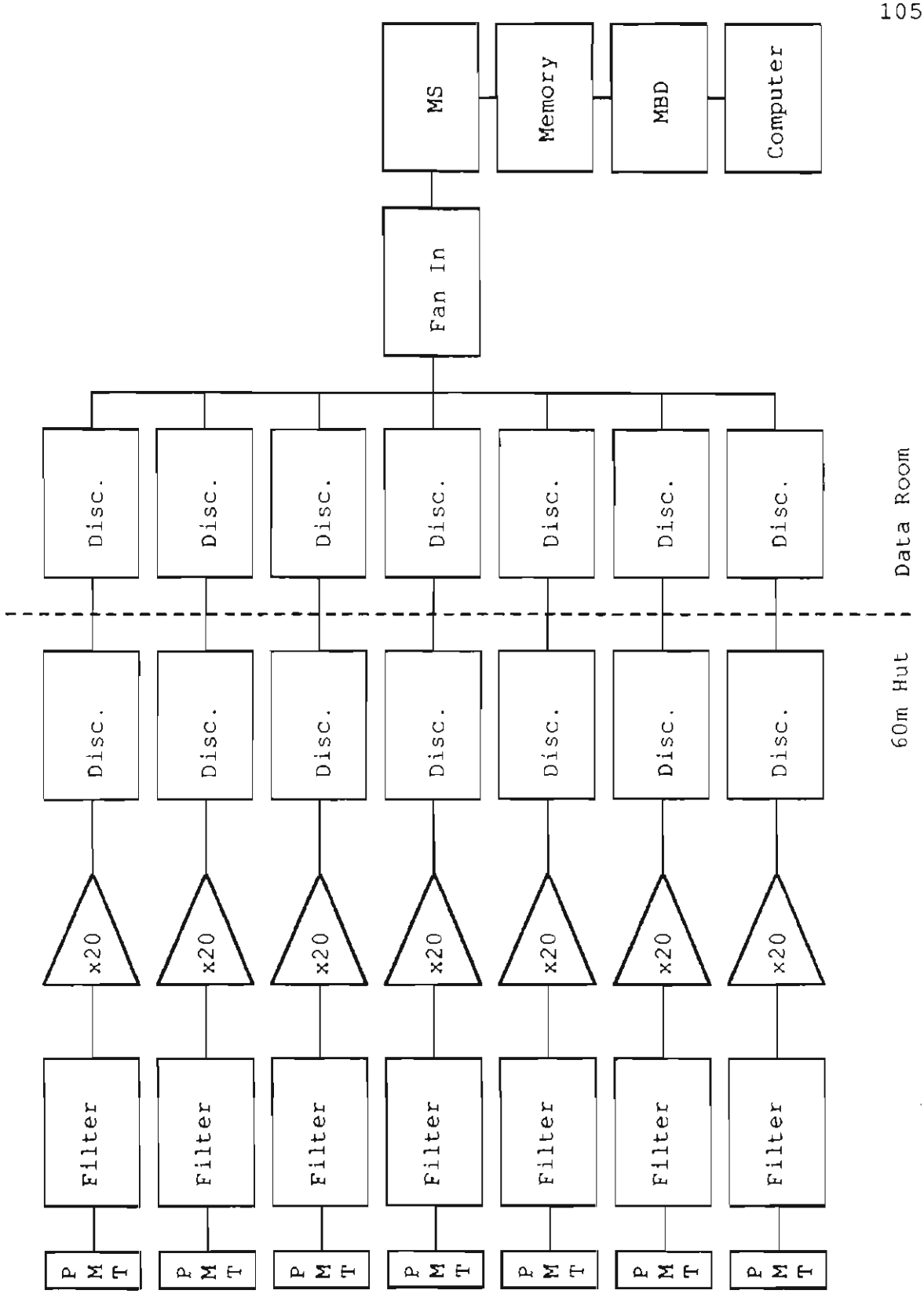
PMT
Filter
x20
Disc.
60m Hut
Data Room
Fan In
MS
Memory
MBD
Computer

Figure 4.3.1.2 Block diagram of the electronics used in current mode.

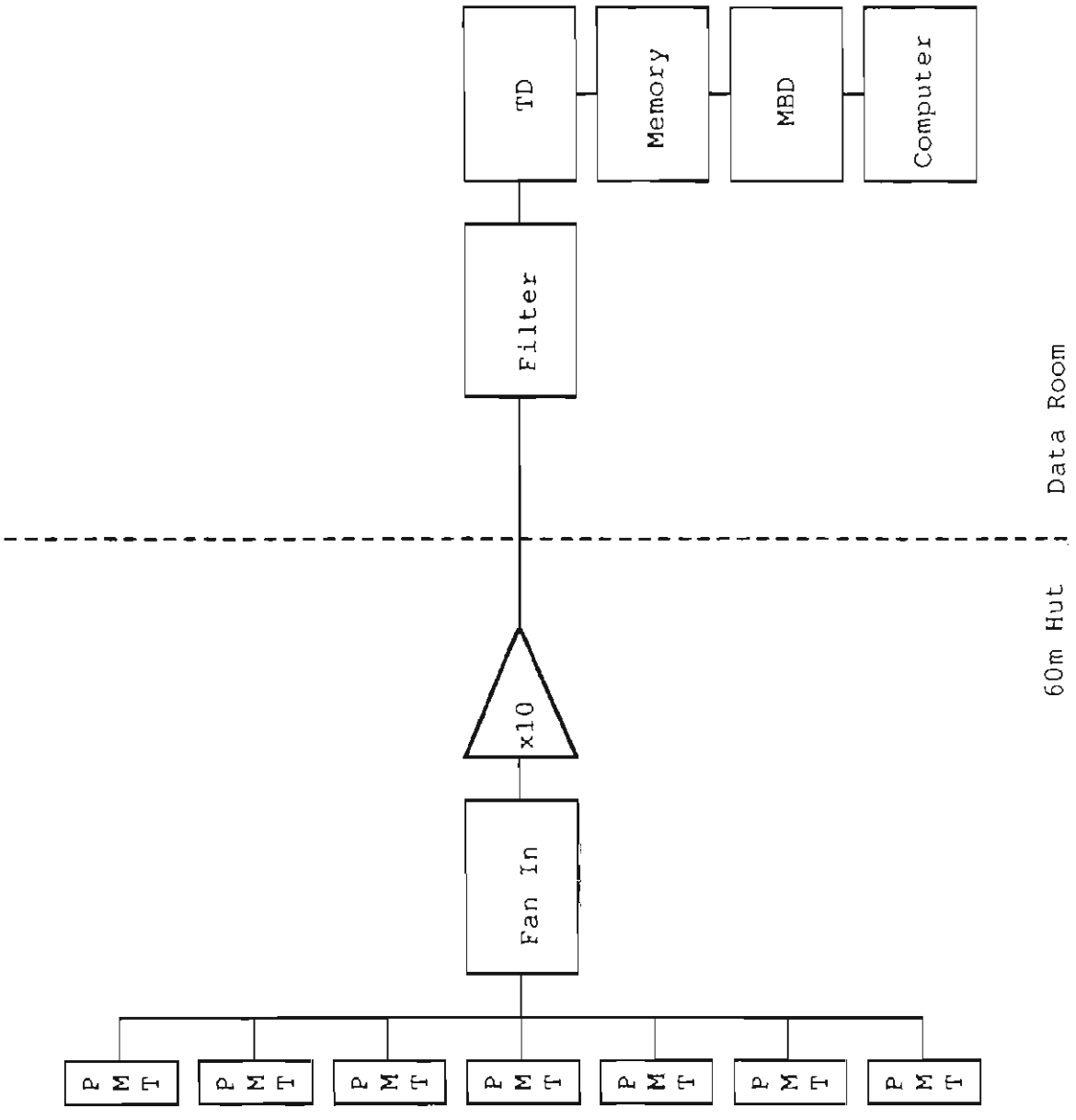
PMT
PMT
PMT
PMT
PMT
PMT
PMT
Fan In
x10
Filter
TD
Memory
MBD
Computer
60m Hut
Data Room

is flipped, it can reverse either by rotating to the right or to the left. This capability allowed an eight step spin sequence to be developed. The sequence proceeds 0,+,-,0,+,0,0,- where '0' indicates noflip (transverse coils off), '+' indicates a flip by rotation to the right, and '-' indicates a flip by rotation to the left. There are two main types of systematic errors that can arise from flipping the spin: 1) The spin flipper may not flip by exactly 180° and 2) The spin flipper magnetic fields may affect the detector. As will be shown below, these two errors are minimized by the eight step spin sequence. A third possible source of error, detector gains which drift with time, is also minimized.

Consider the situation where the spin flipper fails to rotate the spin by 180°. False asymmetries due to this problem can be eliminated by flipping an equal number of times to the right and to the left. During the noflip periods the spin may actually be rotated slightly. To eliminate false asymmetries due to this possibility the cryostat polarization direction was reversed approximately every 24 hours of running.

The presence of magnetic fields can affect the gain of a PMT [Ha89]. Let S be the signal from a PMT. Then S=kG, where k is a constant and G is the PMT gain. The gain can be expanded in terms of a change in magnetic field ΔB,

$$G = G(B_0) + \Delta B \frac{dG}{dB} + \frac{1}{2}\Delta B^2 \frac{d^2G}{dB^2} + \cdots. \qquad (4.3.2.1)$$

Then the signals from flip right, flip left, and noflip are

$$S(+) = kG + \Delta B \frac{k\,dG}{dB} + \frac{1}{2}\Delta B^2 \frac{k^2\,d^2G}{dB^2} + \cdots, \qquad (4.3.2.2a)$$

$$S(-) = kG - \Delta B \frac{k\,dG}{dB} + \frac{1}{2}\Delta B^2 \frac{k^2\,d^2G}{dB^2} + \cdots, \text{ and} \qquad (4.3.2.2b)$$

$$S(0) = kG, \tag{4.3.2.2c}$$

respectively. The asymmetry for the eight step spin sequence is defined as

$$A = \frac{S(+) + S(-) - 2S(0)}{S(+) + S(-) + 2S(0)}. \tag{4.3.2.3}$$

Inserting eqs. (4.3.2.2a)-(4.3.2.2c) into eq. (4.3.2.3) and dropping terms greater than second order yields

$$A = \frac{\Delta B^2}{4G}\frac{d^2G}{dB^2}. \tag{4.3.2.4}$$

An upper limit of 10^{-9} was established for A. These measurements will be described in the following chapter.

A similar analysis can be performed for a time dependent PMT gain. Expanding the gain in terms of the elapsed time during a sequence, Δt, and the time constant for drifts, τ, yields

$$G = G(t_0) + \Delta t\frac{dG}{\tau} + \frac{1}{2}\Delta t^2\frac{d^2G}{\tau^2} + \cdots. \tag{4.3.2.5}$$

Expanding the asymmetry of eq. (4.3.2.3) to a step by step form gives

$$A = \frac{dS}{\Sigma S}, \tag{4.3.2.6}$$

where

$$dS = S(+,\Delta t = 2dt) + S(+,5dt) + S(-,3dt) + S(-,8dt) - S(0,1dt) - S(0,4dt) - S(0,6dt) - S(0,7dt) \text{ and} \tag{4.3.2.7a}$$

$$\Sigma S = S(+,\Delta t = 2dt) + S(+,5dt) + S(-,3dt) + S(-,8dt) + S(0,1dt) + S(0,4dt) + S(0,6dt) + S(0,7dt). \tag{4.3.2.7b}$$

Evaluating the S quantities in eqs. (4.3.2.7a) and (4.3.2.7b) and dropping higher order terms yields

$$A = \left(\frac{dt}{\tau}\right)^3 \frac{d^3G}{G}. \qquad (4.3.2.8)$$

Hence the first non-zero term in the asymmetry is third order in (dt/τ).

4.3.3 Beam Monitoring

The techniques used to monitor the beam were identical for both ^{6}Li glass and ^{3}He ion chamber monitors. Approximately 1μs before the proton beam strikes the neutron production target an electronic "time-zero" pulse (t0) is received at the experiments' data room. In the jargon "t0" is synonymous to "beam burst" (i.e., one t0 equals one beam burst). An electronic gate was set to start accepting counts from the monitor 50μs after t0. The gate was 8ms wide. A delayed t0, t0', was generated 1/60s after t0 and a similar gate applied. The counts from the t0' gate were subtracted from the t0 gate as background not related to the beam.

In this manner a relative beam intensity is measured for each t0. These relative intensities are placed into a histogram after each t0. After 1600 t0's (one eight step spin sequence, 200 t0's per step) are collected the data are summed and an average computed. A window can be set such that if any of the 1600 intensity measurements fall outside the window then the sequence is routed to a "bad" data area. For normal running the window was set at ±8% of the average. The 8% was chosen empirically to eliminate data taken during most beam glitches while still retaining 70-80% of the data as "good" data.

4.3.4 Run Sequencing

Each production data run consists of 32000 t0's and

lasts approximately 30 minutes. The 32000 t0's are separated into 20 eight step spin sequences. A simplified flow chart of the run procedure is shown in figure 4.3.4.1. An operator initiates a run by inputting a set of run parameters (a default set may be requested). The computer first clears its data storage memory and sets all parameters to their newly selected values. An NMR signal is then read to determine the polarization. Once the NMR scans are completed the next t0 starts the data taking. After each t0 data is taken for 8192 times the dwell time and again after the delayed t0. The data obtained for the delayed t0 are subtracted from that obtained at t0, and the result stored in a summing memory. After each t0 the computer checks the spin flipper voltages and the t0 count. Once 200 t0's have been collected, the data are moved to a temporary storage location in the computer. The computer then reads the microwave frequency and, if necessary, applies a correction voltage to the microwave power supply to bring the frequency back to the requested value. The spin flipper state is then changed. After an eight step spin sequence has been completed (1600 t0's) the monitor histogram is checked for bursts with intensities falling outside the permitted window. The data are then moved from temporary storage to either "good" or "bad" data areas. The temporary storage is cleared in preparation for the next sequence. After 20 such sequences (32000 t0's) have been collected the data are archived from volatile memory to disk. All parameters are returned to their initial values and the run is ended.

Figure 4.3.4.1 Flow chart of a normal run sequence.

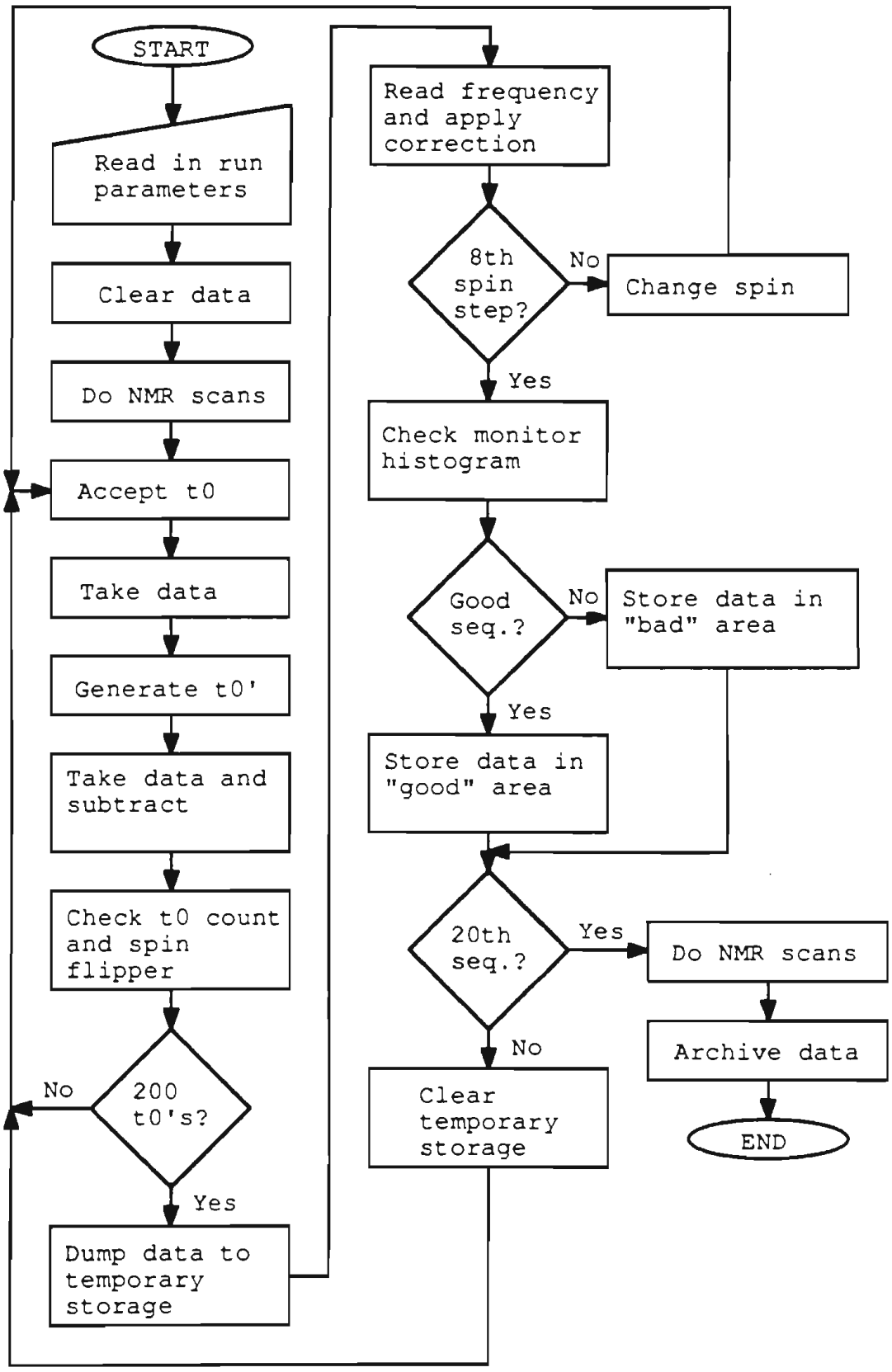
START
Read in run parameters
Clear data
Do NMR scans
Accept t0
Take data
Generate t0'
Take data and subtract
Check t0 count and spin flipper
No
200 t0's?
Yes
Dump data to temporary storage
Read frequency and apply correction
8th spin step?
No
Change spin
Yes
Check monitor histogram
Good seq.?
No
Store data in "bad" area
Yes
Store data in "good" area
20th seq.?
Yes
Do NMR scans
Archive data
END
No
Clear temporary storage

CHAPTER V

Auxiliary Measurements

5.0 Introduction

Before an observed asymmetry is ascribed to parity violation, it must be shown that the asymmetry was not caused by some systematic error. The purpose of the auxiliary measurements was to establish that false asymmetries are zero within their errors. Tests were made on the beam monitors to establish their statistical precision and stability. The magnetic fields of the cryostat, spin flipper, and target chiller were mapped. Possible effects of the spin flipper magnetic fields on the detectors and monitors were investigated. Extensive effort was spent establishing a calibration of the neutron beam polarization. These tests will be described below.

5.1 ^{6}Li glass beam monitor

The ^{6}Li glass beam monitor was installed and tested at the beginning of the 1989 run season. It was tested for statistical precision and short term stability (~hours).

The first item to be checked was the statistical precision of the monitor. The following procedure was used. An electronic gate was set on the monitor and the 60m detector signals. The gates were opened 50μs after the t0 and remained open for 6ms. Counts occurring while the gates were open were summed and the results histogrammed each t0. The ratio R=D/M, where D is the 60m detector count and M is the monitor count, also was calculated and histogrammed each t0. Data were taken in runs of length 4000 t0's. The relationship of the errors in the ratio, detector count,

and monitor count has the form

$$\left(\frac{\sigma_R}{R}\right)^2=\left(\frac{\sigma_D}{D}\right)^2+\left(\frac{\sigma_M}{M}\right)^2. \qquad (5.1.1)$$

The XSYS software package will, on request, calculate the mean and the full width at half maximum (FWHM) of a histogram by fitting it to a Gaussian. With this method the ratio σ_R/R in eq. (5.1.1) was calculated for each run. The ratio σ_D/D also can be calculated from counting statistics, giving

$$\frac{\sigma_D}{D}=\frac{1}{\sqrt{N}}, \qquad (5.1.2)$$

where N is the number of neutrons counted. This was computed for each run. The relative error in the monitor was then calculated using eq. (5.1.1) each run. After many runs were accumulated an average was computed. The average value of σ_M/M was found to be 0.6%. The data from one group of 10 runs is shown in table 5.1.1.

The short term stability of the monitor was checked several times. During each stability measurement, data were taken in the same fashion as the precision tests, except that the data were usually taken in runs of 7500 t0's instead of 4000. A run was taken every 10 to 15 minutes over the course of two to three hours. The ratio of monitor counts divided by detector counts was then plotted as a function of time. Drifts as large as approximately 1% per hour were observed. The results of one stability trial are shown in figure 5.1.1.

No attempt was made to measure the response of the monitor as a function of temperature. However, a temperature probe was placed next to the monitor. The temperature at that location averaged about 25°C and fluctuated by at most

Table 5.1.1

Data from monitor precision tests

Run	R	FWHM	D	$\sigma_M/M(x10^{-3})$
2276	2017.1	46.77	1454.8	3.33
2277	2034.4	58.97	1449.3	8.06
2278	2042.3	60.79	1440.9	8.64
2279	2057.7	46.65	1437.6	2.50
2280	2029.9	54.48	1422.0	6.48
2281	2063.5	51.58	1440.5	5.05
2282	2072.4	51.53	1437.3	5.03
2283	2087.1	57.37	1424.7	7.00
2285	2037.2	47.72	1359.2	9.48
2286	2029.7	55.50	1357.0	6.51

Figure 5.1.1 The ratio of monitor counts to detector counts plotted as a function of time. Each point represents one run and the time corresponds to the beginning of the run. The monitor drifted at a rate of 1% per hour during this trial.

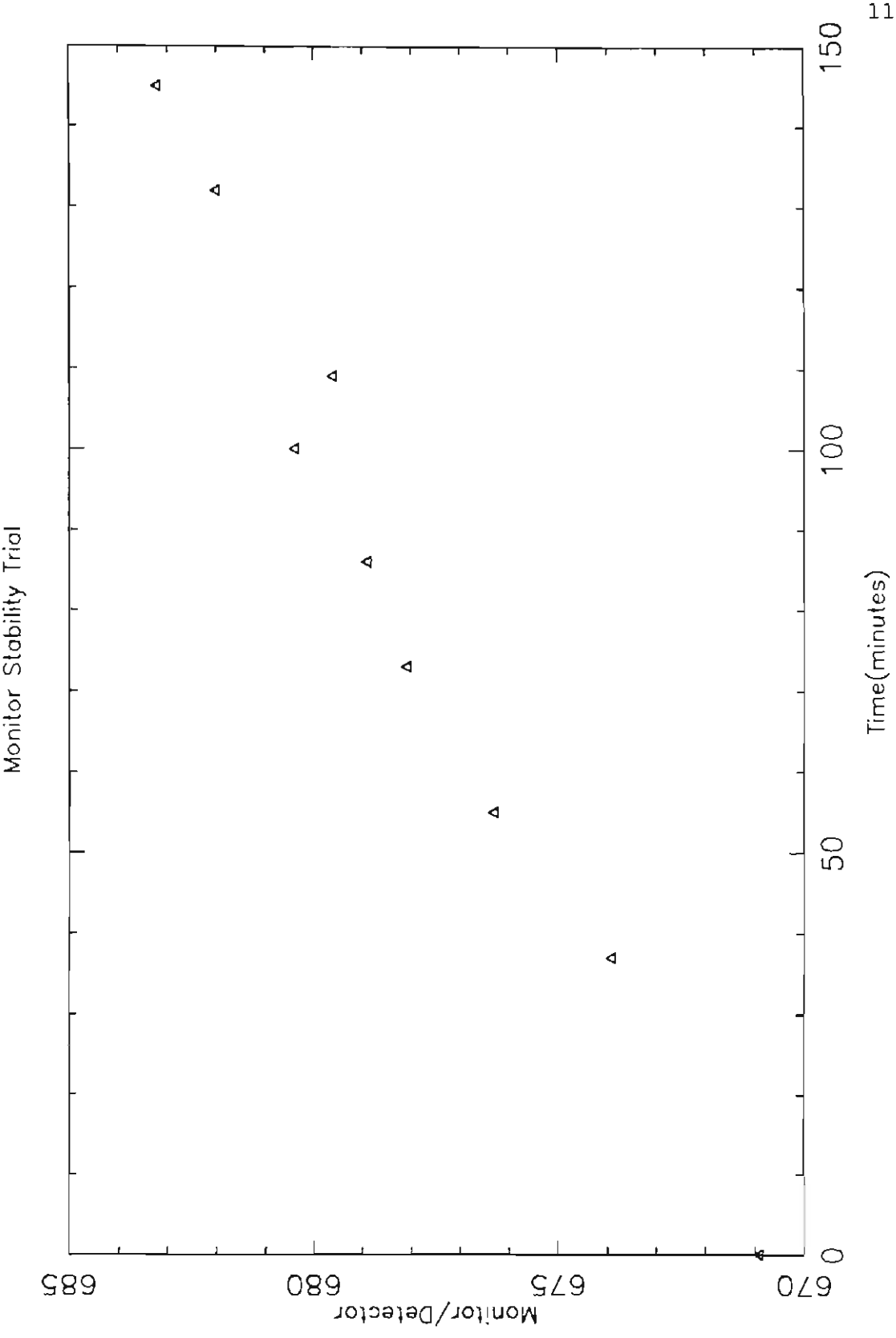
Monitor Stability Trial
Monitor/Detector
685
680
675
670
Time(minutes)
0
50
100
150

±2°C.

5.2 ^{3}He ion chamber beam monitors

Two ^{3}He ion chambers were ordered in early 1989 and arrived at the experimental site later that year. They were installed prior to the 1990 run season. The ion chambers were tested for precision and temperature dependence. They were not tested for stability as ion chambers are known to have very good stability [Pr58]. The ion chambers were also tested for sensitivity to the magnetic fields of the spin flipper.

Since the experiment had two ion chambers, the technique for measuring the precision was somewhat different than that used for the ^{6}Li glass monitor. After initial debugging, the two ion chambers were installed back to back in front of the biological shield flange. An electronic gate was set on the outputs of the two ion chambers; this was similar to the gating scheme used for testing the ^{6}Li glass monitor. The output of each ion chamber was then histogrammed after each t0. A histogram of the ratio of ion chamber number one (IC1) over ion chamber number two (IC2) was also calculated. The error in the ratio is related to the errors for each ion chamber by

$$\left(\frac{\sigma_R}{R}\right)^2=\left(\frac{\sigma_1}{C_1}\right)^2+\left(\frac{\sigma_2}{C_2}\right)^2, \qquad (5.2.1)$$

where $R=C_1/C_2$. Since the two ion chambers are identical $\sigma_1=\sigma_2=\sigma$ and $C_1\sim C_2\sim C$. C_1 and C_2 are not exactly equal because a few neutrons are absorbed by the first ion chamber. Eq. (5.2.1) reduces to

$$\left(\frac{\sigma_R}{R}\right)^2=\frac{2\sigma^2}{C^2}, \qquad (5.2.2)$$

and the error in the ratio is equal to $\sqrt{2}$ times the error in each ion chamber. The quantity σ_R/R was measured to be 0.14% and σ/C was calculated to be 0.1%. The ion chambers were then reversed and the measurement repeated. The same values were obtained.

The ion chamber temperature tests were performed with the ion chambers in their normal running configuration. One ion chamber was in front of the biological shield and the other on the upstream end of the spin flipper. The ion chamber (and its electronics) at the biological shield was wrapped with heat tape. The temperature was slowly increased from 29°C to 50°C and back down again. Data was taken in the same manner as the precision tests. The ratio was then plotted as a function of temperature (Figure 5.2.1). The maximum spread in the ratio over that temperature range was 0.3%.

To prepare for the magnetic field sensitivity test the spin flipper longitudinal solenoids were energized. (The spin flipper was completely off during the previous tests.) Ratio data were again measured, but with the signals routed based on the state of the spin flipper transverse coils. Two types of asymmetries were calculated,

$$\varepsilon_1 = \frac{R(+) - R(-)}{R(+) + R(-)} \text{ and} \qquad (5.2.3a)$$

$$\varepsilon_2 = \frac{R(+) + R(-) - 2R(0)}{R(+) + R(-) + 2R(0)}. \qquad (5.2.3b)$$

Data were taken for a total of 15 runs at 12800 t0's per run. The results for ε_1 and ε_2 were $(-0.8\pm1.5)\times10^{-5}$ and $(+2.7\pm3.3)\times10^{-5}$, respectively. The three ratios, R(+), R(-), and R(0), also were plotted as a function of time and track each other (Figure 5.2.2).

Figure 5.2.1 A plot of the ratio of the counts in IC1 (with heat tape) over counts in IC2. The triangles are runs taken while the ion chamber was being warmed and the squares are runs taken as it cooled.

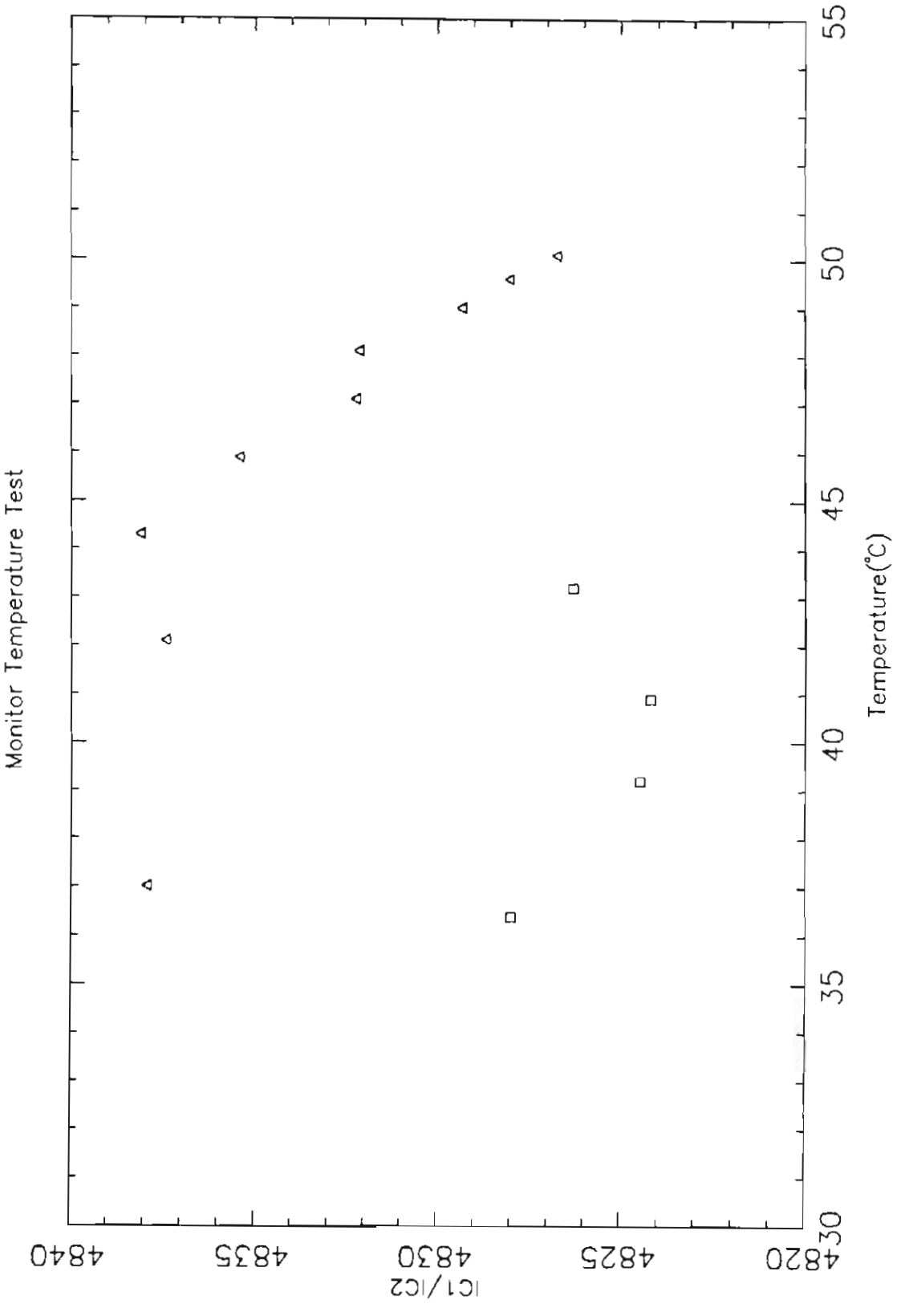
Monitor Temperature Test
IC1/IC2
4820
4825
4830
4835
4840
30
35
40
45
50
55
Temperature(°C)

Figure 5.2.2 A plot of the ratio of the counts in IC1 to the counts in IC2 for spin flipper transverse coils off (dashed line), positive current (dot-dashed line), and negative current (dotted line).

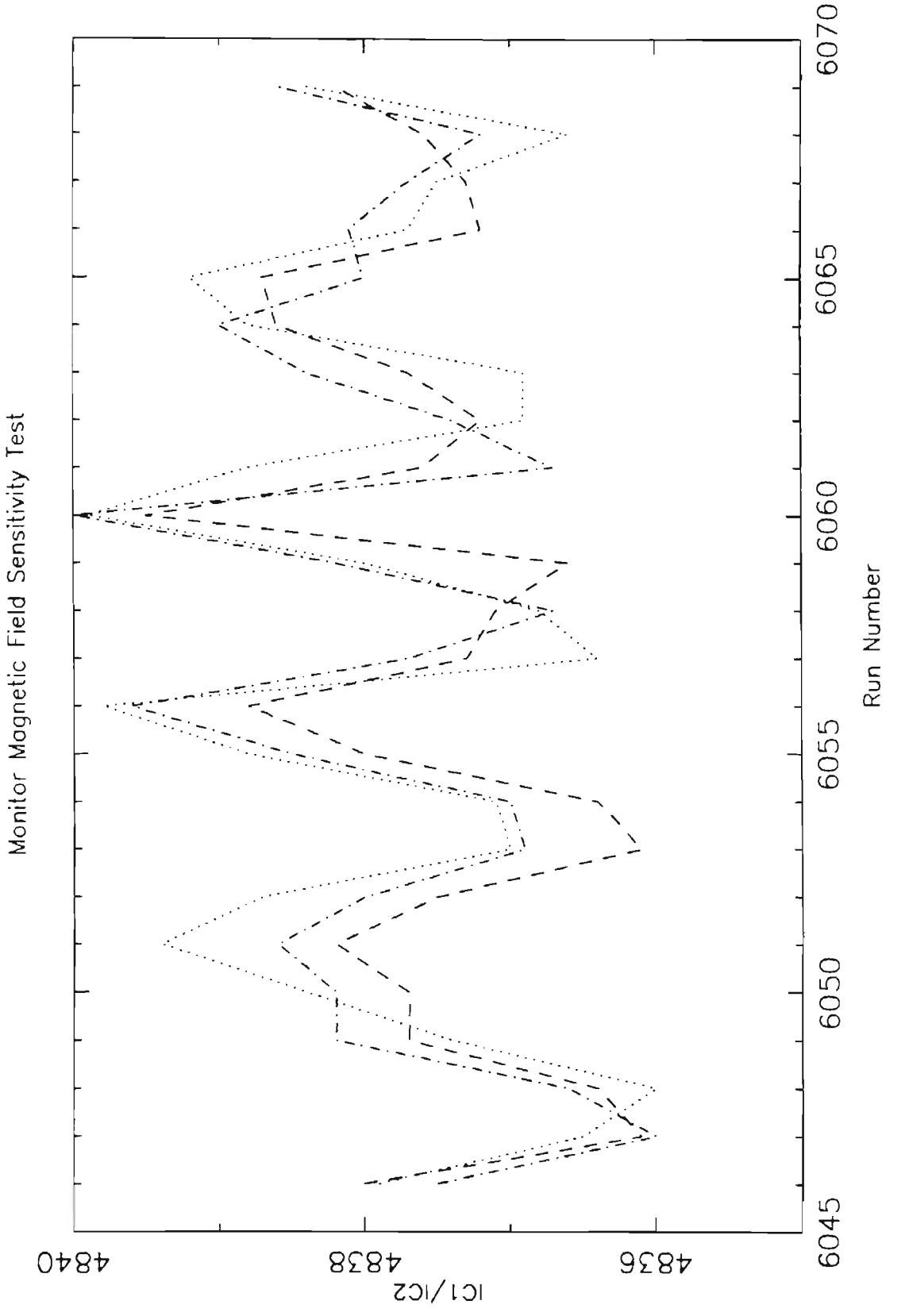
Monitor Magnetic Field Sensitivity Test
IC1/IC2
4836
4838
4840
6045
6050
6055
6060
6065
6070
Run Number

5.3 Magnetic field mapping

During the 1990 run season the magnetic fields of the cryostat, spin flipper, and target chiller were measured. Both the magnitudes and the directions of the fields were measured. For the cryostat the external magnetic fields were measured.

With the superconducting magnet energized at 31 amperes (A) and the longitudinal spin flipper solenoids energized at 4.8A, the on axis field within the spin flipper was mapped. This field map is shown in figure 5.3.1. The convention throughout is that the positive z axis is the beam direction, the positive y axis extends to the right as viewed from the source, and the positive x axis is up. With the spin flipper off there is an approximately constant transverse field in the center region of the spin flipper. It was measured to be B_x=-0.4 gauss and B_y=-0.1 gauss. Because of equipment limitations it was not possible to accurately map the field due to the transverse coils everywhere within the spin flipper. Instead, the peak magnitude and field directions of the coils were individually checked.

The on axis fringe field of the cryostat was measured with the spin flipper off. A field map for the downstream side of the cryostat is shown in figure 5.3.2.

While in position on the downstream end of the spin flipper, the target chiller Helmholtz coils were checked to confirm that they provided a field in the negative z direction. The field magnitudes were measured with the target chiller on the test bench. With 7.0A in the coils, the z axis field was 41.0±0.5 gauss over the target region. Nowhere in the interior of the target chiller did the transverse field components exceed 1 gauss.

Figure 5.3.1 Map of the magnetic field along the z axis of the spin flipper. The upstream end of the spin flipper is at z=0.

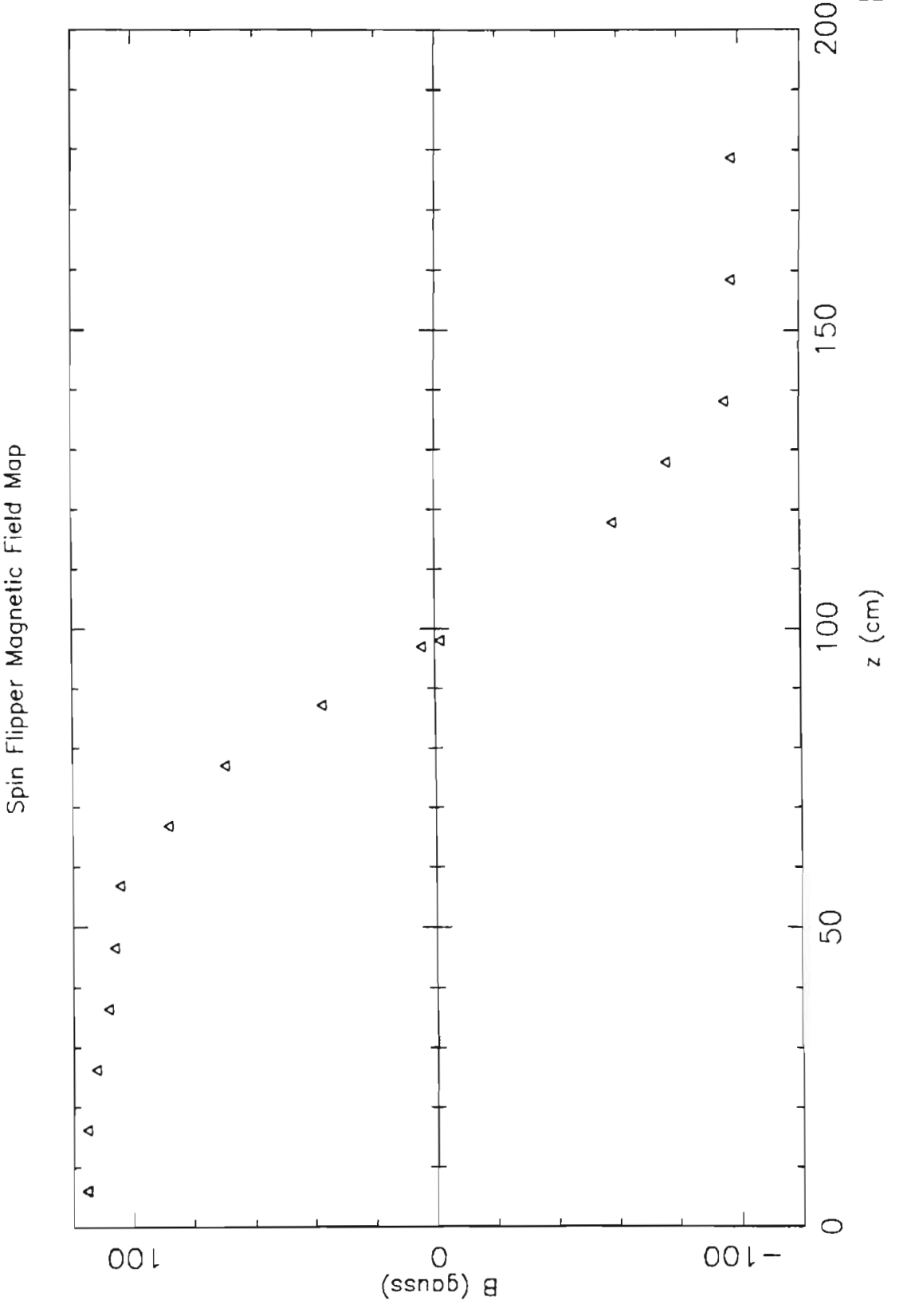
Spin Flipper Magnetic Field Map
B (gauss)
100
0
−100
0
50
100
150
200
z (cm)

Figure 5.3.2 Map of the magnetic field along the z axis of the cryostat. The center of the cryostat is at z=0.

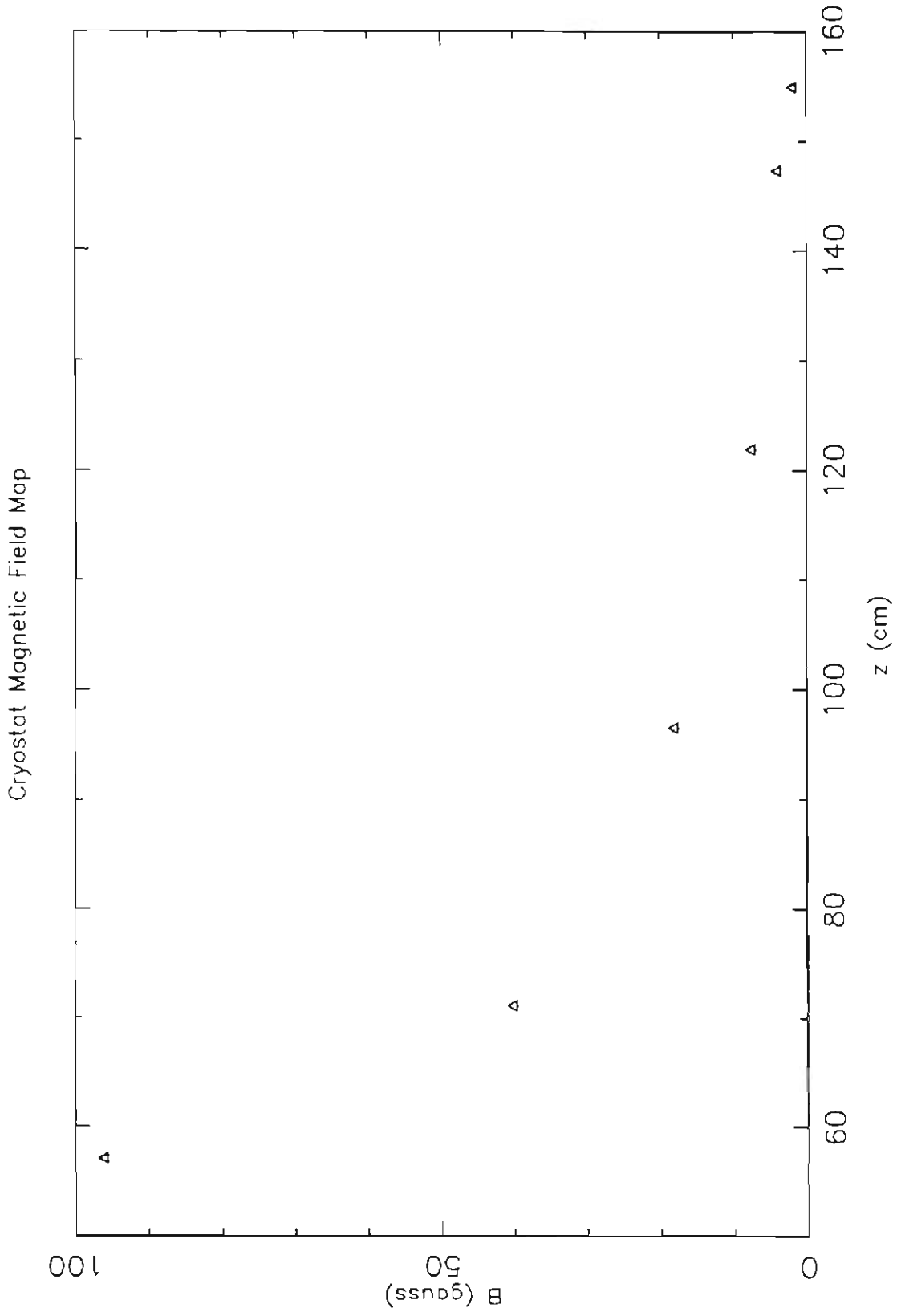
Cryostat Magnetic Field Map
B (gauss)
0
50
100
z (cm)
60
80
100
120
140
160

5.4 Magnetic field sensitivity of the neutron detectors

The object of this measurement was to set a limit on possible false asymmetries due to the effect of the changing spin flipper magnetic field on the detectors. The field at the 60m detector hut due to the spin flipper was very small and had to be measured indirectly. The spin flipper transverse coils were supplied with 9.4A (3.1A normal running). The transverse field was then measured 3m downstream, in the 11m cave. The magnitude at that point was found to be 0.13 gauss. Using the fact that the field of a magnetic dipole decreases as $1/r^3$, the measured value was scaled to obtain the estimated field strength at the detector location. This value was calculated to be 3×10^{-5} gauss.

The phototube manufacturer states that the phototube gain scales as

$$G = G_0 \cos\left(\frac{B}{B_0}\right), \tag{5.4.1}$$

where G_0 is a baseline gain, B is the transverse magnetic field, and B_0 is an unknown scale factor of order one gauss [Ha89]. Since B is very small, the cosine can be expanded and eq. (5.4.1) takes the form

$$G = G_0\left(1 - \frac{1}{2}\left(\frac{B}{B_0}\right)^2\right). \tag{5.4.2}$$

The gain can also be expanded in terms of a change in the magnetic field as in eq. (4.3.2.1), redefining the asymmetry from eq. (4.3.2.3) as A2. Then a new asymmetry is defined as

$$A1 = \frac{S(+) - S(-)}{S(+) + S(-)}. \qquad (5.4.3)$$

This asymmetry corresponds to a spin flip sequence of +,-,+,-. That sequence was chosen to deliberately enhance any effect of the changing magnetic field on the detector. In terms of the gain expansions the two asymmetries take the form

$$A1 = \frac{\Delta B}{G}\frac{dG}{dB} \text{ and} \qquad (5.4.4a)$$

$$A2 = \frac{\Delta B^2}{4G}\frac{d^2G}{dB^2}. \qquad (5.4.4b)$$

Inserting the gain and its derivatives from eq. (5.4.2) into eqs. (5.4.4a) and (5.4.4b) yields

$$A1 = -\frac{\Delta B}{B_0^2}B \text{ and} \qquad (5.4.5a)$$

$$A2 = -\frac{\Delta B^2}{4B_0^2}. \qquad (5.4.5b)$$

The A1 asymmetry can then be related to the A2 asymmetry by

$$A2 = \frac{1}{4}\frac{\Delta B}{B}A1. \qquad (5.4.6)$$

Since A2 is expected to be extremely small, A1 can be measured and A2 calculated. To estimate A2 the values $\Delta B = 3 \times 10^{-5}$ gauss and $B_0 = 0.3$ gauss were used. It was felt that these values would give a generous upper limit on A2.

A total of 16 runs were taken, with 12800 t0's per run. During each t0 the detector counts were normalized with the ion chamber monitor and then routed to either the coil current positive data area or the coil current negative data area. At the end of each run the mean and standard deviation of each data area were computed. These values were inserted into eq. (5.4.3) to obtain a value for A1 for each

run. The mean of **A1** for all the runs was $(-1.5\pm1.4)\times10^{-5}$. This gives a value of -3.8×10^{-10} for **A2**, using the previously stated values for ΔB and B_0. The data are listed in table 5.4.1.

5.5 Polarization Measurements

5.5.0 Introduction

There are two conventional techniques for measuring the proton polarization of the LMN crystals. The two are NMR and transmission. In the latter method the transmission of a neutron beam through the sample is measured. If the crystals are in excellent condition, then the two methods work equally well. Neither method will work absolutely if the crystal set has been damaged or improperly installed. Significant problems were encountered with the crystal set during the 1990 run season. Therefore, a new absolute polarization calibration was introduced, calibration based on the known parity violating asymmetry in ^{139}La.

5.5.1 NMR

Since the NMR coil is wrapped around the outside of the crystals, it measures the polarization near the surface. If the crystals are completely uniform then the polarization near the surface is the same as the polarization of the interior. LMN crystals are susceptible to damage by water. Water, in the form of condensation, can enter the microwave cavity where the crystals are located due to improper warming of the cryostat or a vacuum leak. If a crystal becomes wet, it will start to dissolve and damage the surface. As a consequence the polarization near the

Table 5.4.1

Data from detector magnetic field sensitivity trials

Run	R(+)	R(-)	$A_1 (\times 10^{-5})$
6083	3894.2	3894.7	-6.4
6084	3887.7	3887.7	0.0
6085	3879.6	3880.5	-11.6
6086	3864.1	3864.5	-5.2
6087	3856.6	3856.5	1.3
6088	3847.0	3847.8	-10.4
6089	3821.8	3821.3	6.5
6091	3800.0	3800.5	-6.6
6092	3792.5	3792.5	0.0
6093	3787.1	3787.0	1.3
6094	3778.6	3778.4	2.6
6095	3773.7	3773.8	-1.3
6096	3766.1	3766.2	-1.3
6097	3758.0	3758.0	0.0
6098	3758.3	3758.6	-4.0
6099	3764.1	3763.3	10.6

surface will be different from the rest of the crystal. In this case an NMR scan will not measure the true polarization, but instead will be incorrect by some unknown factor. Because of these possible difficulties the NMR was used only as a relative polarization monitor.

If the crystals are all good, then the proton polarization can be directly calculated from the NMR measurements. When the LMN is cooled and placed in a magnetic field it has a small amount of residual polarization (~0.2%) even with no microwave pumping. This signal must be measured and used as a calibration for subsequent NMR measurements. With that calibration the proton polarization is given by [Ab64a]

$$f_p = \frac{G_{ENH}\frac{A_{ENH}}{S_{ENH}}}{G_{TE}\frac{A_{TE}}{S_{TE}}} P_{TE}(B)\frac{1^\circ K}{T}, \qquad (5.5.1.1)$$

where 'ENH' refers to the signal when the microwaves are on (the enhanced signal), 'TE' refers to the signal when the microwaves are off (the thermal equilibrium signal), G is the circuit amplifier gain, S is the number of times the circuit was scanned, A is the area of the peak (or dip) in the NMR frequency-voltage response function, T is the temperature in degrees Kelvin, and P is the residual polarization for a given magnetic field at 1°K.

The neutron polarization can be determined in the following manner. Let $N_{+(-)}$ be the number of transmitted neutrons with spin parallel (antiparallel) to the z axis. The neutron polarization is given by

$$f_n = \frac{N_+ - N_-}{N_+ + N_-}, \qquad (5.5.1.2)$$

where $N_{+(-)}$ has the form

$$N_{\pm} = N_0 e^{-t\sigma(1\pm f_p P)}. \qquad (5.5.1.3)$$

N_0 is the number of incident neutrons, t is the sample thickness in atoms per barn, $\sigma=\sigma_P+\sigma_A$, where $\sigma_{P(A)}$ is the macroscopic cross section for parallel (antiparallel) neutron scattering, and P is the parallel-antiparallel cross section asymmetry given by

$$P = \frac{\sigma_P - \sigma_A}{\sigma_P + \sigma_A}. \qquad (5.5.1.4)$$

Inserting eqs. (5.5.1.3) and (5.5.1.4) into eq. (5.5.1.2) and simplifying gives

$$f_n = \tanh\left(f_p(\sigma_p - \sigma_A)\frac{t}{2}\right). \qquad (5.5.1.5)$$

5.5.2 Transmission

The transmission through the LMN sample can be obtained using eq. (5.5.1.3). The transmission has the form

$$T = \frac{N_+}{N_0} + \frac{N_-}{N_0} = e^{-\frac{(\sigma_p+\sigma_A)t}{2}} \cosh\left(f_p(\sigma_p - \sigma_A)\frac{t}{2}\right). \qquad (5.5.2.1)$$

Since it is impractical to move the cryostat, an absolute transmission cannot be measured. Instead, by using a beam monitor in conjunction with the detectors at 60m, changes in the transmission can be measured. If the sample is polarized and the microwave power is turned off, the polarization of the sample will decay to its residual value in about 30 minutes. The transmission of the neutron beam is monitored as this relaxation occurs. A sample plot of the relative transmission as a function of time is shown in figure 5.5.2.1. The NMR signal is also measured each time

Figure 5.5.2.1 A sample transmission measurement taken after the microwave pumping was turned off.

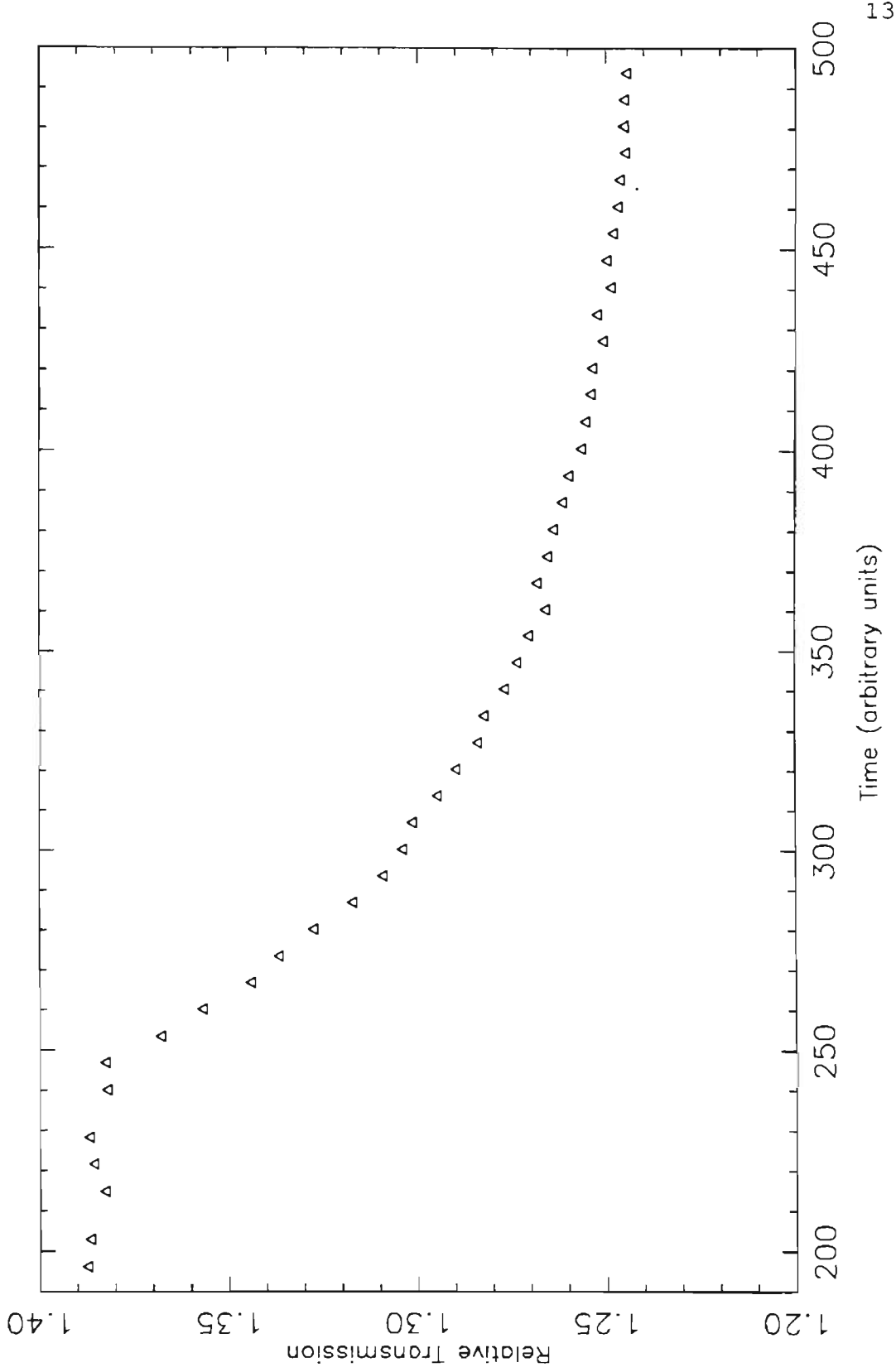
Relative Transmission
1.20
1.25
1.30
1.35
1.40
200
250
300
350
400
450
500
Time (arbitrary units)

transmission and NMR data can be fit to the form

$$T = a_1 \cosh(a_2 A_{NMR}) + a_3 t + a_4 t^2, \qquad (5.5.2.2)$$

where a_1 through a_4 are free parameters, A_{NMR} is as described earlier, and t is the elapsed time during the measurement. The parameters a_3 and a_4 are typically very small, $a_3 \sim 10^{-6}$ and a_4 several orders of magnitude smaller. If the crystal package is in good condition, then this method provides an absolute calibration of the neutron polarization.

However, the crystal package may be defective. There could be an improperly grown crystal, crystals installed with gaps between them, or some other problem. In this case determining the neutron polarization using transmission is invalid, since the transmission technique assumes the entire beam passes through active crystal. A more detailed discussion of how crystal failures affect transmission measurements is given by Yuan *et al.* [Yu91] Fortunately there is a third technique which establishes the neutron polarization absolutely, independent of the detailed condition of the polarizer.

5.5.3 Polarization calibration with ^{139}La

The parity violating asymmetry in the 0.734eV state in ^{140}La is known to be 9.55±0.35% [Yu91]. This was measured using two identical ^{139}La targets in a polarizer-analyzer (PA) experiment. Here the value of the asymmetry is independent of any polarization measurement. To measure the neutron beam polarization, a conventional PNC experiment is performed using a single ^{139}La target. The asymmetry of the 0.734eV resonance is measured. The asymmetry will be equal to $\varepsilon f_n \mathcal{P}$, where ε is the spin flip efficiency, f_n is

the neutron polarization, and $\mathcal{P}$ is the parity violating asymmetry. The value of ε can be calculated, but is very close to one in all cases; the value of $\mathcal{P}$ is available from the PA experiment. The neutron polarization is then determined in a straightforward way. The NMR area is also measured at the same time to obtain a calibration for monitoring of the neutron polarization.

5.5.4 Discussion

During the 1989 run season, the crystal package was in reasonably good condition and the transmission method was used to calibrate the neutron polarization. The single lanthanum experiment was performed and a value of $\mathcal{P}$=9.95±0.45% was obtained using the polarizations obtained from transmission measurements. The absolute polarization obtained from the NMR measurement was about half that determined by the transmission measurement. It was later discovered that this difference was due to melting of the crystal edges. The calibration of the bromine data was based on a transmission measurement performed immediately following the completion of the bromine runs. The average neutron polarization for that period was about 45%.

The 1990 run season brought a new set of problems. The average neutron polarization as indicated by the ^{139}La PNC measurement was about 27%. The transmission measurements gave about 34% and the absolute NMR measurements gave about 39%. Clearly the polarization had decreased substantially from the previous year and there were problems with the crystals which were causing the three measurements to differ. Although a great deal of effort was expended investigating possible causes for the discrepancies, no single explanation was found for all of the observed problems. In

addition the neutron polarization continued to decrease as the season passed. By the end of the run season it was only 15%. The thorium data was taken during the first part of the season. The average neutron polarization was about 25% while the thorium data was taken. The polarization calibration for the thorium data is based on a series of ^{139}La measurements performed about halfway through the thorium data sequence.

CHAPTER VI

Data and Analysis

6.0 Introduction

Results obtained from data measured with two targets, bromine and thorium, are presented here. The bromine data were taken during the second cycle of the 1989 run season. A total of approximately 100 half hour runs were taken with the bromine target over approximately three calendar days. The final data set included 89 runs. The other runs were not used due to various experimental hardware problems. The thorium data were taken during the first cycle of the 1990 run season. A total of approximately 400 half hour runs were accumulated. Due to low beam availability and to interruptions for tests of the cryostat, nearly a calendar month was required to obtain the thorium data. The final data set included 355 runs. Only runs which had an average target temperature less than 175°K were included in the final analysis.

6.1 Procedure for extracting the parity violating asymmetry

6.1.0 Introduction

Two techniques were used to obtain the parity violating asymmetries. In both methods the resonance shape was fit to a multiparameter function. One of the codes used was written within the TRIPLE collaboration and has been named PVIO. It was used for the bromine resonance and all but one of the thorium resonances. The other code used was a neutron resonance analysis code from Oak Ridge National

Laboratory (ORNL) named SAMMY [La89]. The latter code was used to fit one thorium resonance. The two codes will be discussed in the following subsections.

6.1.1 Code PVIO

The code PVIO can fit only one resonance at a time. The data are fit to a function of the form

$$Y_{\pm} = \frac{N(1 \pm \beta)}{k - k_0}\left(1 + \sum_{i=1}^{5} \alpha_i z^i\right) \exp\left(-n\varphi(C)\sigma(B,\sigma_0)\left(1 \pm f_n \mathcal{P}\right)\right). \qquad (6.1.1.1)$$

Spectra for spin up and spin down are fit simultaneously. The detector yield function Y represents either actual neutrons (counting mode) or digitized PMT current (current mode), N is a normalization constant, k is the channel number, k_0 is the resonance peak channel, and β is a normalization adjustment to spectra obtained for spin up and down, when more neutrons were counted in one spin state than the other. The α_i are parameters used to model the beam flux and detector efficiency, while the variable z is given by

$$z = \frac{k - \frac{k_3 + k_4}{2}}{1000}, \qquad (6.1.1.2)$$

where k_3 and k_4 are the lowest and highest channel numbers of a window set to include the resonance. The target thickness n is in atoms per barn and the function $\varphi(C)$ describes the Gaussian resonance broadening. This broadening models the combination of broadening due to Doppler motion, beam burst width, neutron moderation time, and detector response time. The function $\varphi(C)$ depends on energy and on

the parameter C which scales the broadening width. The Breit-Wigner single level cross section $\sigma(B,\sigma_0)$ is a function of parameters B and σ_0, where B scales the natural width and σ_0 scales the peak cross section. The combination $f_n\mathcal{P}$ is the neutron polarization times the parity violating asymmetry. The parameters N, k_0, α_1 through α_5, B, C, σ_0, β, and $f_n\mathcal{P}$ all may be varied in the analysis.

Each resonance was fit on a run by run basis. A fit to a sum of runs was initially used to establish α_1 through α_5, B, and σ_0. These parameters were not varied in the run by run fits. In all cases α_4 and α_5 were zero and in most cases α_2 and α_3 also were zero. Since the spectra were not normalized to the beam flux when this code was used, N and β were allowed to vary for each fit. To compensate for small time drifts in the t0 signal, k_0 was allowed to vary within ±1 channel. For the thorium data C was allowed to vary since the target was not always at a uniform 77°K. C was not varied for the bromine data. The object of each fit was to obtain the product $f_n\mathcal{P}$.

The code has the feature that three windows may be set. The center window is set to include the resonance. The flux part of the function,

$$\frac{N(1\pm\beta)}{k-k_0}\left(1+\sum_{i=1}^{5}\alpha_i z^i\right), \qquad (6.1.1.3)$$

is determined using the two outer windows, which are placed on either side of the resonance but not necessarily contiguous to it. This feature is useful for dealing with cases where two resonances are close in energy to one another but the resonance shapes do not impinge upon one another. In nearly all cases where two resonances are so close in energy that their shapes impinge upon one another this code cannot be used.

The code PVIO was extensively tested on resonances in ^{238}U. It was discovered that the code was very stable if reasonable limits were placed upon it. By setting the parameters a_4 and a_5 to be zero and choosing a_1 through a_3 such that a physically reasonable flux function was obtained, fluctuations in $f_n\mathcal{P}$ were held to less then 30% when all other parameters were allowed to vary. By varying only the parameters which were free in the final analysis, the minimum in the χ^2 space was mapped. In mapping the region where χ^2 went from its minimum to its minimum plus 20%, $f_n\mathcal{P}$ did not vary by more than 11%. The changes in $f_n\mathcal{P}$ appeared to be random.

6.1.2 Code SAMMY

Since the code SAMMY is described in detail by Larson [La89], only a brief overview will be given here. SAMMY is a multilevel, multichannel neutron resonance code, which is based on the R-matrix formalism derived in chapter III. An implementation of Bayes' Theorem is used to fit requested parameters. The minimum set of required parameters include the target mass, the flight path length, the target thickness, at least one ℓ, J, and π set, and a set of

$(E_n, \Gamma_\gamma, \Gamma_n)$ for at least one resonance. Many other features are available, not all of which will be described here. Several types of broadening may be requested, each of which has a set of physically measurable parameters. Also, several types of background may be used. The code has the capability of fitting several different reactions (e.g., transmission, fission, etc.).

SAMMY was used to fit simultaneously the 128.2eV and 129.2eV resonances in ^{233}Th. The 128.2eV resonance is an ℓ=1 resonance and the 129.2eV resonance has ℓ=0. These resonances interfere strongly. Since SAMMY does not have the capability to directly fit a parity violating asymmetry the following model was used. Consider the parity violating asymmetry $f_n\mathcal{P}$ which is defined as

$$f_n\mathcal{P} = \frac{\sigma_p^+ - \sigma_p^-}{\sigma_p^+ + \sigma_p^-}. \qquad (6.1.2.1)$$

The p-wave cross section has the form

$$\sigma_p = \frac{\pi}{k^2}\frac{g\Gamma\Gamma_n}{\left(E - E_p\right)^2 + \left(\frac{\Gamma}{2}\right)^2}. \qquad (6.1.2.2)$$

All available resonance parameters can be varied in calculations with SAMMY. The resonance energy was determined by calibrating the peak channel numbers of many sharp resonances to their known energies. These were fit to eq. (4.1.2.1) to obtain a flight path length and time zero channel. The energy for the resonance in question was determined using the fitted parameters and then held fixed. Since the broadening widths are very much larger than the gamma width, the gamma width is held fixed. To fit the p-wave resonance the procedure was first to obtain the broadening and background parameters from other nearby res-

onances. The spin up and spin down spectra were then fit with only the neutron width variable. Using the fact that $\Gamma \sim \Gamma_\gamma$ and substituting eq. (6.1.2.2) into eq. (6.1.2.1), the parity violating asymmetry becomes

$$f_n \mathcal{P} = \frac{\Gamma_n^+ - \Gamma_n^-}{\Gamma_n^+ + \Gamma_n^-}. \qquad (6.1.2.3)$$

In this way $f_n \mathcal{P}$ is obtained for each run. Note that SAMMY fits neutron transmission spectra, not raw detector yields as does PVIO. The transmission for each run was calculated for each spin state (i.e., up and down) for each run, using a target out run. The monitor counts for each spin state were used to obtain the correct normalization.

6.2 Bromine data

The neutron cross sections for the bromine isotopes have not been well studied. Both bromine isotopes have ground state spin 3/2. Only a few large s-wave resonances are known in each isotope. A p-wave resonance was discovered in ^{82}Br by Alfimenkov *et al.* [Al83] in 1983, which was assigned E_n=0.88eV, Γ_γ=190meV, and $g\Gamma_n$=5.8x10^{-5}meV (g=(2J+1)/8 for ^{82}Br). A listing of known bromine resonances in the first 200eV and their resonance parameters is given in table 6.2.1. The parameters are from Mughabghab, Divadeenam, and Holden [Mu81]. At present the 0.88eV resonance is the only known p-wave resonance in either bromine isotope. Alfimenkov *et al.* also measured a PNC effect on the 0.88eV resonance, and obtained a value of 2.4±0.4% for $\mathcal{P}$.

The bromine data taken during this experiment was obtained using a dwell time of 1μs per channel. This gave an

Table 6.2.1

Bromine resonance parameters

E_n (eV)	Isotope	$2g\Gamma_n$ (meV)	J	ℓ
0.88	81	0.0001		1
35.8	79	53.85	2	
53.6	79	24.89	1	
101.1	81	201.		
135.5	81	329.		
158.0	79	0.7542		
189.3	79	55.0	1	
192.4	79	3.606		

effective energy range of approximately 0.2eV to 50eV. The 0.88eV resonance was clearly observed (Figure 6.2.1 (top)). The higher energy portion of the bromine spectrum is shown in figure 6.2.2. The 0.88eV resonance was fit with the code PVIO. Values of $f_n\mathcal{P}$ were obtained for each of the 89 runs. The neutron polarization was calculated using eq. (5.5.1.5) for each run. The proton polarization was obtained by using the fit parameters of eq. (5.5.2.2) corresponding to a transmission measurement performed immediately following the completion of the bromine runs. The spin flip efficiency was 96%. An additional 5% depolarization was due to the sample being outside the spin flipper. A PNC effect was also observed on the 0.88eV resonance. A value of 1.77±0.33% was obtained for $\mathcal{P}$. This is in agreement with the value ($\mathcal{P}$=2.4±0.4%) quoted by Alfimenkov *et al*. The 89 individual values of $\mathcal{P}$ are shown as a histogram in figure 6.2.1 (bottom).

The bootstrap method [Ef79] was applied to the distribution of $\mathcal{P}$ values for the 0.88eV resonance in order to test for non-Gaussian errors. For the calculation 10000 samples were generated in order to determine the bootstrap distribution. The standard deviation of the bootstrap distribution was identical to the standard deviation of the mean of the distribution of $\mathcal{P}$ values. The result indicates that no non-Gaussian errors were present.

Figure 6.2.1

(top) Sample fit to the 0.88eV resonance. The top curve is the flux portion of the fitting function and the bottom curve is the fit to the resonance plus the flux. The data displayed are for one spin state of a single run.

(bottom) Histogram of the 89 values of $\mathcal{P}$ obtained from fits to the 0.88eV resonance

^{81}Br Transmission Spectrum

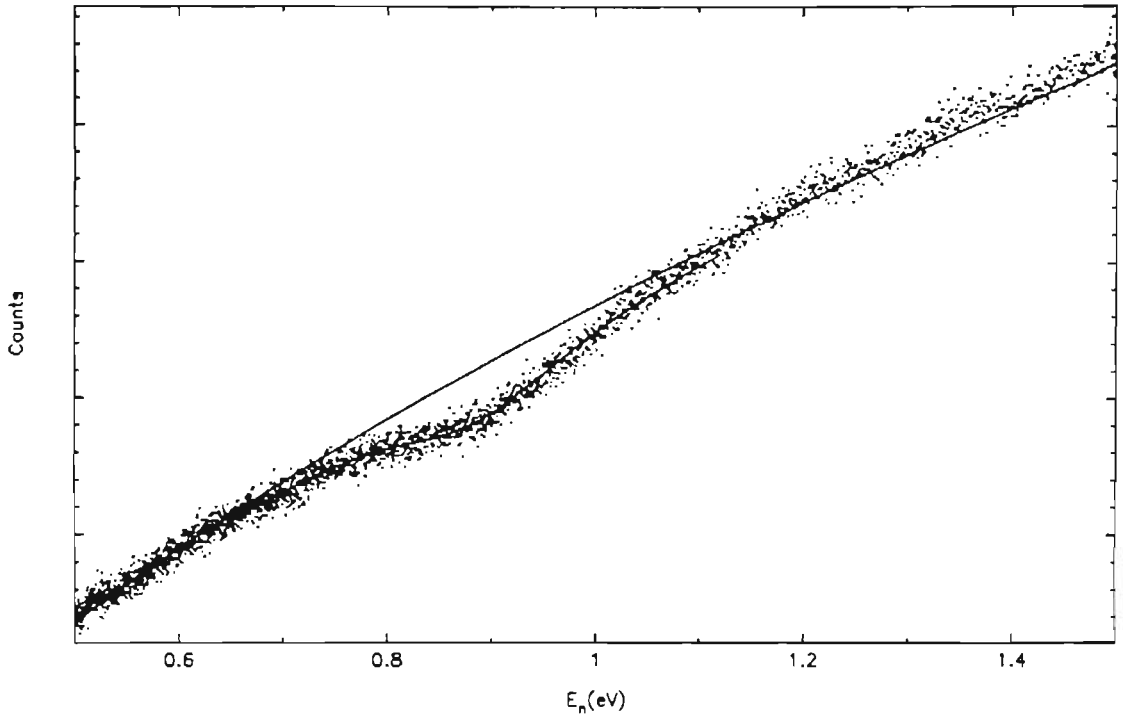

E_n=0.88eV

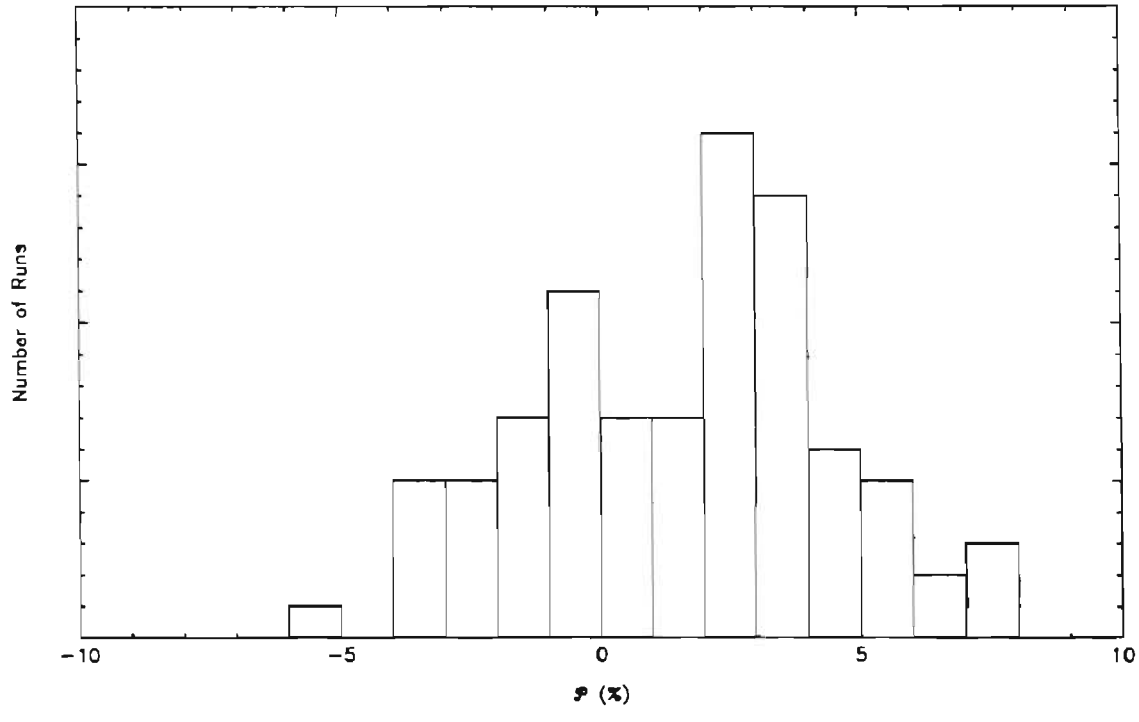

Figure 6.2.2 Natural bromine transmission spectrum. The data are the sum of the 89 runs used in the analysis of the 0.88eV resonance.

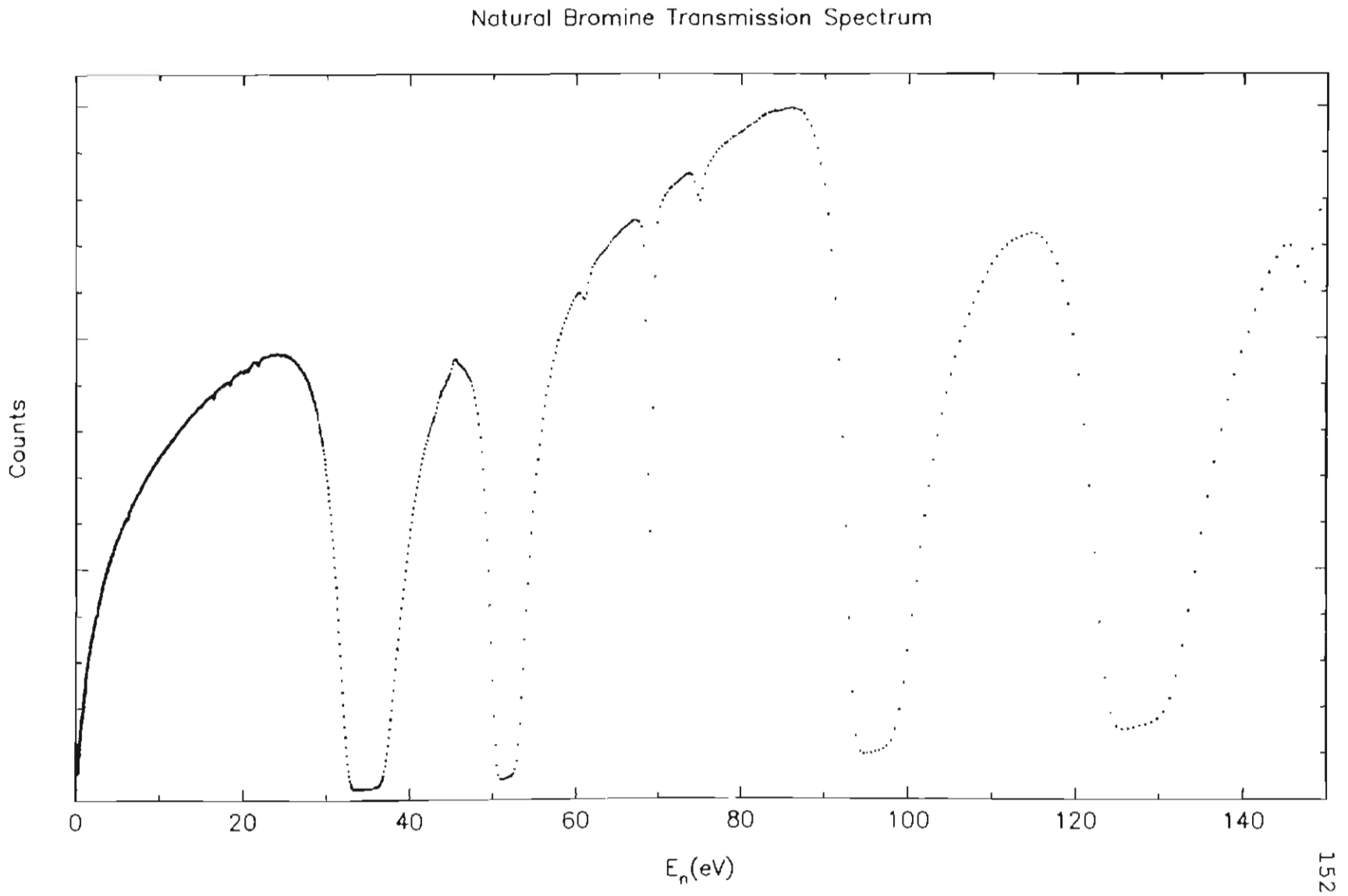
Natural Bromine Transmission Spectrum
Counts
0
20
40
60
80
100
120
140
E_n(eV)

6.3 Thorium data

6.3.0 Introduction

The neutron cross section of thorium was originally studied in detail because of its close proximity to uranium in the periodic table. Although the fission cross section of ^{232}Th is nearly zero, there is still appreciable interest in ^{232}Th for use in breeder reactors. Consequently neutron resonance spectroscopy experiments on ^{232}Th have continued. Many of these experiments will be described in the following subsection.

Only one prior PNC measurement on ^{232}Th has been reported. Krupchitsky [Kr89] stated that Alfimenkov had made a measurement on the 8.3eV p-wave resonance in 1987; Krupchitsky quotes a value of $\mathcal{P}$=1.79±0.92%. Our value of 1.45±0.25% for $\mathcal{P}$ for the 8.3eV resonance is in agreement with the value from Alfimenkov and has much smaller error.

6.3.1 Thorium resonance data

Many experiments have been performed to locate the resonances and to measure the parameters of ^{232}Th neutron resonances [Ol82a][Pe82][Co78][Ra72][Fo71][Ri69][As66][Bo64][Ga64]. The two most recent evaluations are by Bhat [Bh79] and by Olsen [Ol82b]. The resonance energies and their assigned parameters for the first 500eV from Bhat and from Olsen are listed separately in tables 6.3.1.1 (Bhat) and 6.3.1.2 (Olsen). There are several discrepancies between the two evaluations. These discrepancies and their effects on the present analysis will be discussed below.

The 54.1eV resonance was reported in only one previous measurement [Fo71]. This measurement was performed during

Table 6.3.1.1

^{232}Th resonance parameters from [Bh79]

E_n (eV)	ℓ	$g\Gamma_n$ (meV)	Γ_γ (meV)
8.33	1	0.00023	29.0
13.13	1	0.00019	
21.79	0	2.09	24.0
23.46	0	3.72	26.3
36.97	1	0.0011	
38.19	1	0.00062	
41.03	1	0.00059	
47.05	1	0.0016	
58.78	1	0.0085	
59.51	0	3.95	24.7
64.51	1	0.001	
69.19	0	43.6	23.0
90.14	1	0.005	
98.07	1	0.004	
103.66	1	0.0052	
113.03	0	13.0	25.4
120.85	0	22.0	23.8
128.21	1	0.073	
129.19	0	3.40	26.5
145.86	1	0.087	
148.05	1	0.012	
154.32	0	0.21	19
167.17	1	0.019	
170.39	0	60.5	24.7
178.90	1	0.038	
192.70	0	16.5	25.0
196.25	0	0.083	

Table 6.3.1.1 (continued)

E_n (eV)	ℓ	$g\Gamma_n$ (meV)	Γ_γ (meV)
199.35	0	10.0	21.6
202.5	1	0.030	
211.0	1	0.016	
219.5	1	0.052	
221.3	0	30.0	25.4
251.7	0	31.5	26.0
263.2	0	22.0	23.9
285.9	0	30.6	23.6
290.5	1	0.070	
299.8	1	0.041	
302.7	1	0.14	
305.6	0	28.9	25.1
309.4	1	0.053	
321.8	1	0.04	
329.0	0	74	26.0
338 3	1	0.051	
341.9	0	38.9	25.3
361.4	1	0.088	
365.4	0	26.1	23
369.5	0	25.6	23.2
380.6	1	0.14	
391.5	0	0.16	
401.0	0	11.0	25
402.8	1	0.1	
411.9	1	0.23	
420.9	0	0.52	
454.3	0	1.2	
459.0	1	0.065	

Table 6.3.1.1 (continued)

E_n (eV)	ℓ	$g\Gamma_n$ (meV)	Γ_γ (meV)
462.8	0	63.4	21.5
466.4	1	0.12	
470.6	1	0.048	
476.5	0	0.16	
489.0	0	59	19.2

Table 6.3.1.2

^{232}Th resonance parameters from [0182b]

E_n(eV)	ℓ	Γ_n(meV)	Γ_γ(meV)
-22.2	0	6.2665	21.2
-2.952	0	0.9227	21.2
8.3505	1	0.000275	24.4
13.124	1	0.0002095	24.4
21.806	0	2.06	25.1
23.464	0	3.85	26.6
36.991	1	0.0009407	24.4
38.191	1	0.0005758	24.4
41.032	1	0.0005868	24.4
47.044	1	0.001531	24.4
49.875	1	0.0004833	24.4
54.156	1	0.0011	24.4
58.771	1	0.008976	24.4
59.519	0	3.80	24.0
64.499	1	0.0006940	24.4
69.232	0	43.2	23.0
90.167	1	0.006145	24.4
98.069	1	0.003976	24.4
103.66	1	0.00554	24.4
112.05	1	0.003939	24.4
113.03	0	13.13	23.5
117.82	1	0.00197	24.4
120.87	0	22.51	24.0
128.20	1	0.06857	24.4
129.19	0	3.381	19.2
145.86	1	0.08919	24.4
148.05	1	0.01035	24.4

Table 6.3.1.2 (continued)

E_n (eV)	ℓ	Γ_n (meV)	Γ_γ (meV)
154.36	0	0.1986	24.4
167.17	1	0.01865	24.4
170.39	0	61.25	25.3
178.96	1	0.0294	24.4
192.72	0	16.9	21.5
196.25	1	0.08172	24.4
199.40	0	10.24	19.4
202.72	1	0.0305	24.4
211.00	1	0.01629	24.4
219.52	0	0.04364	24.4
221.29	0	30.25	24.5
232.15	1	0.013	24.4
234.35	1	0.02	24.4
242.41	1	0.04192	24.4
251.65	0	31.78	26.1
258.43	1	0.009885	24.4
263.23	0	22.22	21.6
272.76	1	0.019	24.4
276.97	1	0.035	24.4
285.91	0	31.03	22.5
290.58	1	0.06269	24.4
299.84	1	0.04152	24.4
302.68	1	0.1415	24.4
305.62	0	28.88	22.0
309.47	0	0.05641	24.4
321.83	1	0.04434	24.4
329.11	0	74.48	26.9
335.23	1	0.03466	24.4

Table 6.3.1.2 (continued)

E_n (eV)	ℓ	Γ_n (meV)	Γ_γ (meV)
338.34	1	0.05361	24.4
342.00	0	38.89	21.5
352.00	1	0.077	24.4
361.35	1	0.08999	24.4
365.36	0	26.06	24.4
369.49	0	25.71	24.4
380.72	1	0.1229	24.4
391.83	1	0.1445	24.4
401.10	0	11.12	24.4
402.92	0	0.1059	24.4
411.99	1	0.2114	24.4
421.03	0	0.5025	24.4
427.34	1	0.019	24.4
454.47	0	1.227	24.4
459.20	1	0.06548	24.4
462.77	0	64.07	24.4
466.41	1	0.1068	24.4
470.87	1	0.04362	24.4
476.58	1	0.1282	24.4
489.05	0	58.57	24.4

a 1970 detonation of a nuclear explosive device at the Nevada Test Site (NTS). The 54.1eV resonance was assigned a neutron width of 1.1×10^{-3}meV. No evidence of this resonance was observed in the current experiment. Given the width assigned by Forman *et al.*, the resonance should have been clearly visible in the current data. It was concluded that the 54.1eV resonance is not a ^{232}Th resonance.

The 112.1eV and 117.8eV resonances were reported in an unpublished Ph.D. dissertation [Ri69] based on an experiment performed at Saclay. The two resonances were assigned neutron widths of 3.9×10^{-3}meV and 2.0×10^{-3}meV, respectively. No evidence of the 112.1eV and 117.8eV resonances was observed in the current data. With the assigned widths these resonances should also have been observed clearly in the current data. It was concluded that the 112.1eV and 117.8eV resonances are not ^{232}Th resonances.

The 196.2eV and 391.8eV resonances were assigned ℓ=0 in the 1979 Bhat evaluation. A capture gamma ray measurement was performed by Corvi *et al.* [Co78] to examine decays to the ground and first few excited states of ^{233}Th. These gamma ray decays were used to establish the ℓ values of most resonances. Their analysis indicated that both the 196.2eV and the 391.8eV were ℓ=1.

The 219.5eV and 309.5eV resonances were assigned ℓ=1 in the 1979 Bhat evaluation. Both are very small resonances which were assigned ℓ=0 by Keyworth and Moore [Ke78]. Keyworth and Moore changed the ℓ assignment to force agreement with a Porter-Thomas distribution. The energy resolution in the present experiment was not sufficient to allow either resonance to be fit.

The resonances at 49.9eV, 232.1eV, 234.4eV, 242.2eV, 258.4eV, 272.8eV, 277.0eV, 335.2eV, and 352.0eV were not listed in the 1979 Bhat evaluation. All were reported by

either Forman *et al.* [Fo71], or Ribon [Ri69], or both. All of these resonances are clearly observed in the present data. It was concluded that they are all ^{232}Th ℓ=1 resonances.

For the purposes of this analysis the parameters of the 1982 Olsen evaluation were used. The only exceptions were the 54.1eV, 112.1eV, and 117.8eV resonances. As previously stated, there was no evidence in the present experiment for these resonances. The thorium spectrum is shown as a function of energy in figures 6.3.1.1 through 6.3.1.9. The complete thorium spectrum up to 400eV is shown in figure 6.3.1.10. The data displayed are the sum of the 355 runs analyzed.

6.3.2 Analysis of thorium resonances

The thorium data were measured using a dwell time of 200ns per channel. The effective energy window for this dwell time is 6eV to 400eV. No resonances above 400eV were analyzed due to the poor energy resolution and low detector efficiency.

There are 39 p-wave resonances listed by the 1982 Olsen evaluation in the first 400eV of ^{233}Th. Of the 39 p-wave levels listed, 23 were fit and values of $\mathcal{P}$ were obtained. The 128.2eV resonance was fit with the code SAMMY. The other 22 resonances were fit with the code PVIO. Values of $f_n\mathcal{P}$ were obtained for each resonance each run. The neutron polarization was calculated each run by calibrating the NMR area to measurements of ^{139}La. The spin flip efficiencies were taken from the numerical simulations described in section 4.2.2. Two of the remaining 16 resonances, the 47.0eV and 321.8eV were not fit because they interfered with a contaminant resonance. The other 14 resonances were not

Figure 6.3.1.1 Thorium transmission spectrum from 0-25eV. The data are the sum of the 355 runs used in the resonance analysis.

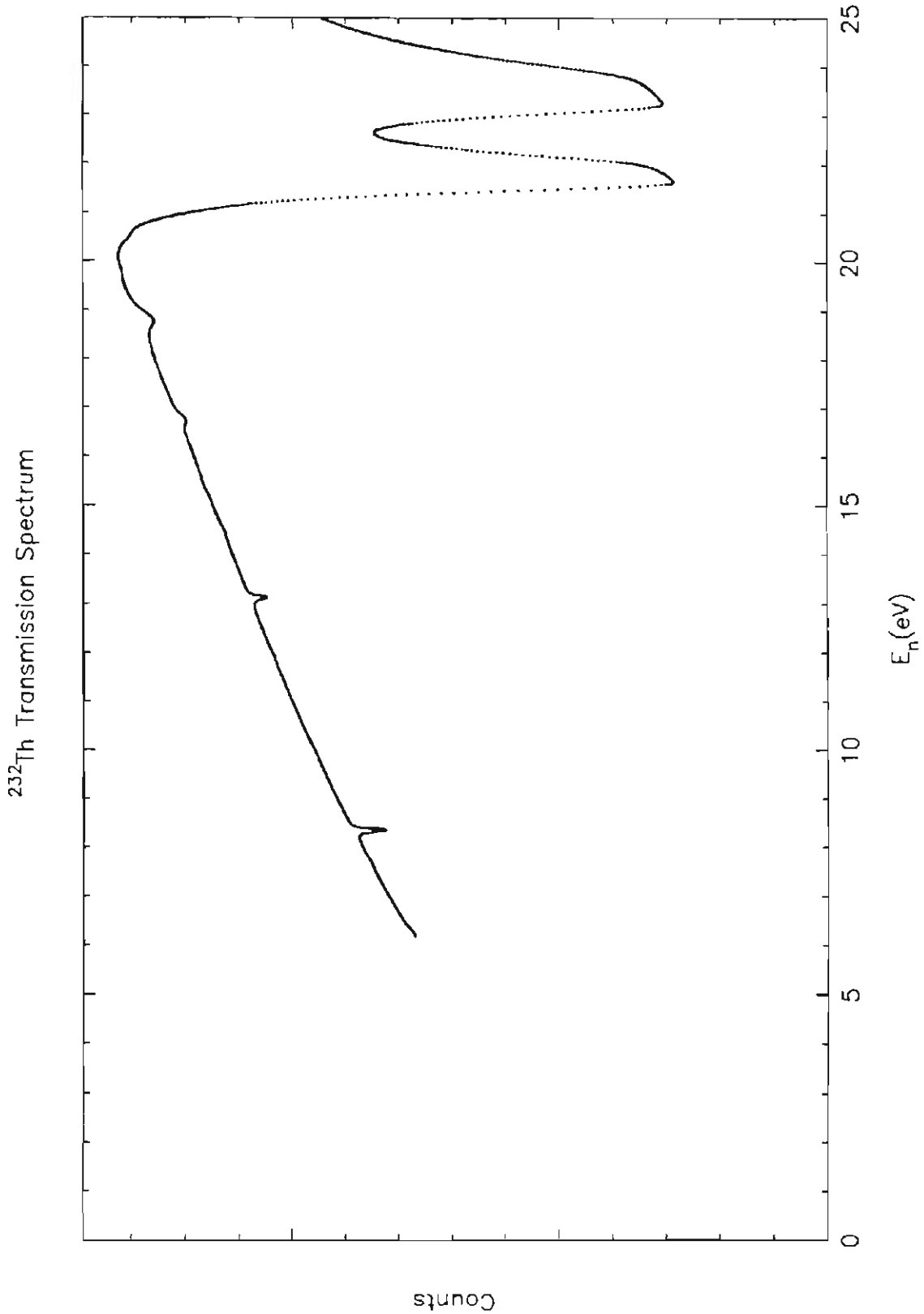
^{232}Th Transmission Spectrum
Counts
0
5
10
15
20
25
E_n(eV)

Figure 6.3.1.2 Thorium transmission spectrum from 25-50eV. The data are the sum of the 355 runs used in the resonance analysis.

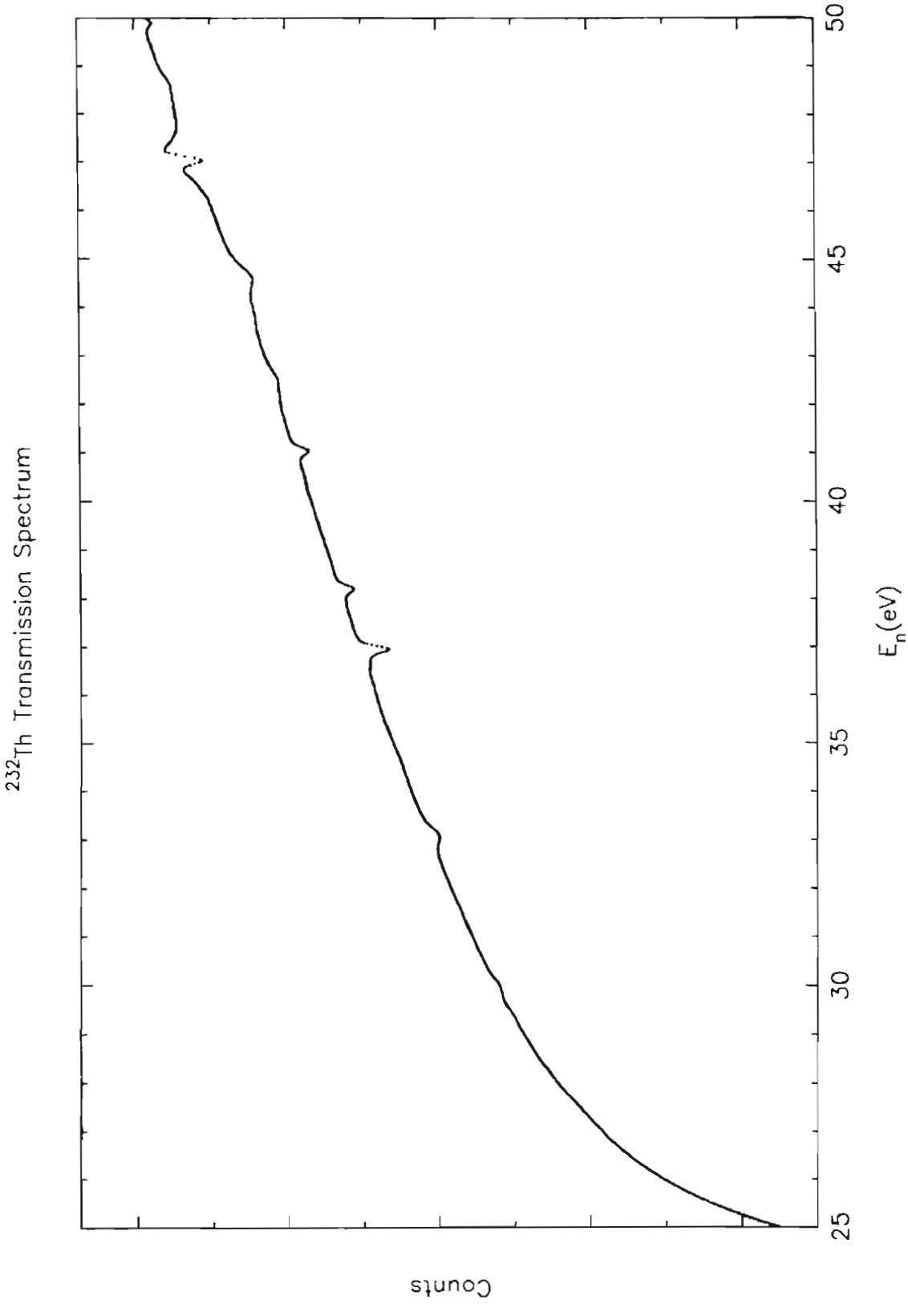
^{232}Th Transmission Spectrum
Counts
25
30
35
40
45
50
E_n(eV)

Figure 6.3.1.3 Thorium transmission spectrum from 50-100eV. The data are the sum of the 355 runs used in the resonance analysis.

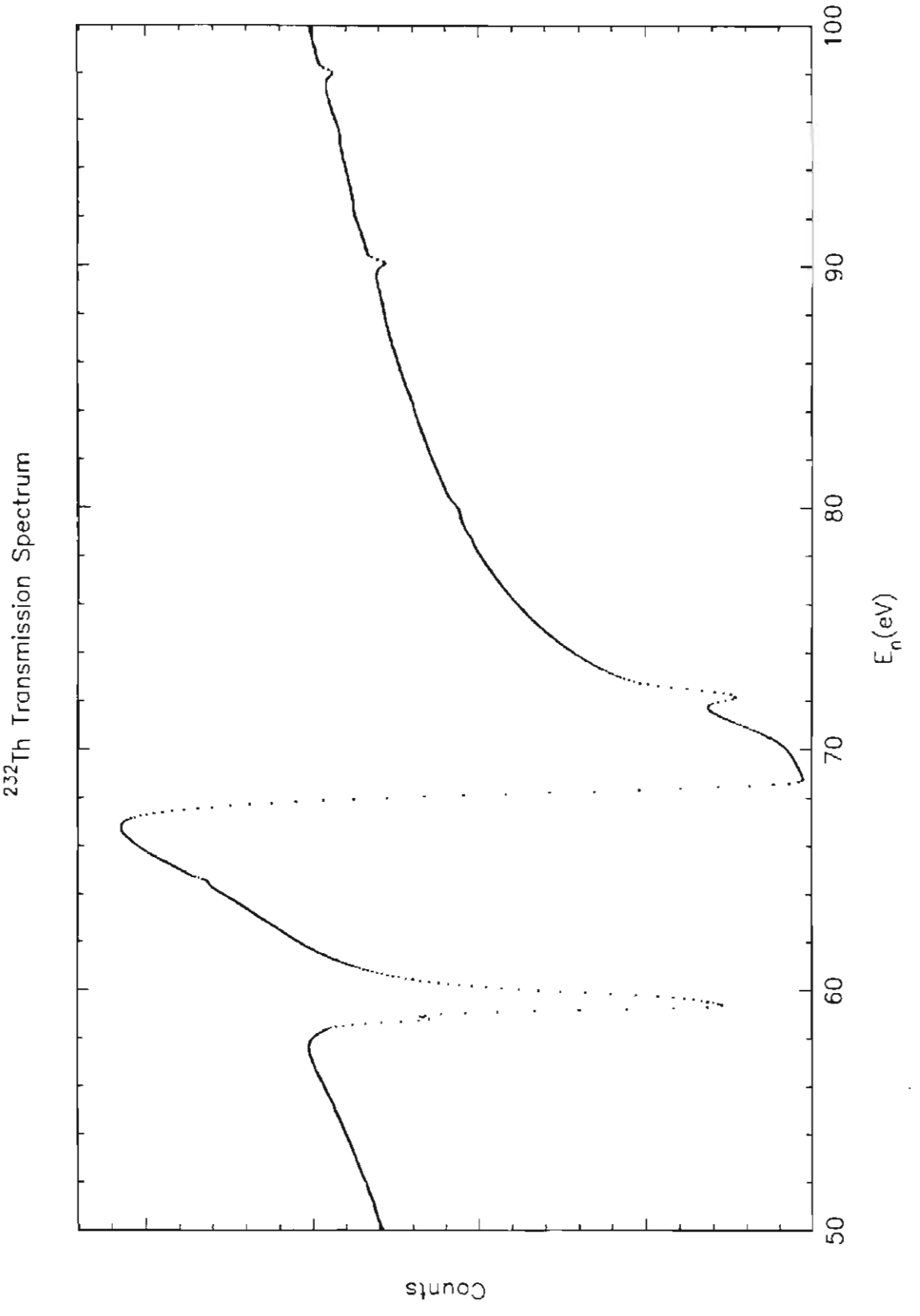
^{232}Th Transmission Spectrum
Counts
50
60
70
80
90
100
E_n(eV)

Figure 6.3.1.4 Thorium transmission spectrum from 100-150eV. The data are the sum of the 355 runs used in the resonance analysis.

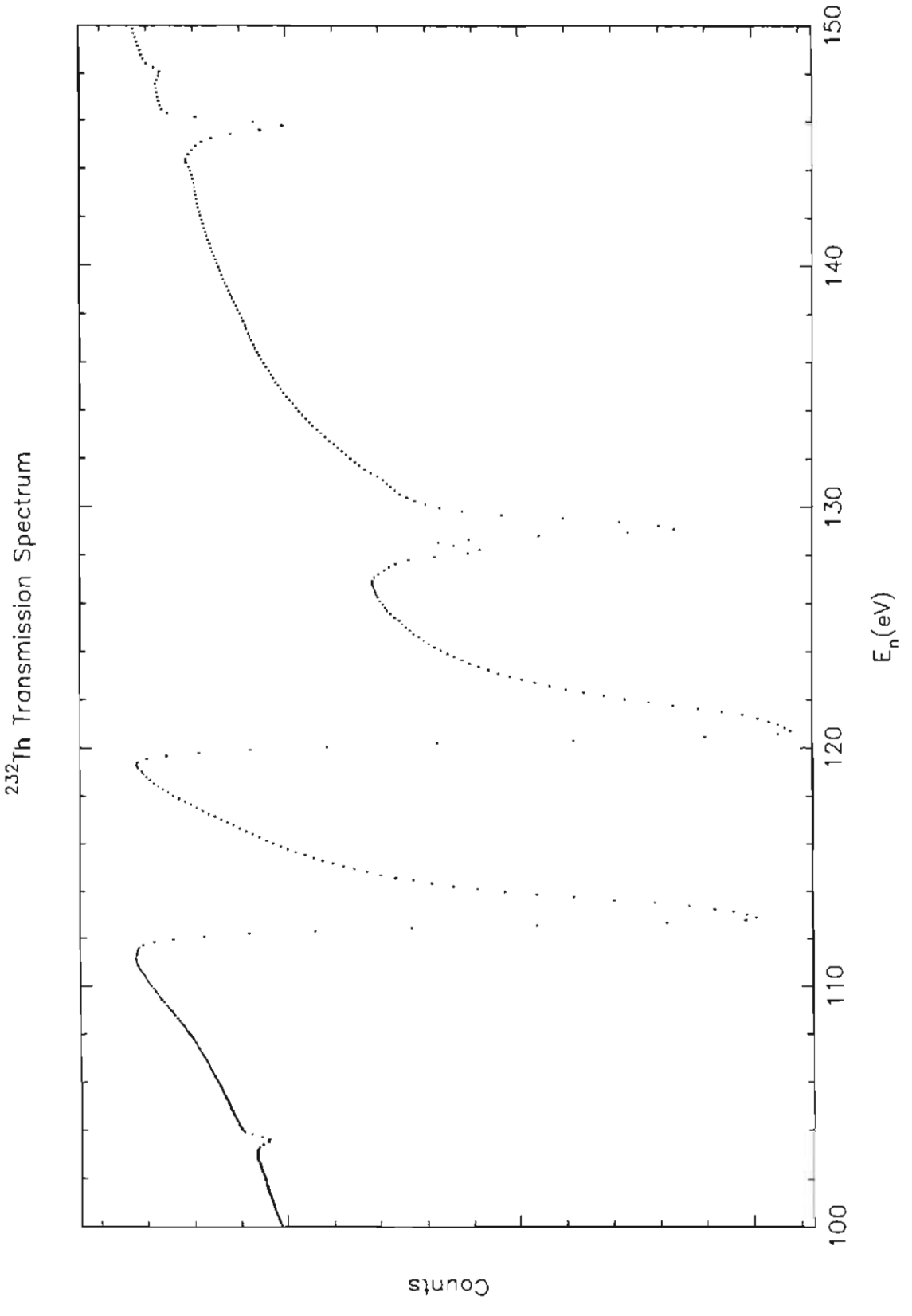
^{232}Th Transmission Spectrum
Counts
100
110
120
130
140
150
E_n(eV)

Figure 6.3.1.5 Thorium transmission spectrum from 150-200eV. The data are the sum of the 355 runs used in the resonance analysis.

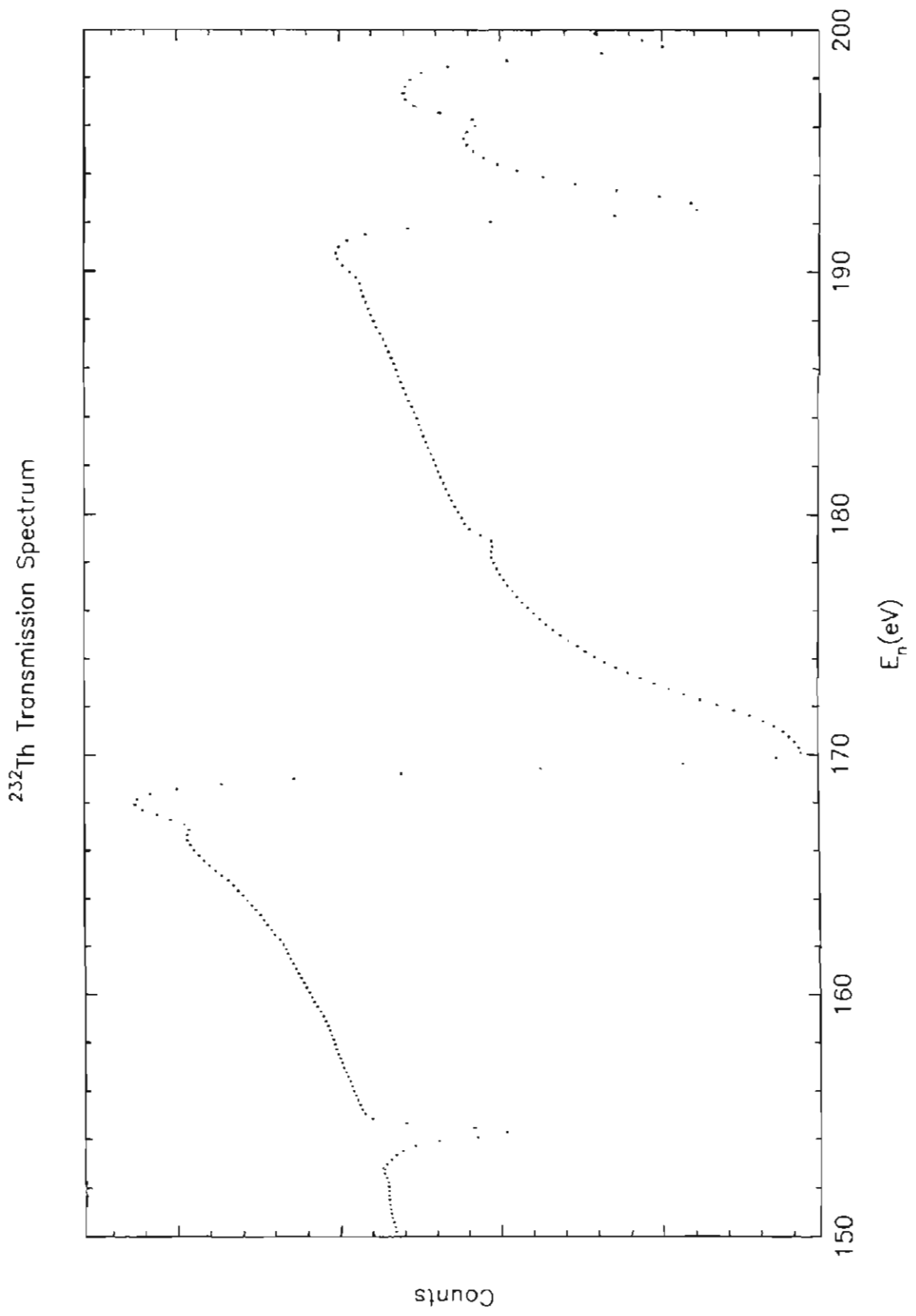
^{232}Th Transmission Spectrum
Counts
150
160
170
180
190
200
E_n(eV)

Figure 6.3.1.6 Thorium transmission spectrum from 200-250eV. The data are the sum of the 355 runs used in the resonance analysis.

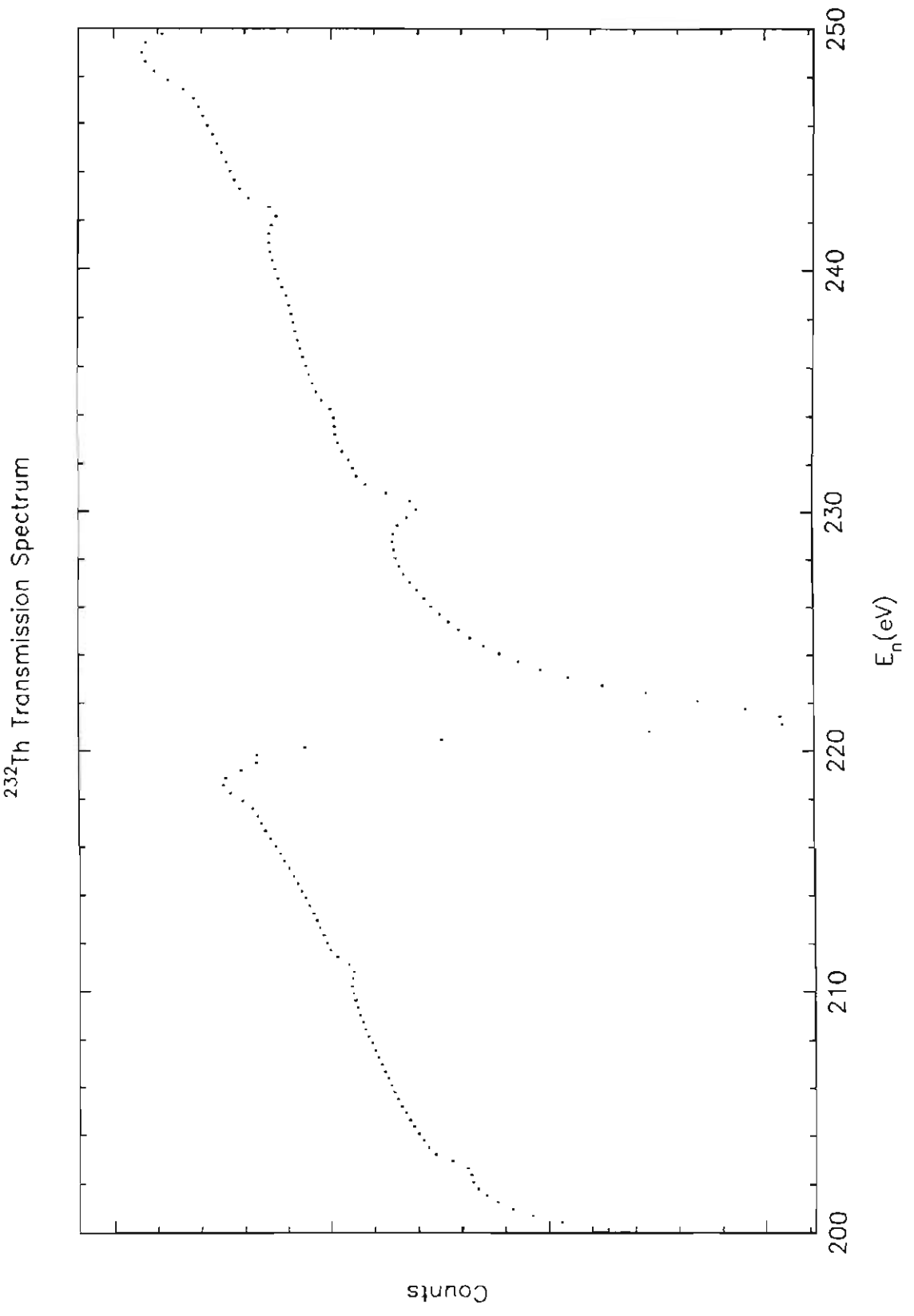
^{232}Th Transmission Spectrum
Counts
200
210
220
230
240
250
E_n(eV)

Figure 6.3.1.7 Thorium transmission spectrum from 250-300eV. The data are the sum of the 355 runs used in the resonance analysis.

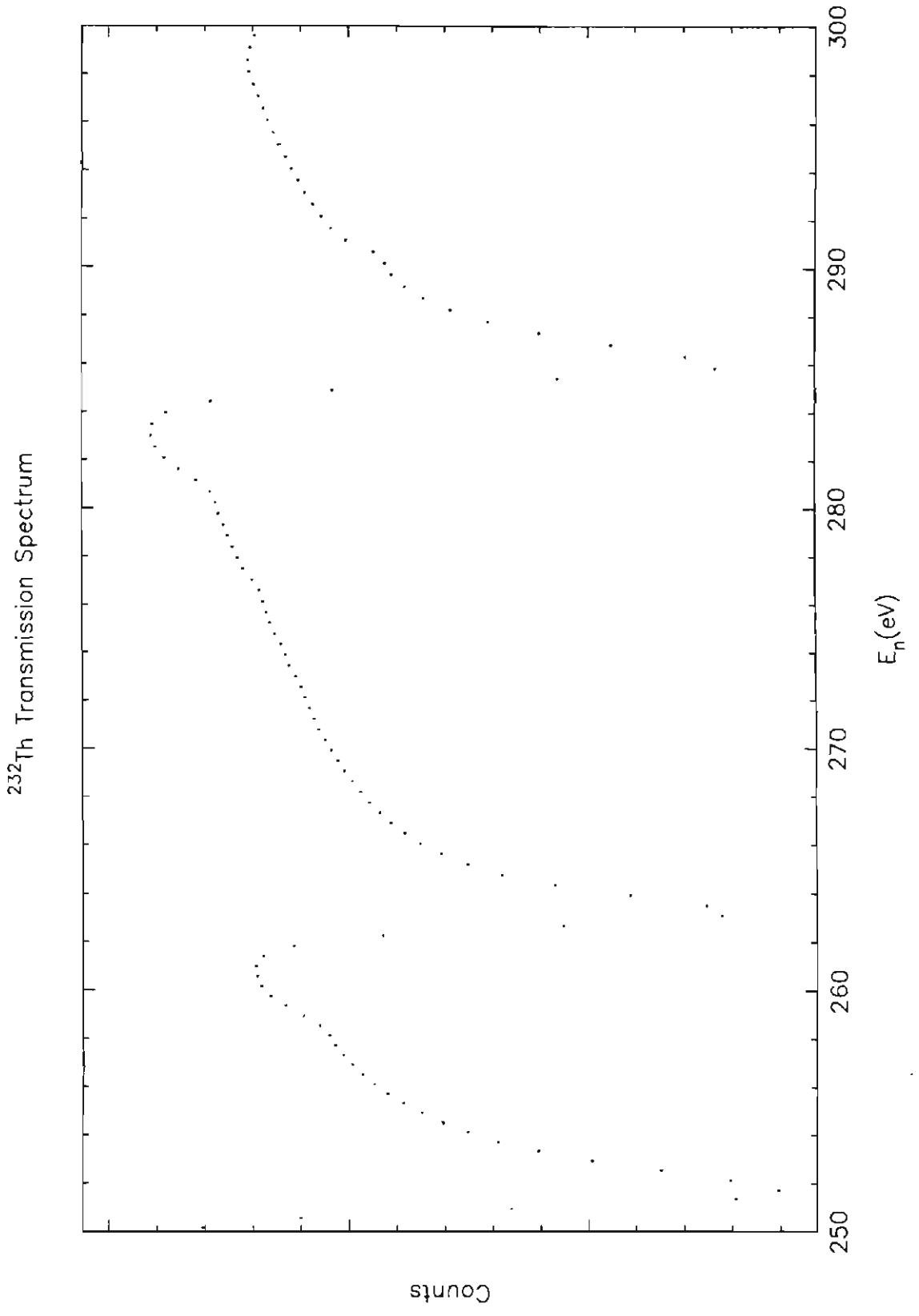
^{232}Th Transmission Spectrum
Counts
250
260
270
280
290
300
E_n(eV)

Figure 6.3.1.8 Thorium transmission spectrum from 300-350eV. The data are the sum of the 355 runs used in the resonance analysis.

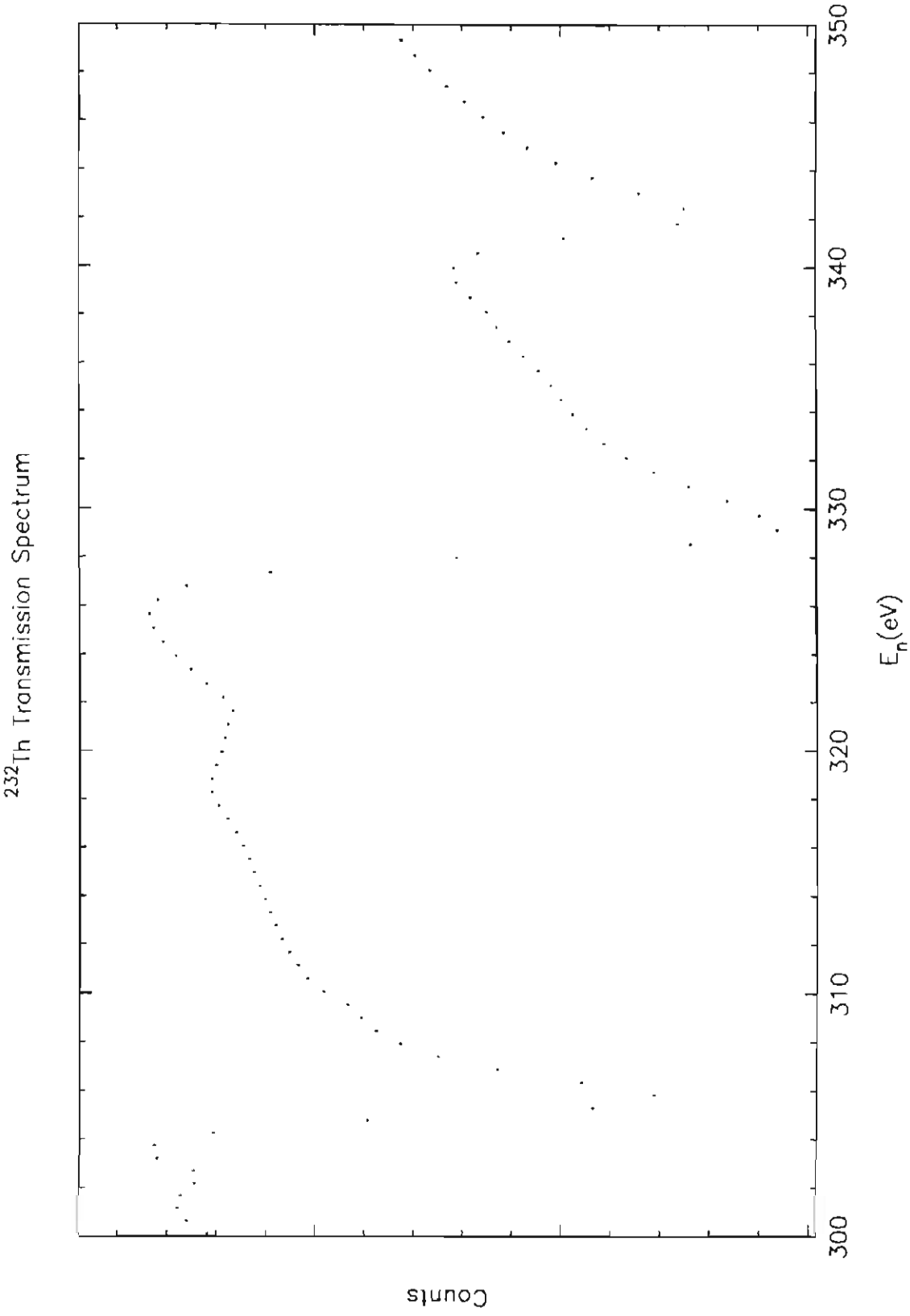
^{232}Th Transmission Spectrum
Counts
300
310
320
330
340
350
E_n(eV)

Figure 6.3.1.9 Thorium transmission spectrum from 350-400eV. The data are the sum of the 355 runs used in the resonance analysis.

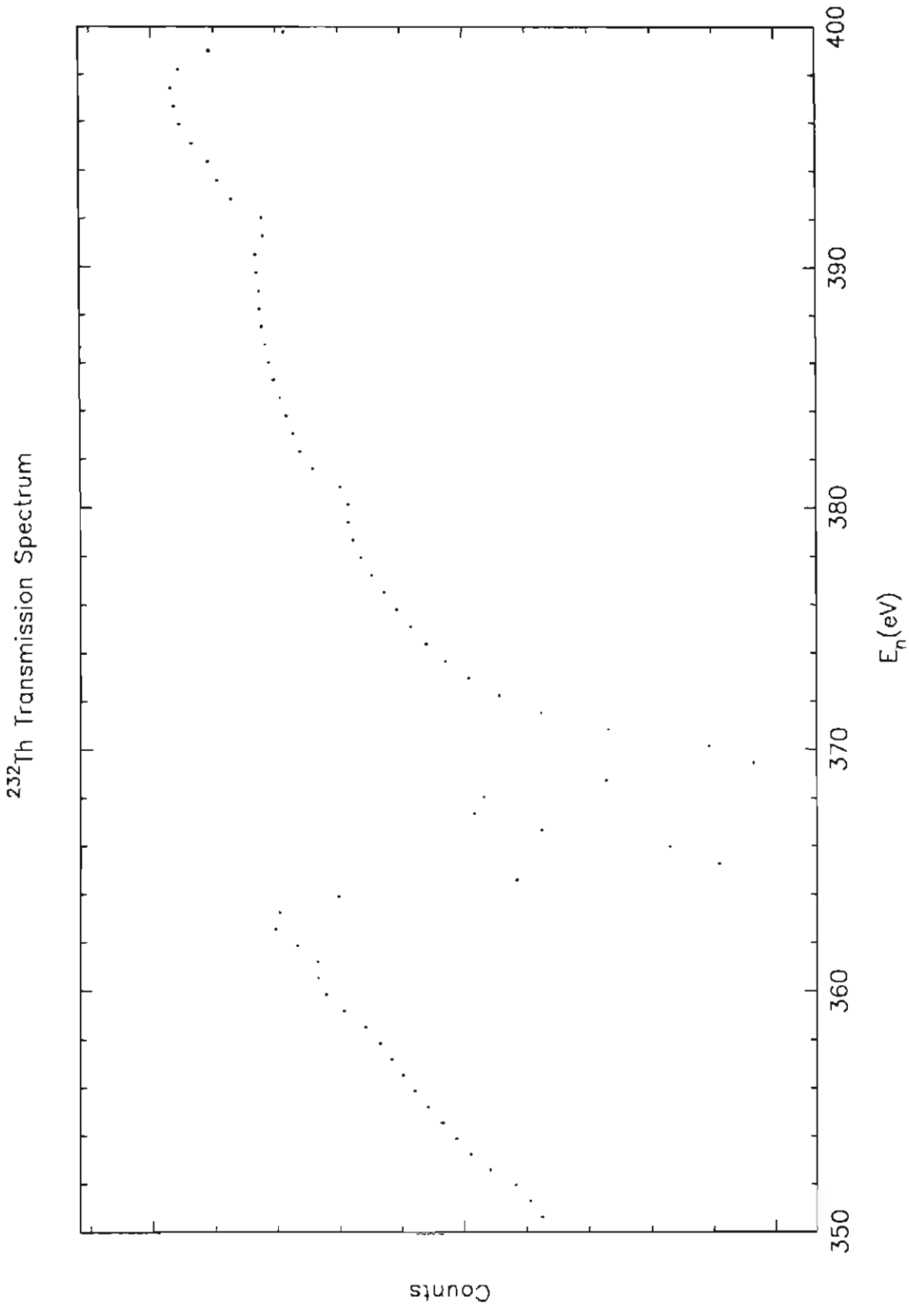
^{232}Th Transmission Spectrum
Counts
350
360
370
380
390
400
E_n(eV)

Figure 6.3.1.10 Thorium transmission spectrum from 0-400eV. The data are the sum of the 355 runs used in the resonance analysis.

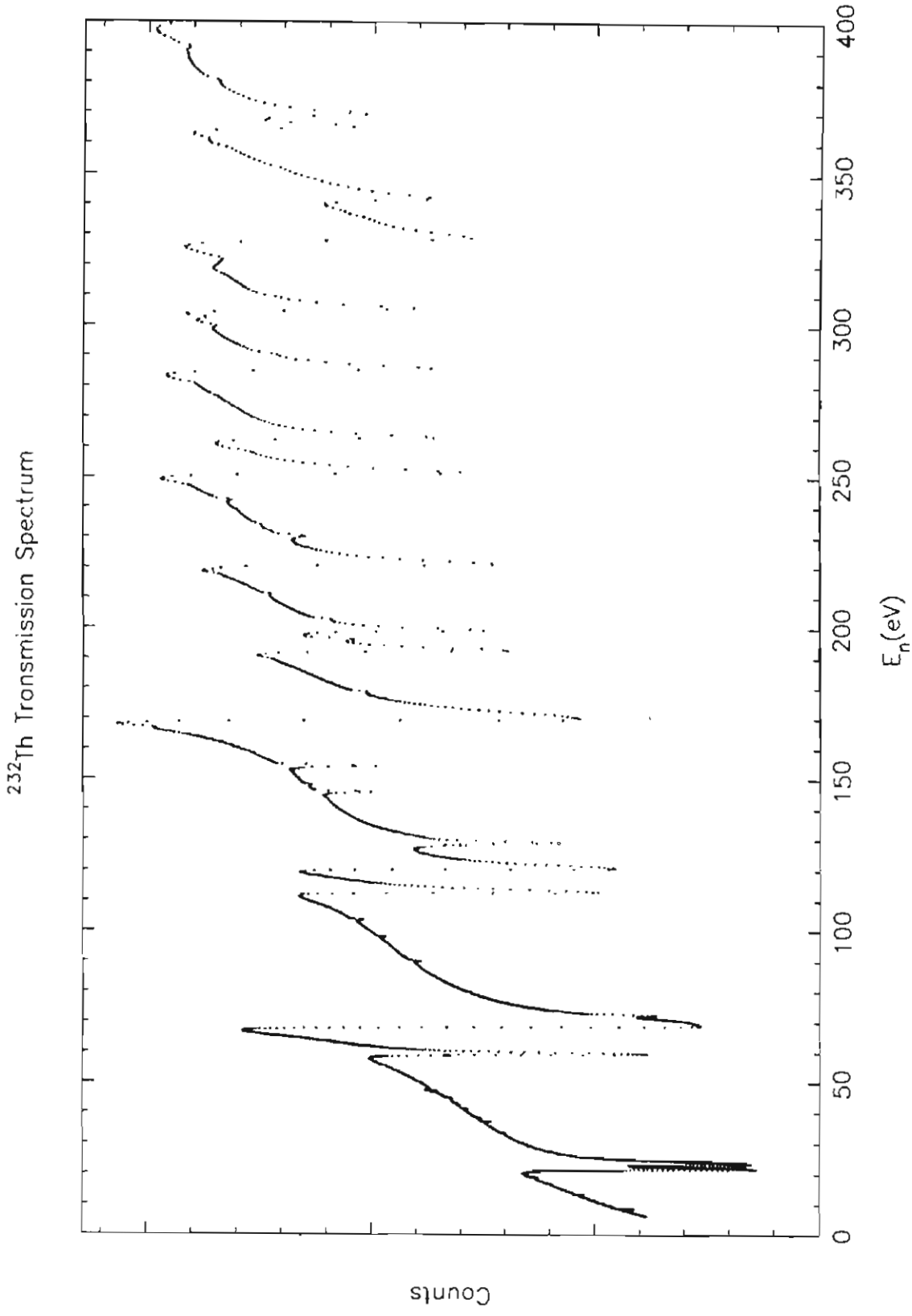
^{232}Th Transmission Spectrum
Counts
0
50
100
150
200
250
300
350
400
E_n(eV)

fit because the energy resolution at their energy was not sufficiently good to permit the resonances to be accurately fit. The $\mathcal{P}$ values are tabulated for the 23 p-wave resonances in table 6.3.2.1. The $\mathcal{P}$ values are weighted averages of the 355 individual $\mathcal{P}$ values obtained from a fit to each run. The weighting factors were the errors assigned to the values of $f_n\mathcal{P}$ by the fitting code. Since all runs were of the same length and had approximately the same number of neutrons, the weighted averages are not significantly different from the standard mean. The errors quoted are the standard deviation of the mean of the 355 individual values of $\mathcal{P}$ from each run; this is a very robust method of calculating errors. The values of $\mathcal{P}$ are also displayed graphically as a function of energy in figure 6.3.2.1.

Seven effects with relative significance greater than 2.4 standard deviations were observed. These are marked by asterisks in table 6.3.2.1. Only 0.3 effects greater than 2.4 standard deviations would be expected to occur by random fluctuations. Shown in figures 6.3.2.2 through 6.3.2.24 are sample fits to the resonances and histograms of the individual $\mathcal{P}$ values from each run.

The distribution of $\mathcal{P}$ values for each of the 23 ^{232}Th resonances was bootstrapped in the same manner as the 0.88eV bromine resonance. The standard deviations of the bootstrap distributions were, on average, 19% smaller than the standard deviations of the means of the distributions of $\mathcal{P}$ values. The bootstrap distributions were, however, symmetric about the mean. The reason for the width of the bootstrap distributions being smaller than the conventional

Table 6.3.2.1

Parity violating asymmetries of thorium resonances

E_n (eV)	$\mathcal{P}$ (%)	Relative Significance (Std. Dev.)
8.3	1.48±0.25	5.9*
13.1	0.74±0.62	1.2
37.0	2.46±0.97	2.5*
38.2	10.88±2.27	4.8*
41.0	-2.23±2.14	1.0
49.9	-1.08±2.99	0.4
64.5	9.78±2.08	4.7*
90.2	-1.05±1.00	1.1
98.1	-0.01±1.38	0.0
103.7	-0.43±1.04	0.4
128.2	1.31±0.18	7.3*
145.9	-0.03±0.22	0.1
148.1	-4.91±2.79	1.8
167.2	3.45±1.19	2.9*
179.0	-1.47±1.28	1.1
196.2	1.10±0.46	2.4*
202.7	2.17±1.43	1.5
211.0	1.76±1.85	1.0
242.3	-0.04±1.20	0.0
299.8	-1.56±1.68	0.9
302.7	-1.75±1.04	1.7
380.7	1.10±1.76	0.6
391.8	-0.67±1.62	0.4

Figure 6.3.2.1 Parity violating asymmetries for thorium resonances.

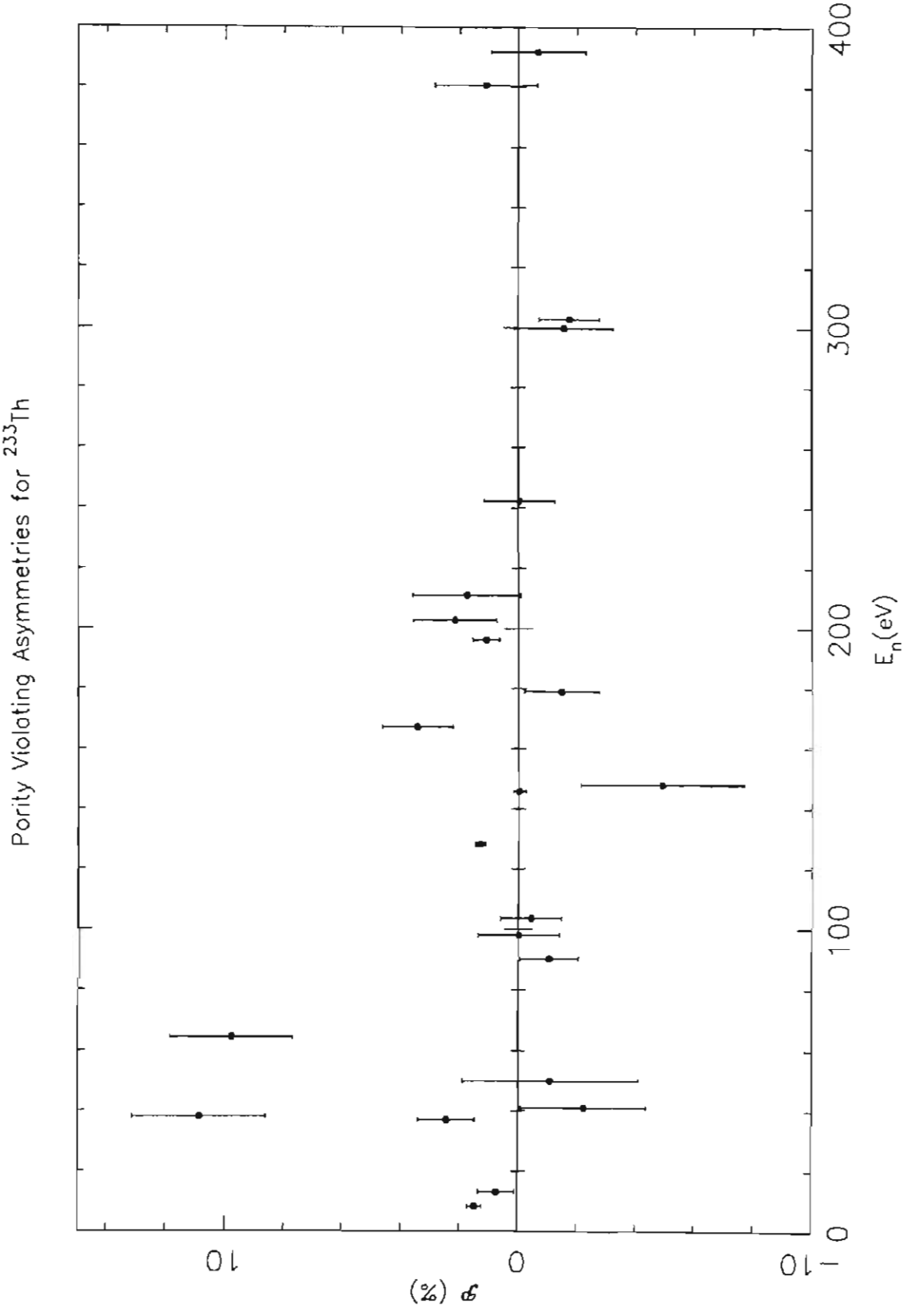
Pority Violating Asymmetries for ^{233}Th
σ_p (%)
10
0
-10
0
100
200
300
400
E_n(eV)

Figure 6.3.2.2

(top) Sample fit to the 8.3eV resonance. The top curve is the flux portion of the fitting function and the bottom curve is the fit to the resonance plus the flux. The data displayed are for one spin state of a single run.

(bottom) Histogram of the 355 $\mathcal{P}$ values obtained from fits to the 8.3eV resonance.

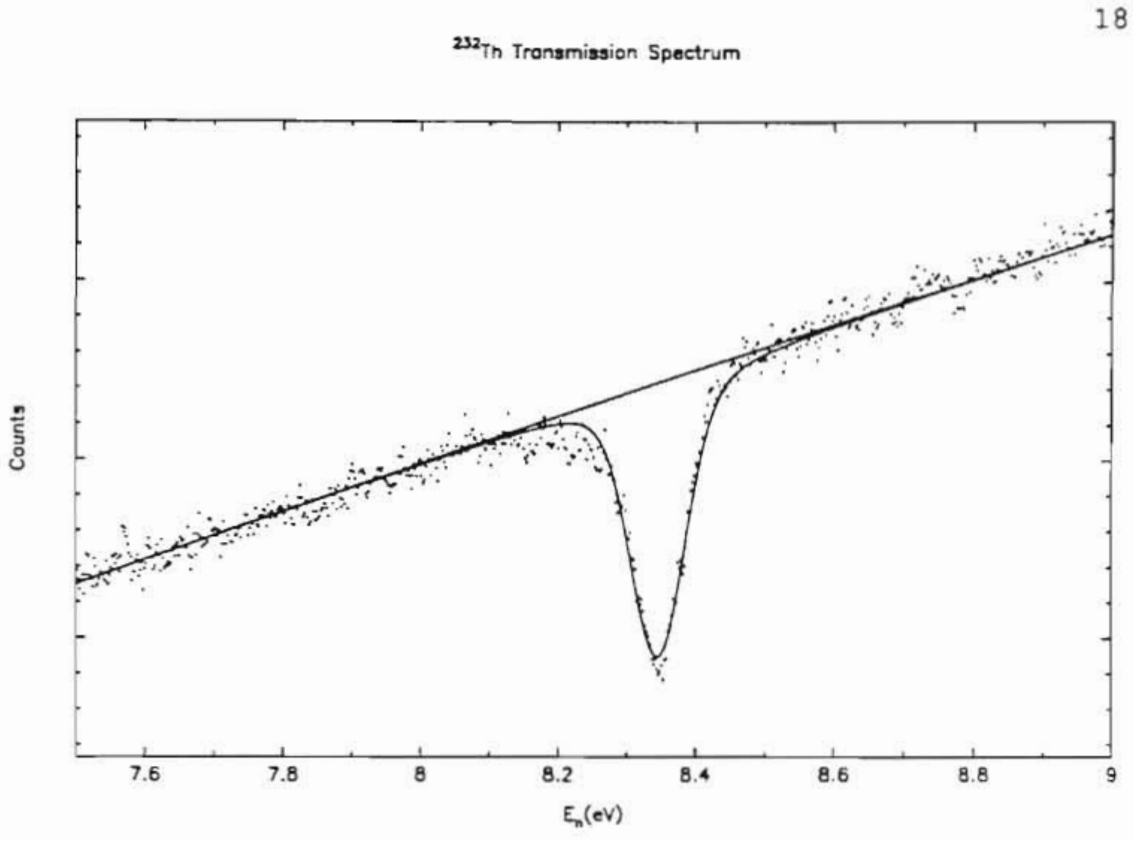
^{232}Th Transmission Spectrum
Counts
7.6
7.8
8
8.2
8.4
8.6
8.8
9
E_n(eV)

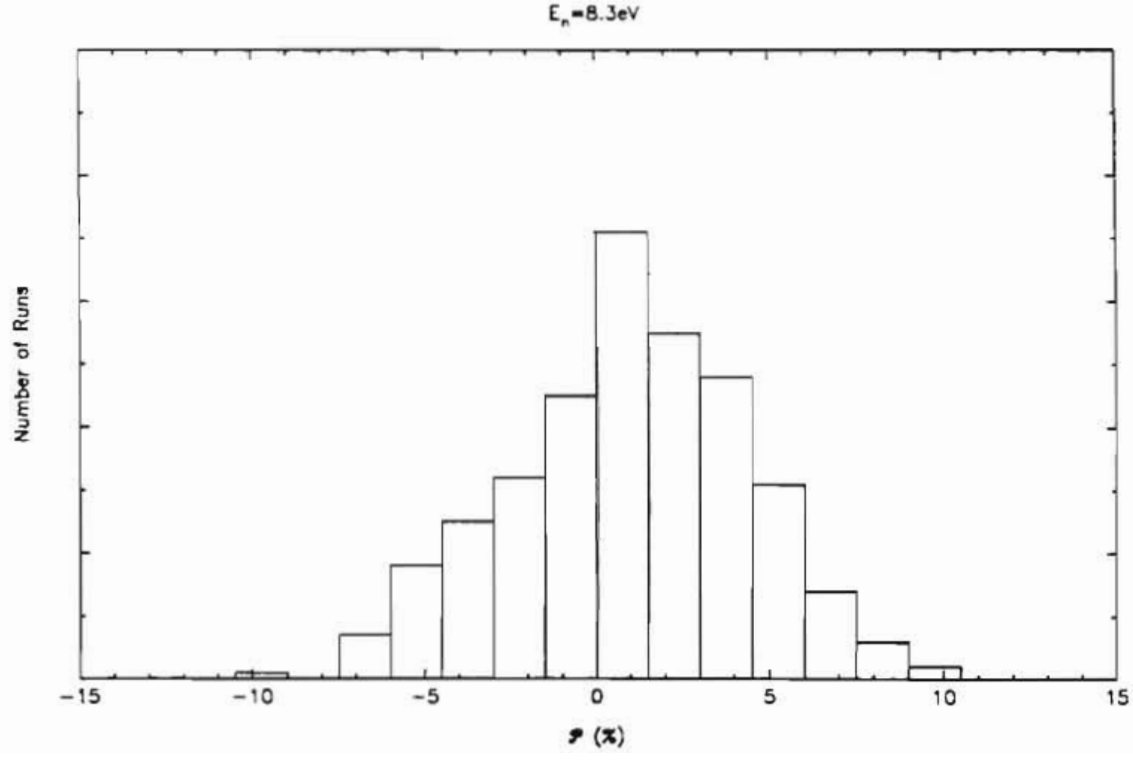
E_n=8.3eV
Number of Runs
−15
−10
−5
0
5
10
15
χ

Figure 6.3.2.3

(top) Sample fit to the 13.1eV resonance. The top curve is the flux portion of the fitting function and the bottom curve is the fit to the resonance plus the flux. The data displayed are for one spin state of a single run.

(bottom) Histogram of the 355 $\mathcal{P}$ values obtained from fits to the 13.1eV resonance.

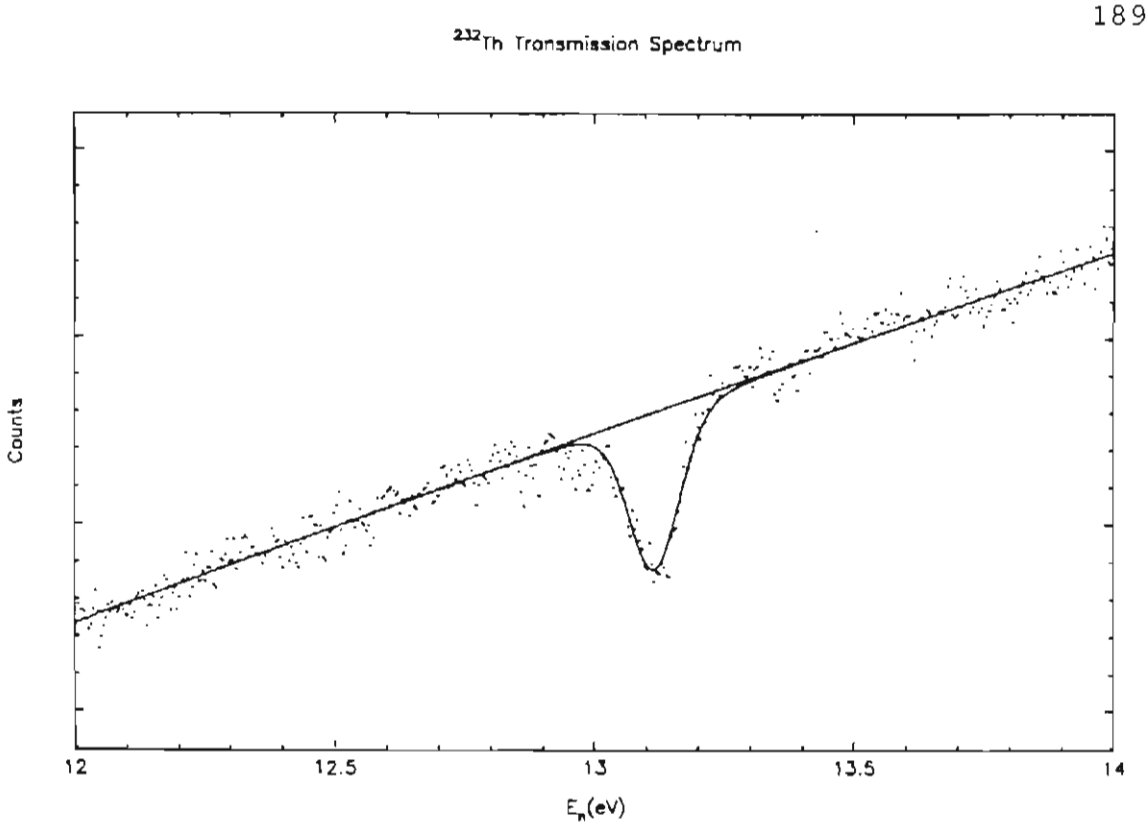
^{232}Th Transmission Spectrum
Counts
12
12.5
13
13.5
14
E_n(eV)

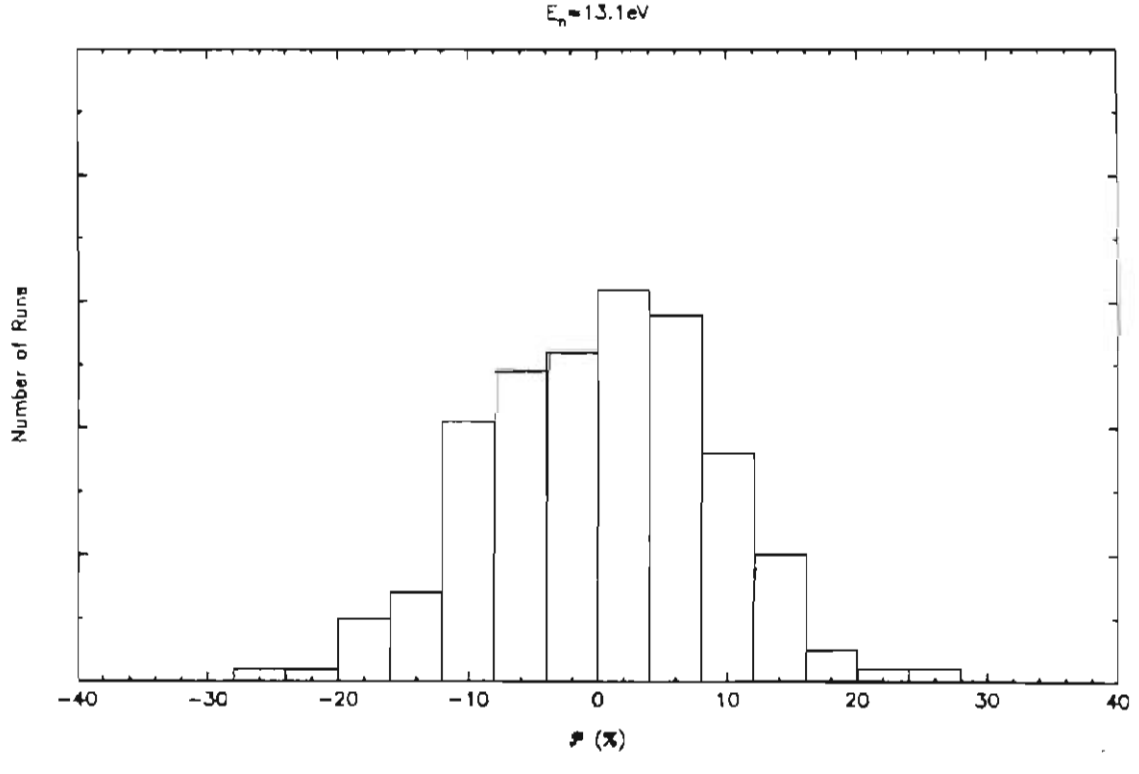
E_n=13.1eV
Number of Runs
−40
−30
−20
−10
0
10
20
30
40
Φ (%)

Figure 6.3.2.4

(top) Sample fit to the 37.0eV resonance. The top curve is the flux portion of the fitting function and the bottom curve is the fit to the resonance plus the flux. The data displayed are for one spin state of a single run.

(bottom) Histogram of the 355 $\mathcal{P}$ values obtained from fits to the 37.0eV resonance.

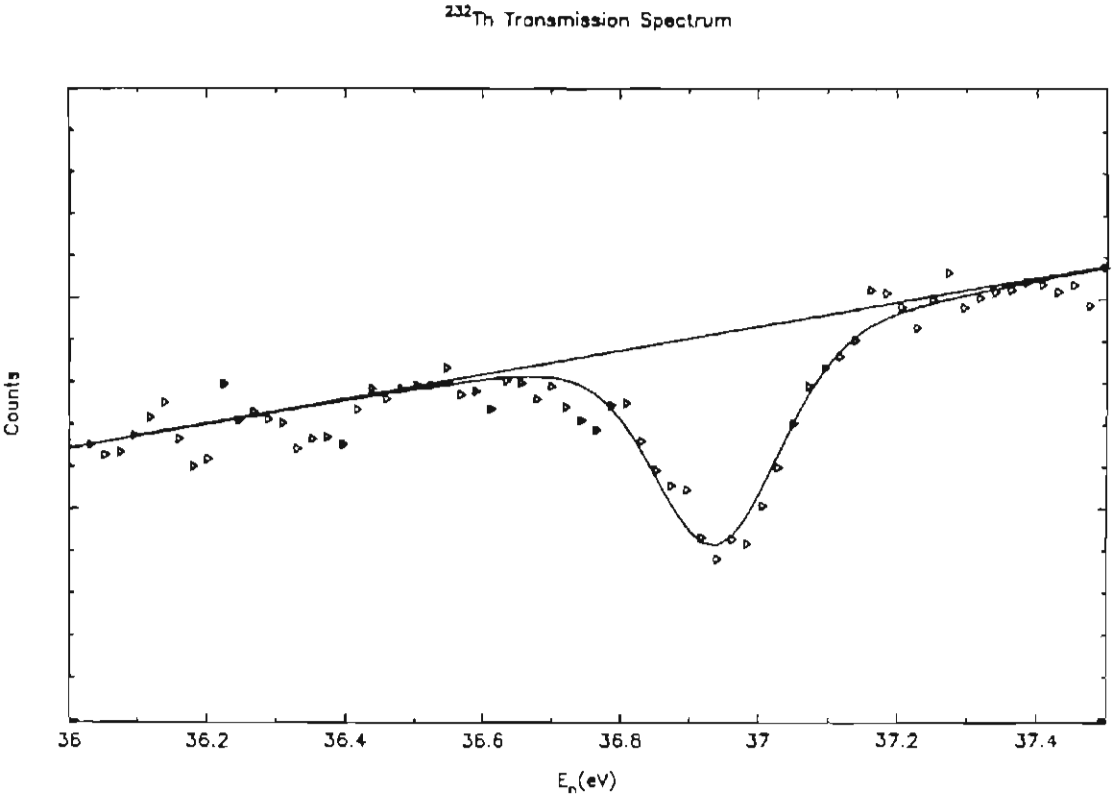
^{232}Th Transmission Spectrum
Counts
36
36.2
36.4
36.6
36.8
37
37.2
37.4
E_n(eV)

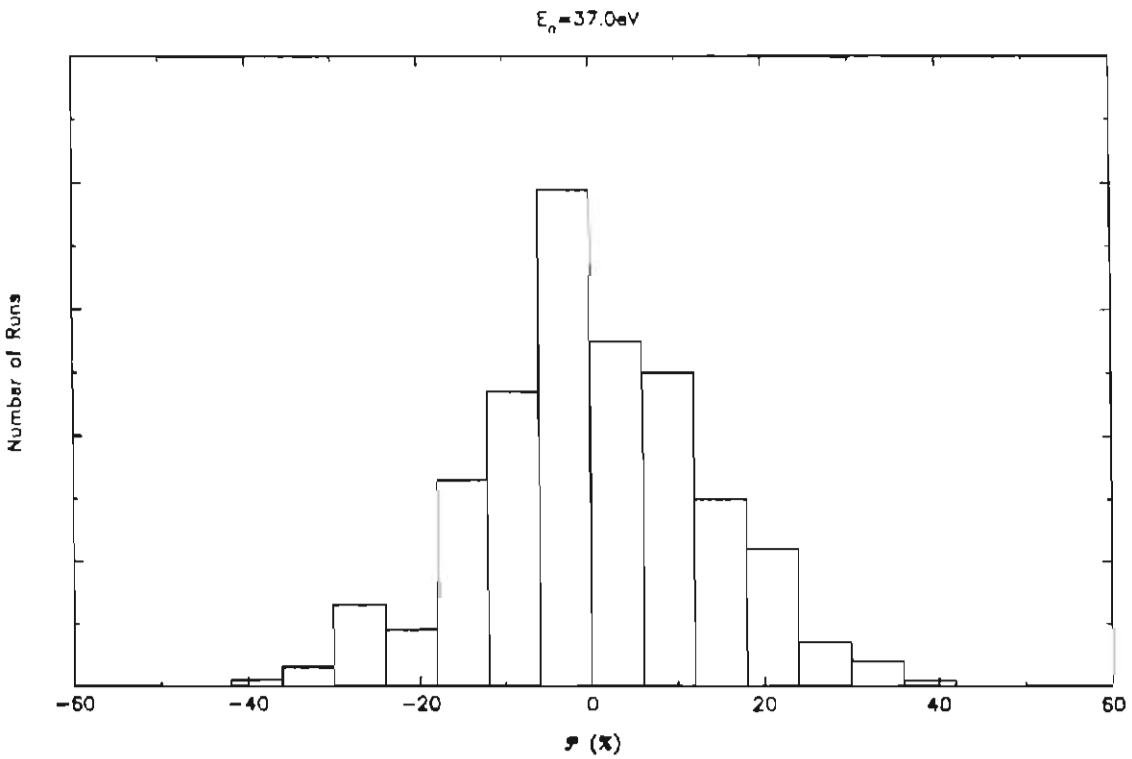
E_n=37.0eV
Number of Runs
−60
−40
−20
0
20
40
60
$\mathcal{P}$ (%)

Figure 6.3.2.5

(top) Sample fit to the 38.2eV resonance. The top curve is the flux portion of the fitting function and the bottom curve is the fit to the resonance plus the flux. The data displayed are for one spin state of a single run.

(bottom) Histogram of the 355 $\mathcal{P}$ values obtained from fits to the 38.2eV resonance.

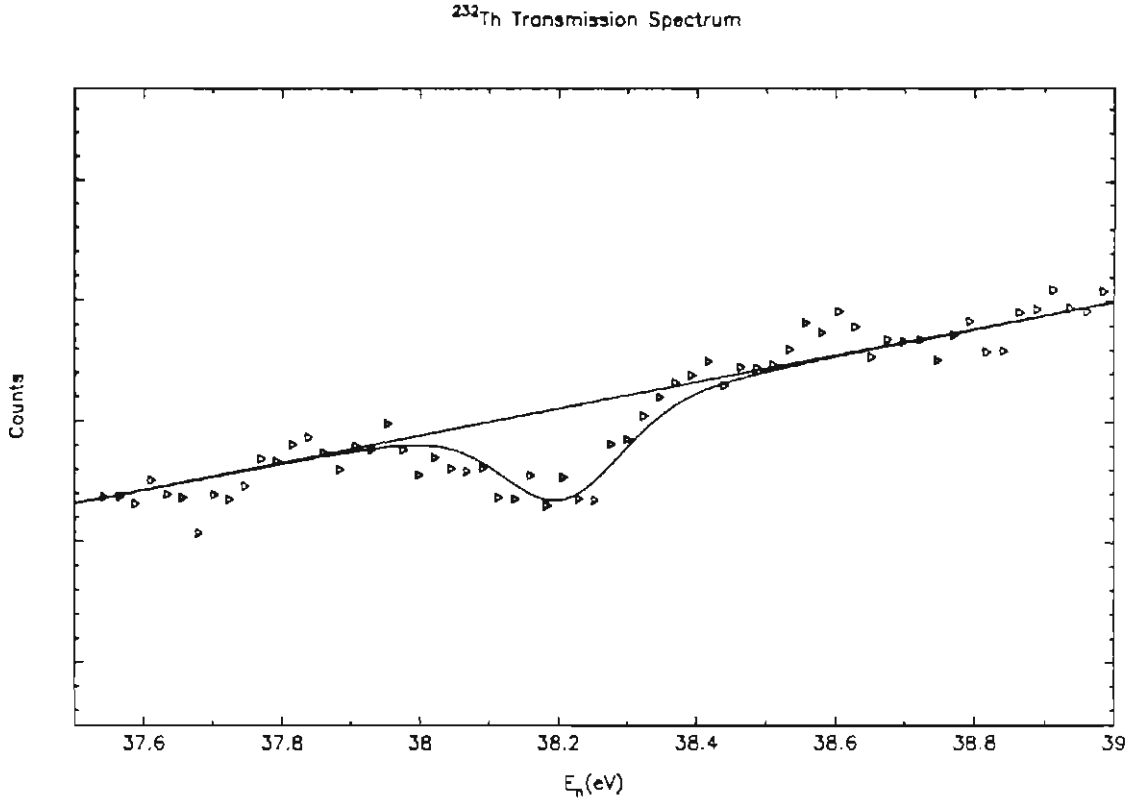
^{232}Th Transmission Spectrum
Counts
37.6
37.8
38
38.2
38.4
38.6
38.8
39
E_n(eV)

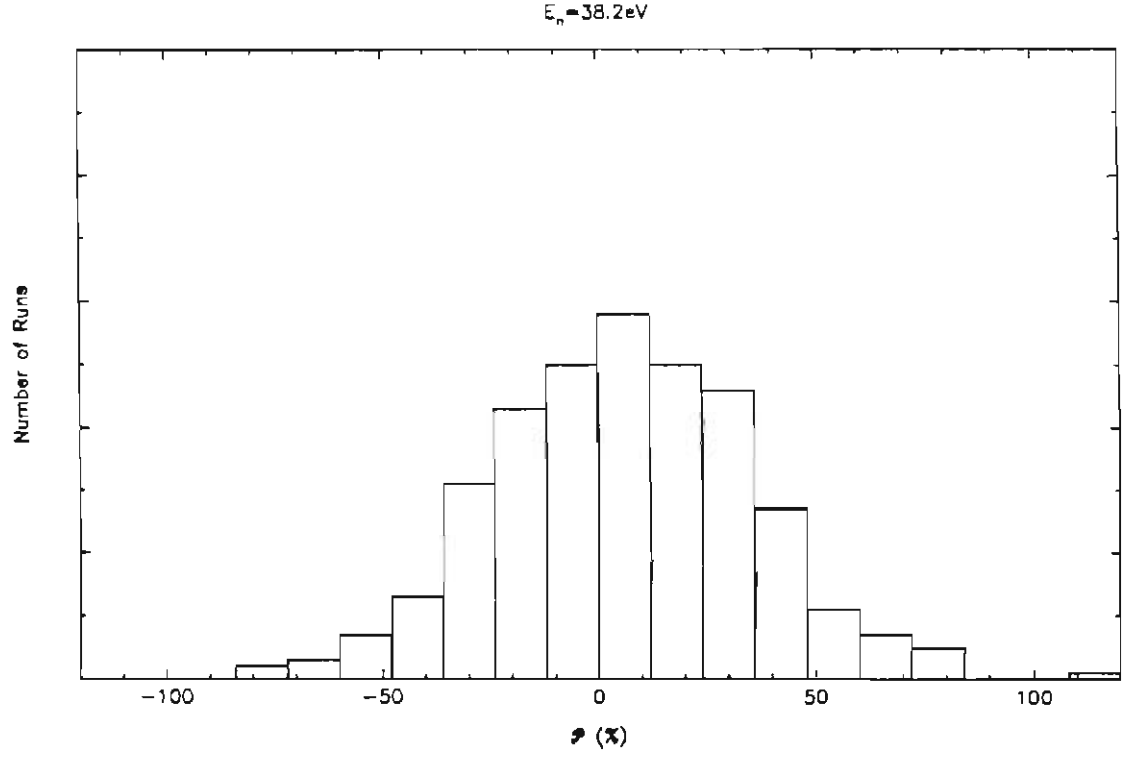
E_n=38.2eV
Number of Runs
−100
−50
0
50
100
$\mathcal{P}$ (%)

Figure 6.3.2.6

(top) Sample fit to the 41.0eV resonance. The top curve is the flux portion of the fitting function and the bottom curve is the fit to the resonance plus the flux. The data displayed are for one spin state of a single run.

(bottom) Histogram of the 355 $\mathcal{P}$ values obtained from fits to the 41.0eV resonance.

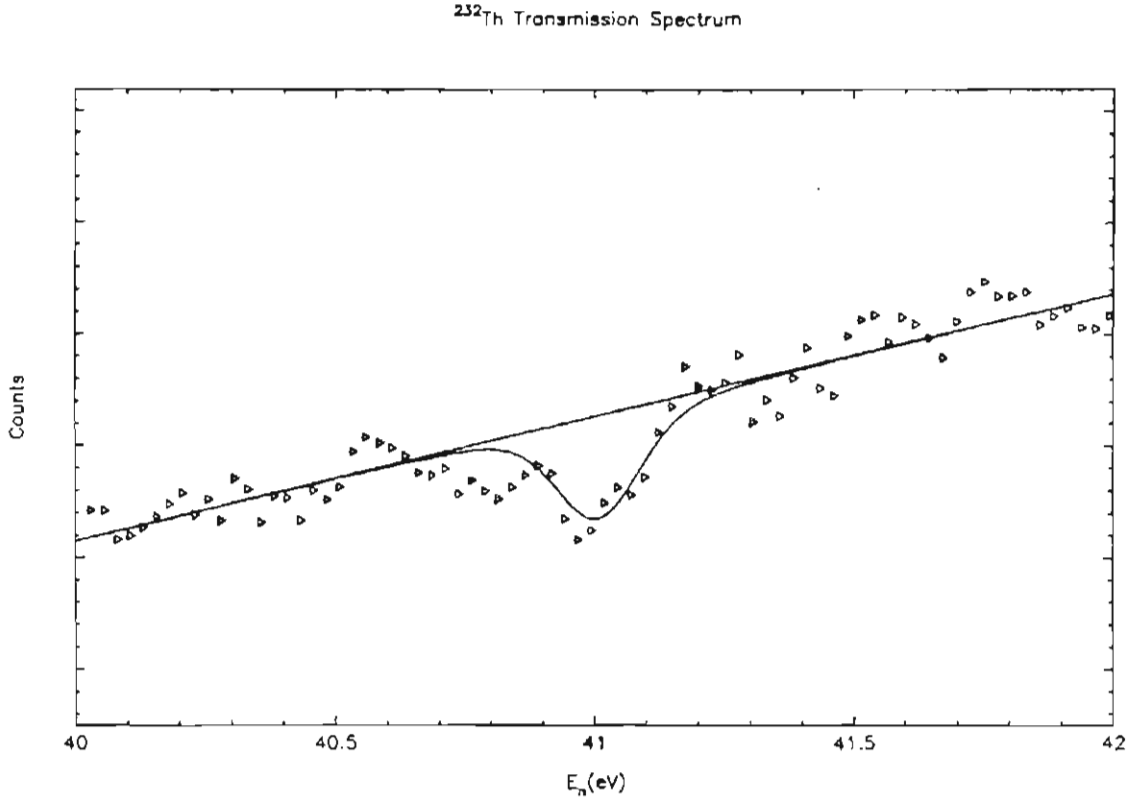
^{232}Th Transmission Spectrum
Counts
40
40.5
41
41.5
42
E_n(eV)

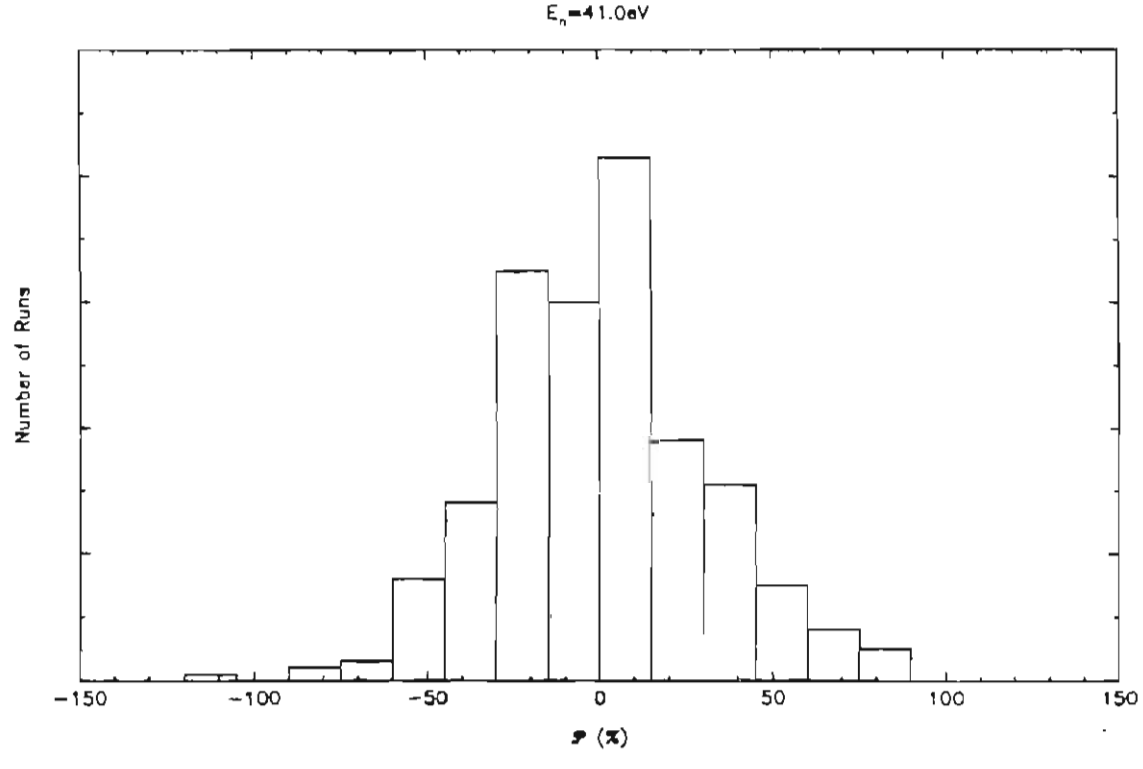
E_n=41.0eV
Number of Runs
−150
−100
−50
0
50
100
150
χ

Figure 6.3.2.7

(top) Sample fit to the 49.9eV resonance. The top curve is the flux portion of the fitting function and the bottom curve is the fit to the resonance plus the flux. The data displayed are for one spin state of a single run.

(bottom) Histogram of the 355 $\mathcal{P}$ values obtained from fits to the 49.9eV resonance.

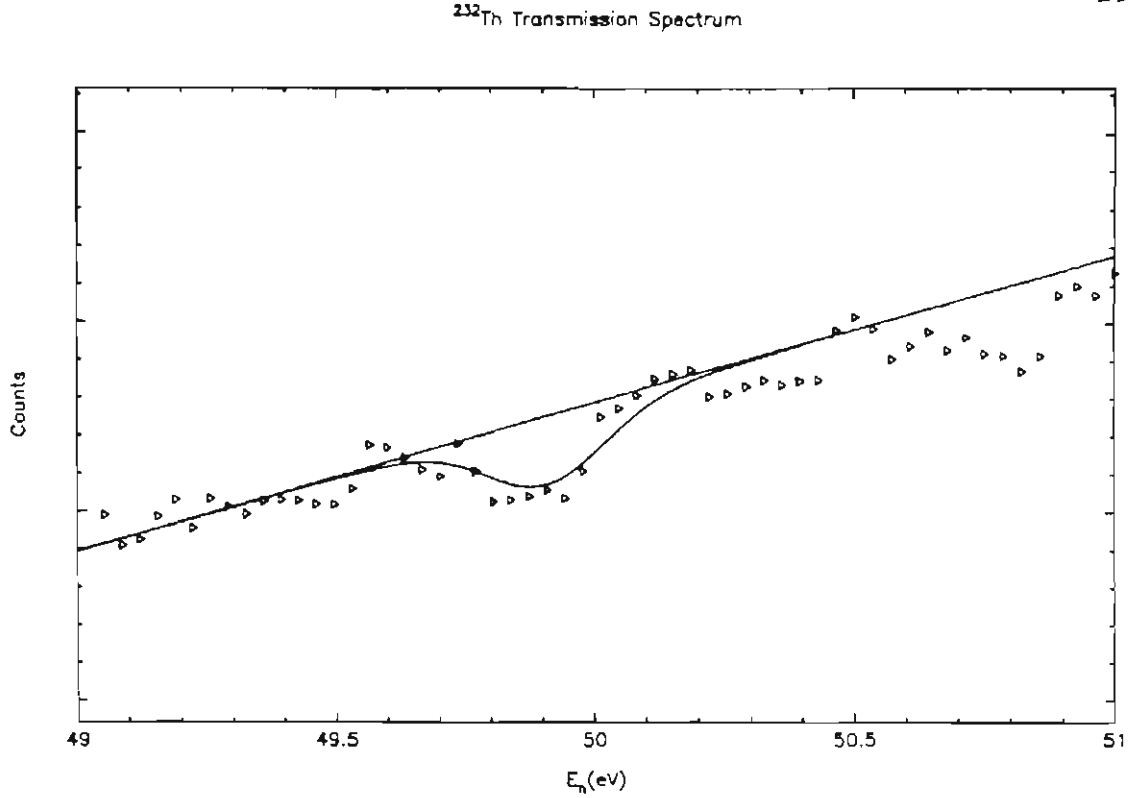
^{232}Th Transmission Spectrum
Counts
49
49.5
50
50.5
51
E_n(eV)

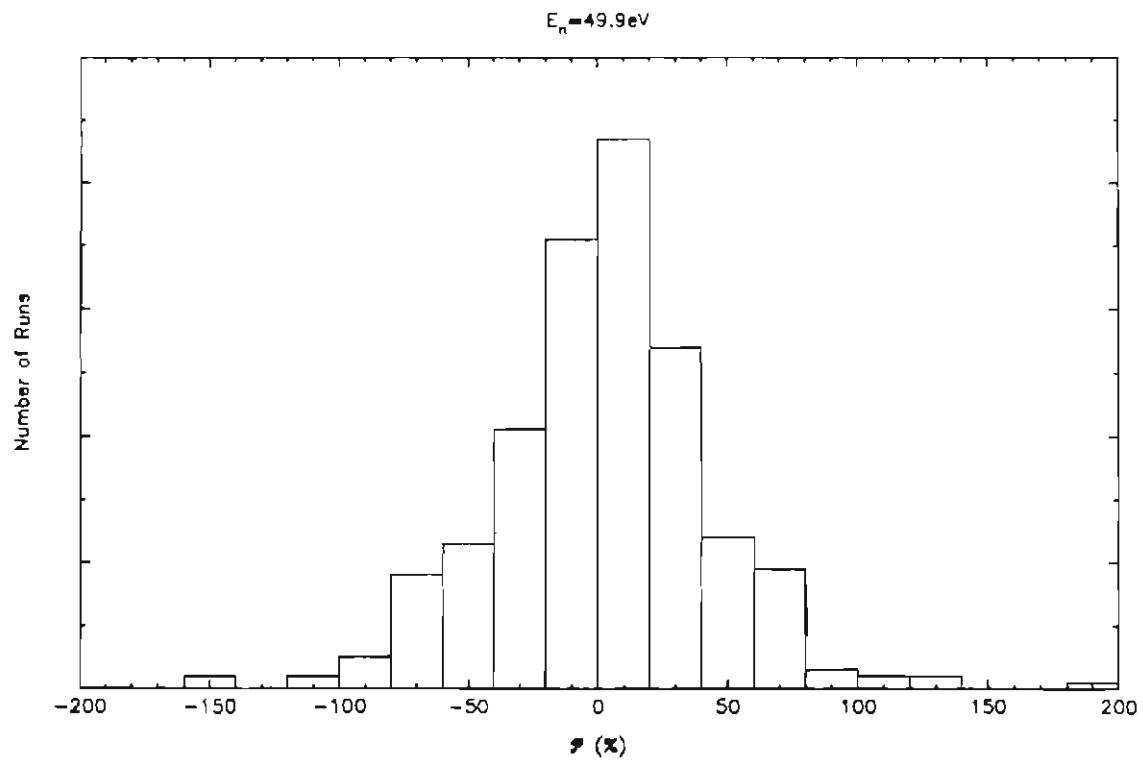
E_n=49.9eV
Number of Runs
−200
−150
−100
−50
0
50
100
150
200
ρ (%)

Figure 6.3.2.8

(top) Sample fit to the 64.5eV resonance. The top curve is the flux portion of the fitting function and the bottom curve is the fit to the resonance plus the flux. The data displayed are for one spin state of a single run.

(bottom) Histogram of the 355 $\mathcal{P}$ values obtained from fits to the 64.5eV resonance.

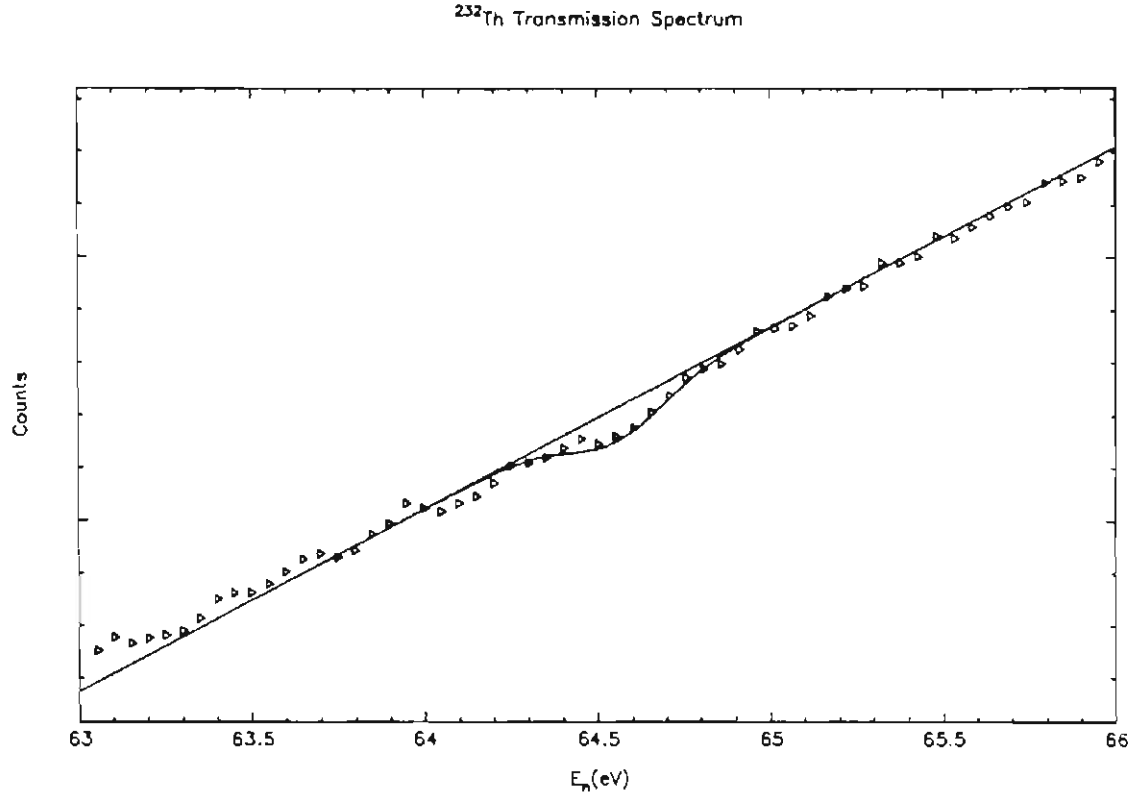
^{232}Th Transmission Spectrum
Counts
63
63.5
64
64.5
65
65.5
66
E_n(eV)

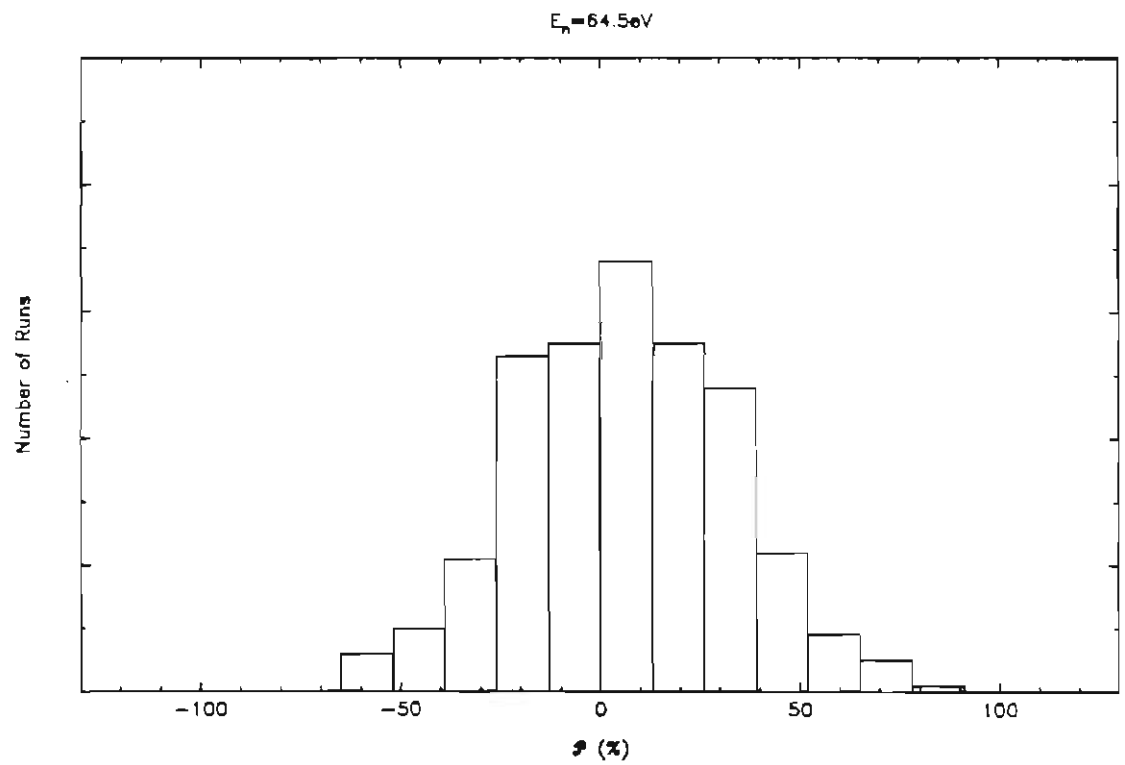
E_n=64.5eV
Number of Runs
−100
−50
0
50
100
$\mathcal{P}$ (%)

Figure 6.3.2.9

(top) Sample fit to the 90.2eV resonance. The top curve is the flux portion of the fitting function and the bottom curve is the fit to the resonance plus the flux. The data displayed are for one spin state of a single run.

(bottom) Histogram of the 355 $\mathcal{P}$ values obtained from fits to the 90.2eV resonance.

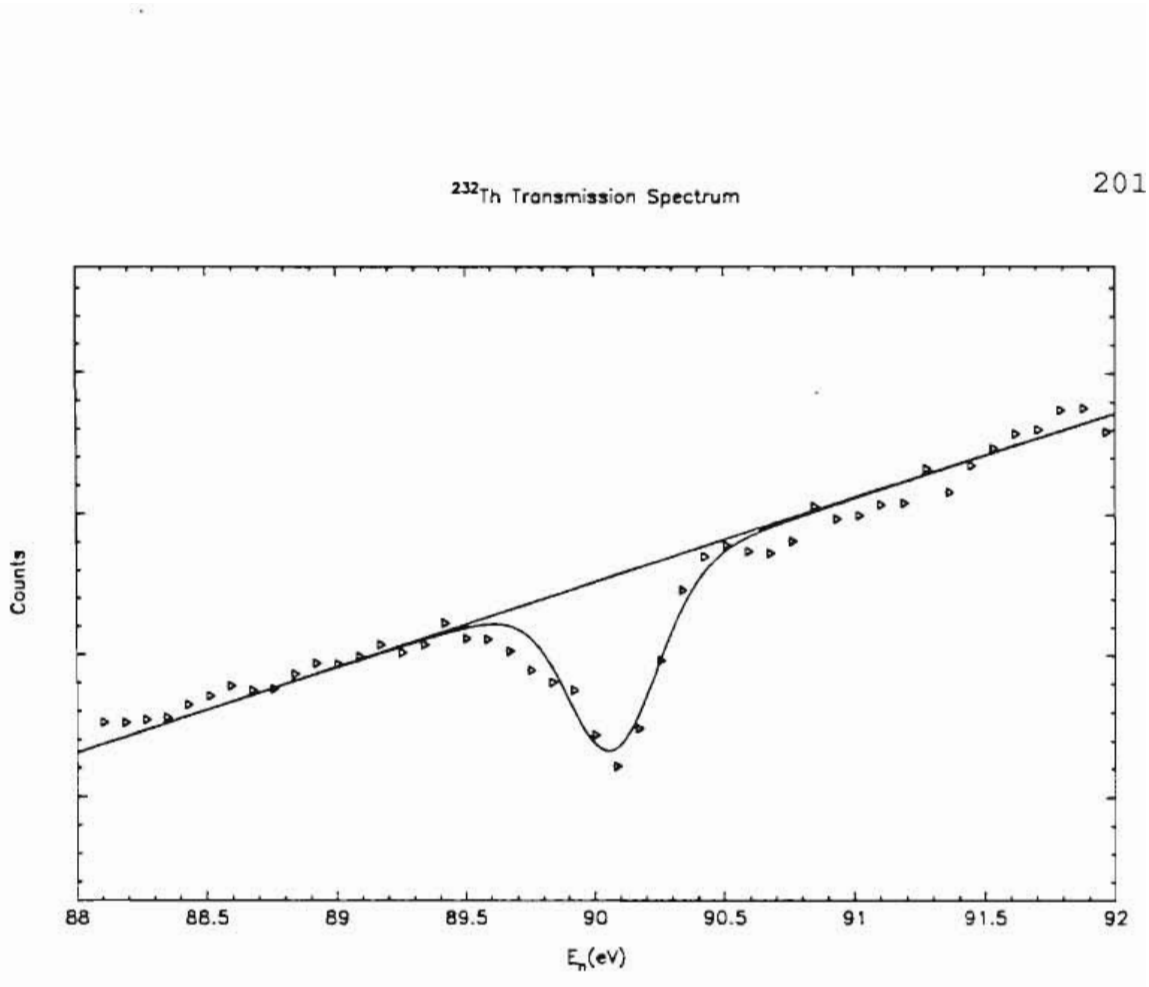
^{232}Th Transmission Spectrum
Counts
88
88.5
89
89.5
90
90.5
91
91.5
92
E_n(eV)

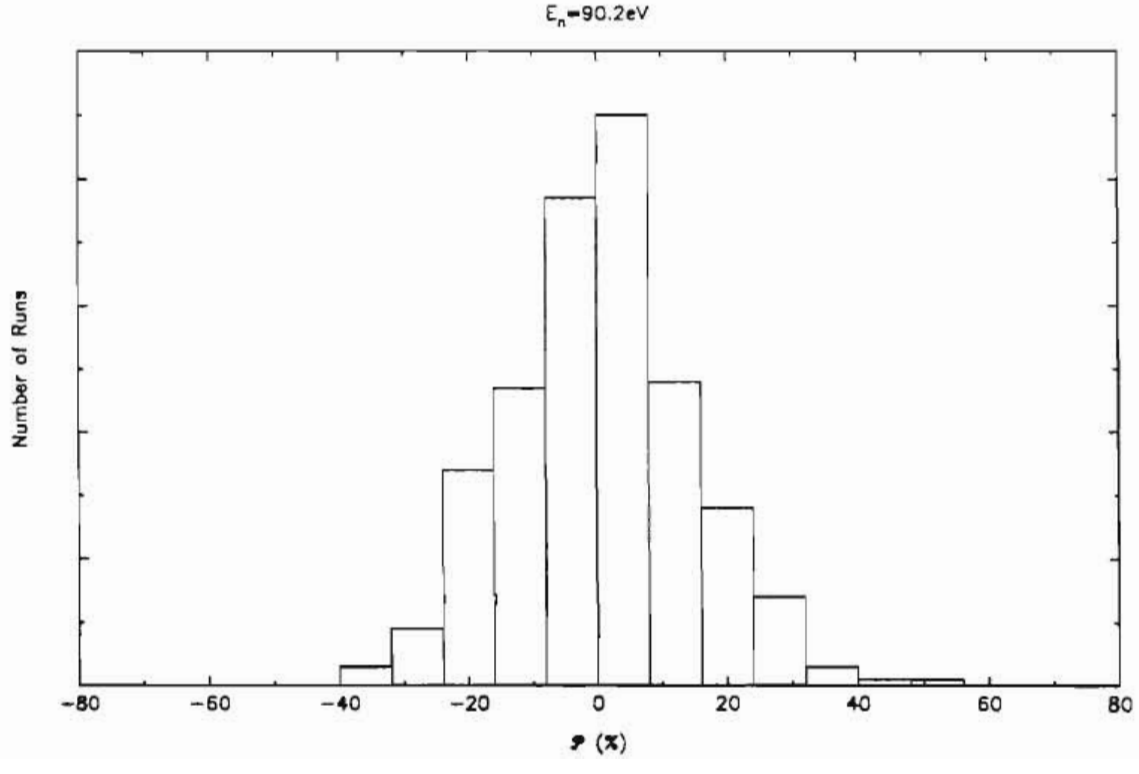
E_n=90.2eV
Number of Runs
-80
-60
-40
-20
0
20
40
60
80
$\mathcal{P}$ (%)

Figure 6.3.2.10

(top) Sample fit to the 98.1eV resonance. The top curve is the flux portion of the fitting function and the bottom curve is the fit to the resonance plus the flux. The data displayed are for one spin state of a single run.

(bottom) Histogram of the 355 $\mathcal{P}$ values obtained from fits to the 98.1eV resonance.

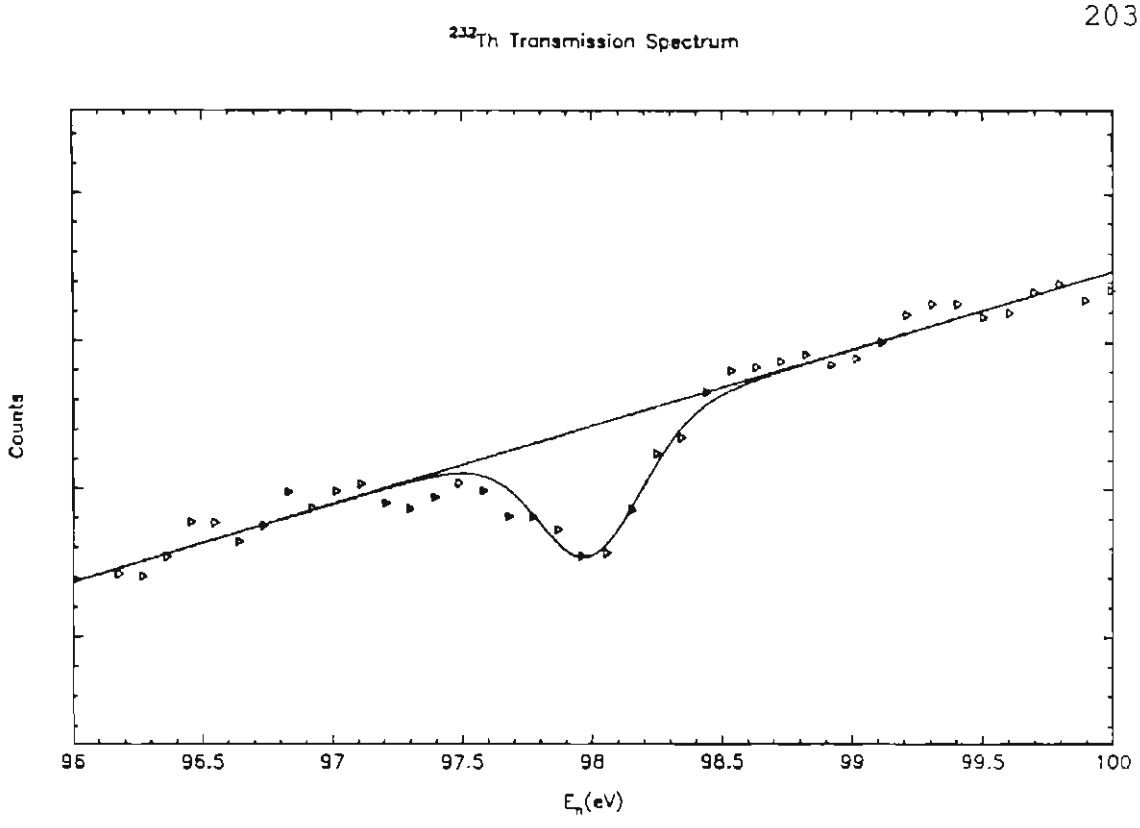
^{232}Th Transmission Spectrum
Counts
96
96.5
97
97.5
98
98.5
99
99.5
100
E_n(eV)

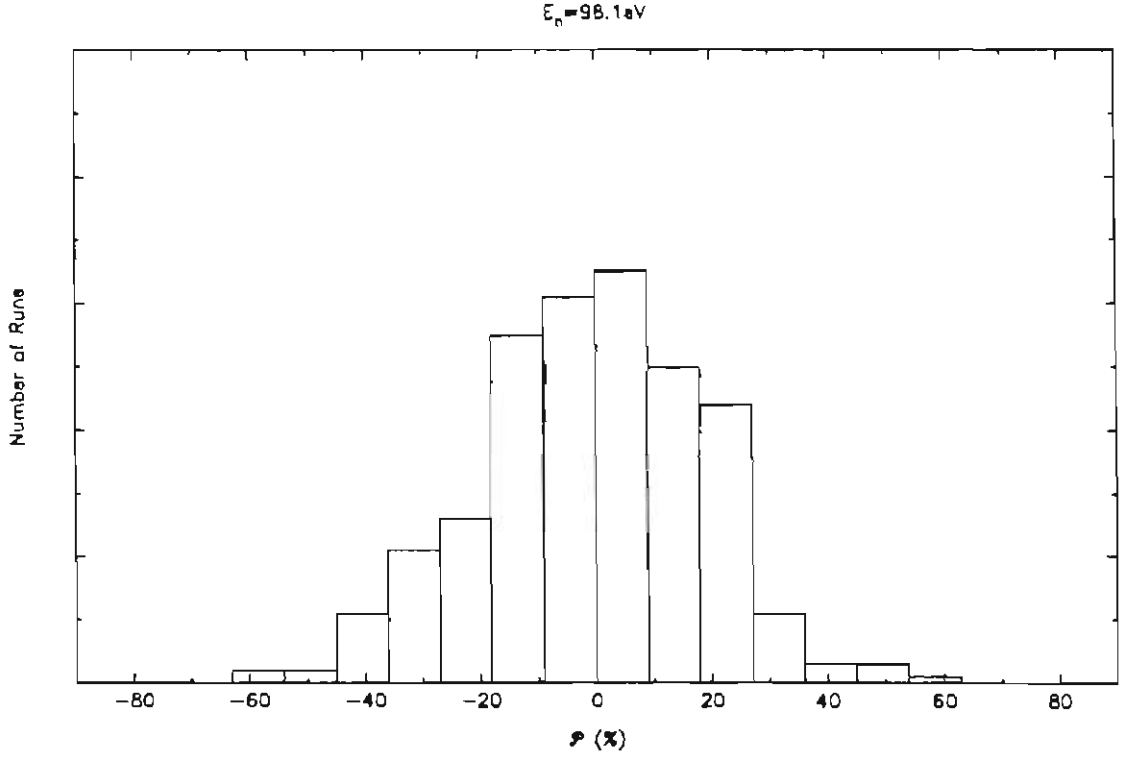
E_n=98.1eV
Number of Runs
−80
−60
−40
−20
0
20
40
60
80
P (%)

Figure 6.3.2.11

(top) Sample fit to the 103.7eV resonance. The top curve is the flux portion of the fitting function and the bottom curve is the fit to the resonance plus the flux. The data displayed are for one spin state of a single run.

(bottom) Histogram of the 355 $\mathcal{P}$ values obtained from fits to the 103.7eV resonance.

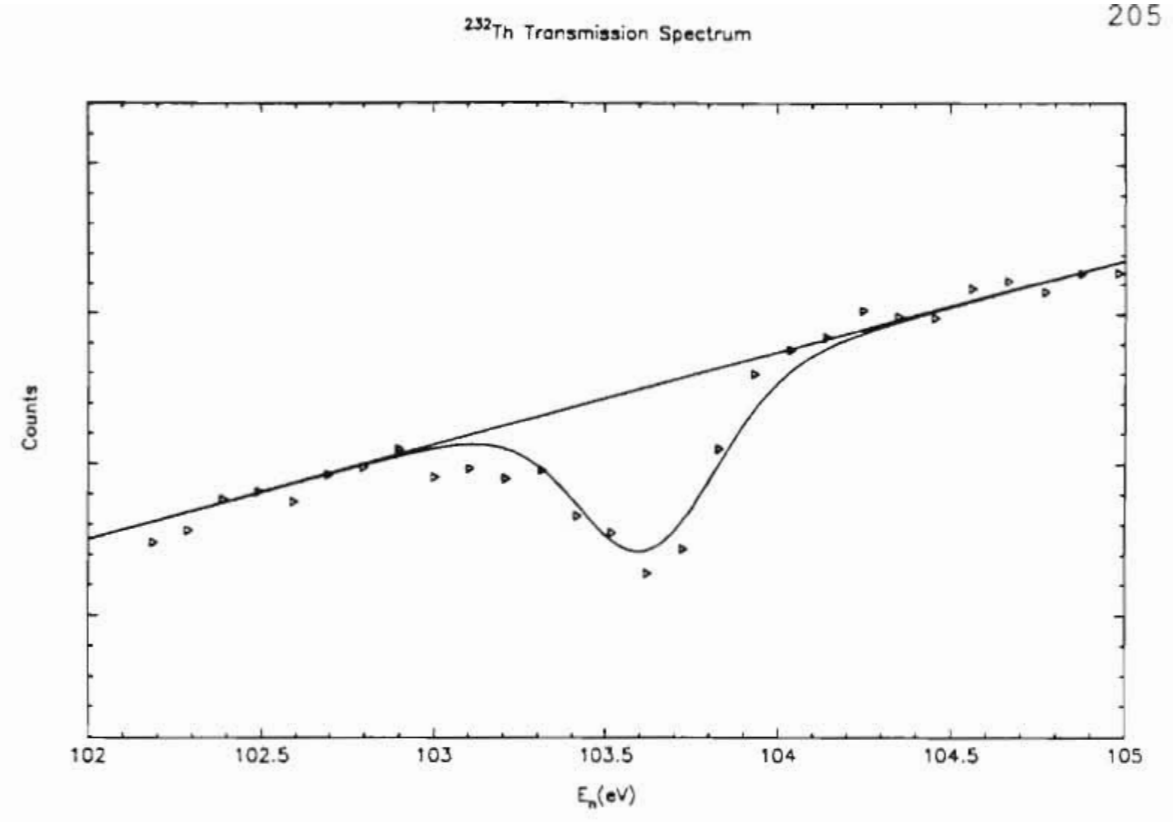
^{232}Th Transmission Spectrum
Counts
102
102.5
103
103.5
104
104.5
105
E_n(eV)

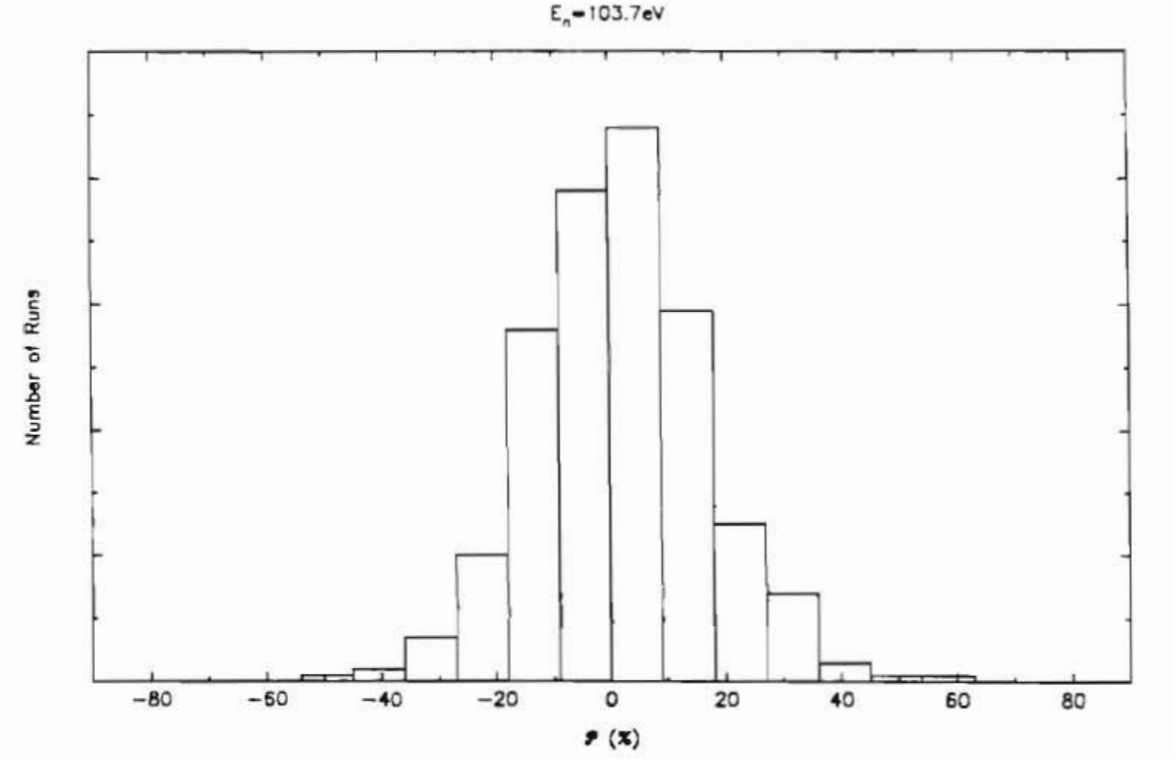
E_n=103.7eV
Number of Runs
−80
−60
−40
−20
0
20
40
60
80
χ (%)

Figure 6.3.2.12

(top) Sample fit to the 128.2eV resonance. The solid line is a fit from code SAMMY. The data displayed are for one spin state of a single run.

(bottom) Histogram of the 355 $\mathcal{P}$ values obtained from fits to the 128.2eV resonance.

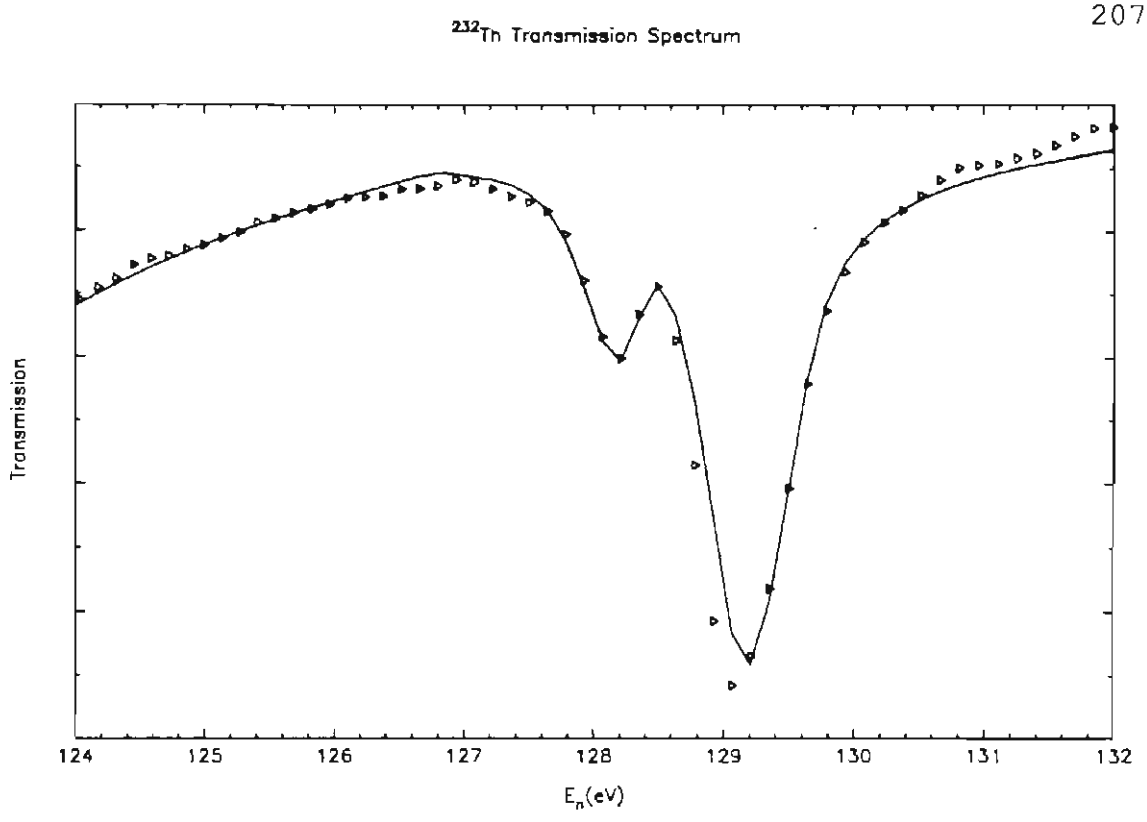
^{232}Th Transmission Spectrum
Transmission
124
125
126
127
128
129
130
131
132
E_n(eV)

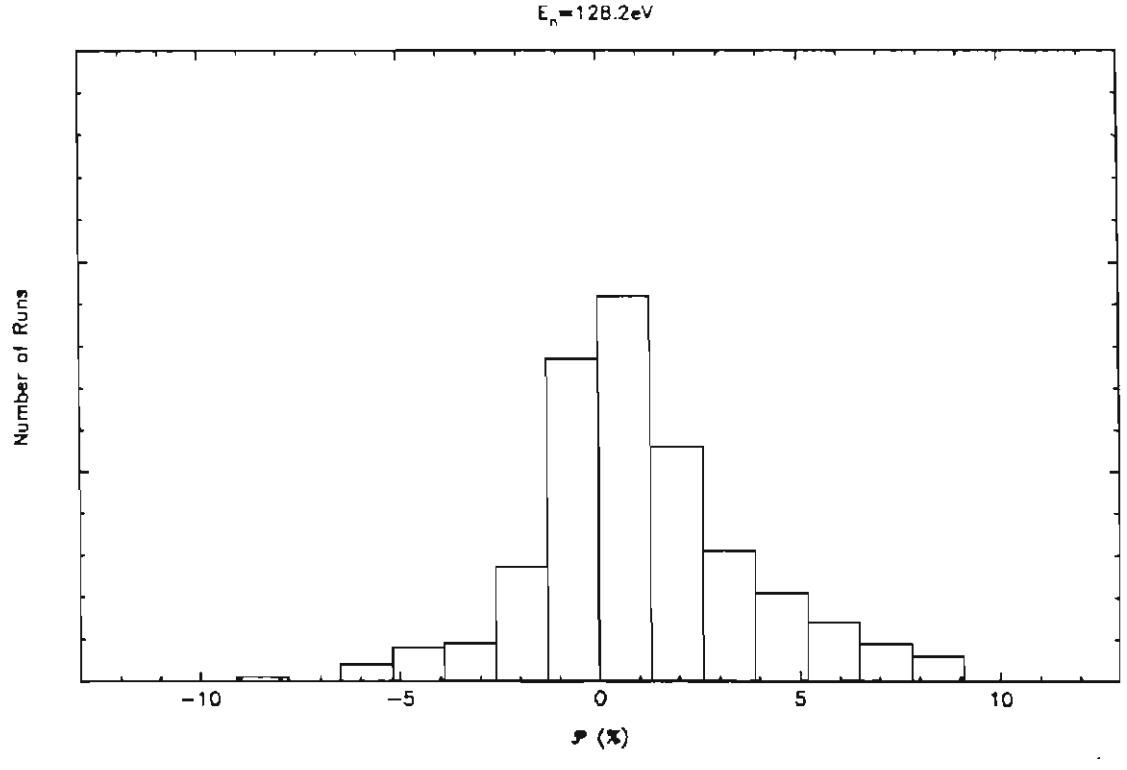
E_n=128.2eV
Number of Runs
−10
−5
0
5
10
P (%)

Figure 6.3.2.13

(top) Sample fit to the 145.9eV resonance. The top curve is the flux portion of the fitting function and the bottom curve is the fit to the resonance plus the flux. The data displayed are for one spin state of a single run.

(bottom) Histogram of the 355 $\mathcal{P}$ values obtained from fits to the 145.9eV resonance.

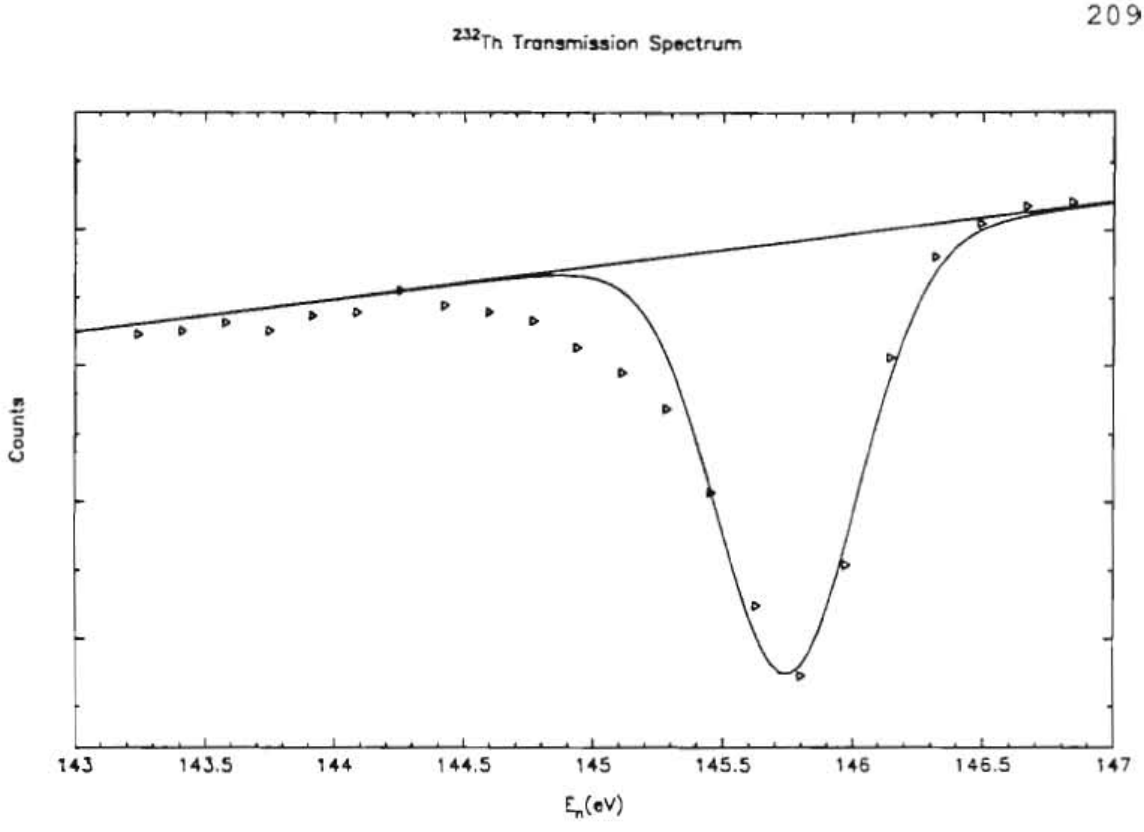
^{232}Th Transmission Spectrum
Counts
143
143.5
144
144.5
145
145.5
146
146.5
147
E_n(eV)

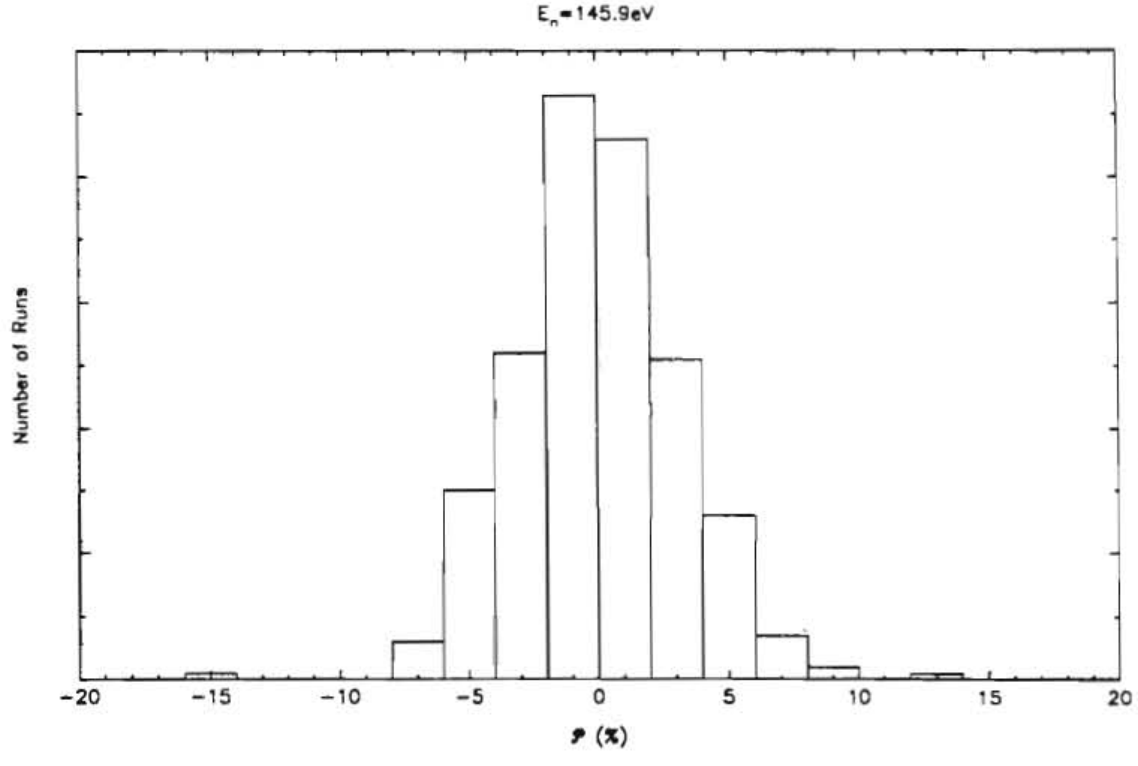
E_n=145.9eV
Number of Runs
−20
−15
−10
−5
0
5
10
15
20
P (%)

Figure 6.3.2.14

(top) Sample fit to the 148.1eV resonance. The top curve is the flux portion of the fitting function and the bottom curve is the fit to the resonance plus the flux. The data displayed are for one spin state of a single run.

(bottom) Histogram of the 355 $\mathcal{P}$ values obtained from fits to the 148.1eV resonance.

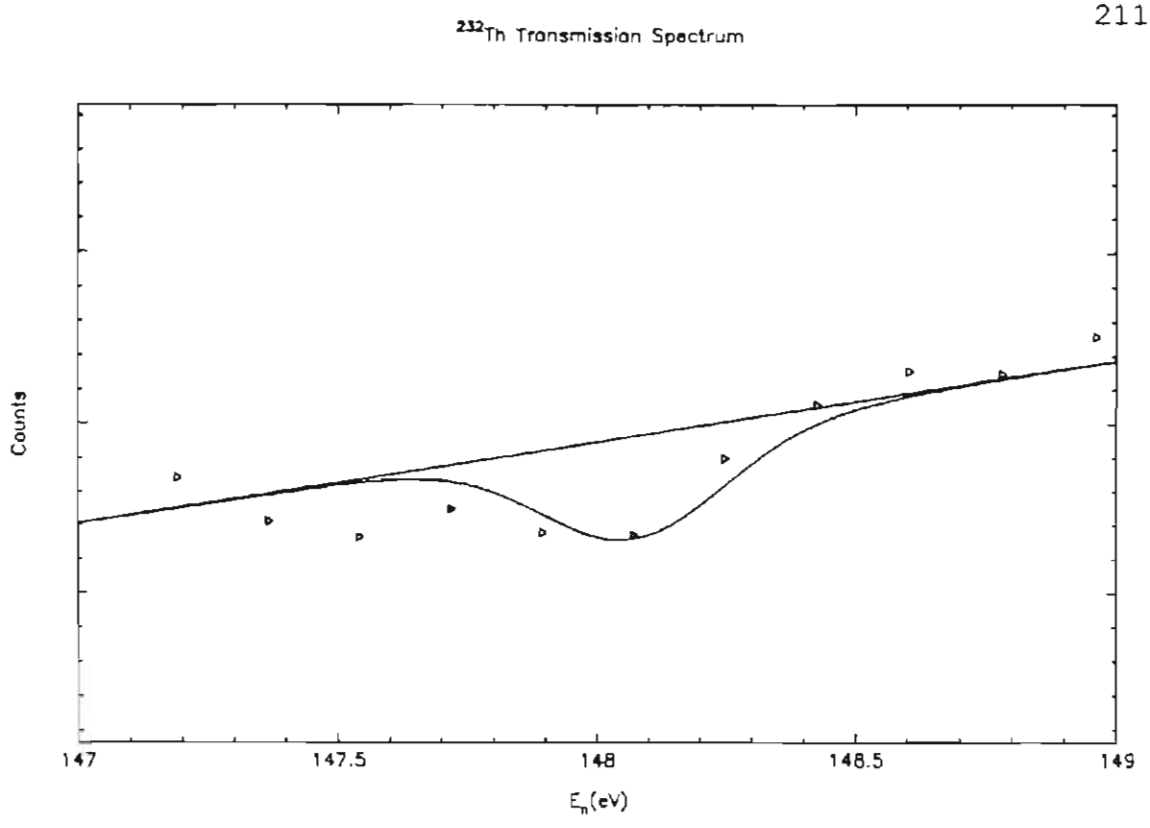
^{232}Th Transmission Spectrum
Counts
147
147.5
148
148.5
149
E_n(eV)

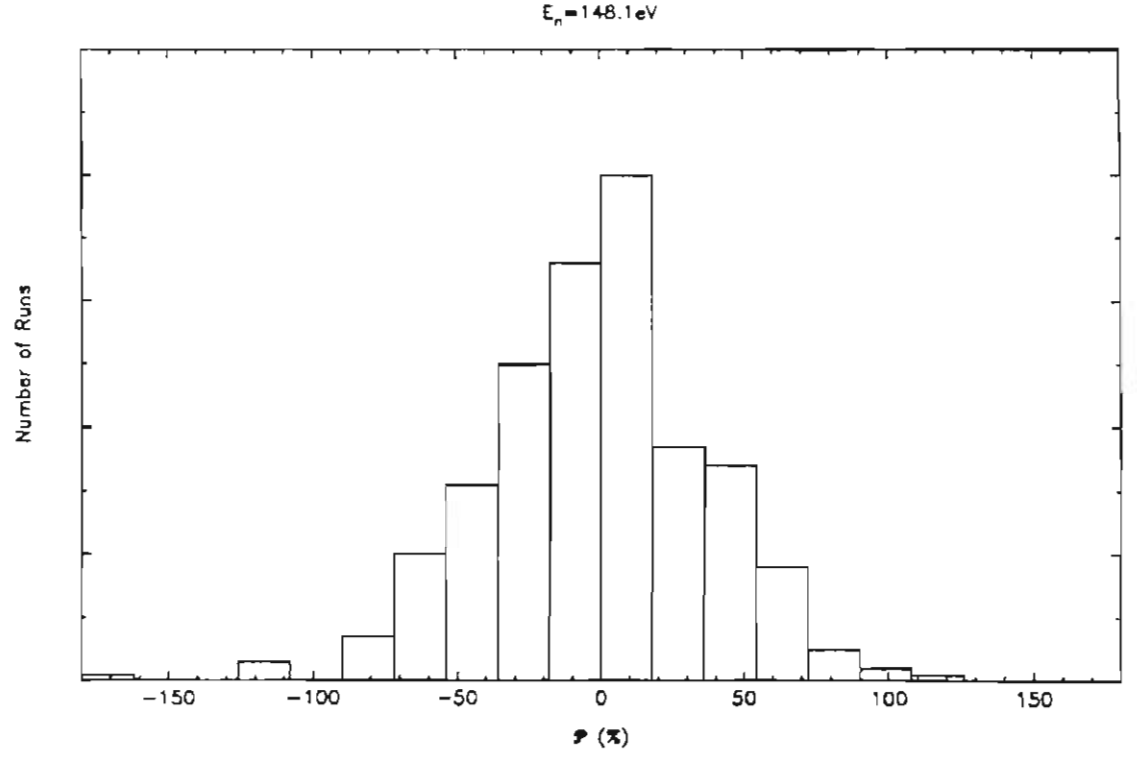
E_n=148.1eV
Number of Runs
−150
−100
−50
0
50
100
150
P (%)

Figure 6.3.2.15

(top) Sample fit to the 167.2eV resonance. The top curve is the flux portion of the fitting function and the bottom curve is the fit to the resonance plus the flux. The data displayed are for one spin state of a single run.

(bottom) Histogram of the 355 $\mathcal{P}$ values obtained from fits to the 167.2eV resonance.

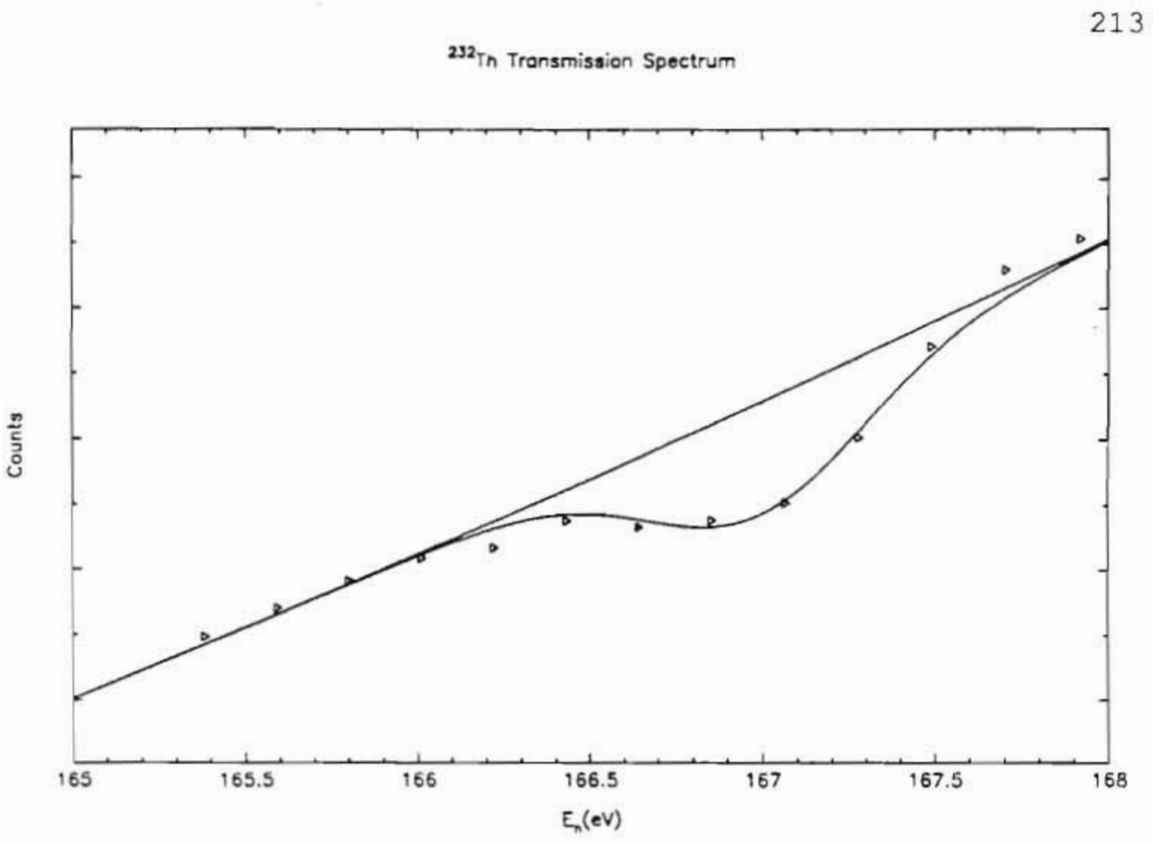
^{232}Th Transmission Spectrum
Counts
165
165.5
166
166.5
167
167.5
168
E_n(eV)

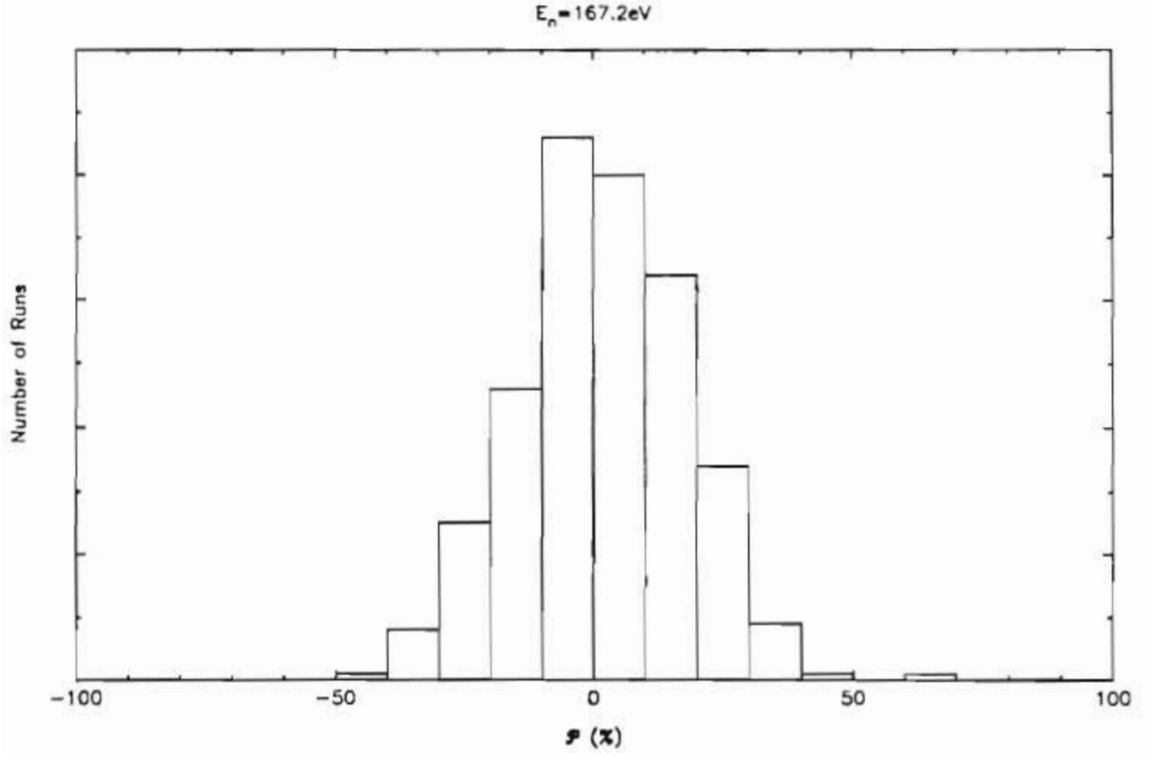
E_n=167.2eV
Number of Runs
−100
−50
0
50
100
P (%)

Figure 6.3.2.16

(top) Sample fit to the 179.0eV resonance. The top curve is the flux portion of the fitting function and the bottom curve is the fit to the resonance plus the flux. The data displayed are for one spin state of a single run.

(bottom) Histogram of the 355 $\mathcal{P}$ values obtained from fits to the 179.0eV resonance.

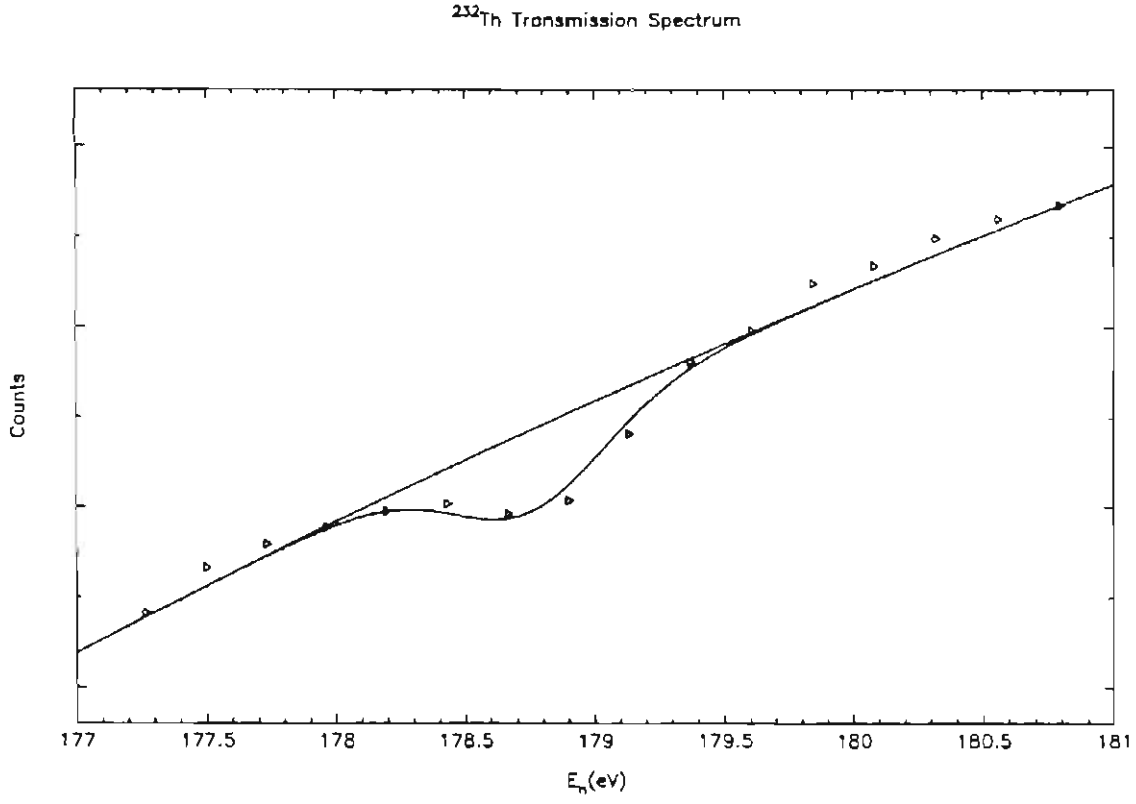
^{232}Th Transmission Spectrum
Counts
177
177.5
178
178.5
179
179.5
180
180.5
181
E_n(eV)

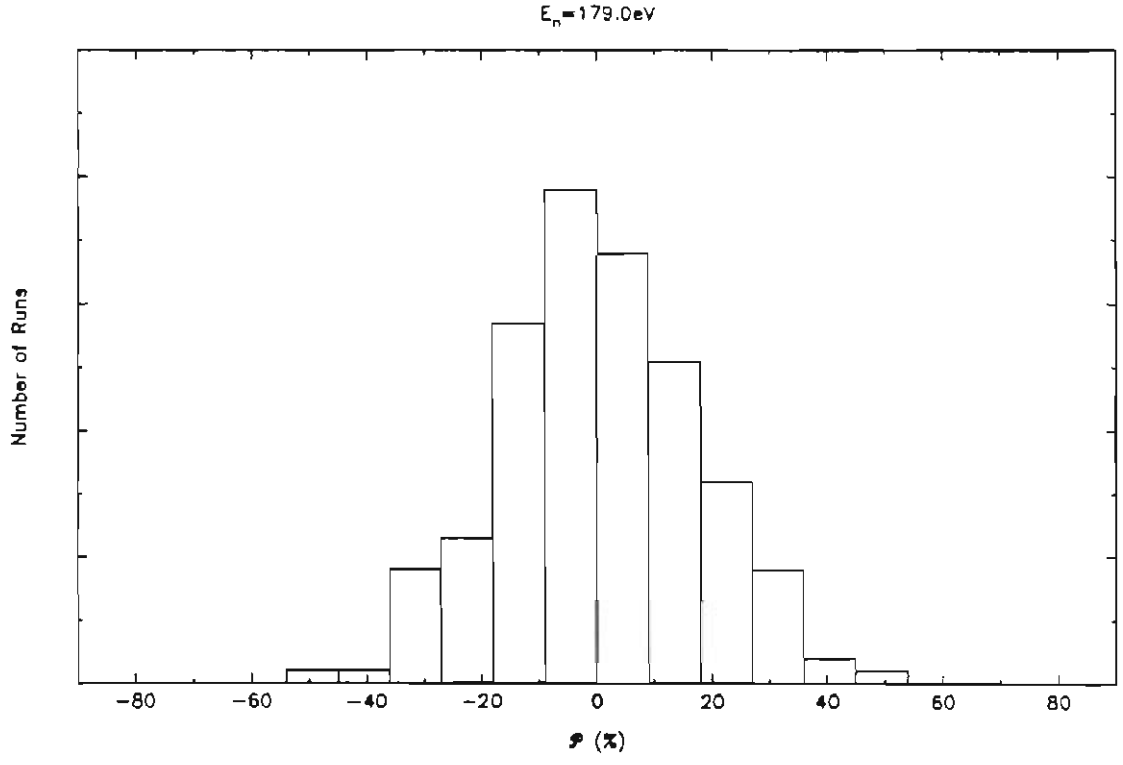
E_n=179.0eV
Number of Runs
−80
−60
−40
−20
0
20
40
60
80
℘ (%)

Figure 6.3.2.17

(top) Sample fit to the 196.2eV resonance. The top curve is the flux portion of the fitting function and the bottom curve is the fit to the resonance plus the flux. The data displayed are for one spin state of a single run.

(bottom) Histogram of the 355 $\mathcal{P}$ values obtained from fits to the 196.2eV resonance.

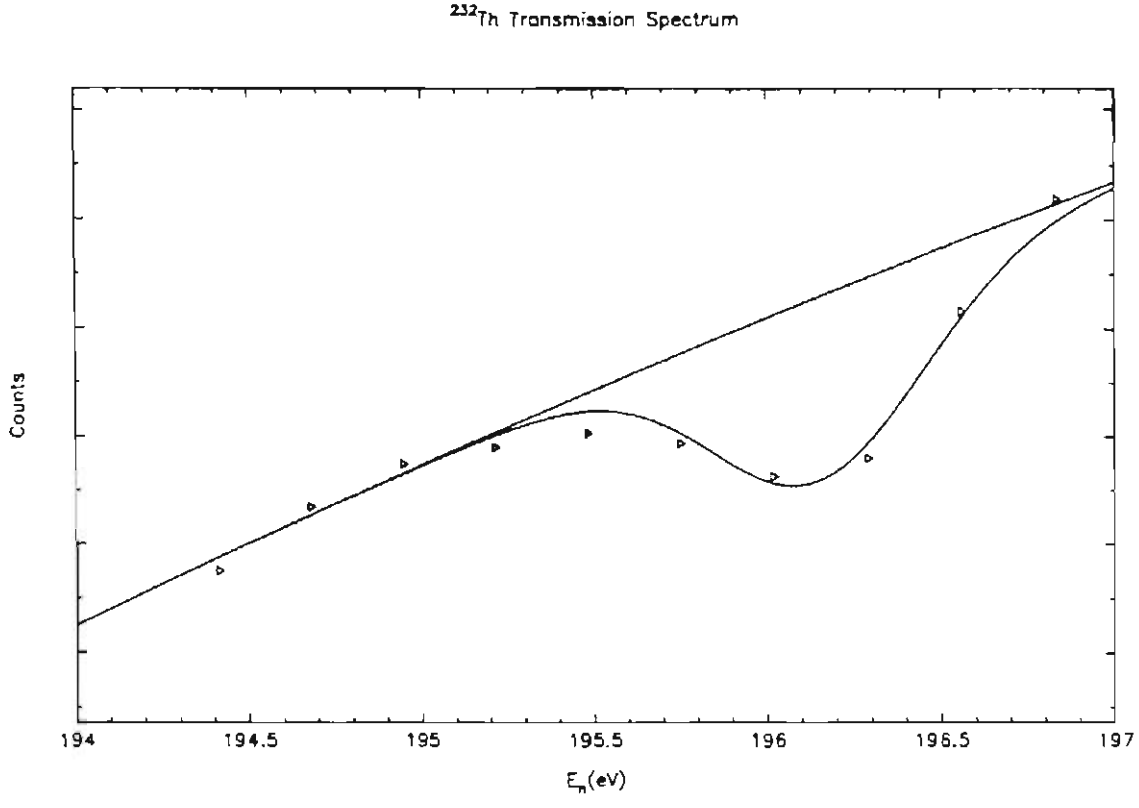
^{232}Th Transmission Spectrum
Counts
194
194.5
195
195.5
196
196.5
197
E_n(eV)

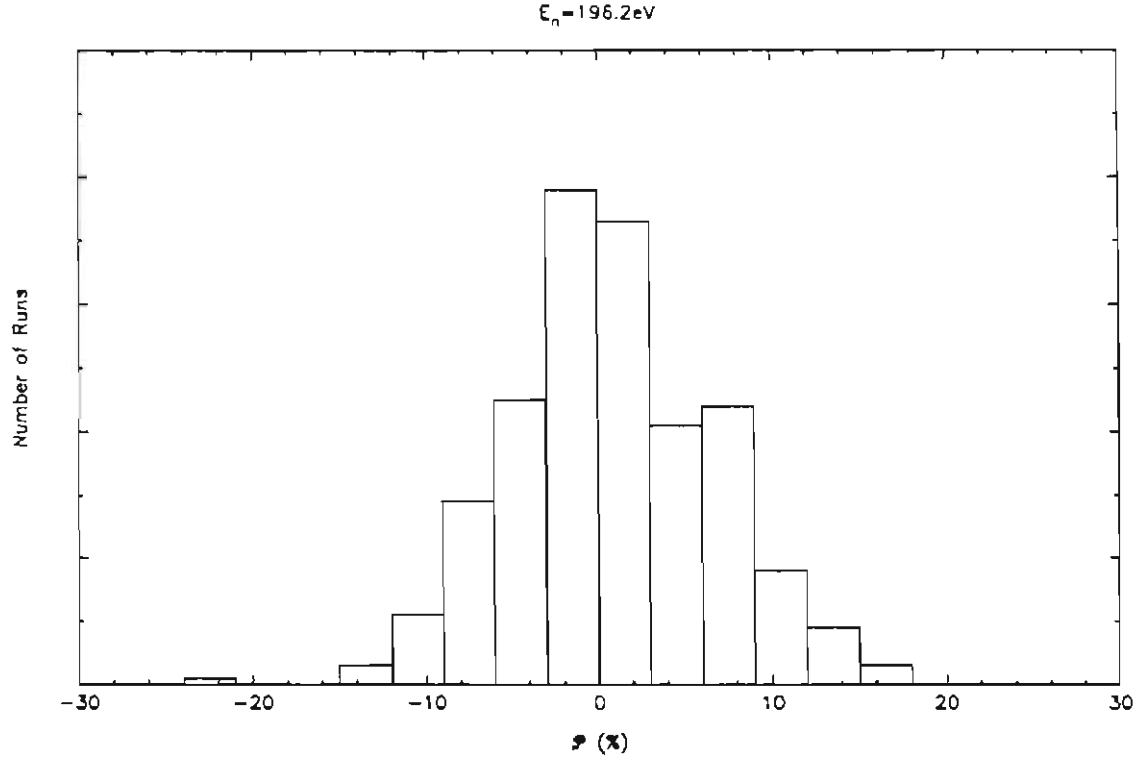
E_n=196.2eV
Number of Runs
−30
−20
−10
0
10
20
30
ρ (%)

Figure 6.3.2.18

(top) Sample fit to the 202.7eV resonance. The top curve is the flux portion of the fitting function and the bottom curve is the fit to the resonance plus the flux. The data displayed are for one spin state of a single run.

(bottom) Histogram of the 355 $\mathcal{P}$ values obtained from fits to the 202.7eV resonance.

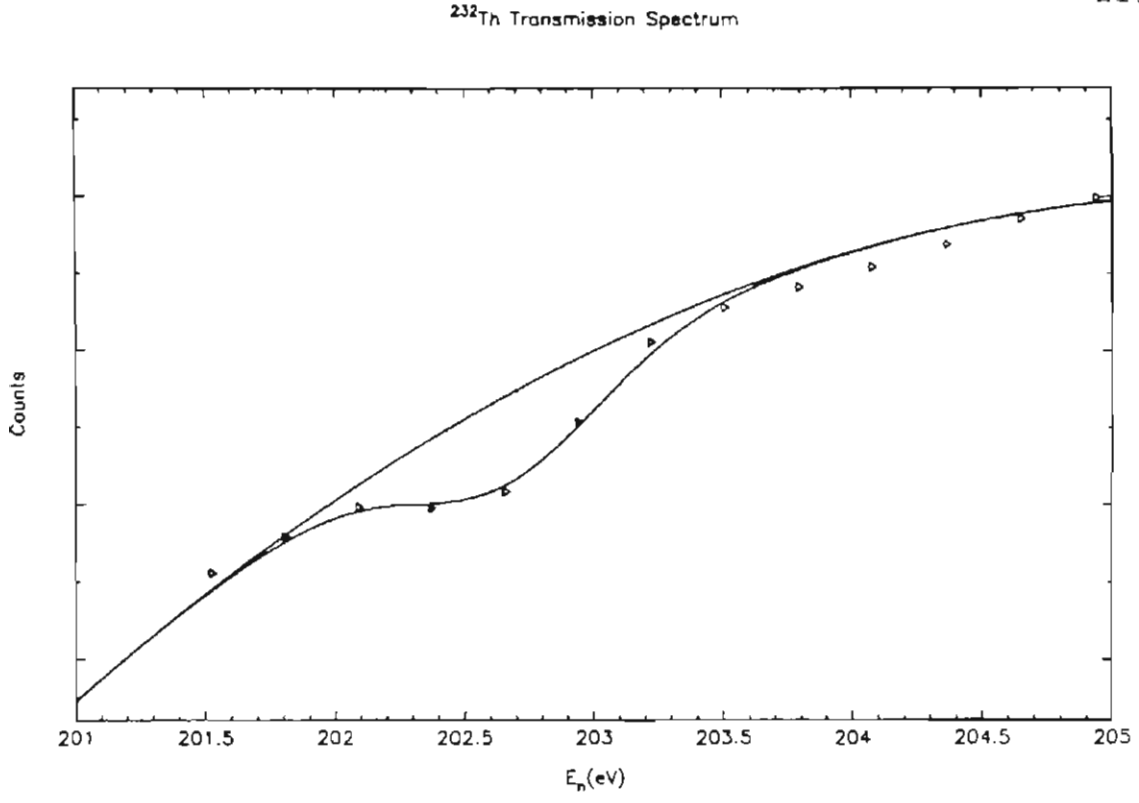
^{232}Th Transmission Spectrum
Counts
201
201.5
202
202.5
203
203.5
204
204.5
205
E_n(eV)

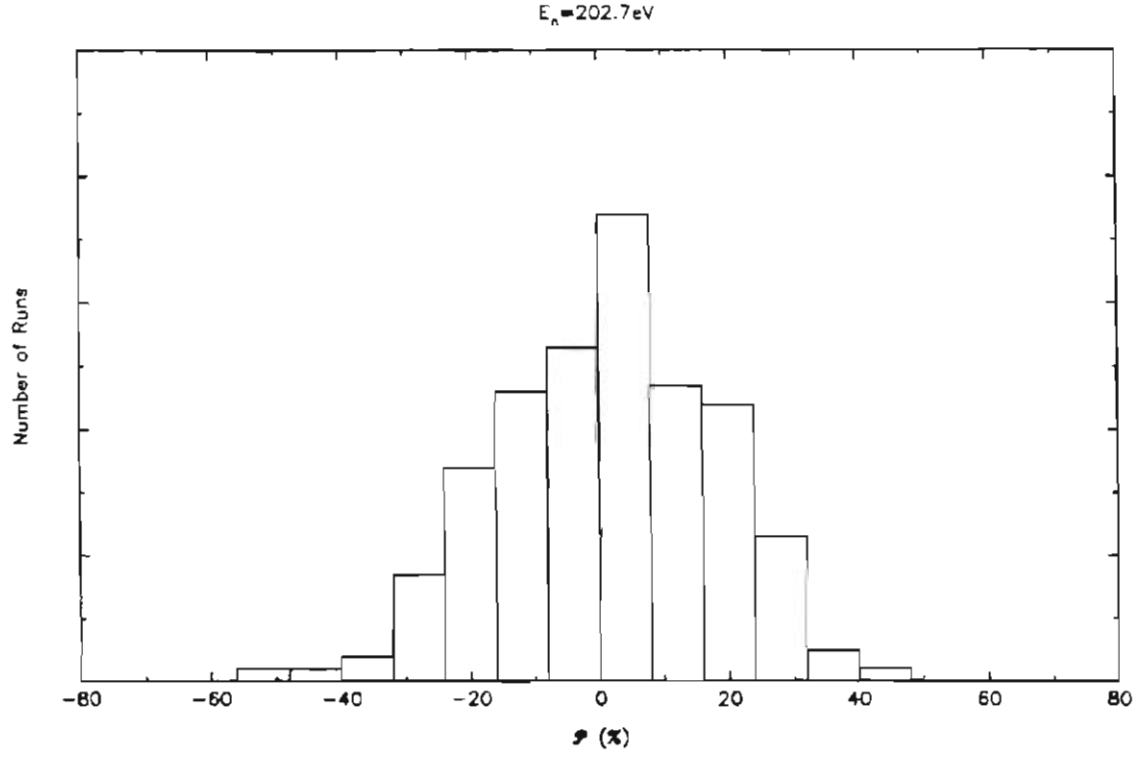
E_n=202.7eV
Number of Runs
-80
-60
-40
-20
0
20
40
60
80
ρ (%)

Figure 6.3.2.19

(top) Sample fit to the 211.0eV resonance. The top curve is the flux portion of the fitting function and the bottom curve is the fit to the resonance plus the flux. The data displayed are for one spin state of a single run.

(bottom) Histogram of the 355 $\mathcal{P}$ values obtained from fits to the 211.0eV resonance.

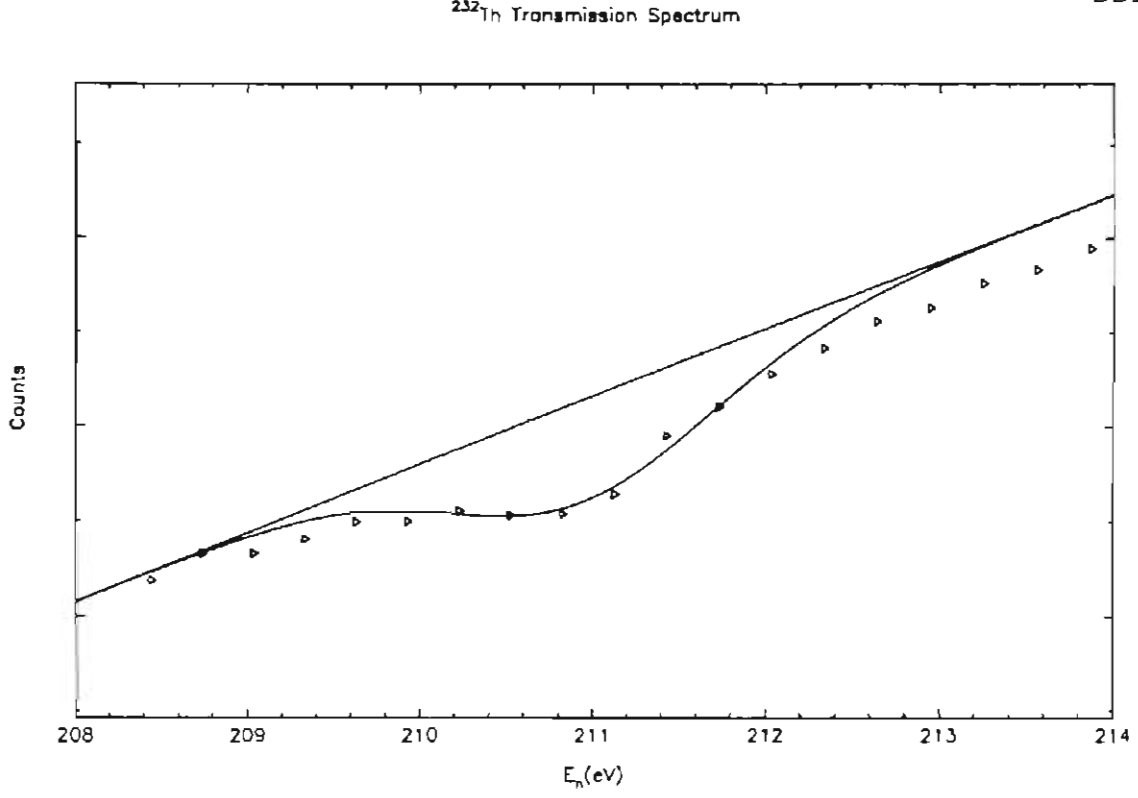
^{232}Th Transmission Spectrum
Counts
208
209
210
211
212
213
214
E_n(eV)

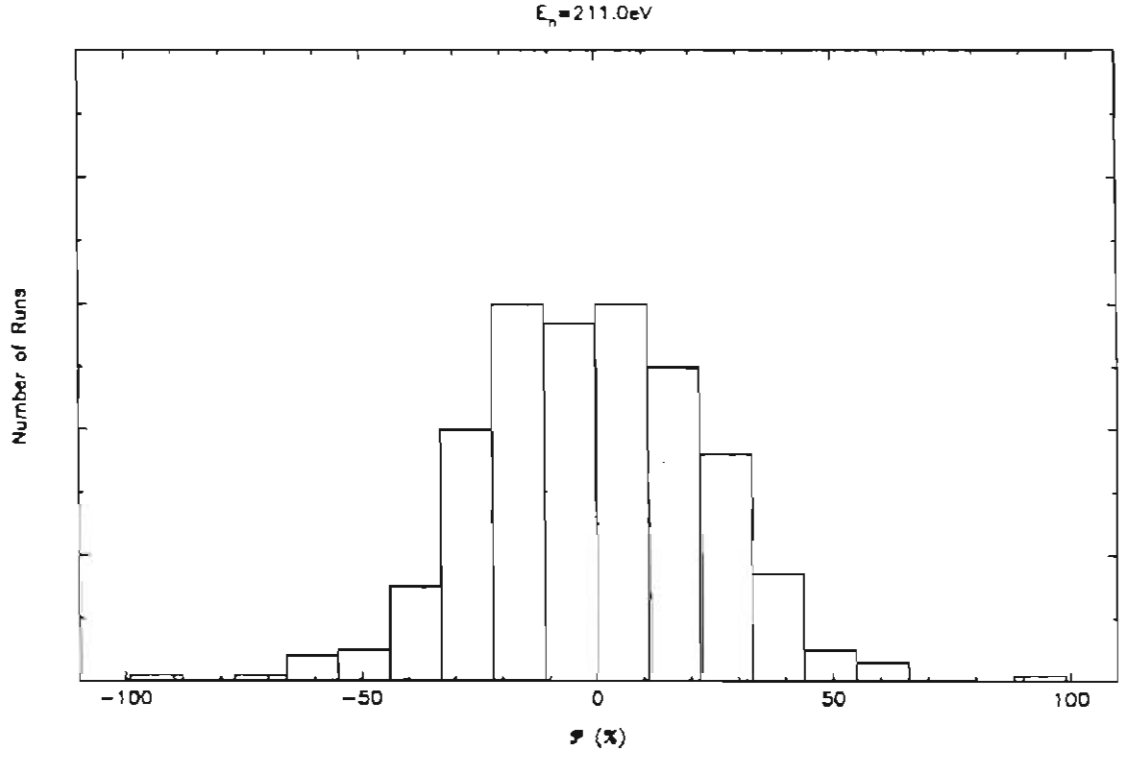
E_n=211.0eV
Number of Runs
−100
−50
0
50
100
ρ (%)

Figure 6.3.2.20

(top) Sample fit to the 242.3eV resonance. The top curve is the flux portion of the fitting function and the bottom curve is the fit to the resonance plus the flux. The data displayed are for one spin state of a single run.

(bottom) Histogram of the 355 $\mathcal{P}$ values obtained from fits to the 242.3eV resonance.

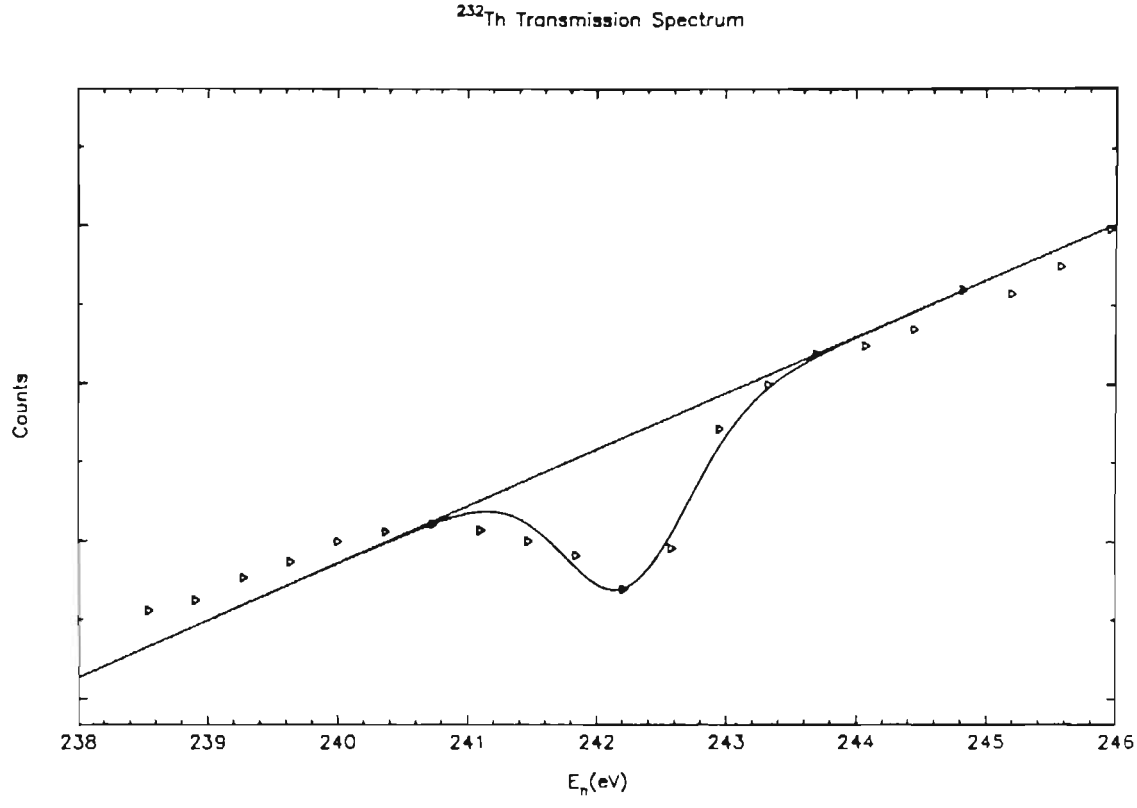
^{232}Th Transmission Spectrum
Counts
238
239
240
241
242
243
244
245
246
E_n(eV)

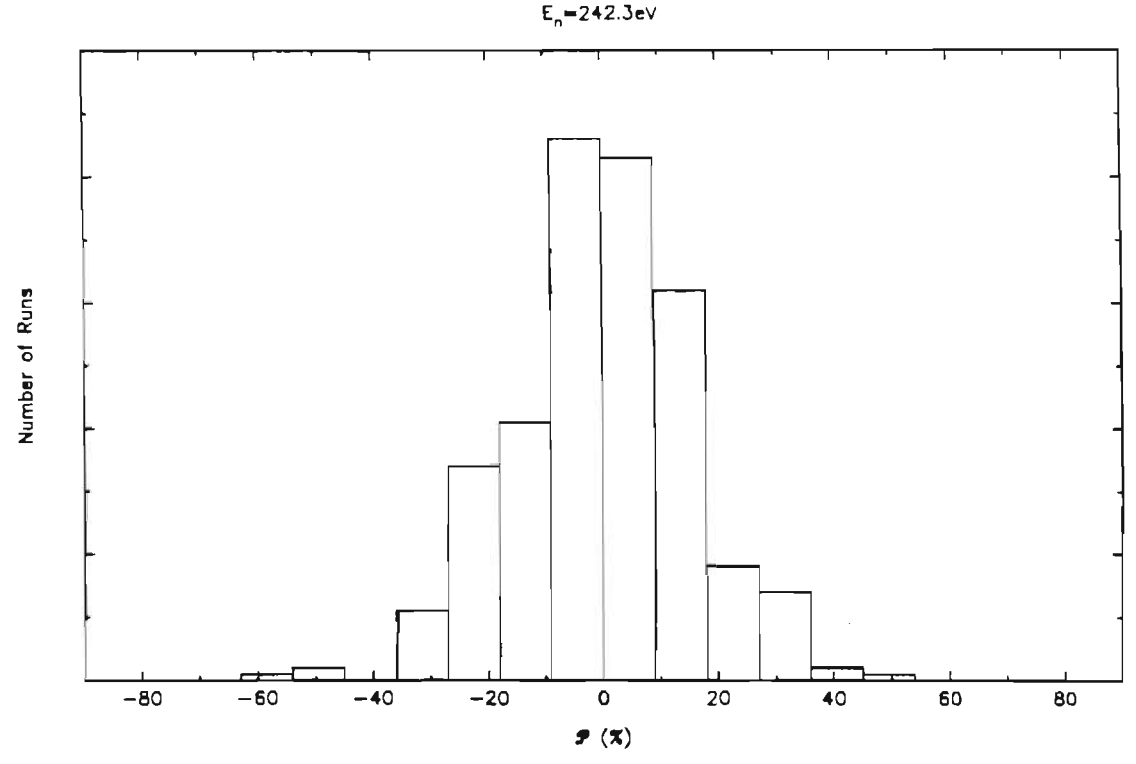
E_n=242.3eV
Number of Runs
−80
−60
−40
−20
0
20
40
60
80
P (%)

Figure 6.3.2.21

(top) Sample fit to the 299.8eV resonance. The top curve is the flux portion of the fitting function and the bottom curve is the fit to the resonance plus the flux. The data displayed are for one spin state of a single run.

(bottom) Histogram of the 355 $\mathcal{P}$ values obtained from fits to the 299.8eV resonance.

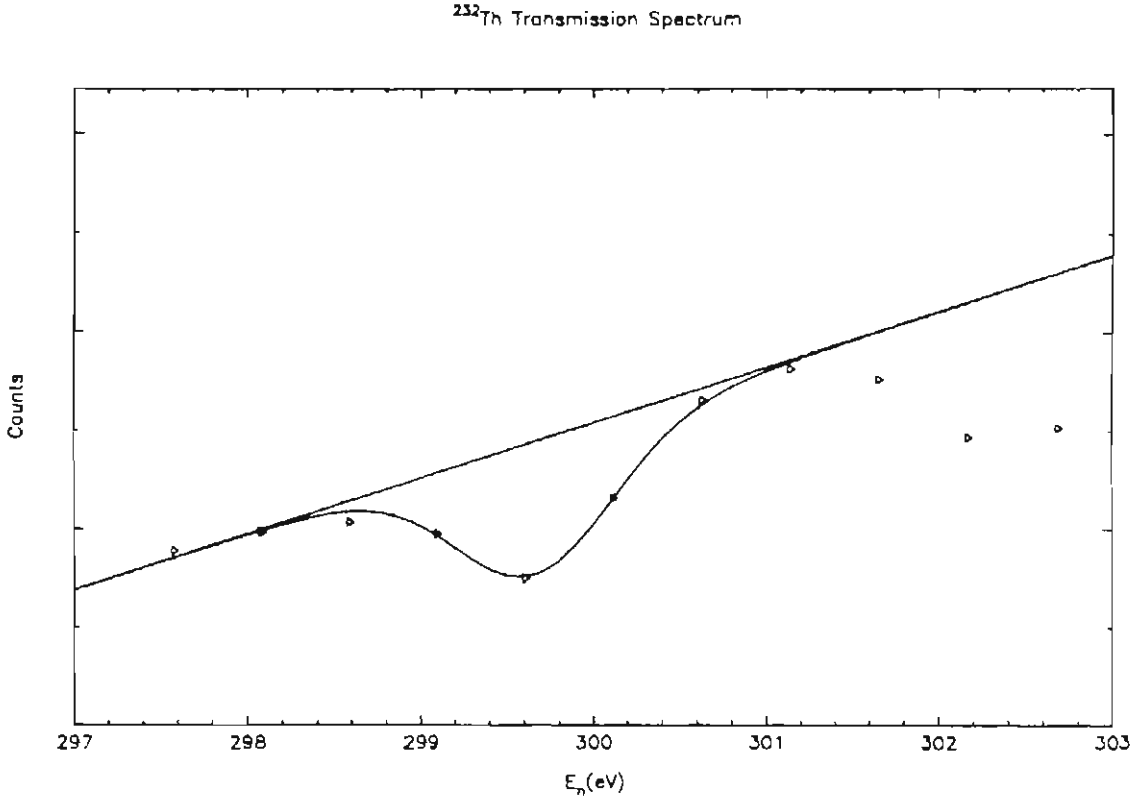
^{232}Th Transmission Spectrum
Counts
297
298
299
300
301
302
303
E_n(eV)

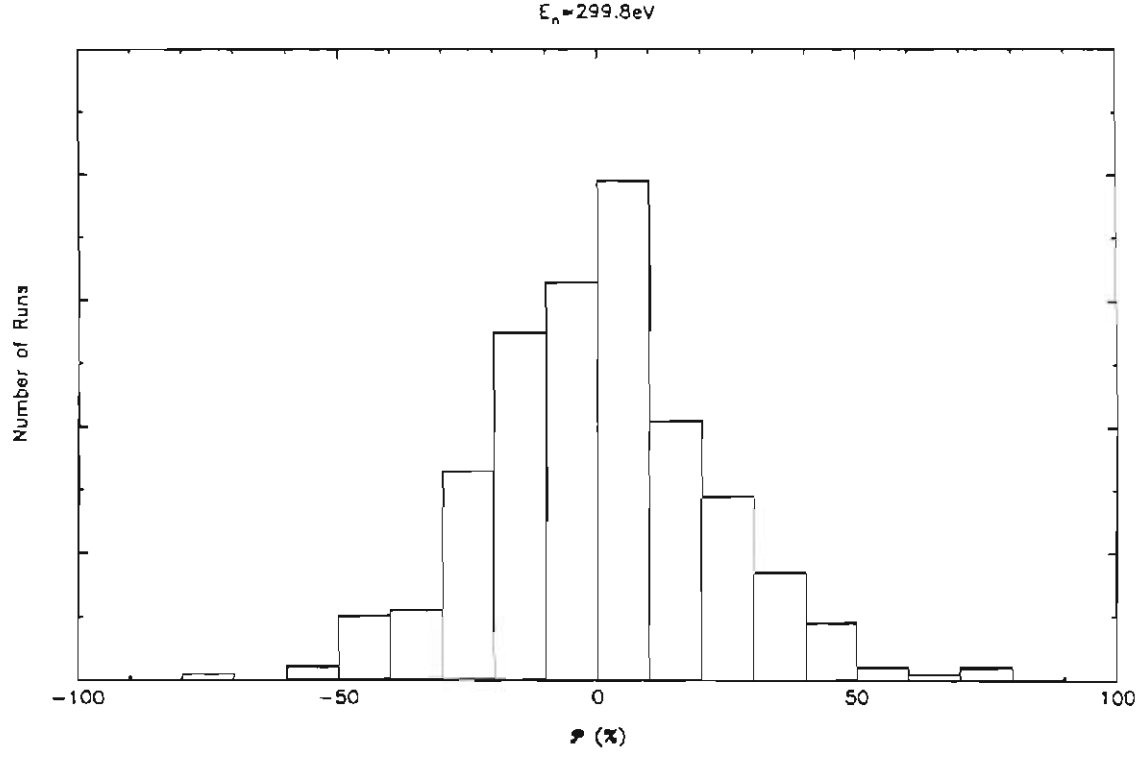
E_n=299.8eV
Number of Runs
−100
−50
0
50
100
ρ (%)

Figure 6.3.2.22

(top) Sample fit to the 302.7eV resonance. The top curve is the flux portion of the fitting function and the bottom curve is the fit to the resonance plus the flux. The data displayed are for one spin state of a single run.

(bottom) Histogram of the 355 $\mathcal{P}$ values obtained from fits to the 302.7eV resonance.

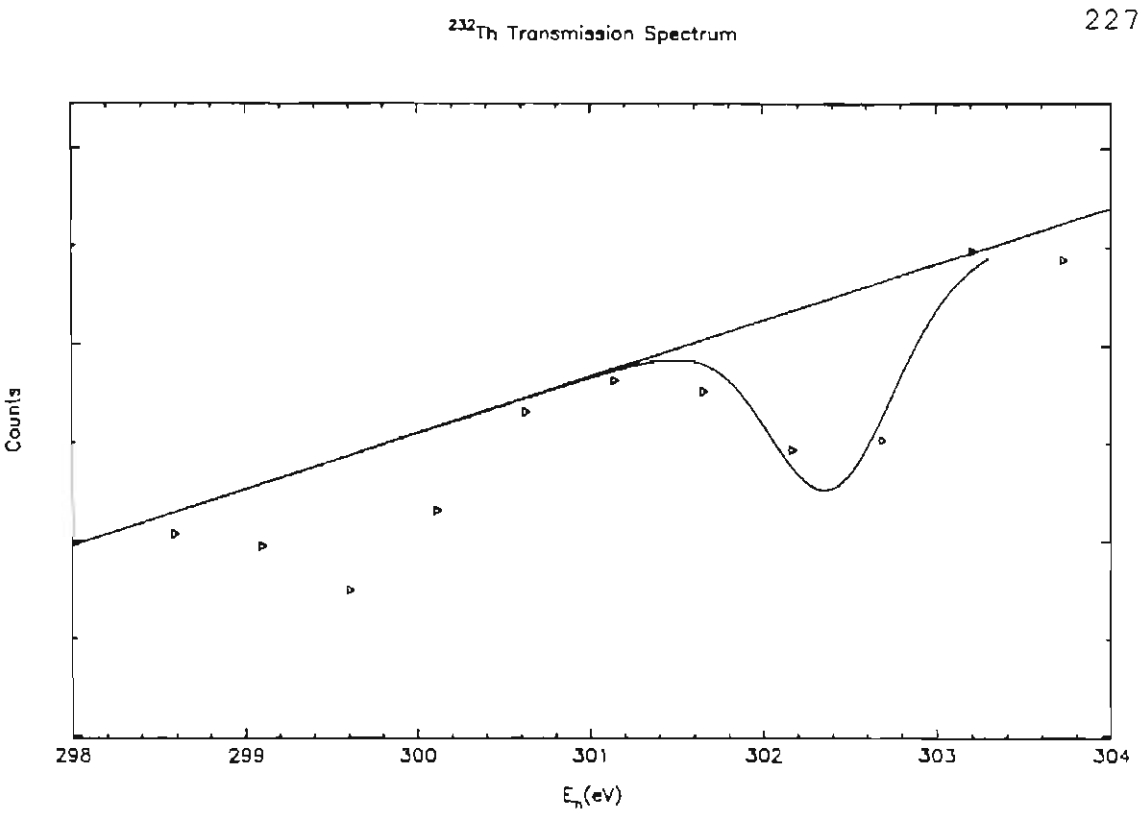
^{232}Th Transmission Spectrum
Counts
298
299
300
301
302
303
304
E_n(eV)

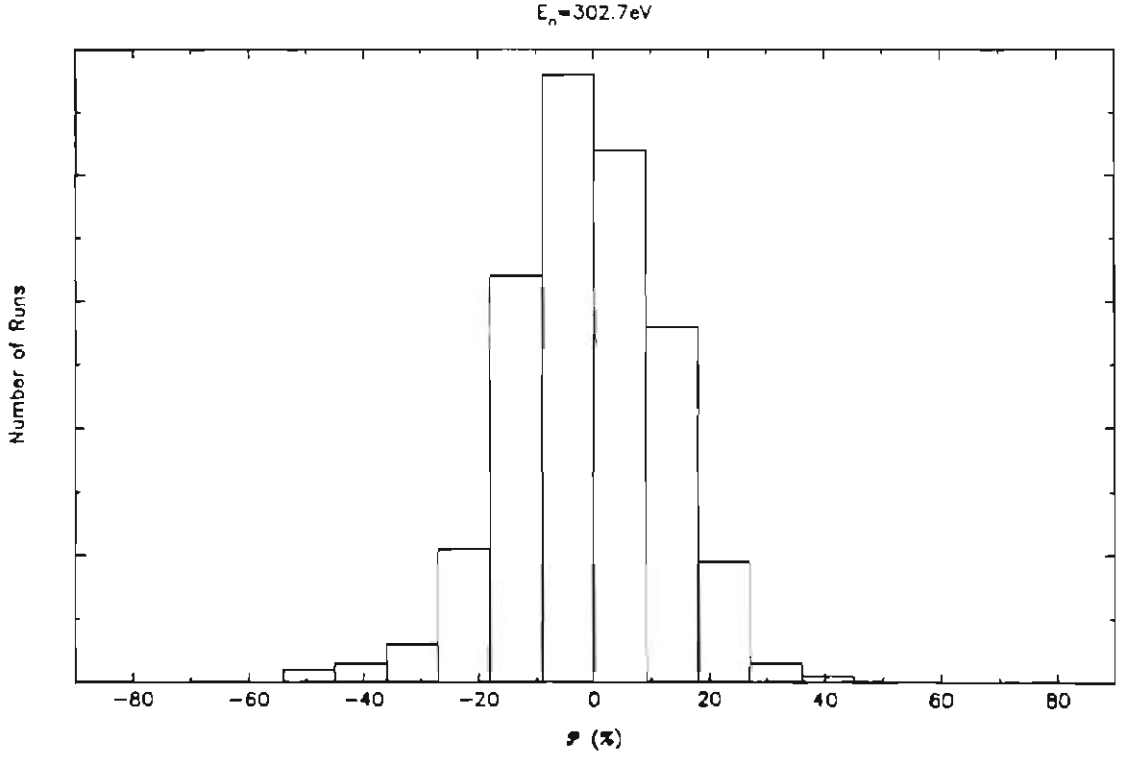
E_n=302.7eV
Number of Runs
−80
−60
−40
−20
0
20
40
60
80
ρ (%)

Figure 6.3.2.23

(top) Sample fit to the 380.7eV resonance. The top curve is the flux portion of the fitting function and the bottom curve is the fit to the resonance plus the flux. The data displayed are for one spin state of a single run.

(bottom) Histogram of the 355 $\mathcal{P}$ values obtained from fits to the 380.7eV resonance.

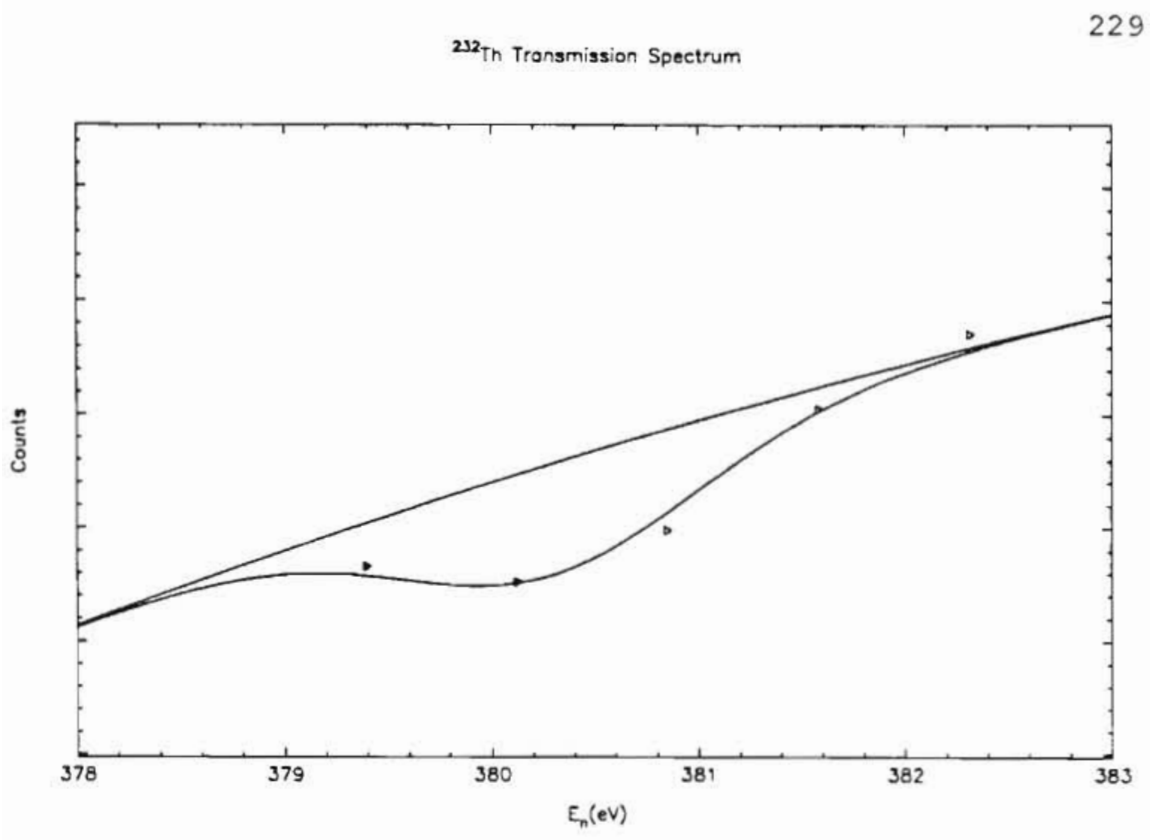
^{232}Th Transmission Spectrum
Counts
378
379
380
381
382
383
E_n(eV)

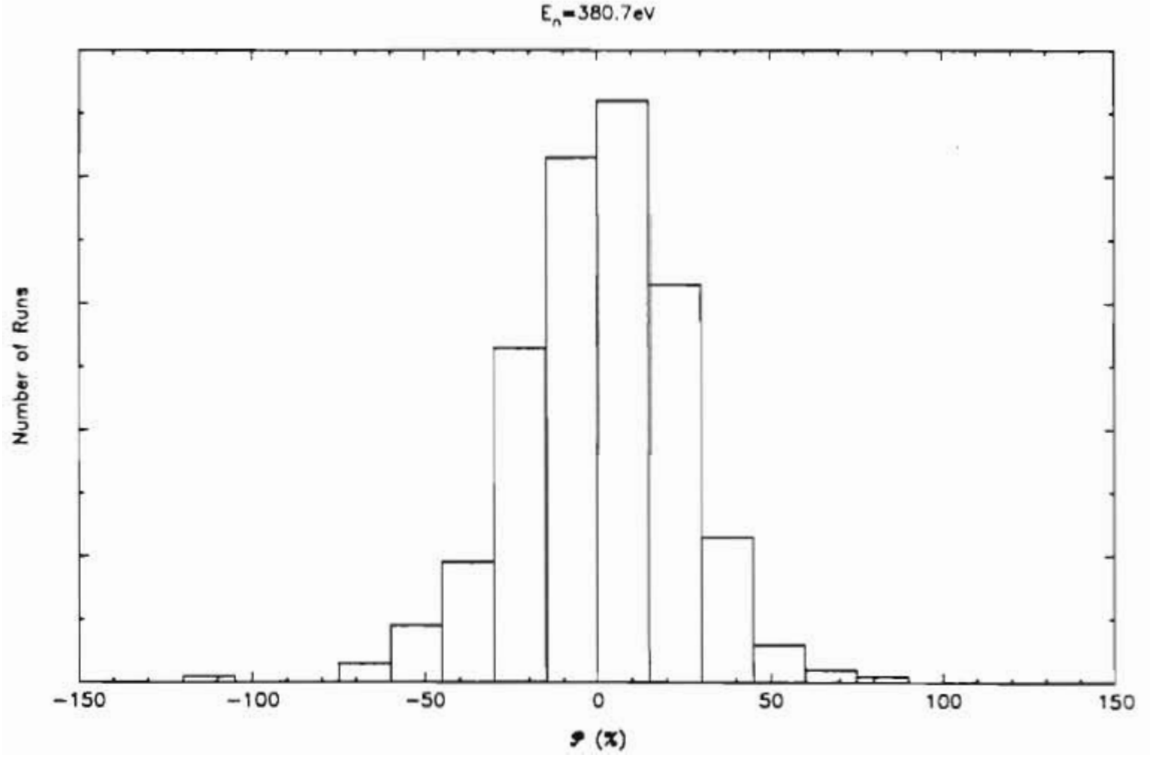
E_n=380.7eV
Number of Runs
−150
−100
−50
0
50
100
150
$\mathcal{P}$ (%)

Figure 6.3.2.24

(top) Sample fit to the 391.8eV resonance. The top curve is the flux portion of the fitting function and the bottom curve is the fit to the resonance plus the flux. The data displayed are for one spin state of a single run.

(bottom) Histogram of the 355 $\mathcal{P}$ values obtained from fits to the 391.8eV resonance.

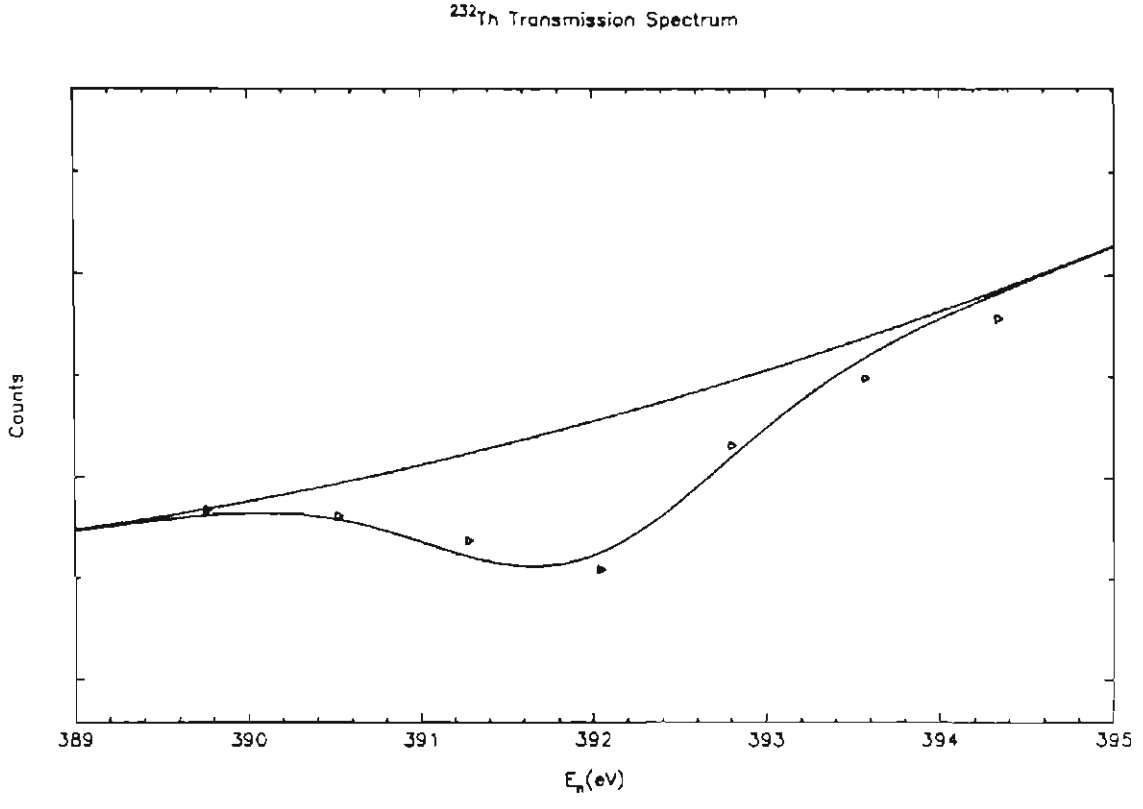
^{232}Th Transmission Spectrum
Counts
389
390
391
392
393
394
395
E_n(eV)

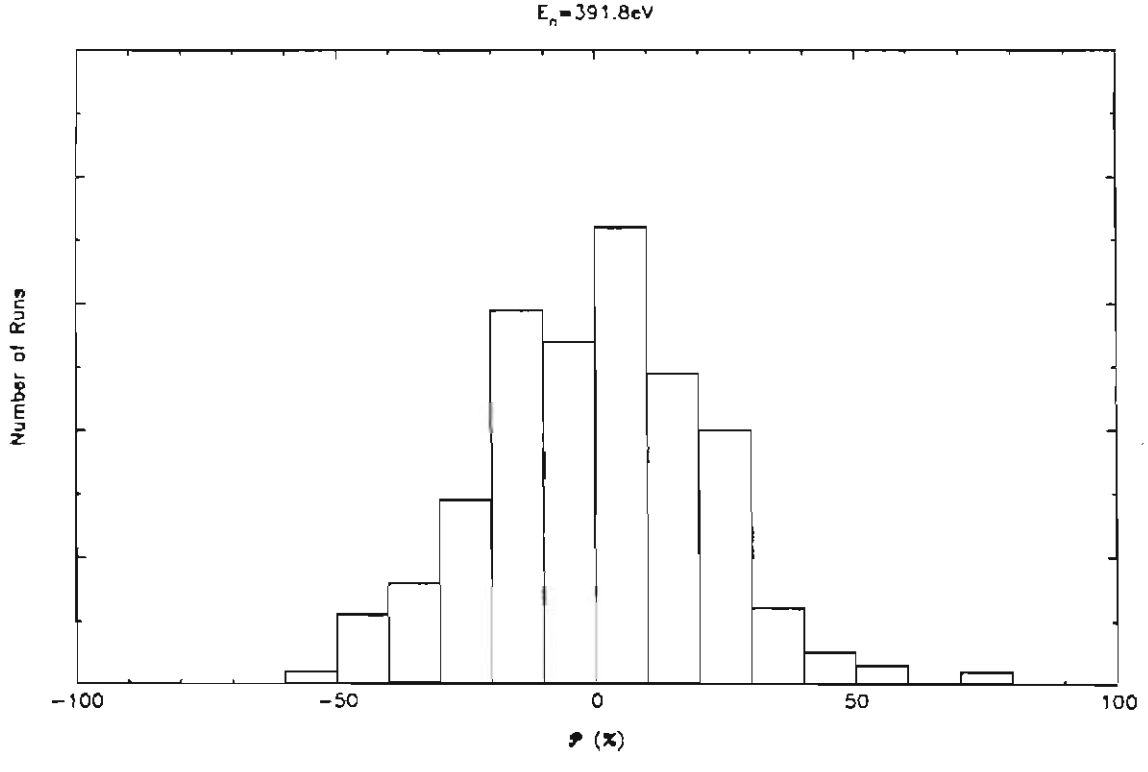
E_n=391.8eV
Number of Runs
−100
−50
0
50
100
φ (%)

width is not known at present.

Several strong s-wave resonances in ^{156}Gd, ^{157}Gd, and ^{186}W were observed as small peaks due to trace contamination of the ^{232}Th target. By analyzing the peak heights, the gadolinium contamination was determined to be less than 0.05% and the tungsten less than 0.004%. Additionally, resonances due to the ^{139}La in the LMN crystals and to ^{63}Cu and ^{65}Cu in the brass collimator and copper target chiller were observed. Since large s-wave resonances should show no parity violation, the 16.7eV ^{157}Gd, the 18.8eV ^{186}W, the 33.2eV ^{156}Gd and the 230.0eV ^{65}Cu resonances were fit to test for systematic errors. No significant effects were observed. The results are tabulated in table 6.3.2.2. Shown in figures 6.3.2.25 through 6.3.2.28 are sample fits and histograms for the four contaminant resonances.

The parity violating asymmetries were measured as a function of the cryostat spin direction to verify that the sign of the asymmetries reversed when the cryostat spin was reversed. All significant asymmetries reversed sign.

The raw asymmetry, ε, where

$$\varepsilon = \frac{N_+ - N_-}{N_+ + N_-}, \qquad (6.3.2.1)$$

of the summed data was examined over off-resonance energy intervals. The presence of a non-zero average ε in an off-resonance region would indicate a false asymmetry. All data were consistent with zero asymmetry. Asymmetries for sample regions near the 64.5eV resonance are listed in table 6.3.2.3. The peak value of ε on the 64.5eV resonance was 3×10^{-4}.

It is interesting to note that the six PNC effects observed with statistical significance greater then 2.5 standard deviations (σ>2.5) all have positive sign. Of the

Table 6.3.2.2

Parity violating asymmetries of contaminant s-wave resonances

E(eV)	Isotope	$\mathcal{P}$(%)
16.7	^{158}Gd	-0.08±1.27
18.8	^{187}W	-0.08±0.69
33.2	^{157}Gd	-1.39±2.52
230.0	^{66}Cu	0.45±0.66

Figure 6.3.2.25

(top) Sample fit to the 16.7eV ^{157}Gd resonance. The top curve is the flux portion of the fitting function and the bottom curve is the fit to the resonance plus the flux. The data displayed are for one spin state of a single run.

(bottom) Histogram of the 355 $\mathcal{P}$ values obtained from fits to the 16.7eV ^{157}Gd resonance.

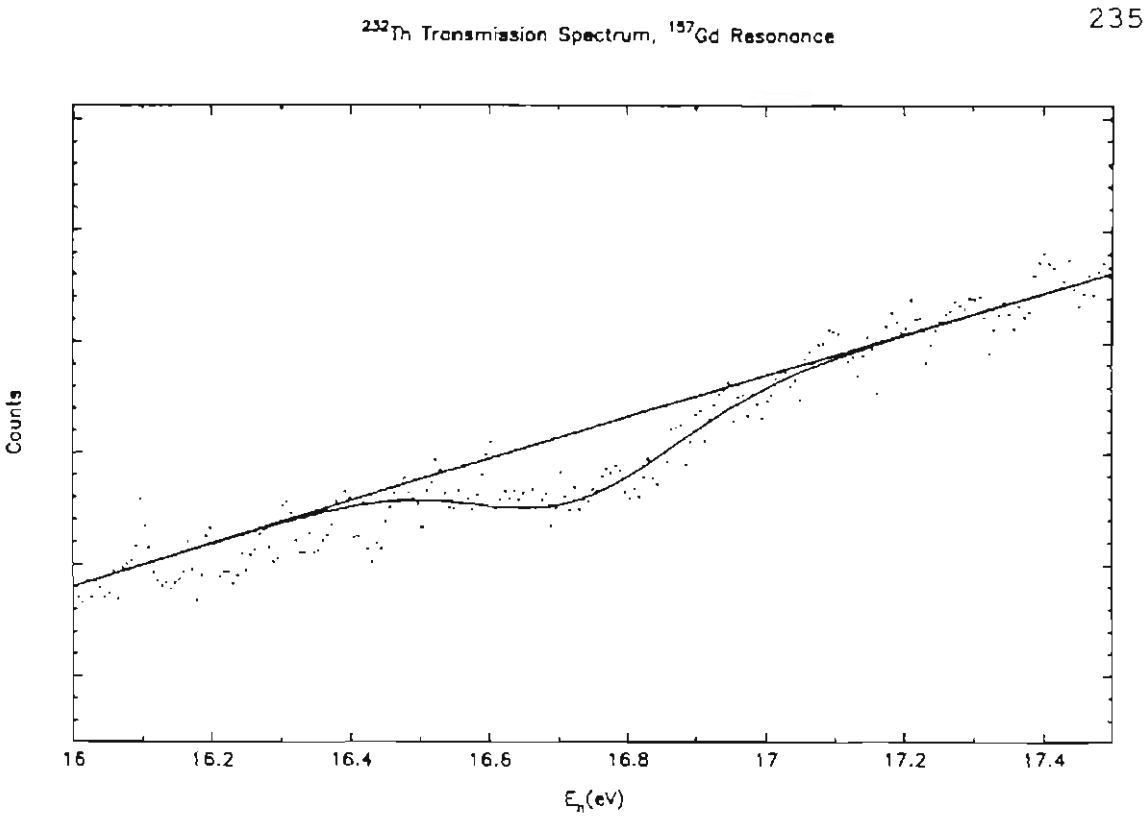
^{232}Th Transmission Spectrum, ^{157}Gd Resonance
Counts
16
16.2
16.4
16.6
16.8
17
17.2
17.4
E_n(eV)

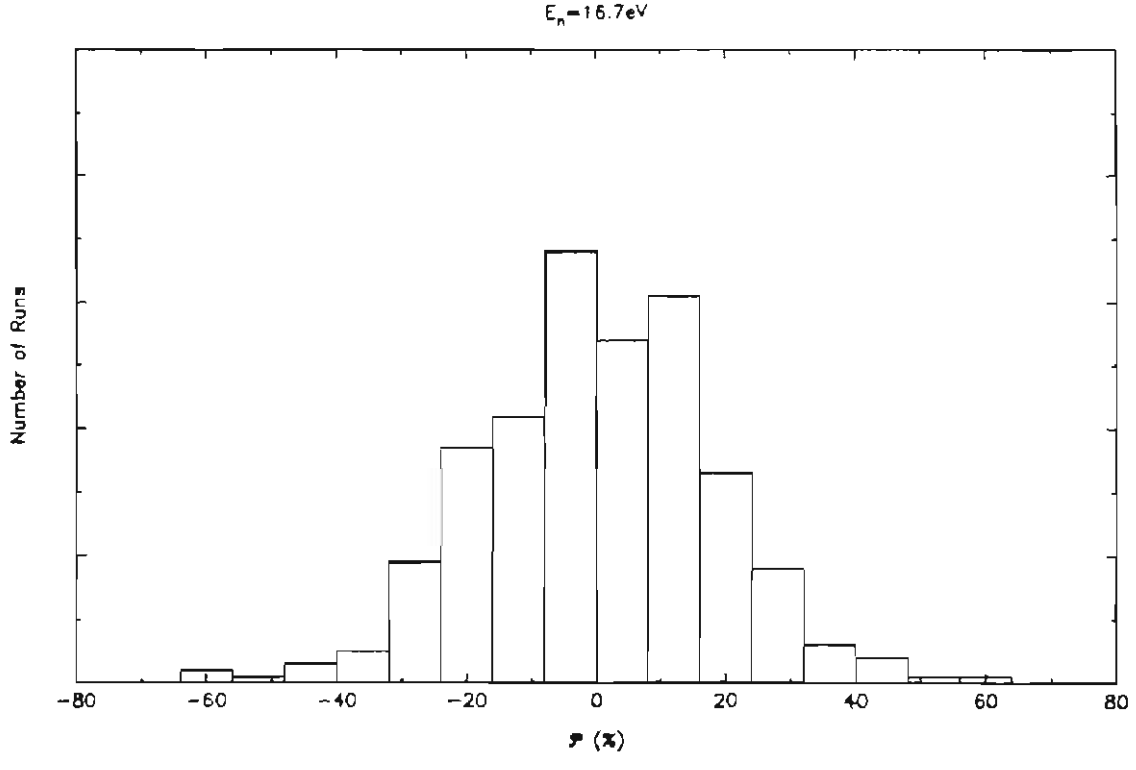
E_n=16.7eV
Number of Runs
−80
−60
−40
−20
0
20
40
60
80
P (%)

Figure 6.3.2.26

(top) Sample fit to the 18.8eV ^{187}W resonance. The top curve is the flux portion of the fitting function and the bottom curve is the fit to the resonance plus the flux. The data displayed are for one spin state of a single run.

(bottom) Histogram of the 355 $\mathcal{P}$ values obtained from fits to the 18.8eV ^{187}W resonance.

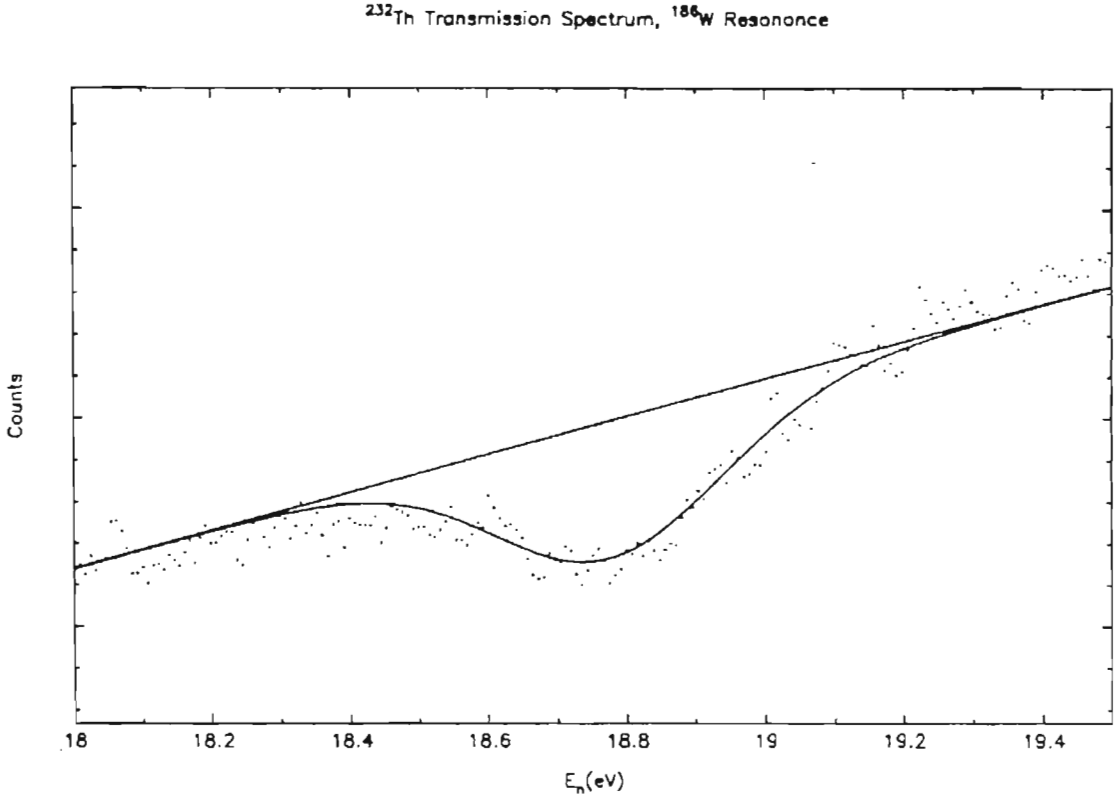
^{232}Th Transmission Spectrum, ^{186}W Resonance
Counts
18
18.2
18.4
18.6
18.8
19
19.2
19.4
E_n(eV)

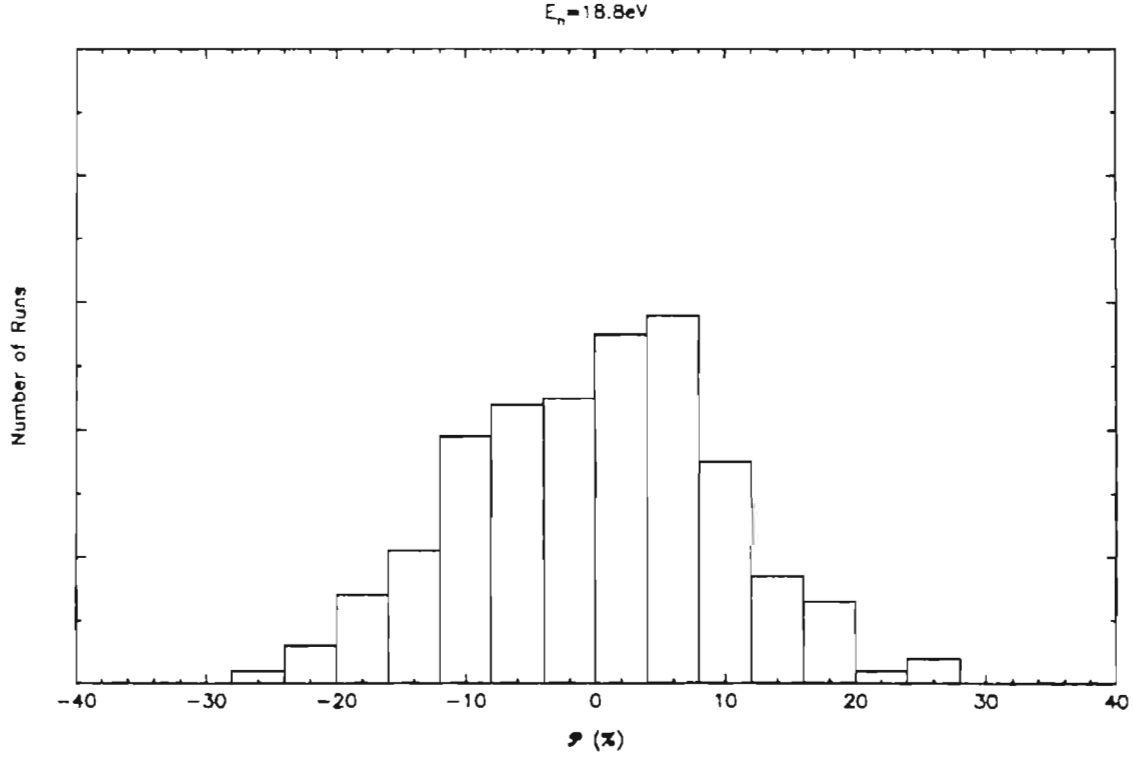
E_n=18.8eV
Number of Runs
-40
-30
-20
-10
0
10
20
30
40
$\mathcal{P}$ (%)

Figure 6.3.2.27

(top) Sample fit to the 33.2eV ^{158}Gd resonance. The top curve is the flux portion of the fitting function and the bottom curve is the fit to the resonance plus the flux. The data displayed are for one spin state of a single run.

(bottom) Histogram of the 355 $\mathcal{P}$ values obtained from fits to the 33.2eV ^{158}Gd resonance.

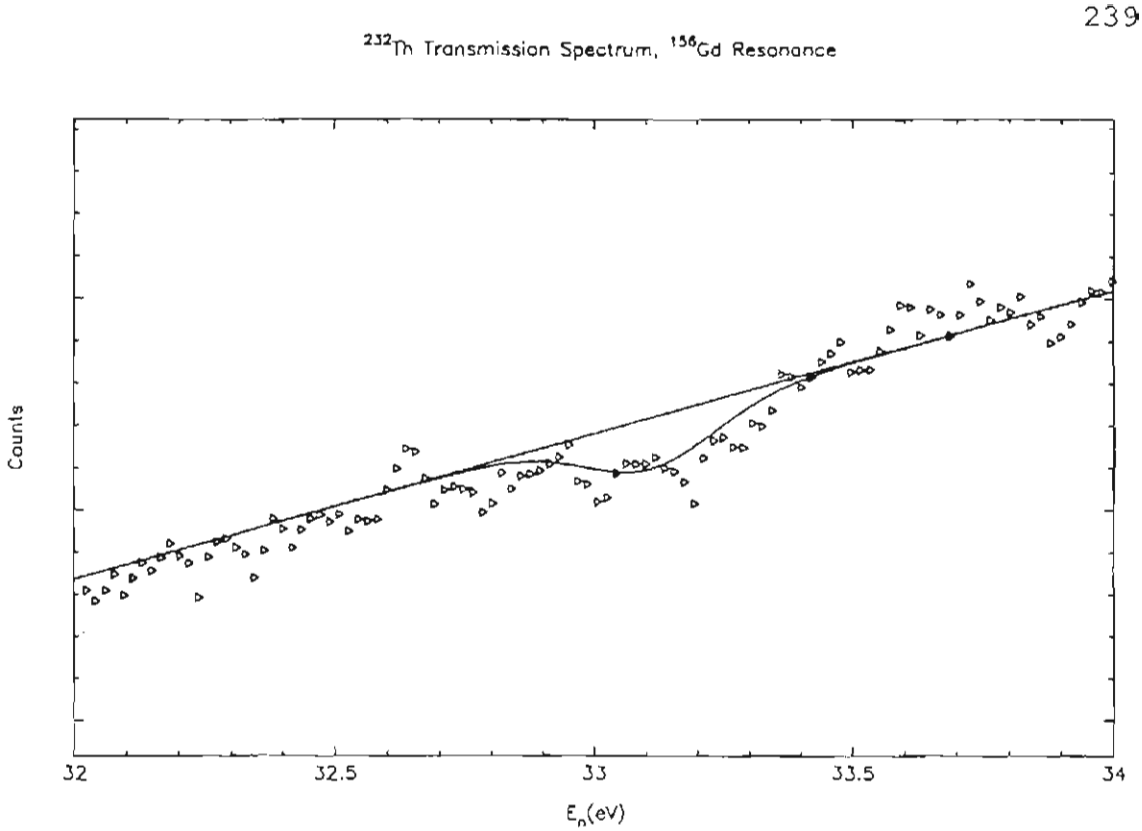
^{232}Th Transmission Spectrum, ^{156}Gd Resonance
Counts
32
32.5
33
33.5
34
E_n(eV)

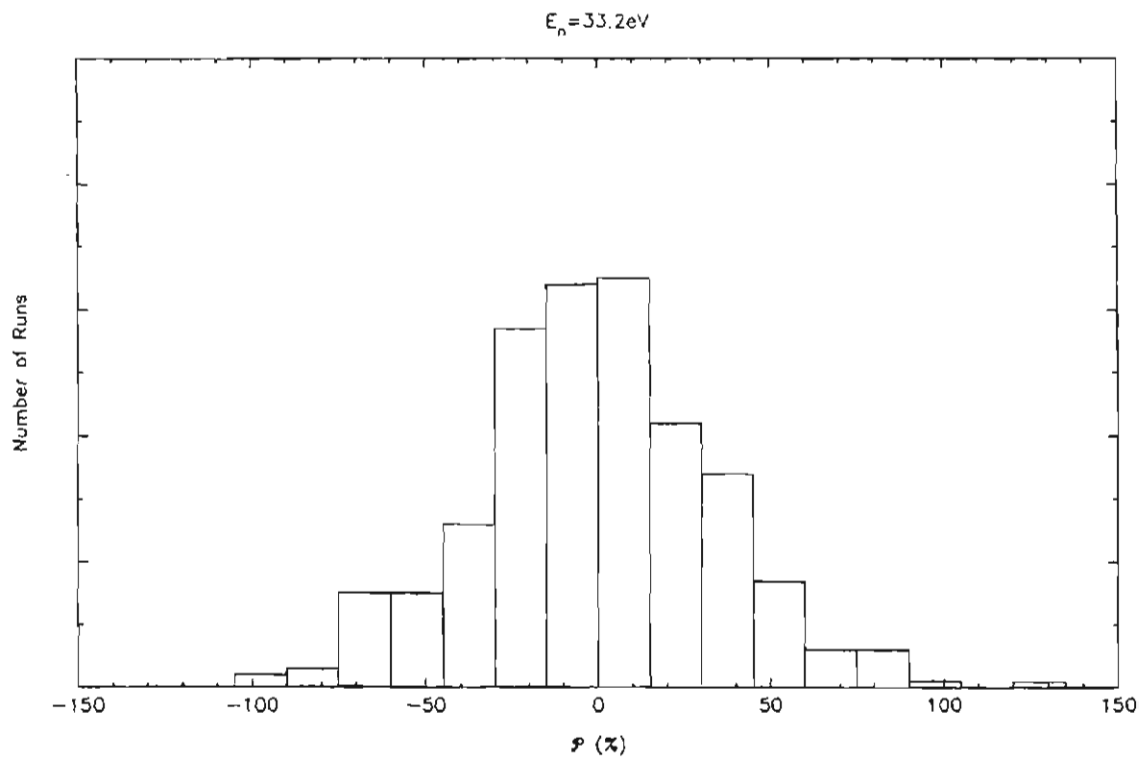
E_n=33.2eV
Number of Runs
−150
−100
−50
0
50
100
150
$\mathcal{P}$ (%)

Figure 6.3.2.28

(top) Sample fit to the 230.0eV ^{66}Cu resonance. The top curve is the flux portion of the fitting function and the bottom curve is the fit to the resonance plus the flux. The data displayed are for one spin state of a single run.

(bottom) Histogram of the 355 $\mathcal{P}$ values obtained from fits to the 230.0eV ^{66}Cu resonance.

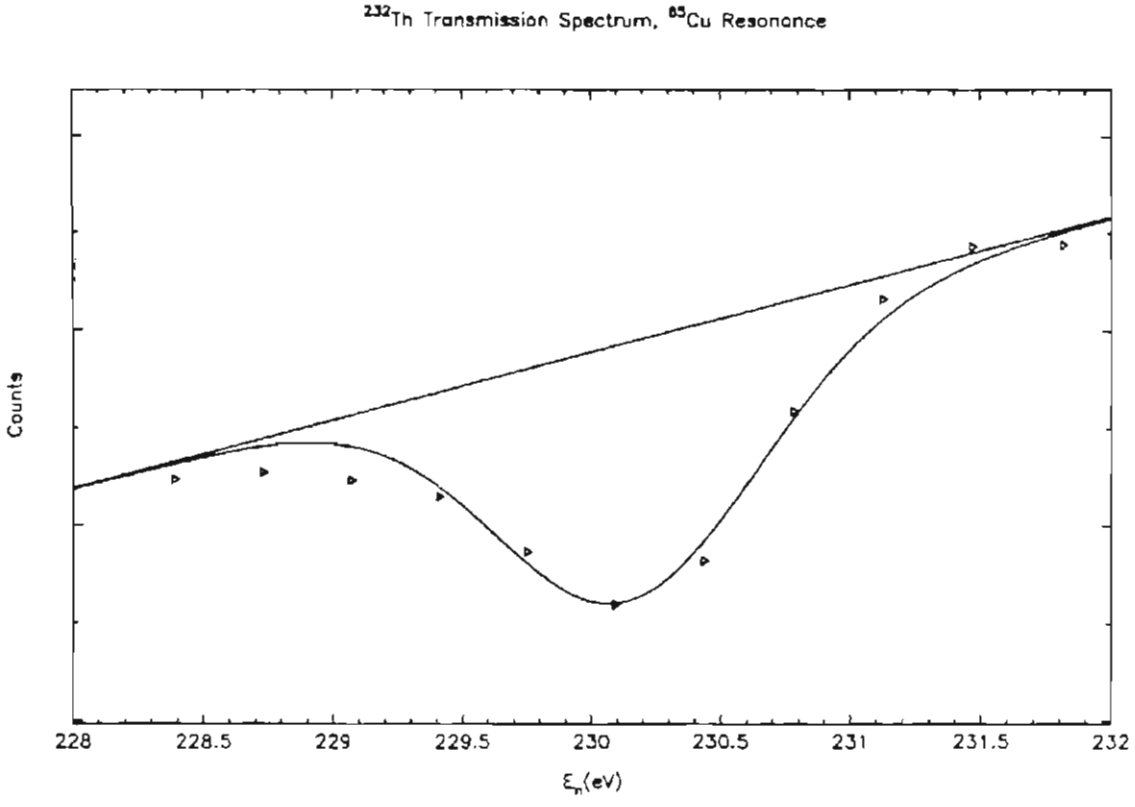
^{232}Th Transmission Spectrum, ^{65}Cu Resonance
Counts
228
228.5
229
229.5
230
230.5
231
231.5
232
E_n(eV)

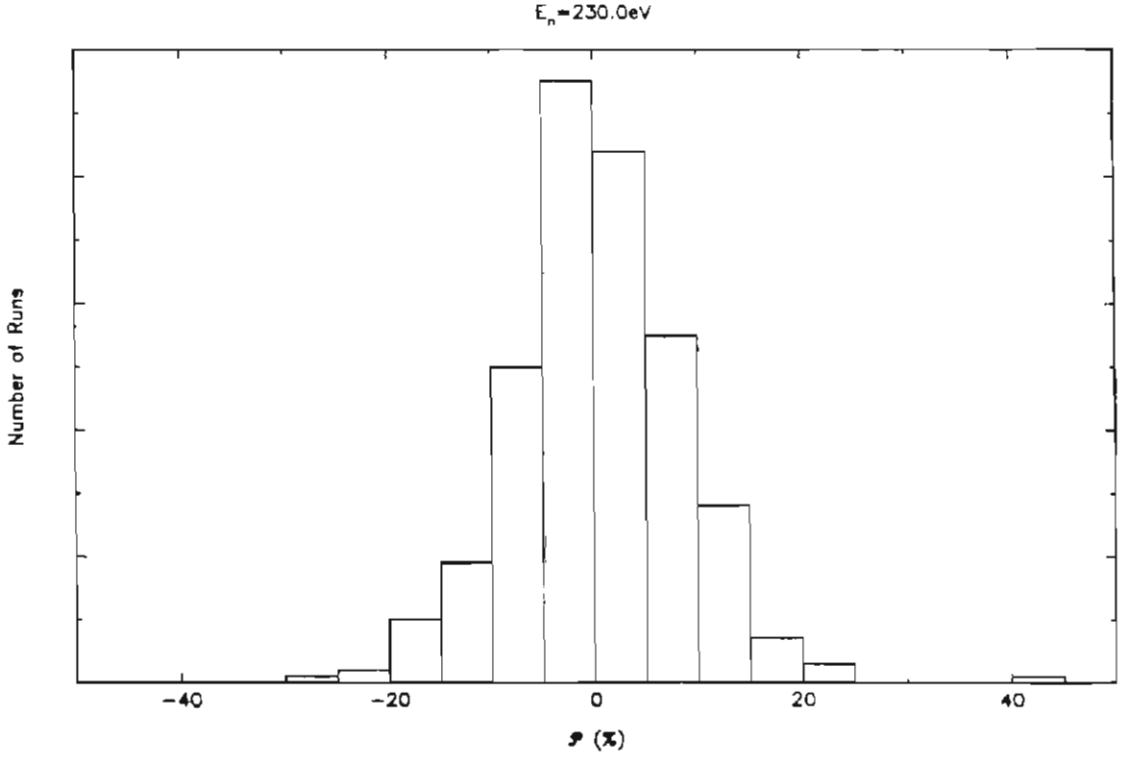
E_n=230.0eV
Number of Runs
-40
-20
0
20
40
P (%)

Table 6.3.2.3

Average raw asymmetries near the 64.5eV resonance

E_{min} (eV)	E_{max} (eV)	Average ε ($\times 10^{-5}$)
60	65	-3.2±8.3
65	70	-1.2±7.6
70	75	0.6±7.2
75	80	-1.4±9.4
80	85	5.5±7.4

five other observed PNC effects with $\sigma>2.5$, (One each in ^{81}Br, ^{111}Cd [Al83], ^{117}Sn [Al83], ^{139}La [Yu91], and ^{238}U [Bo90].) all except ^{111}Cd also have positive sign. (The signs can be determined relative to the effect in ^{139}La.) Therefore 10 of the 11 observed PNC effects with $\sigma>2.5$ have the same sign. The probability of this occurring at random is 0.5%.

This result may indicate that the statistical model adopted here is not a complete explanation of PNC in compound nuclear phenomena. Other models of parity mixing include coupling to a giant 0^- resonance [Ka83] and variations of the valence model [Za83][Za85][No86][Za87]. The valence model probably holds the most promise of predicting sign correlations, but seems unlikely to explain completely the observed data. A combination of two mechanisms may be required to explain the observed behavior. This apparent correlation in sign clearly deserves additional experimental and theoretical attention.

6.3.3 Extraction of matrix elements

The goal of experiments of this type is not only to observe individual cases of parity violation but also to determine the matrix element of the PNC interaction. An expression for the parity violating asymmetry in terms of the PNC matrix element $\mathbf{V}$ was given in eq. (2.4.1). That expression was derived for the mixing of a single p-wave level with a single s-wave level. In the case of thorium, each p-wave resonance strongly mixes with, on average, two or three s-wave resonances. (The bromine data cannot be analyzed in this manner, since no information is known about the spins of the bromine resonances.) Therefore the matrix element cannot be calculated using either eq. (2.4.1) or eq. (3.4.18). Instead an RMS matrix element,

M, is determined. The technique is described below.

Consider the case where the ith p-wave level mixes with the jth s-wave level. Then the portion of the parity violating asymmetry from that pair is

$$\mathcal{P}_{ij} = \frac{2V_{ij}}{E_i - E_j}\sqrt{\frac{\Gamma_{nj}(E_i)}{\Gamma_{ni}(E_i)}}. \qquad (6.3.3.1)$$

The channel spin mixing ratio is unity for a zero spin target. The observed parity violating asymmetry is then

$$\mathcal{P}_i = \sum_j \frac{2V_{ij}}{E_i - E_j}\sqrt{\frac{\Gamma_{nj}(E_i)}{\Gamma_{ni}(E_i)}} = \sum_j A_{ij}V_{ij}. \qquad (6.3.3.2)$$

The A_{ij} coefficients can be calculated from the known resonance parameters and are considered constants. The A_{ij} coefficients are tabulated in Appendix B. The matrix elements are assumed to be independent and random variables which are from a Gaussian distribution of zero mean and variance M^2.

It is convenient to introduce a new quantity

$$Q_i = \frac{\mathcal{P}_i}{\sqrt{\sum_j A_{ij}^2}}. \qquad (6.3.3.3)$$

The values for Q_i for the 23 thorium resonances analyzed are listed in table 6.3.3.1. The sum of independent Gaussianly distributed random quantities with zero mean is itself a Gaussianly distributed quantity with zero mean. Therefore, the Q_i are drawn from the same distribution as the individual matrix elements, V_{ij}. This implies that the RMS matrix element, M, can be determined from the experimentally measured set of $\mathcal{P}_i$ values without having to

Table 6.3.3.1

Q_i values of the thorium resonances

E_n (eV)	Q_i (meV)
8.3	0.61±0.10
13.1	0.20±0.17
37.0	1.28±0.51
38.2	4.49±0.94
41.0	-0.91±0.88
49.9	-0.30±0.82
64.5	0.90±0.19
90.2	-0.97±0.92
98.1	-0.01±1.02
103.7	-0.30±0.72
128.2	0.86±0.12
145.9	-0.10±0.74
148.1	-5.42±3.08
167.2	0.97±0.33
179.0	-1.25±1.09
196.2	0.98±0.41
202.7	1.66±1.09
211.0	1.58±1.66
242.4	-0.05±1.64
299.8	-1.45±1.57
302.7	-1.73±1.03
380.7	2.91±4.66
391.8	-2.35±5.68

determine each individual value of V_{ij}.

For a zero spin target there are two possible values for the spin of a p-wave resonance. A p-wave resonance may have J=1/2 or J=3/2. Only the J=1/2 p-wave levels can interfere with the s-wave levels, which are all J=1/2. On statistical grounds, it is expected that 2/3 of the p-waves will have J=3/2 and 1/3 will have J=1/2. Deviations from the 1/3 to 2/3 ratio are expected to be small in ^{233}Th [Eg88]. The Q_i values for the J=3/2 resonances are then assumed to be drawn from a Gaussian of the form

$$\frac{1}{\sqrt{2\pi}\sigma_{Q_i}} e^{-\frac{Q_i^2}{2\sigma_{Q_i}^2}}, \qquad (6.3.3.4)$$

while the Q_i values for the J=1/2 resonances are assumed to be drawn from

$$\frac{1}{\sqrt{2\pi}\sqrt{\sigma_{Q_i}^2 + M^2}} e^{-\frac{Q_i^2}{2\left(\sigma_{Q_i}^2+M^2\right)}}. \qquad (6.3.3.5)$$

The quantity σ_{Qi} is the experimental error on Q_i. Given that any particular p-wave resonance has 1/3 probability of being J=1/2 and 2/3 probability of being J=3/2, a likelihood function, L(M), can be constructed for the thorium data set. The likelihood function takes the form

$$L(M) = \prod_{i=1}^{23}\left[\frac{1}{3}\frac{1}{\sqrt{2\pi}\sqrt{\sigma_{Q_i}^2 + M^2}} e^{-\frac{Q_i^2}{2\left(\sigma_{Q_i}^2+M^2\right)}} + \frac{2}{3}\frac{1}{\sqrt{2\pi}\sigma_{Q_i}} e^{-\frac{Q_i^2}{2\sigma_{Q_i}^2}}\right]. \qquad (6.3.3.6)$$

A plot of the likelihood function for thorium is shown in figure 6.3.3.1. The most probable value for M is 1.39meV. The upper and lower limits of the most compact 68% confidence interval are 2.02meV and 0.97meV, respectively. A

Figure 6.3.3.1 Plot of the likelihood function for ^{233}Th.

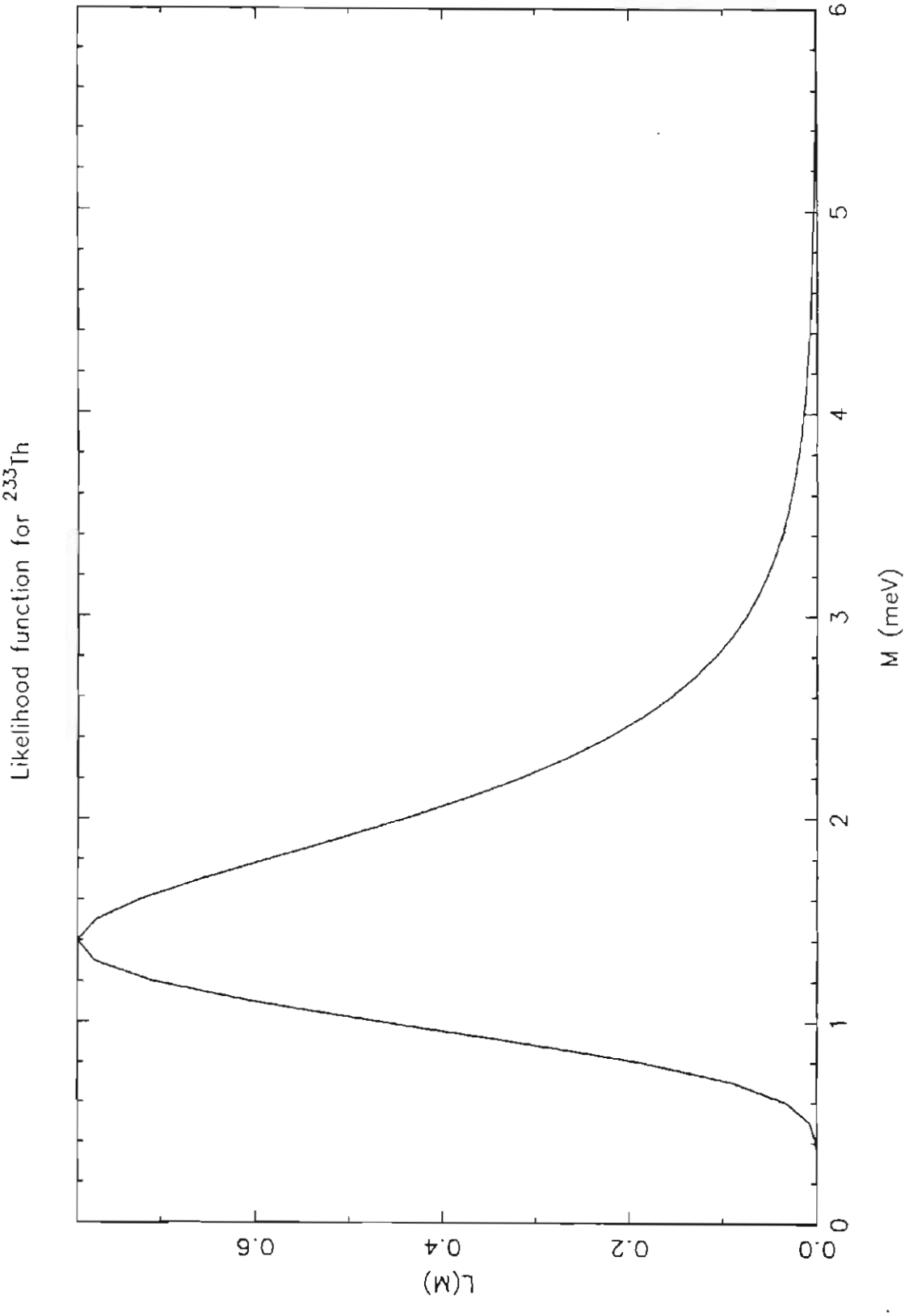
Likelihood function for ^{233}Th
L(M)
0.0
0.2
0.4
0.6
0
1
2
3
4
5
6
M (meV)

detailed description of the likelihood technique can be found in Kreyszig [Kr72].

The Q_i values used in the likelihood analysis were calculated using eq. (6.3.3.3). The A_{ij} coefficients were calculated including all s-waves up to 500eV and two known bound s-waves. The neutron widths were evaluated at the energy of the p-wave resonances. The distribution of Q values for ^{233}Th was bootstrapped. The standard deviation of the bootstrap distribution was identical to the standard deviation of the distribution of Q values.

It is convenient to define a parity violating spreading width,

$$\Gamma_{pv} = 2\pi \frac{M^2}{D}, \qquad (6.3.3.7)$$

where M is the RMS parity violating matrix element and D is the level spacing. Spreading widths are not expected to show much sensitivity to nuclear mass or excitation energy. Using the s-wave level spacing of 16.4eV for ^{232}Th gives $\Gamma_{PV}=(7.4\ +8.2\ -3.8)\times10^{-7}$eV. This compares to $\Gamma_{PV}=(1.0\ +2.4\ -0.7)\times10^{-7}$eV for ^{238}U [Bo90] and $\Gamma_{pv}\sim10^{-7}$eV for light nuclei [Ad85]. French *et al.* [Fr88a][Fr88b] have used the techniques of random matrix theory and statistical nuclear spectroscopy to establish the connection between time reversal invariance violation in the compound nucleus system and in the NN interaction. French *et al.* define the quantity

$$\alpha^2_{TRIV} = \frac{\Gamma_{TRIV}}{2\pi\times10^5 eV}, \qquad (6.3.3.8)$$

where Γ_{TRIV} is the spreading width for time reversal invariance violation and α is the ratio of the time reversal in-

variance violating part of the effective NN interaction to the time reversal invariance conserving part. Assuming this argument to be general for other symmetry violations, then the quantity α_{PV} can be defined as

$$\alpha_{PV}^2 = \frac{\Gamma_{PV}}{2\pi x 10^5 eV}, \qquad (6.3.3.9)$$

similar to the time reversal invariance case. For ^{232}Th $|\alpha_{PV}|=1.1x10^{-6}$ as compared to $4x10^{-7}$ for ^{238}U, giving an estimate for the magnitude of the parity violation in the NN interaction which is in qualitative agreement with theoretical predictions.

CHAPTER VII

Summary

A brief history of the major experiments which observed parity violation in compound nuclei was given. The discovery of an extremely large longitudinal asymmetry in the scattering of neutrons from the E_n=0.734eV resonance of ^{139}La by the Dubna group initiated new interest in parity violation studies. A qualitative argument was given for the extremely large magnitude of the parity violation effect in lanthanum.

The formalism required to analyze a parity violation experiment using the neutron transmission technique was derived. Explicit results were given for a zero spin target.

The apparatus used in the present experiment was described at length. Functional details of the LAMPF/PSR/LANSCE system were provided and an absolute measurement of the LANSCE flux reported. The mechanics of the polarization of the neutron beam were discussed. A magnetic neutron spin flipper was described and results of calculations of the spin flip efficiency were presented. Two neutron beam monitoring systems were described. The neutron detection and data acquisition system was described, including signal processing by the current mode.

Precision and stability tests of the ^{6}Li glass neutron beam monitor were reported, as well as tests of the precision and temperature dependence of the ^{3}He ion chamber neutron beam monitors. Measurements of the susceptibility of the efficiency of the ^{3}He ion chambers to the magnetic fields of the spin flipper also were reported. The mapping of the magnetic fields of the cryostat, spin flipper, and target chiller was described and maps of the cryostat and

spin flipper beam axis magnetic fields presented. Two conventional techniques for the measurement of the neutron beam polarization were discussed. A method to determine the neutron beam polarization which utilized the known parity violating asymmetry in ^{139}La was discussed.

A target chiller, used to cool the target to liquid nitrogen temperature and therefore reduce the Doppler width, was described in Appendix A. Test results to illustrate the effectiveness of the target chiller also were presented.

The analysis techniques used to extract parity violating asymmetries from the experimental data were described. A method for extracting an root-mean-square parity mixing matrix element from a set of parity violating asymmetries was presented. This method is valid for neutron resonances in a zero spin target.

Parity violation was observed for the 0.88eV resonance in ^{81}Br. A 5.4 standard deviation effect was observed, with a value for the parity violating asymmetry of $1.77\pm0.33\%$.

A total of 23 resonances in ^{232}Th were studied for parity violation at neutron energies up to 400eV. Seven parity violations with statistical significance greater than 2.4 standard deviations were observed. Four of these resonances had greater than 4.7 standard deviation effects; the most significant effect was 7.3 standard deviations on the 128.2eV state. Two very large effects were observed: 10.88% on the 38.2eV state and 9.78% on the 64.5eV state.

Four s-wave states in contaminants in the thorium target (one each in ^{158}Gd, ^{187}W, ^{157}Gd, and ^{66}Cu) were studied for parity violation to test for systematic errors. No significant effects were observed.

The root-mean-square parity mixing matrix element M was determined for ^{233}Th. The most likely value was $M=1.39meV$. The lower and upper limits of the most compact

68% confidence interval were determined to be 0.97meV and 2.02meV respectively.

The spreading width Γ_{pv} was determined to be 7.4×10^{-7}eV for ^{233}Th, in qualitative agreement with the spreading widths for other nuclei, both light and heavy. The parameter α_p, introduced by French *et al.*, was determined to be 1.1×10^{-6} for ^{233}Th, in approximate agreement with the theoretical strength of the parity violating part of the NN interaction relative to the parity conserving part.

APPENDIX A

Target Chiller

A.0 Introduction

The observed energy resolution of an NTOF experiment has many contributions. In addition to the natural width of the resonance, these contributions can be grouped into two categories, those due to finite timing resolution and those due to the Doppler effect. There are many contributions to the timing resolution, including a long beam pulse width, a long moderation time, and a short flight path. It would require the expenditure of a large amount of effort and money to make a significant improvement to the overall time resolution. On the other hand, the Doppler effect involves only the target. The Doppler width can be reduced by a factor of two for most heavy metals by cooling the target with LN to 77°K. Cooling below 77°K results in little additional decrease of the Doppler width because the crystal structure of most heavy metals reaches the one phonon vibrational state at around 50°K.

The target chiller described below was designed to be a relatively simple, low maintenance device. The only maintenance required is a periodic fill of liquid nitrogen. The target chiller was constructed in the TUNL shops. Approximately five man-days were required to construct the target chiller. The details of the design and the functional tests are described in the following sections.

A.1 Theory

The Doppler width is conventionally defined as

$$\Delta = \sqrt{\frac{4EkT}{A}}, \qquad \text{(A.1.1)}$$

where E is the neutron energy, k is Boltzmann's constant, T is the temperature, and A is the mass of the nucleus. Note that this width increases as $\sqrt{E}$. For a nucleus such as ^{238}U, the Doppler width is comparable to the natural width at 1eV. At 100eV the Doppler width completely dominates the natural width. Since the Doppler width scales as $\sqrt{T}$, reducing the target temperature by a factor of four (e.g., 300°K to 77°K) reduces the Doppler width by a factor of two. Extensive discussions of Doppler broadening of neutron resonances are given by Foderaro [Fo71a] and by Larson [La89].

The width of eq. (A.1.1) was derived under the assumption that the velocity distribution of the target nucleus is Maxwellian. It was shown by Lamb [La39] that the distribution for atoms bound by a Hooke's law force is Maxwellian, but that the Maxwell temperature parameter, T_{eff}, was not equal to the thermodynamic temperature, T. Although Hooke's law is an overly simple model, the basic predictions are qualitatively reasonable. At low temperatures most solids behave approximately like the Debye model [Fo71a]. The effective temperature for Debye model solids is given by

$$T_{eff} = \frac{3}{2}\theta_D \int_0^1 \nu^3 \operatorname{ctnh}\left(\frac{\nu\theta_D}{2T}\right) d\nu, \qquad \text{(A.1.2)}$$

where θ_D is the Debye temperature and ν is the lattice vibrational frequency. The Debye temperature of uranium is 200°K. This implies an effective temperature of 309°K at 300°K and 110°K at 77°K. Therefore, the Doppler width of uranium would be expected to decrease by a factor of 1.7 when cooled to 77°K.

A.2 Design considerations

There were several fixed design requirements for the target chiller: to bolt onto the downstream end of the spin flipper using an existing bolt circle, to provide a uniform axial magnetic guide field over the target region, and to hold targets of up to 2.5 inches diameter. All of these requirements were met in the final design.

Consideration was given to providing a guide field with a solenoid or with Helmholtz coils. At first the choice of a solenoid was preferred, since a solenoid could be a simple extension of the spin flipper. However, the solenoid option introduced severe complications in the design of the cryogenic vessel. Therefore, it was decided to use Helmholtz coils. The coils consist of 80 turns each of 16 gauge stranded copper wire. The coils are wound on 12" ID Lucite forms. The cross sectional area of each coil set is one square inch.

The design of the cryogenic vessel was complicated by the fact that the target chiller must allow the neutron beam to pass through the cold target. Another design goal was that the chiller would only require filling twice a day. The final design is shown in two perspectives in figures A.2.1 and A.2.2. The cryogenic portion of the target chiller consists of two vessels. The inner vessel contains the liquid nitrogen and is in direct contact with the target. The thermal contact of the target with the cold walls of the inner vessel provides for the conduction of heat out of the target. The outer vessel contains and supports the inner vessel and the target. The presence of the outer vessel allows the space between the two vessels to be evacuated, minimizing heat transfer into the inner vessel and target.

The inner vessel is constructed of two concentric copper cylinders, one 2 1/2" in diameter and the other 5" in

Figure A.2.1 Side view of the target chiller. The drawing is 1/2 scale. Unless otherwise indicated all materials are drawn to scale.

Target Chiller, Side View

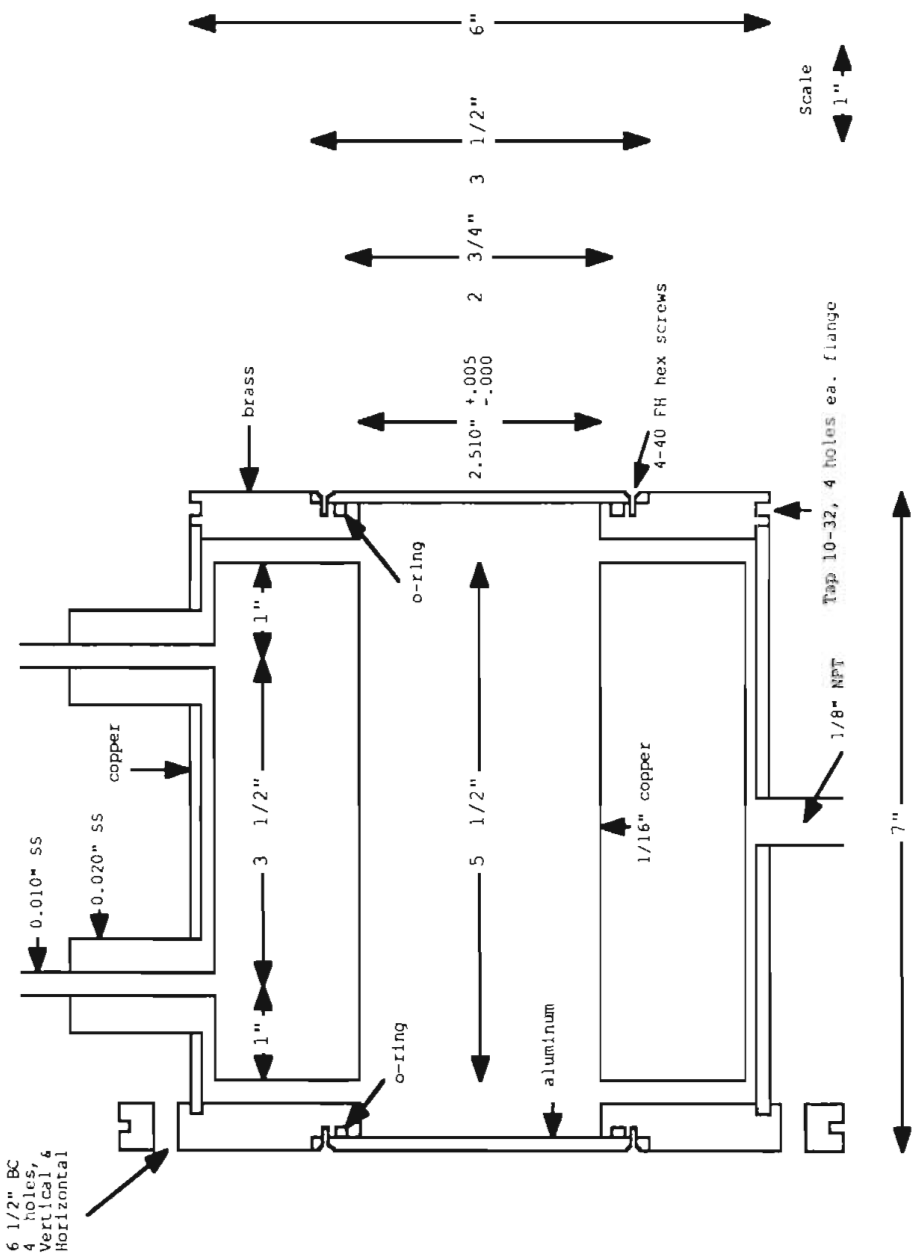

Figure A.2.2 End view of the target chiller. The drawing is 1/4 scale. Unless otherwise indicated all materials are drawn to scale.

Target Chiller, End View

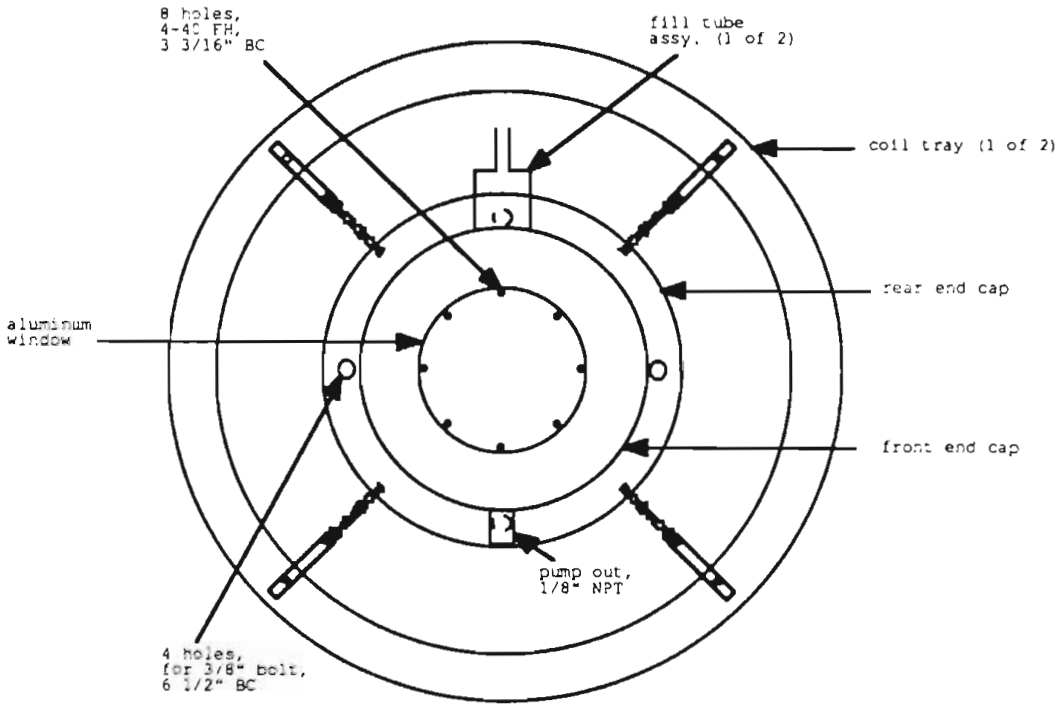

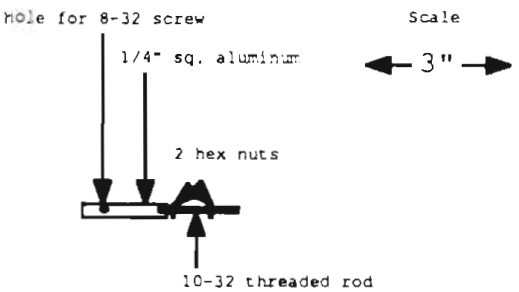

Coil Support Detail

diameter. A 5" diameter copper disk with a 2.5" diameter center hole was silver soldered to each end of the cylinders to complete the vessel. The minimum wall thickness for an inner cryogenic vessel in cylindrical form can be calculated [Ba85] from

$$t = \frac{pD}{2sw - 1.2p}, \qquad \text{(A.2.1)}$$

where p is the pressure differential across the wall, D is the ID of the wall, s is the allowable stress of the wall material, and w is the weld efficiency. The parameters required for the chiller design are p=15psi, D=5", s=6700psi, and w=0.6. These parameters give a wall thickness of 0.010". This thickness was increased to 0.0625" to allow for the added load of the target.

The outer vessel is constructed of a 6" copper pipe with brass end caps. The end caps have a 2.5" diameter hole in their centers. An aluminum window covers each hole. The minimum wall thickness for an outer cryogenic vessel in cylindrical form can be calculated from

$$t = \left[\frac{p_c(1-\nu^2)}{2E}\right]^{1/3} D_o, \qquad \text{(A.2.2)}$$

where p_c is the collapse pressure, E is Young's modulus of the material, ν is Poisson's ratio of the material, and D_o is the OD of the vessel. The parameters for this design are p_c=30psi, E=1.7x10^{7}psi, ν=0.33, and D_o=6". This gives a required wall thickness of 0.055". This thickness was increased to 0.125" to allow for the additional loading from the target and the 0.5" thick end caps.

The fill and vent tubes to the inner vessel are 0.25" diameter stainless steel (SS) tubing, 0.010" wall thick-

ness. The inner vessel is suspended by these tubes such that the inner and outer vessel both have the same centerline. The tubes are connected to the outer vessel by 1.25" diameter SS tubing, 0.020" wall thickness. The use of SS tubing is to minimize heat conduction into the inner vessel. The space between the inner and outer vessels is evacuated through a pump out located on the bottom side of the chiller.

A.3 Tests of the chiller

The target chiller was first tested for liquid nitrogen retention time. A simple liquid nitrogen level sensor was constructed for this test. A design by Alvarez [Al89] was used. A schematic diagram for the sensor circuit is shown in figure A.3.1. The sensor diodes were threaded into the vent tube, with the lower sensor about 2/3 of the way down from the top of the chiller. A brass slug was placed inside the chiller to simulate a target. When the target chiller was completely filled it took an average of 10 to 11 hours for the lower sensor to become uncovered. An additional four to five hours were required for all the liquid nitrogen to boil off.

The magnetic field mapping of the chiller was previously described in section 5.3.

The cooling ability of the target chiller was tested using a ^{238}U target. The target was placed in the target chiller which was subsequently mounted in place on the downstream end of the spin flipper. Before any liquid nitrogen was poured into the target chiller, two half hour data runs were taken using a 500ns dwell time. The region of four to five eV is shown in figure A.3.2. This allowed the lowest energy resonances to be observed where the timing resolution is not significant and the Doppler width is comparable to the natural width. The target chiller was

Figure A.3.1 Schematic diagram of the LN level sensor circuit. The two LED's to the left are the sensor diodes. The AND gates are 7408, the inverting triggers are 7414, and the transistors are 2N3908.

Liquid Nitrogen Level Sensor Circuit

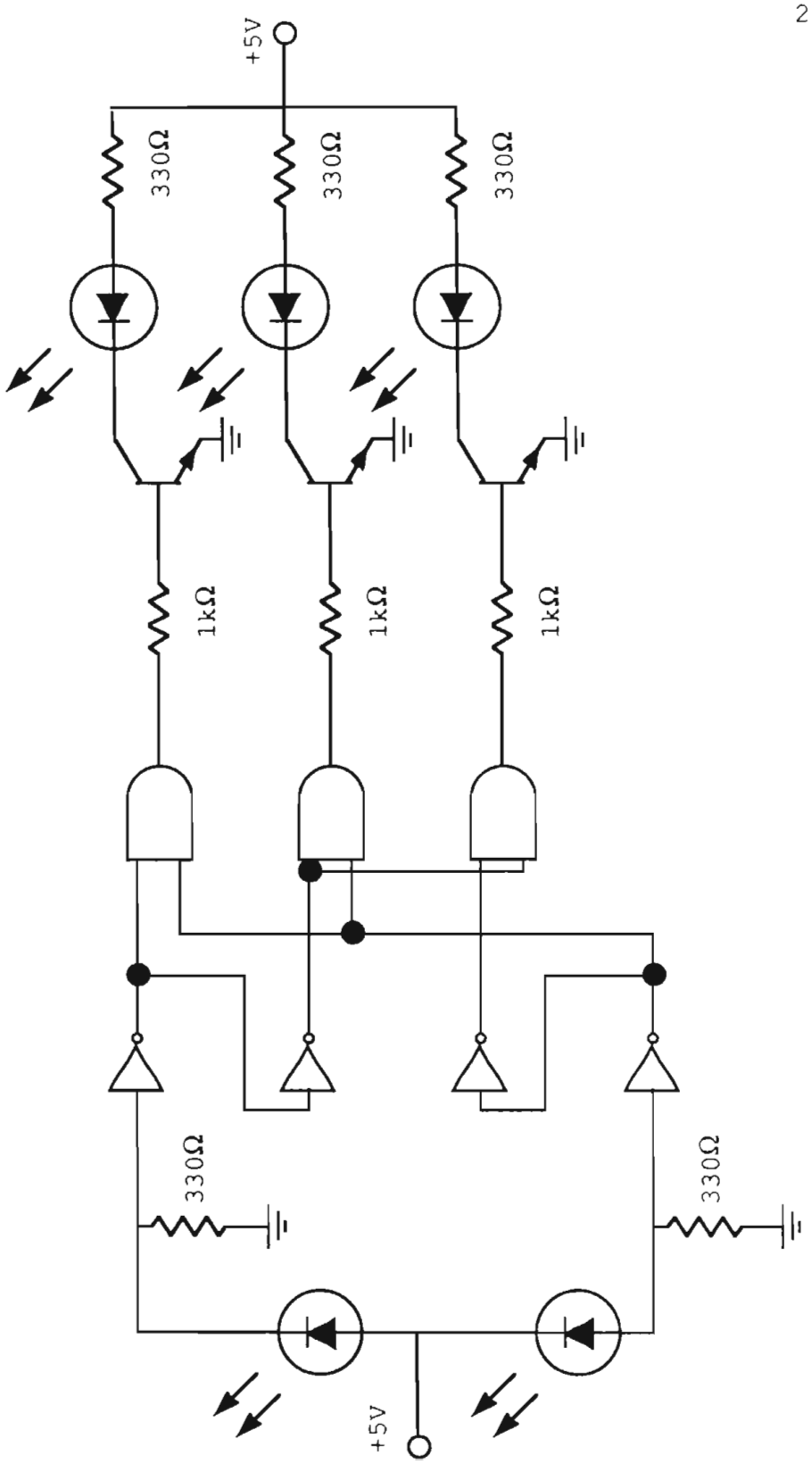

Figure A.3.2 Transmission spectrum of the region 4eV to 5eV in ^{238}U. The target is at room temperature.

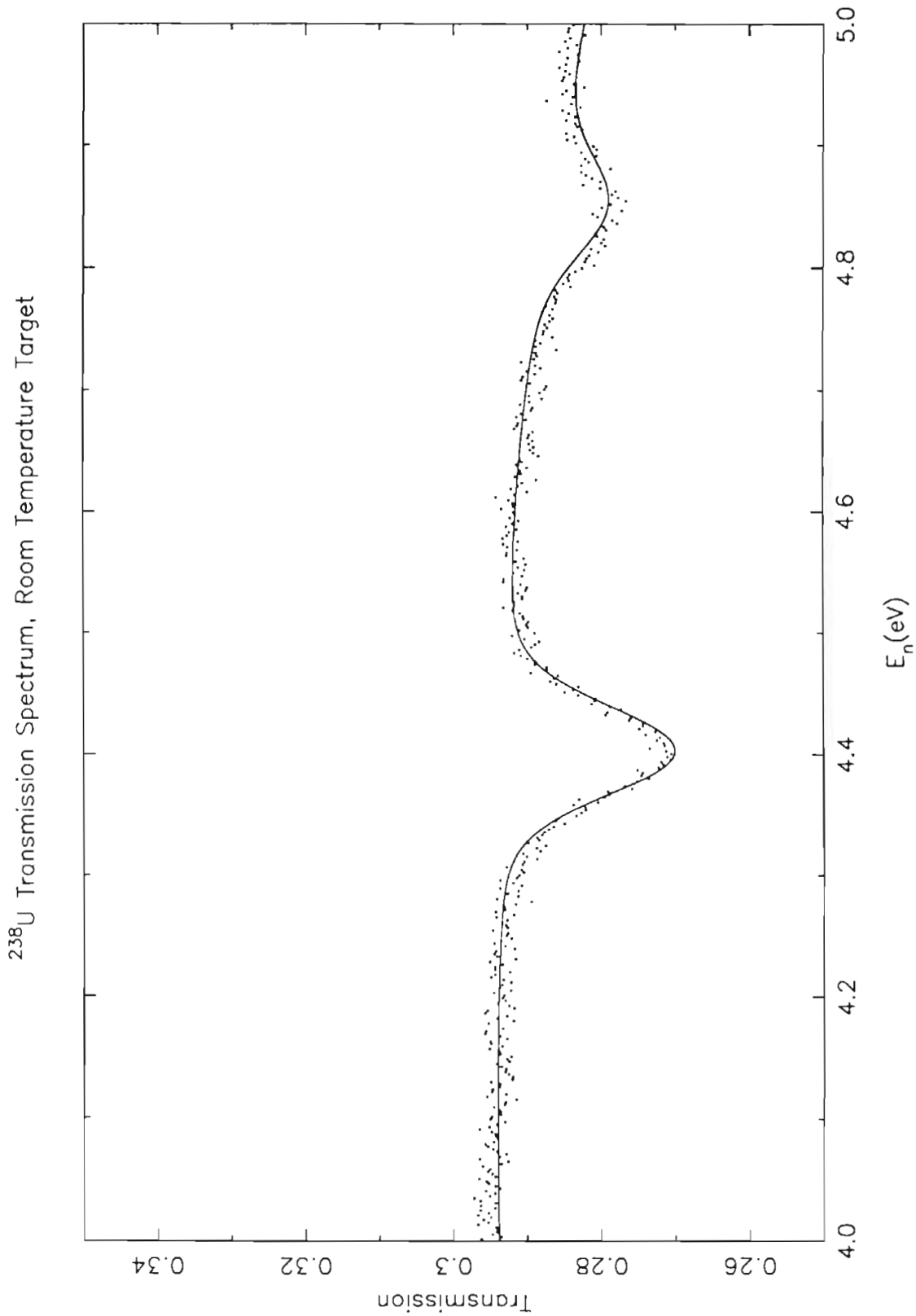
^{238}U Transmission Spectrum, Room Temperature Target
Transmission
0.26
0.28
0.3
0.32
0.34
4.0
4.2
4.4
4.6
4.8
5.0
E_n(eV)

then filled with liquid nitrogen and four more half hour runs were taken. No change in resonance widths was observed between the fifth and sixth runs. The same energy region as in figure A.3.2 is shown for the final run in figure A.3.3. The 4.4eV ^{238}U and the 4.8eV ^{235}U resonances were fit in the first and last of the six runs using the code SAMMY. The resonance parameters of Moxon [Mo89] were used. The effective target temperature was varied until the best fit was obtained. For the warm target run a value of 311°K was obtained and a value of 114°K was obtained for the cold target run. This translates into an actual temperature of 302°K and 81°K for the warm and cold target runs, respectively. The effectiveness of the target chiller was clearly demonstrated.

Figure A.3.3 Transmission spectrum of the region 4eV to 5eV in ^{238}U. The target has been cooled with liquid nitrogen. The flattening of the peak of the 4.4eV resonance is an artificial effect of the current mode.

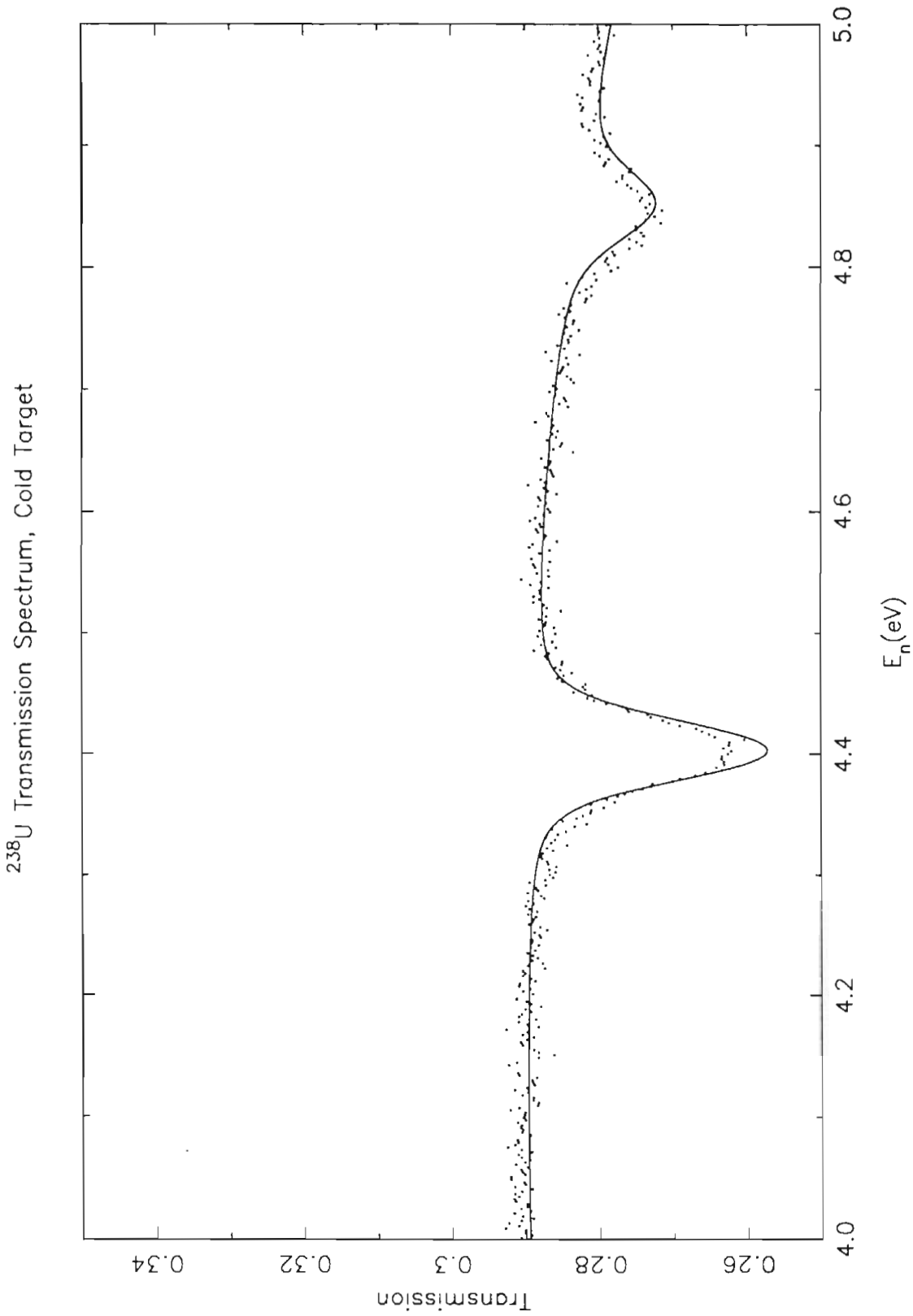
^{238}U Transmission Spectrum, Cold Target
Transmission
0.26
0.28
0.3
0.32
0.34
4.0
4.2
4.4
4.6
4.8
5.0
E_n(eV)

APPENDIX B

Tabulation of the A_{ij} coefficients

This appendix contains a tabulation of the A_{ij} coefficients for the 23 p-wave resonances analyzed in ^{233}Th. The subscript 'i' labels the p-wave resonances and the subscript 'j' labels the s-wave resonances. The coefficients are grouped by the ith p-wave resonance. The sum of the squares of the coefficients for each p-wave resonance is also given at the end of the listing of each p-wave resonance.

E_i (eV) = 8.3505

E_j (eV)	A_{ij} (meV^{-1})
-22.200	7.7389E-03
-2.952	1.3329E-02
21.806	1.0120E-02
23.464	1.2094E-02
59.519	2.8120E-03
69.232	7.6731E-03
113.030	2.1765E-03
120.870	2.6072E-03
129.190	9.2533E-04
154.360	1.7753E-04
170.390	2.7407E-03
192.720	1.2269E-03
199.400	9.1383E-04
219.520	5.2691E-05
221.290	1.3730E-03
251.650	1.1927E-03
263.230	9.4134E-04
285.910	1.0006E-03
305.620	8.8643E-04
309.470	3.8555E-05
329.110	1.2951E-03
342.000	8.9107E-04
365.360	6.7053E-04
369.490	6.5655E-04
401.100	3.8897E-04
402.920	3.7741E-05
421.030	7.7744E-05
454.470	1.1025E-04
462.770	7.7861E-04
489.050	6.9409E-04

$\sqrt{\sum A_{ij}^2} = 2.4205E-02$

E_i (eV) = 13.1240

E_j (eV)	A_{ij} (meV^{-1})
-22.200	8.5860E-03
-2.952	1.2021E-02
21.806	2.0120E-02
23.464	2.2676E-02
59.519	3.9784E-03
69.232	1.0681E-02
113.030	2.9255E-03
120.870	3.4927E-03
129.190	1.2358E-03
154.360	2.3543E-04
170.390	3.6225E-03
192.720	1.6157E-03
199.400	1.2023E-03
219.520	6.9156E-05
221.290	1.8016E-03
251.650	1.5606E-03
263.230	1.2306E-03
285.910	1.3061E-03
305.620	1.1557E-03
309.470	5.0255E-05
329.110	1.6864E-03
342.000	1.1597E-03
365.360	8.7182E-04
369.490	8.5351E-04
401.100	5.0511E-04
402.920	4.9007E-05
421.030	1.0090E-04
454.470	1.4296E-04
462.770	1.0094E-03
489.050	8.9932E-04

$\sqrt{\sum A_{ij}^2} = 3.6396E-02$

E_i(eV)= 36.9910

E_j(eV)	A_{ij}(meV^{-1})
-22.200	3.1331E-03
-2.952	2.9584E-03
21.806	7.0340E-03
23.464	1.0599E-02
59.519	5.0100E-03
69.232	1.1365E-02
113.030	2.3503E-03
120.870	2.7434E-03
129.190	9.5130E-04
154.360	1.7323E-04
170.390	2.6114E-03
192.720	1.1394E-03
199.400	8.4321E-04
219.520	4.7816E-05
221.290	1.2443E-03
251.650	1.0604E-03
263.230	8.3186E-04
285.910	8.7519E-04
305.620	7.6945E-04
309.470	3.3421E-05
329.110	1.1155E-03
342.000	7.6459E-04
365.360	5.7184E-04
369.490	5.5936E-04
401.100	3.2911E-04
402.920	3.1921E-05
421.030	6.5530E-05
454.470	9.2414E-05
462.770	6.5182E-04
489.050	5.7894E-04

$\sqrt{\sum A_{ij}^2}$ =1.9119E-02

E_i (eV) = 38.1910

E_j (eV)	A_{ij} (meV^{-1})
-22.200	3.9566E-03
-2.952	3.7005E-03
21.806	8.3990E-03
23.464	1.2543E-02
59.519	6.8181E-03
69.232	1.5209E-02
113.030	3.0767E-03
120.870	3.5859E-03
129.190	1.2418E-03
154.360	2.2550E-04
170.390	3.3951E-03
192.720	1.4794E-03
199.400	1.0945E-03
219.520	6.2014E-05
221.290	1.6137E-03
251.650	1.3739E-03
263.230	1.0775E-03
285.910	1.1331E-03
305.620	9.9582E-04
309.470	4.3251E-05
329.110	1.4431E-03
342.000	9.8900E-04
365.360	7.3947E-04
369.490	7.2329E-04
401.100	4.2543E-04
402.920	4.1263E-05
421.030	8.4695E-05
454.470	1.1941E-04
462.770	8.4219E-04
489.050	7.4790E-04

$\sqrt{\sum A_{ij}^2} = 2.4236E-02$

E_i (eV) = 41.0320

E_j (eV)	A_{ij} (meV^{-1})
-22.200	3.8110E-03
-2.952	3.4910E-03
21.806	7.2188E-03
23.464	1.0604E-02
59.519	7.9328E-03
69.232	1.6884E-02
113.030	3.2254E-03
120.870	3.7451E-03
129.190	1.2928E-03
154.360	2.3312E-04
170.390	3.4992E-03
192.720	1.5199E-03
199.400	1.1236E-03
219.520	6.3538E-05
221.290	1.6531E-03
251.650	1.4043E-03
263.230	1.1006E-03
285.910	1.1560E-03
305.620	1.0151E-03
309.470	4.4080E-05
329.110	1.4697E-03
342.000	1.0068E-03
365.360	7.5229E-04
369.490	7.3576E-04
401.100	4.3243E-04
402.920	4.1941E-05
421.030	8.6055E-05
454.470	1.2126E-04
462.770	8.5508E-04
489.050	7.5905E-04

$\sqrt{\sum A_{ij}^2} = 2.4399E-02$

E_i (eV) = 49.8750

E_j (eV)	A_{ij} (meV^{-1})
-22.200	3.8683E-03
-2.952	3.3629E-03
21.806	5.7208E-03
23.464	8.1609E-03
59.519	1.7594E-02
69.232	2.8459E-02
113.030	4.2542E-03
120.870	4.8727E-03
129.190	1.6625E-03
154.360	2.9255E-04
170.390	4.3455E-03
192.720	1.8674E-03
199.400	1.3769E-03
219.520	7.7344E-05
221.290	2.0112E-03
251.650	1.6959E-03
263.230	1.3261E-03
285.910	1.3876E-03
305.620	1.2150E-03
309.470	5.2737E-05
329.110	1.7543E-03
342.000	1.2002E-03
365.360	8.9479E-04
369.490	8.7481E-04
401.100	5.1292E-04
402.920	4.9740E-05
421.030	1.0194E-04
454.470	1.4336E-04
462.770	1.0105E-03
489.050	8.9589E-04

$\sqrt{\sum A_{ij}^2} = 3.6528E-02$

E_i (eV) = 64.4990

E_j (eV)	A_{ij} (meV^{-1})
-22.200	2.8617E-03
-2.952	2.3438E-03
21.806	3.3471E-03
23.464	4.6743E-03
59.519	3.0321E-02
69.232	1.0358E-01
113.030	4.9267E-03
120.870	5.4612E-03
129.190	1.8139E-03
154.360	3.0271E-04
170.390	4.4012E-03
192.720	1.8514E-03
199.400	1.3581E-03
219.520	7.5322E-05
221.290	1.9568E-03
251.650	1.6271E-03
263.230	1.2670E-03
285.910	1.3164E-03
305.620	1.1469E-03
309.470	4.9733E-05
329.110	1.6475E-03
342.000	1.1243E-03
365.360	8.3499E-04
369.490	8.1583E-04
401.100	4.7628E-04
402.920	4.6177E-05
421.030	9.4435E-05
454.470	1.3236E-04
462.770	9.3228E-04
489.050	8.2472E-04

$\sqrt{\sum A_{ij}^2} = 1.0860E-01$

E_i (eV) = 90.1670

E_j (eV)	A_{ij} (meV^{-1})
-22.200	8.0686E-04
-2.952	6.2039E-04
21.806	7.6386E-04
23.464	1.0508E-03
59.519	1.8003E-03
69.232	8.5570E-03
113.030	3.8215E-03
120.870	3.6640E-03
129.190	1.0988E-03
154.360	1.5485E-04
170.390	2.1229E-03
192.720	8.4585E-04
199.400	6.1291E-04
219.520	3.2986E-05
221.290	8.5502E-04
251.650	6.8910E-04
263.230	5.3164E-04
285.910	5.4410E-04
305.620	4.6901E-04
309.470	2.0301E-05
329.110	6.6669E-04
342.000	4.5272E-04
365.360	3.3358E-04
369.490	3.2552E-04
401.100	1.8841E-04
402.920	1.8259E-05
421.030	3.7185E-05
454.470	5.1774E-05
462.770	3.6414E-04
489.050	3.2076E-04

$\sqrt{\sum A_{ij}^2} = 1.0826E-02$

E_i(eV)= 98.0960

E_j(eV)	A_{ij}(meV^{-1})
-22.200	9.5692E-04
-2.952	7.2588E-04
21.806	8.6904E-04
23.464	1.1924E-03
59.519	1.8160E-03
69.232	7.8800E-03
113.030	7.4281E-03
120.870	6.2717E-03
129.190	1.7509E-03
154.360	2.2431E-04
170.390	2.9910E-03
192.720	1.1639E-03
199.400	8.3910E-04
219.520	4.4616E-05
221.290	1.1555E-03
251.650	9.2010E-04
263.230	7.0741E-04
285.910	7.1999E-04
305.620	6.1824E-04
309.470	2.6742E-05
329.110	8.7552E-04
342.000	5.9349E-04
365.360	4.3610E-04
369.490	4.2537E-04
401.100	2.4548E-04
402.920	2.3786E-05
421.030	4.8372E-05
454.470	6.7199E-05
462.770	4.7239E-04
489.050	4.1552E-04

$\sqrt{\sum A_{ij}^2}$ =1.3535E-02

E_i (eV) = 103.6600

E_j (eV)	A_{ij} (meV^{-1})
-22.200	7.8559E-04
-2.952	5.9094E-04
21.806	6.9571E-04
23.464	9.5314E-04
59.519	1.3632E-03
69.232	5.6745E-03
113.030	1.0169E-02
120.870	7.1286E-03
129.190	1.8317E-03
154.360	2.1381E-04
170.390	2.7832E-03
192.720	1.0622E-03
199.400	7.6261E-04
219.520	4.0162E-05
221.290	1.0394E-03
251.650	8.2002E-04
263.230	6.2880E-04
285.910	6.3730E-04
305.620	5.4565E-04
309.470	2.3590E-05
329.110	7.7057E-04
342.000	5.2167E-04
365.360	3.8254E-04
369.490	3.7301E-04
401.100	2.1479E-04
402.920	2.0810E-05
421.030	4.2277E-05
454.470	5.8634E-05
462.770	4.1204E-04
489.050	3.6206E-04

$\sqrt{\sum A_{ij}^2} = 1.4417E-02$

E_i (eV) = 128.2000

E_j (eV)	A_{ij} (meV^{-1})
-22.200	1.9706E-04
-2.952	1.4399E-04
21.806	1.6044E-04
23.464	2.1876E-04
59.519	2.6262E-04
69.232	9.9308E-04
113.030	1.8827E-03
120.870	5.0169E-03
129.190	1.4158E-02
154.360	1.2421E-04
170.390	1.3195E-03
192.720	4.3949E-04
199.400	3.0738E-04
219.520	1.5274E-05
221.290	3.9369E-04
251.650	2.9466E-04
263.230	2.2274E-04
285.910	2.2075E-04
305.620	1.8618E-04
309.470	8.0285E-06
329.110	2.5919E-04
342.000	1.7432E-04
365.360	1.2653E-04
369.490	1.2318E-04
401.100	7.0173E-05
402.920	6.7950E-06
421.030	1.3734E-05
454.470	1.8897E-05
462.770	1.3257E-04
489.050	1.1591E-04

$\sqrt{\sum A_{ij}^2} = 1.5263E-02$

E_i (eV) = 145.8600

E_j (eV)	A_{ij} (meV^{-1})
-22.200	1.5970E-04
-2.952	1.1492E-04
21.806	1.2460E-04
23.464	1.6952E-04
59.519	1.8918E-04
69.232	6.9204E-04
113.030	7.8781E-04
120.870	1.3326E-03
129.190	7.6144E-04
154.360	3.4617E-04
170.390	2.0552E-03
192.720	5.4798E-04
199.400	3.7017E-04
219.520	1.7147E-05
221.290	4.3998E-04
251.650	3.1138E-04
263.230	2.3205E-04
285.910	2.2512E-04
305.620	1.8724E-04
309.470	8.0551E-06
329.110	2.5733E-04
342.000	1.7207E-04
365.360	1.2380E-04
369.490	1.2036E-04
401.100	6.7943E-05
402.920	6.5760E-06
421.030	1.3236E-05
454.470	1.8092E-05
462.770	1.2674E-04
489.050	1.1036E-04

$\sqrt{\sum A_{ij}^2} = 2.9907E-03$

E_i (eV) = 148.0500

E_j (eV)	A_{ij} (meV^{-1})
-22.200	4.6450E-04
-2.952	3.3370E-04
21.806	3.6078E-04
23.464	4.9071E-04
59.519	5.4362E-04
69.232	1.9824E-03
113.030	2.1761E-03
120.870	3.6101E-03
129.190	1.9831E-03
154.360	1.3740E-03
170.390	6.6492E-03
192.720	1.6938E-03
199.400	1.1372E-03
219.520	5.2073E-05
221.290	1.3352E-03
251.650	9.3687E-04
263.230	6.9674E-04
285.910	6.7384E-04
305.620	5.5936E-04
309.470	2.4056E-05
329.110	7.6740E-04
342.000	5.1273E-04
365.360	3.6846E-04
369.490	3.5814E-04
401.100	2.0193E-04
402.920	1.9543E-05
421.030	3.9312E-05
454.470	5.3690E-05
462.770	3.7603E-04
489.050	3.2727E-04

$\sqrt{\sum A_{ij}^2} = 9.0671E-03$

E_i (eV) = 167.1700

E_j (eV)	A_{ij} (meV^{-1})
-22.200	3.2068E-04
-2.952	2.2745E-04
21.806	2.4061E-04
23.464	3.2669E-04
59.519	3.4331E-04
69.232	1.2252E-03
113.030	1.0809E-03
120.870	1.6274E-03
129.190	7.5621E-04
154.360	5.1974E-04
170.390	3.5426E-02
192.720	2.2741E-03
199.400	1.3914E-03
219.520	5.4593E-05
221.290	1.3875E-03
251.650	8.8228E-04
263.230	6.4154E-04
285.910	6.0078E-04
305.620	4.8887E-04
309.470	2.0956E-05
329.110	6.5889E-04
342.000	4.3679E-04
365.360	3.1025E-04
369.490	3.0102E-04
401.100	1.6774E-04
402.920	1.6225E-05
421.030	3.2462E-05
454.470	4.3973E-05
462.770	3.0744E-04
489.050	2.6625E-04

$\sqrt{\sum A_{ij}^2} = 3.5685E-02$

E_i (eV) = 178.9600

E_j (eV)	A_{ij} (meV^{-1})
-22.200	2.4457E-04
-2.952	1.7233E-04
21.806	1.8031E-04
23.464	2.4460E-04
59.519	2.5068E-04
69.232	8.8592E-04
113.030	7.1911E-04
120.870	1.0509E-03
129.190	4.6751E-04
154.360	2.1926E-04
170.390	1.0783E-02
192.720	3.4209E-03
199.400	1.7774E-03
219.520	5.7085E-05
221.290	1.4372E-03
251.650	8.3071E-04
263.230	5.9246E-04
285.910	5.4038E-04
305.620	4.3292E-04
309.470	1.8511E-05
329.110	5.7571E-04
342.000	3.7946E-04
365.360	2.6724E-04
369.490	2.5896E-04
401.100	1.4311E-04
402.920	1.3836E-05
421.030	2.7580E-05
454.470	3.7150E-05
462.770	2.5942E-04
489.050	2.2390E-04

$\sqrt{\sum A_{ij}^2} = 1.1765E-02$

E_i (eV) = 196.2500

E_j (eV)	A_{ij} (meV^{-1})
-22.200	1.3824E-04
-2.952	9.6594E-05
21.806	9.9702E-05
23.464	1.3511E-04
59.519	1.3441E-04
69.232	4.6975E-04
113.030	3.4968E-04
120.870	4.9707E-04
129.190	2.1297E-04
154.360	7.9034E-05
170.390	2.1935E-03
192.720	8.1847E-03
199.400	7.0791E-03
219.520	6.1072E-05
221.290	1.4913E-03
251.650	6.6902E-04
263.230	4.5752E-04
285.910	3.9564E-04
305.620	3.0773E-04
309.470	1.3097E-05
329.110	3.9935E-04
342.000	2.6054E-04
365.360	1.8080E-04
369.490	1.7481E-04
401.100	9.5251E-05
402.920	9.2031E-06
421.030	1.8231E-05
454.470	2.4329E-05
462.770	1.6956E-04
489.050	1.4554E-04

$\sqrt{\sum A_{ij}^2} = 1.1230E-02$

E_i(eV)= 202.7200

E_j(eV)	A_{ij}(meV^{-1})
-22.200	2.2156E-04
-2.952	1.5438E-04
21.806	1.5864E-04
23.464	2.1491E-04
59.519	2.1178E-04
69.232	7.3761E-04
113.030	5.3542E-04
120.870	7.5543E-04
129.190	3.2052E-04
154.360	1.1297E-04
170.390	2.8953E-03
192.720	4.7678E-03
199.400	1.1084E-02
219.520	1.3959E-04
221.290	3.3183E-03
251.650	1.2500E-03
263.230	8.3573E-04
285.910	7.0367E-04
305.620	5.3975E-04
309.470	2.2922E-05
329.110	6.9275E-04
342.000	4.4991E-04
365.360	3.1023E-04
369.490	2.9967E-04
401.100	1.6231E-04
402.920	1.5678E-05
421.030	3.0976E-05
454.470	4.1179E-05
462.770	2.8677E-04
489.050	2.4560E-04

$\sqrt{\sum A_{ij}^2}$ =1.3069E-02

E_i (eV) = 211.0000

E_j (eV)	A_{ij} (meV^{-1})
-22.200	2.9534E-04
-2.952	2.0512E-04
21.806	2.0966E-04
23.464	2.8391E-04
59.519	2.7670E-04
69.232	9.5990E-04
113.030	6.7746E-04
120.870	9.4815E-04
129.190	3.9815E-04
154.360	1.3331E-04
170.390	3.1857E-03
192.720	3.6048E-03
199.400	4.3843E-03
219.520	3.8043E-04
221.290	8.2765E-03
251.650	2.0795E-03
263.230	1.3382E-03
285.910	1.0800E-03
305.620	8.1126E-04
309.470	3.4345E-05
329.110	1.0246E-03
342.000	6.6112E-04
365.360	4.5176E-04
369.490	4.3580E-04
401.100	2.3410E-04
402.920	2.2603E-05
421.030	4.4499E-05
454.470	5.8849E-05
462.770	4.0938E-04
489.050	3.4956E-04

$\sqrt{\sum A_{ij}^2} = 1.1134E-02$

E_i (eV) = 242.4100

E_j (eV)	A_{ij} (meV^{-1})
-22.200	1.6798E-04
-2.952	1.1543E-04
21.806	1.1605E-04
23.464	1.5695E-04
59.519	1.4791E-04
69.232	5.0714E-04
113.030	3.3107E-04
120.870	4.5378E-04
129.190	1.8567E-04
154.360	5.5346E-05
170.390	1.1593E-03
192.720	8.5585E-04
199.400	7.6314E-04
219.520	9.1387E-05
221.290	2.6025E-03
251.650	5.9042E-03
263.230	2.1665E-03
285.910	1.2003E-03
305.620	7.8374E-04
309.470	3.2547E-05
329.110	9.0079E-04
342.000	5.6125E-04
365.360	3.6605E-04
369.490	3.5078E-04
401.100	1.8099E-04
402.920	1.7442E-05
421.030	3.3769E-05
454.470	4.3606E-05
462.770	3.0186E-04
489.050	2.5433E-04

$\sqrt{\sum A_{ij}^2} = 7.3032E-03$

E_i (eV) = 299.8400

E_j (eV)	A_{ij} (meV^{-1})
-22.200	1.4626E-04
-2.952	9.9118E-05
21.806	9.7570E-05
23.464	1.3175E-04
59.519	1.1928E-04
69.232	4.0357E-04
113.030	2.4297E-04
120.870	3.2655E-04
129.190	1.3054E-04
154.360	3.5496E-05
170.390	6.8346E-04
192.720	4.2069E-04
199.400	3.4629E-04
219.520	2.7598E-05
221.290	7.4148E-04
251.650	1.1996E-03
263.230	1.3056E-03
285.910	3.9720E-03
305.620	9.0824E-03
309.470	2.4017E-04
329.110	2.8274E-03
342.000	1.4049E-03
365.360	7.2788E-04
369.490	6.7819E-04
401.100	3.0056E-04
402.920	2.8780E-05
421.030	5.2741E-05
454.470	6.3369E-05
462.770	4.3262E-04
489.050	3.5130E-04

$\sqrt{\sum A_{ij}^2} = 1.0704E-02$

E_i(eV) = 302.6800

E_j(eV)	A_{ij}(meV^{-1})
-22.200	7.8719E-05
-2.952	5.3318E-05
21.806	5.2442E-05
23.464	7.0809E-05
59.519	6.4008E-05
69.232	2.1646E-04
113.030	1.2995E-04
120.870	1.7454E-04
129.190	6.9717E-05
154.360	1.8904E-05
170.390	3.6313E-04
192.720	2.2252E-04
199.400	1.8285E-04
219.520	1.4473E-05
221.290	3.8855E-04
251.650	6.1511E-04
263.230	6.5787E-04
285.910	1.7914E-03
305.620	9.6951E-03
309.470	1.8495E-04
329.110	1.7001E-03
342.000	8.1789E-04
365.360	4.1312E-04
369.490	3.8389E-04
401.100	1.6790E-04
402.920	1.6069E-05
421.030	2.9324E-05
454.470	3.5051E-05
462.770	2.3907E-04
489.050	1.9365E-04

$\sqrt{\sum A_{ij}^2} = 1.0126E-02$

E_i (eV) = 380.7200

E_j (eV)	A_{ij} (meV^{-1})
-22.200	7.2126E-05
-2.952	4.8264E-05
21.806	4.6634E-05
23.464	6.2886E-05
59.519	5.5063E-05
69.232	1.8434E-04
113.030	1.0462E-04
120.870	1.3877E-04
129.190	5.4643E-05
154.360	1.4075E-05
170.390	2.5954E-04
192.720	1.4790E-04
199.400	1.1835E-04
219.520	8.4843E-06
221.290	2.2540E-04
251.650	2.7635E-04
263.230	2.5101E-04
285.910	3.6007E-04
305.620	4.3129E-04
309.470	2.0028E-05
329.110	9.8936E-04
342.000	9.4381E-04
365.360	1.9157E-03
369.490	2.5952E-03
401.100	9.2138E-04
402.920	8.2451E-05
421.030	9.7832E-05
454.470	8.1977E-05
462.770	5.3005E-04
489.050	3.7858E-04

$\sqrt{\sum A_{ij}^2} = 3.7768E-03$

E_i (eV) = 391.8300

E_j (eV)	A_{ij} (meV^{-1})
-22.200	6.5200E-05
-2.952	4.3570E-05
21.806	4.2017E-05
23.464	5.6653E-05
59.519	4.9437E-05
69.232	1.6534E-04
113.030	9.3306E-05
120.870	1.2362E-04
129.190	4.8610E-05
154.360	1.2463E-05
170.390	2.2898E-04
192.720	1.2971E-04
199.400	1.0359E-04
219.520	7.3728E-06
221.290	1.9573E-04
251.650	2.3635E-04
263.230	2.1302E-04
285.910	2.9938E-04
305.620	3.4899E-04
309.470	1.6095E-05
329.110	7.5622E-04
342.000	6.8123E-04
365.360	1.0326E-03
369.490	1.2118E-03
401.100	1.8816E-03
402.920	1.5331E-04
421.030	1.2545E-04
454.470	8.9653E-05
462.770	5.6946E-04
489.050	3.9184E-04

$\sqrt{\sum A_{ij}^2} = 2.8522E-03$

BIBLIOGRAPHY

Ab64 Abov, Y.G., Krupchitsky, P.A., and Oratovsky, Y.A., Phys. Lett. **12**,25(1964).

Ab64a Abragam, A. and Borghini, M., Progress in Low Temperature Physics, North-Holland, **4**,384(1964).

Ab68 Abov, Y.G. *et al.*, Phys. Lett. **B27**,16(1968).

Ab72 Abov, Y.G. *et al.*, Yad. Fiz. **16**,1218(1972).

Ad75 Adelburger, E.G. *et al.*, Phys. Rev. Lett. **34**,402(1975).

Ad83 Adelburger, E.G. *et al.*, Phys. Rev. **C27**,2833(1983).

Ad84 Adelburger, E.G., Hoodbhay, P., and Brown, B.A., Phys. Rev. **C30**,456(1984).

Ad85 Adelburger, E.G. and Haxton, W.C., Annu. Rev. Nucl. Part. Sci. **35**,501(1985).

Ah82 Ahrens, G. *et al.*, Nucl. Phys. **A390**,486(1982).

Al61 Alburger, D.E. *et al.*, Phil. Mag. **6**,171(1961).

Al71 Allison, P.W. *et al.*, IEEE Trans. Nucl. Sci. **ns-18**,126(1971).

Al72 Alberi, J., Wilson, R., and Schroeder, I.G., Phys. Rev. Lett. **29**,518(1972).

Al83 Alfimenkov, V.P. *et al.*, Nucl. Phys. **A398**,93(1983).

Al84 Alfimenkov, V.P. *et al.*, Sov. Phys. Usp. **27**,797(1984).

Al89 Alvarey, M., Sbriz, L., and Cordero, M., Am. J. Phys. **57**,954(1989).

As66 Ashgar, M. *et al.*, Nucl. Phys. **76**,196(1966).

As85 Anaso, Y. *et al.*, J. Phys. Soc. Jpn. **54**,3734(1985).

Av84 Avenier, M. *et al.*, Phys. Lett. **B137**,125(1984).

Av85 Avenier, M. *et al.*, Nucl. Phys. **A436**,83(1985).

Av86 Avenier, M. *et al.*, Nucl. Phys. **A459**,335(1986).

Ba78 Barnes, C.L. *et al.*, Phys. Rev. Lett. **40**,840(1978).

Ba80 Balzer, R. *et al.*, Phys. Rev. Lett. **44**,699(1980).

Ba85 Barron, R.F., Cryogenic Systems, Oxford University Press, 1985.

Be37 Bethe, H.A., Rev. Mod. Phys. **9**,69(1937).

Be79 Benkoula, H. *et al.*, Phys. Lett. **B71**,287(1979).

Bh79 Bhat, M.L. *et al.*, BNL-NCS-17541, 1979.

Bi52 Biedenharn, L.C., Blatt, J.M., and Rose, M.E., Rev. Mod. Phys. **24**,249(1952).

Bi80 Bizetti, P.G. *et al.*, Lett. Nuovo Cimento **29**,167(1980).

Bi87 Biryukov, S.A. *et al.*, Sov. J. Nucl. Phys. **45**,937(1987).

Bl52 Blatt, J.M. and Weisskopf, V.F., Theoretical Nuclear Phyics, J. Wiley and Sons, 1952.

Bl60 Blin-Stoyle, R.J., Phys. Rev. **118**,1605(1960).

Bl61 Blin-Stoyle, R.J., Phys. Rev. **120**,181(1961).

Bl73 Blin-Stoyle, R.J., Fundamental Interactions and the Nucleus, North-Holland, 1973.

Bo37 Bohr, N., Nature **137**,344(1937).

Bo59 Boehm, F. and Hauser, U., Nucl. Phys. **14**,615(1959/60).

Bo64 Bollinger, L.M. and Thomas, G.E., Phys. Lett. **8**,45(1964).

Bo89 Bowman, C.D., Bowman, J.D., and Yuan, V.W., Phys. Rev. **C39**,1721(1989).

Bo89a Bowman, J.D., private communication, 1989.

Bo90 Bowman, J.D. *et al.*, Phys. Rev. Lett. **65**,1192(1990).

Bo90a Bowman, J.D. *et al.*, Nucl. Instrum. Methods **A297**,183(1990).

Br40 Breit, G., Phys. Rev. **58**,1068(1940).

Br59 Bromley, D.A. *et al.*, Phys. Rev. **114**,759(1959).

Bu81 Bunakov, V.E. and Gudkov, V.P., Z. Phys. **A303**,285(1981).

Bu83 Bunakov, V.E. and Gudkov, V.P., Nucl. Phys. **A401**,93(1983).

Ca77 Cavaignac, J.F. *et al.*, Phys. Lett. **B67**,148(1977).

Co53 Coester, F. and Jauch, J.M., Helv. Phys. Acta **26**,3(1953).

Co78 Corvi, F., Pasquariello, G., and van der Veer, T., Proceedings of an International Conference on Neutron Physics and Nuclear Data, OECD Nuclear Energy Agency, 1978, p712.

Da76 Danilyan, G.V. *et al.*, Yad. Fiz. **24**,34(1976).

Da77 Danilyan, G.V. *et al.*, Preprint ITEP-4 (Moscow 1977).

Da78 Danilyan, G.V. *et al.*, Yad. Fiz. **27**,42(1978).

De57 Devons, S. and Goldfarb, L.J.B., "Angular Correlations", Handbuch der Physik, v.42, 1957.

De80 Desplanques, B., Donahue, J.G., and Holstein, B.R., Ann. Phys. (NY) **124**,449(1980).

De84 Desplanques, B., J. Phys. Colloq. **45**,55(1984).

Ed55 Edmonds, A.R., Angular Momentum in Quantum Mechanics, CERN55-26, 1955.

Ef79 Efron, B., SIAM Rev. **21**,460(1979).

Eg88 von Egidy, T., Schmidt, H.H., and Behkami, A.N., Nucl. Phys. **A481**,189(1988).

Fa53 Fano, U., Phys. Rev. **90**,577(1953).

Fe34 Fermi, E., Z. Phys. **88**,161(1934).

Fe73 Feshbach, E. and Tadic, D., Phys. Reports **C6**,123(1973).

Fi83 Fifield, L.K. *et al.*, Nucl. Phys. **A394**,1(1983).

Fo71 Forman, L. *et al.*, Proceedings of the Third Conference on Neutron Cross Section Technology, National Technical Information Service, 1971, p.735.

Fo71a Foderaro, A., Elements of Neutron Interaction Theory, The MIT Press, 1971.

Fo80 Forte, M. *et al.*, Phys. Rev. Lett. **45**,2088(1980).

Fr88a French, J.B. *et al.*, Ann. Phys. (NY) **181**,198(1988).

Fr88b French, J.B. *et al.*, Ann. Phys. (NY) **181**,235(1988).

Ga57 Garwin, R.L. *et al.*, Phys. Rev. **108**,1589(1957).

Ga64 Garg, J.B. *et al.*, Phys. Rev. **134**,B985(1964).

Ga73 Gari, M., Phys. Reports **C6**,317(1973).

Gi89 Gilmore, J.S., Robinson, H.A., and Russell, G.J., Advanced Neutron Sources 1988, Institute of Physics, 1989, p.469.

Go90 Gould, C.R. *et al.*, Int. J. Mod. Phys. A **5**,2181(1990).

Gr61 Grodzins, L. and Genovese, F., Phys. Rev. **121**,228(1961).

Ha59 Haas, R., Leipuner, L.B., and Adair, R.K., Phys. Rev. **116**,122(1959).

Ha89 Photomultiplier Tubes, Hamamatsu Corp., 360 Foothill Rd., PO Box 6910, Bridgewater, NJ 08807, 1989.

Ha89a ENDF/B-VI data file for ^{1}H (National Nuclear Data Center, BNL, Upton, NY, 1989), evaluation by G.A. Hale *et al.*

He58 Heer, E., Roberts, A., and Tinlot, J., Phys. Rev. **111**,645(1958).

He78 Henley, E.M., J. Phys. Soc. Jpn. Suppl. **44**,812(1978).

He82 Henneck, R. *et al.*, Phys. Rev. Lett. **48**,725(1982).

He82a Heckel, B. *et al.*, Phys. Lett. **B119**,298(1982).

Hu89 Hughes, H.G., III, Advanced Neutron Sources 1988, Institute of Physics, 1989, p.455.

Je63 Jefferies, C.D., Dynamic Nuclear Orientation, Interscience, 1963.

Ka61 Kaufmann, W. and Waffler, H., Nucl. Phys. **24**,62(1961).

Ka83 Kadmenskii, S.G., Markuskev, V.P., and Furman, V.I., Sov. J. Nucl. Phys. **37**,345(1983).

Ke73 Keyworth, G.A. *et al.*, Phys. Rev. **C8**,2352(1973).

Ke78 Keyworth, G.A. and Moore, M.S., Proceedings of an International Conference on Neutron Physics and Nuclear Data, OECD Nuclear Energy Agency, 1978, p.241.

Ki81 King, S.E., Lau, Y.C., and Gould, C.R., IEEE Trans. Nucl. Sci. **ns-28**,3822(1981).

Ki82 Kimura, M., Carpenter, J.M., and Mildner, D.F.R., Nucl. Instrum. Methods **198**,433(1982).

Kn68 Knapp, E.A. *et al.*, Rev. Sci. Instrum. **39**,979(1968).

Ko81 Kolomensky, E.A. *et al.*, Phys. Lett. **B107**,272(1981).

Kr72 Kreyszig, E., Advanced Engineering Mathematics, John Wiley and Sons, 1972.

Kr87 Krupchitsky, P.A., Fundamental Research with Polarized Slow Neutrons, Springer-Verlag, 1987.

Kr88 Krane, K.S., Introductory Nuclear Physics, John Wiley and Sons, 1988.

Kr89 Krupchitsky, P.A., Nucl. Instrum. Methods **A284**,71(1989).

Ku59 Kuehner, J.A. *et al.*, Phys. Rev. **114**,775(1959).

La39 Lamb, W.E., Jr., Phys. Rev. **55**,190(1939).

La58 Lane, A.M. and Thomas, R.G., Rev. Mod. Phys. **30**,257(1958).

La89 Larson, N.M., ORNL/TM-9179/R2, 1989.

Le56 Lee, T.D. and Yang, C.N., Phys. Rev. **104**,254(1956).

Lo69 Lobashov, V.M. *et al.*, Phys. Lett. **B30**,39(1969).

Ma89 Masuda, Y. *et al.*, Nucl. Phys. **A504**,269(1989).

Ma89a Macek, R.J., Advanced Neutron Sources 1988, Institute of Physics, 1989, p.91.

Mi64 Michel, F.C., Phys. Rev. **133**,B329(1964).

Mi89 Mitchell, G.E., Nucl. Instrum. Methods **B40/41**,474(1989).

Mo89 ENDF/B-VI data file for ^{238}U (National Nuclear Data Center, BNL, Upton, NY, 1989), evaluation by M. Moxon.

Mu81 Mughabghab, S.F., Divadeenam, M., and Holden, N.E., Neutron Cross Sections Volume 1, Academic Press, 1981.

Na67 Nagle, D.A. *et al.*, Rev. Sci. Instrum. **38**,1583(1967).

Ne74 Neubeck, K., Schober, H., and Waffler, H., Phys. Rev. **C10**,320(1974).

No86 Noguera, S. and Desplanques, B., Nucl. Phys. **A457**,189(1986).

Ol81 Olsen, D.K. and Ingle, R.W., ORNL/TM-7661, 1981.

Ol82a Olsen, D.K., Ingle, R.W., and Portney, J.L., Nucl. Sci. Eng. **82**,289(1982).

Ol82b Olsen, D.K., ORNL/TM-8056, 1982.

Pe82 Perey, R.B. *et al.*, Nucl. Sci. Eng. **80**,189(1982).

Pr58 Price, W.J., Nuclear Radiation Detection, McGraw-Hill, 1958.

Pr62 Preston, M.A., Physics of the Nucleus, Addison-Wesley, 1962.

Ra42 Racah, G., Phys. Rev. **62**,438(1942).

Ra72 Rahn, F. *et al.*, Phys. Rev. **C6**,1854(1972).

Ri69 Ribon, P., Ph.D. dissertation, University of Paris, 1969.

Ro90 Robinson, H.A., private communication, 1990.

Ru90 Russell, G.J., private communication, 1990.

Sc68 Schiff, L.I., Quantum Mechanics, McGraw-Hill, 1968.

Se58 Segel, R.E., Kane, J.V., and Wilkinson, D.H., Phil. Mag. **3**,204(1958).

Se61 Segel, R.E., Olness, J.W., and Sprenkel, E.L., Phys. Rev. **123**,1382(1961).

Se61a Segel, R.E., Olness, J.W., and Sprenkel, E.L., Phil. Mag. **6**,163(1961).

Sn78 Snover, K.A. *et al.*, Phys. Rev. Lett. **41**,145(1978).

St74 Stodolsky, L., Phys. Lett. **50B**,352(1974).

Su82 Sushkov, O.P. and Flambaum, V.U., Sov. Phys. Usp. **25**,1(1982).

Ta57 Tanner, N., Phys. Rev. **107**,1203(1957).

Vl61 Vladimirsky, V.V. and Andreev, V.N., Zh. Eskp. Teor. Fiz. **41**,663(1961).

Vo62 Vogt, E., Rev. Mod. Phys. **34**,723(1962).

Wa67 Warming, E. *et al.*, Phys. Lett. **B25**,200(1967).

Wa69 Warming, E. *et al.*, Phys. Lett. **B29**,564(1969).

Wi47 Wigner, E.P. and Eisenbud, L., Phys. Rev. **72**,29(1947).

Wi58a Wilkinson, D.H., Phys. Rev. **109**,1603(1958).

Wi58b Wilkinson, D.H., Phys. Rev. **109**,1610(1958).

Wi58c Wilkinson, D.H., Phys. Rev. **109**,1614(1958).

Wu57 Wu, C.S. *et al.*, Phys. Rev. **105**,1413(1957).

Yo87 Yoder, N.R., IUCF XSYS Manual, IUCF, 1987.

Yu91 Yuan, V.W. *et al.*, Phys. Rev. **C** (to be published).

Za83 Zaretskii, D.F. and Sirotkin, V.K., Sov. J. Nucl. Phys. **37**,361(1983).

Za85 Zaretskii, D.F. and Sirotkin, V.K., Sov. J. Nucl. Phys. **42**,561(1985).

Za87 Zaretskii, D.F. and Sirotkin, V.K., Sov. J. Nucl. Phys. **45**,808(1987).